Numerical Methods in Shape Spaces and Optimal Branching Patterns

Dissertation

zur Erlangung des Doktorgrades (Dr. rer. nat.)
der Mathematisch-Naturwissenschaftlichen Fakultät
der Rheinischen Friedrich-Wilhelms-Universität Bonn

vorgelegt von

Behrend Heeren

aus Kamp-Lintfort

Bonn, November 2016

Summary

The contribution of this thesis is twofold. The main part deals with numerical methods in the context of *shape space analysis*, where the shape space at hand is considered as a *Riemannian manifold*. In detail, we apply and extend the *time-discrete geodesic calculus* (established by Rumpf and Wirth [WBRS11, RW15]) to the space of *discrete shells*, *i.e.* triangular meshes with fixed connectivity. The essential building block is a variational time-discretization of geodesic curves, which is based on a local approximation of the squared Riemannian distance on the manifold. On physical shape spaces this approximation can be derived *e.g.* from a *dissimilarity measure*. The dissimilarity measure between two shell surfaces can naturally be defined as an elastic deformation energy capturing both membrane and bending distortions. Combined with a non-conforming discretization of a physically sound thin *shell model* the time-discrete geodesic calculus applied to the space of discrete shells is shown to be suitable to solve important problems in computer graphics and animation. For example, shape interpolation and extrapolation can be performed consistently within the proposed framework, since the geodesic calculus is based on a classical Riemannian structure. In a Riemannian manifold, interpolation and extrapolation can be realized by computing shortest geodesics and by applying the exponential map, respectively.

To extend the existing calculus, we introduce a generalized *spline functional* based on the covariant derivative along a curve in shape space whose minimizers can be considered as *Riemannian splines*. We establish a corresponding time-discrete functional that fits perfectly into the framework of Rumpf and Wirth, and prove this discretization to be consistent. Several numerical simulations reveal that the optimization of the spline functional—subject to appropriate constraints—can be used to solve the *multiple interpolation* problem in shape space, *e.g.* to realize keyframe animation. To enable efficient computations in the space of discrete shells we make use of an approximative scheme, *i.e.* we compute classical cubic splines in the space of mesh descriptors (the space of edge lengths, triangle volumes and dihedral angles) and project the solution back to the manifold.

Based on the spline functional, we further develop a simple *regression model* which generalizes linear regression to nonlinear shape spaces. In detail, a conventional data term measuring the deviation of the regression curve from the input data is augmented by the spline functional, which acts as a penalty term. In the limit, the corresponding minimizer is given by a geodesic curve that fits the given data best. Practically, the penalty approach enables to control the fitting curve in a user-defined manner. Numerical examples based on real data from anatomy and botany show the capability of the model.

Finally, we apply the *statistical analysis* of elastic shape spaces presented by Rumpf and Wirth [RW09b, RW11a] to the space of discrete shells. To this end, we compute a Fréchet mean within a class of shapes bearing highly nonlinear variations and perform a principal component analysis with respect to the metric induced by the Hessian of an elastic shell energy. In particular, our model is shown to outperform a standard Procrustes analysis, *i.e.* applying the Euclidean metric to the vector of nodal positions.

The last part of this thesis deals with the optimization of microstructures arising *e.g.* at austenite-martensite interfaces in shape memory alloys. For a corresponding scalar problem, Kohn and Müller [KM92, KM94] proved existence of a minimizer and provided a lower and an upper bound for the optimal energy. To establish the upper bound, they studied a particular branching pattern generated by mixing two different martensite phases. We perform a finite element simulation based on subdivision surfaces that suggests a topologically different class of branching patterns to represent an optimal microstructure. Based on these observations we derive a novel, low dimensional family of patterns and show—numerically and analytically—that our new branching pattern results in a significantly better upper energy bound.

Contents

Nomenclature

Some symbols are ambiguous but unique in the present context. For a functional $\mathcal{W} = \mathcal{W}[y_1, \ldots, y_n]$, the first Gâteaux derivative w.r.t. y_i (resp. the ith argument) is denoted by either $\partial_{y_i}\mathcal{W}$ or $\partial_i\mathcal{W}$ or $\mathcal{W}_{,i}$.

Differential geometry:

$\mathcal{M}$	generic Riemannian manifold or shape space, finite or infinite dimensional
g, g_p	generic Riemannian metric (at $p \in \mathcal{M}$)
dist	Riemannian distance
$x : \omega \subset \mathbb{R}^d \to \mathcal{M}$	(local) parametrization of finite dimensional manifold
$\frac{D}{dt}$	covariant derivative along a curve
g, h	first and second fund. form of an embedded surface in $\mathbb{R}^3$, respectively; either as bilinear form or as matrix representation in $\mathbb{R}^{2,2}$
$S : T_p\mathcal{M} \to T_p\mathcal{M}$	embedded shape operator; endomorphism on tangent space
s	matrix rep. of shape operator in parameter domain, *i.e.* $s = g^{-1}h \in \mathbb{R}^{2,2}$

Geodesic calculus:

K	order resp. stepsize of time-discrete quantities; stepsize is given by $\tau = K^{-1}$
$\mathcal{W}$	approximation of squared Riemannian distance, *i.e.* dissimilarity measure
$\mathcal{L}, L^K$	(time-discrete) length functional (of order K)
$\mathcal{E}, E^K$	(time-discrete) path energy (of order K)
$\mathcal{F}, F^K$	(time-discrete) spline energy (of order K)
$\exp, (\text{EXP}^K)$	(time-discrete) exponential map (of order K)
$\log, (\frac{1}{K}\text{LOG})$	(time-discrete) logarithm (of order K)
$\text{P}, \mathbf{P}$	(time-discrete) parallel transport map

Physical symbols:

$\mathcal{S}_\delta \subset \mathbb{R}^3$	thin shell with thickness $\delta > 0$
δ	physical thickness of a thin shell
$\mathcal{S} \subset \mathbb{R}^3$	mid-layer of a thin shell; embedded surface
$\phi : \mathcal{S} \to \mathbb{R}^3$	generic deformation of a smooth shell
$\mathcal{G}[\phi]$	tangential distortion tensor w.r.t. ϕ, *i.e.* $\mathcal{G}[\phi] = g^{-1}g_\phi \in \mathbb{R}^{2,2}$ (pointwise)
$\mathcal{W}$	generic deformation energy; dissimilarity measure
W	generic energy density
η	bending parameter $\eta = \delta^2$
λ, μ	Lamé-Navier coefficients

Discrete shells:

$\mathbf{S}$	discrete shell, *i.e.* nodal positions of a triangle mesh
$\mathcal{N}, \mathcal{T}, \mathcal{E}$	set of nodes, faces and edges, respectively, of a triangle mesh
X, T, E	node, face and edge, respectively, of a triangle mesh
Φ	discrete deformation, *i.e.* piecewise affine transformation acting on $\mathbf{S}$
$\mathbf{W}$	discrete deformation energy resp. discrete dissimilarity measure
G_T, H_T	piecewise-constant, discrete first and second fund. forms as matrices in $\mathbb{R}^{2,2}$
B_T	matrix rep. of piecewise-constant discrete shape operator; $B_T = G_T^{-1}H_T$
$\mathcal{G}[\Phi]_T$	piecewise-constant, discrete distortion tensor
N, N_T, N_E	normal on triangle mesh; either associated with a face T or an edge E
θ_E	dihedral angle associated with an edge E
d_E	area associated with an edge E; $d_E = \frac{1}{3}(|T| + |T'|)$, if $E = T \cap T'$

1 Introduction

Numerical methods in shape spaces

Computer animation films have become increasingly popular within the last two decades. Artists in animation studios design sophisticated characters of rising complexity and authenticity. The character models are typically represented by triangle meshes consisting of tens or even hundreds of thousands of degrees of freedoms. Moreover, animators are able to generate movements of these artificial creatures that are almost indistinguishable from natural motions. The development of flexible and effective tools supporting artists in creating such authentic animations is linked to the mathematics of shape spaces. In particular, a comprehensive understanding of both the geometry and the physics of natural deformations and motion paths of complex shapes is essential for the creation of realistic models and efficient algorithms.
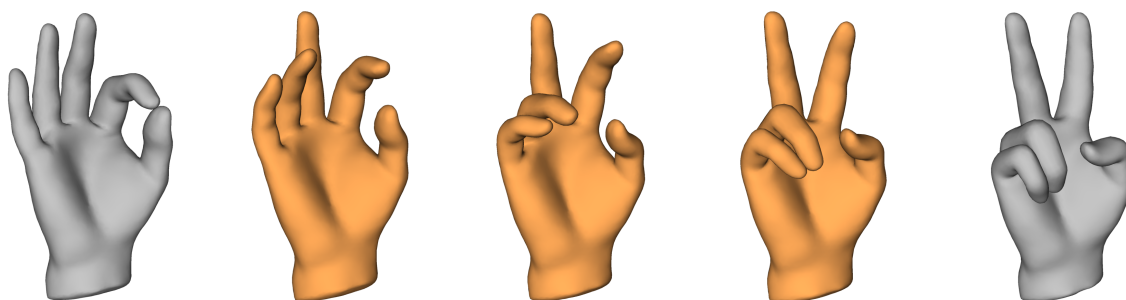
Figure 1.1: *Morphing by means of interpolation (orange) computed between two input shapes (gray).*

The *numerical methods in shape spaces* developed in this thesis are designed to be useful in various applications in computer graphics and animation. Typical problems in this field of activity are for instance:

- Morphing. Given two different poses of a complex shape, one aims at computing a natural and visually appealing transformation, *i.e.* an *interpolation*, between them. In Fig. 1.1 we show the morphing between two hand shapes.

- Keyframe animation. Given a sequence of character poses, so-called keyframes, one aims at computing a realistic deformation path meeting all of the keyframes, *i.e.* a *multiple interpolation*. As one can see in Fig. 1.2, a smooth keyframe animation is in general *not* realizable by morphing consecutive keyframes.

- Shape modeling. Given a certain character pose one wants to (i) identify infinitesimal variations that represent natural movements and (ii) *extrapolate* these small variations to create an animation sequence of this motion. This method is referred to as "animation without animating", *cf*. Fig. 1.3.

- Detail transfer. When animating *e.g.* a running sequence of a character, one first designs the physical motion on a coarse scale (for example, by using shape modeling and keyframe animation). Afterwards, the fine scale details, *e.g.* the wrinkles on the skin, are added to a single frame of the sequence. A desirable aim is that these details are then automatically transferred to the entire sequence in a visually appealing manner.
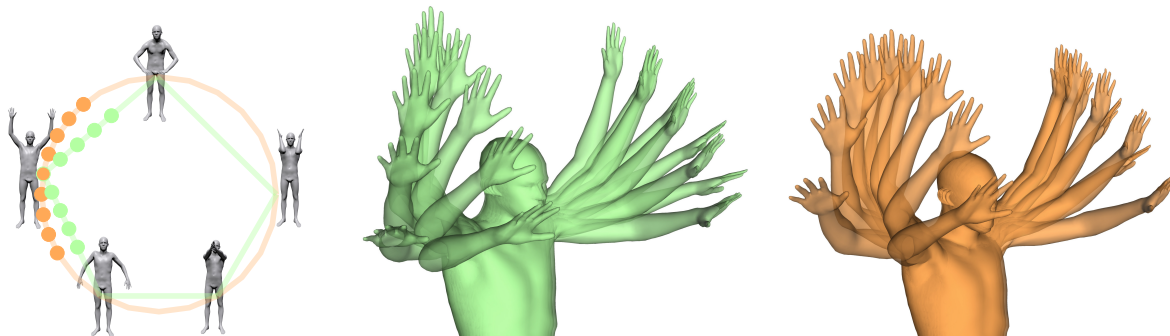
Figure 1.2: *A keyframe animation (orange) allows for a temporally smooth interpolation of a given set of keyframe poses (gray, left), in contrast to a consecutive morphing technique (green).*

What is the contribution of this thesis?   Although there exists a variety of established methods to solve these problems, we identify and address two main issues in existing approaches. First, several problems are frequently tackled with independent and heuristic approaches, which often disregard important *geometric* features. For example, nonlinear operations are transferred to linear operations in a different space and afterwards the linear solution is projected back onto the original space [SZGP05, WDAH10, FB11]. Thereby, some geometric intuition is lost in the final projection step and the relation between the actual nonlinear solution and the projected linear solution is often hard to understand. However, it might be obvious to apply existing and established methods to new problems once a geometric understanding is at hand. Second, the investigation and incorporation of relevant *physical* properties is often missing or distorted by linearization artefacts [BS08]. For example, a geometrically accurate approach is augmented by a non-physical regularization [KMP07]. Nevertheless, the existing heuristic or linearized approaches typically outperform geometrically and physically sophisticated methods in terms of efficiency and computation times. Since performance is an (if not *the*) important quantity in animation business, nonlinear physics-based methods are often considered as practically not feasible. One goal of this thesis is to propose a comprehensive *geometric calculus* that induces consistent tools for multiple applications in computer graphics that allow for a geometric interpretation. This leads to the notion of shape spaces that are equipped with the mathematical structure of a Riemannian manifold. Furthermore, we aim at a sound *physical model* to realize visually appealing simulation results induced by potentially large and global deformations without using non-physical or artificial terms for regularization. In particular, we are interested in a model that is invariant with respect to rigid body motions. Finally, the corresponding temporal and spatial discretization is supposed to allow for robust and efficient simulations. Hence, the entire modeling and discretization problem is a delicate balancing act between geometric consistency and physical soundness on the one hand and efficiency and practicability on the other hand.
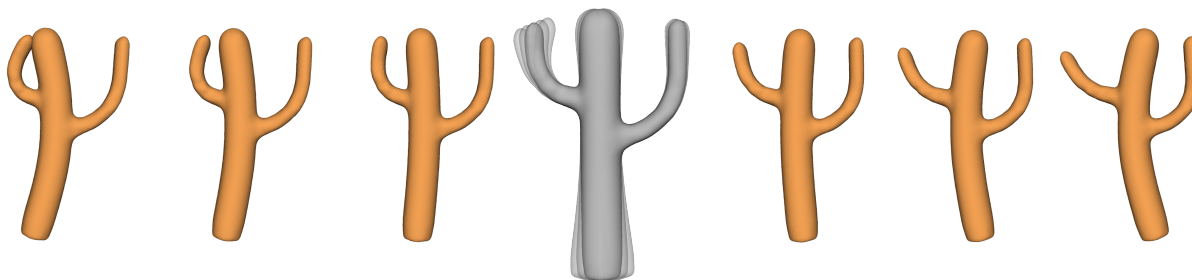
Figure 1.3: *Shape modeling: we determine plausible, infinitesimal variations of a neutral cactus pose (gray) and compute extrapolations to create realistic motion paths (orange).*

How can we benefit from a Riemannian structure? It is due to Kendall [Ken84] that complex shapes, *e.g.* curves, images or solid materials, are considered as individual elements or points in a high or even infinite dimensional space, *i.e.* the *shape space*. Initially, this space is just a collection of shapes without any mathematical structure. In particular, most shape spaces cannot be considered as linear vector spaces. Nevertheless, one is interested in performing mathematical operations on the set of shapes, for instance, for two given shapes one wants to compute a connecting path (*cf.* Fig. 1.1). The notion of an optimal or shortest path then induces naturally a distance measure which allows *e.g.* for a statistical analysis. It is a well-established ansatz to consider a given shape space as a *Riemannian manifold*. In a nutshell, a Riemannian manifold can be described as a collection of points that is locally equivalent to the Euclidean space, together with a so-called *Riemannian metric*, *i.e.* an instruction how to measure local variations. On a Riemannian manifold the notion of a connecting path and hence a (locally) shortest path, a so-called *geodesic*, is intrinsically given. Thereby, a geodesic connecting two points can be considered as the solution of the interpolation problem. Similarly, one can extrapolate by extending geodesic paths via the *exponential map* or transport details via the *parallel transport*—both are inherent concepts in Riemannian manifold theory. Hence the mathematical structure of a Riemannian manifold leads to the solution of a couple of problems relevant *e.g.* in computer graphics. In chapter 2 we review different approaches to shape space modeling in the literature and in chapter 3 we provide a brief summary on relevant concepts in Riemannian manifolds.

What is a suitable time-discretization? In a Riemannian setup, shortest curves, *i.e.* geodesics, are defined as *time-continuous* objects. To introduce a temporal discretization we make use of the so-called *time-discrete geodesic calculus* developed by Martin Rumpf, Benedikt Wirth and coworkers in a sequence of papers, *cf.* *e.g.* [Wir09, WBRS11, RW13]. This discrete calculus is based on a variational time-discretization of geodesic curves and can be applied to a wide range of shape spaces. Besides the notion of time-discrete geodesics, the framework additionally provides time-discrete analogons for several basic but crucial geometric operators, *e.g.* for the exponential map and for parallel transport. Under certain assumptions on the underlying manifold, Rumpf and Wirth [RW15] have shown consistency and convergence of all time-discrete operators to their corresponding continuous counterparts.
From a practical point of view, the entire variational time-discretization is based on a local approximation of the squared Riemannian distance. In particular, one does not need to have an explicit notion of the Riemannian metric—although the distance is induced by the metric, one can also recover the metric from the distance. This circumstance is useful especially when dealing with physical shape spaces: here the a priori definition of a suitable Riemannian metric is not obvious whereas the derivation of a physically meaningful *dissimilarity measure* is feasible. Eventually, exactly this dissimilarity measure represents the approximation of the squared Riemannian distance. In chapter 4, we provide a brief but comprehensive summary of the time-discrete geodesic calculus proposed by Rumpf and Wirth and present a consistency proof of a time-discrete covariant derivative.

Which shape space is appropiate for animation? Although characters in animation movies appear as *solid* bodies they are represented typically as *hollow* objects, whose "skin" is described *e.g.* by triangle meshes in the computer. This is due to the fact that the physical simulation of a solid is computationally much harder than the corresponding simulation of the surface of that solid: if the solid is represented within a (regular) grid with grid size h, one needs $O(h^{-3})$ grid points to represent the interior but only $O(h^{-2})$ points to represent the surface. To obtain visually appealing animations the surface is modeled physically as a *thin shell*, which is a three-dimensional material whose thickness is very small when compared to other directions. Mathematically, a shell is represented by the midlayer of the material which is typically described by a two-dimensional surface in $\mathbb{R}^3$. In order to deal with shells in the computer, this *midsurface* is discretized *e.g.* by a polyhedral surface, hence the shape space considered here is the space of triangle meshes, also referred to as (discrete) shell space.

However, the physical modeling starts in the continuous setup, where we consider thin shells as being made of an *elastic* material. Intuitively, elasticity accounts for the desired property that the object is able to be deformed without being disrupted or irreversible damaged. An elastic deformation is hence characterized by being reversible in the sense that the material will return to its initial shape and size when the outer forces are removed. The elastic energy associated with the deformation of one shell into another shell will eventually represent the dissimilarity measure on the shell space—the key ingredient of the variational time-discretization. Although perfect elasticity is an approximation of the real world, simulations based on elastic materials look indeed very natural and are mathematically well established [Cia88, CM08]. Nevertheless, we eventually drop the pure elastic model and consider *viscous* transformations. This results in a physical model that allows for the notion of paths—a concept that is axiomatically not present in elasticity theory. From a physical point of view, one can think of a viscous deformation as the concatenation of many infinitesimally small elastic deformations with subsequent stress relaxation.

As mentioned above, the surface or shell representation seems to be advantageous in terms of the number of degrees of freedom. Nevertheless, the deformation of a shell is physically much more involved than the deformation of a solid. A reason for this is that the mathematical description of a shell deformation depends on the first and second fundamental forms of the shell's midsurface, which are highly nonlinear geometric objects. The differences become obvious when considering discretized surfaces, *e.g.* triangle meshes. Typically, the elastic deformation of a solid can be described by means of the standard linear finite elements method (FEM) as only first derivatives of the deformation are involved in the energy. However, the numerical treatment of surface bending requires second derivatives of the deformation resp. derivatives of the normal field which cannot be described by linear FEM. In particular, it is not straightforward how to describe a derivative of a normal on a triangle mesh in the first place as a polyhedral surface is naturally equipped with a piecewise constant normal field. One opportunity to resolve this problem is to make use of higher order conforming methods, *e.g.* one introduces additional degrees of freedom possibly without any geometric meaning that lead to large linear systems. In contrast, we consider a non-conforming method in the spirit of *Discrete Differential Geometry*, whose degrees of freedom are given by the nodal positions only. To this end, we propose a discrete shape operator on triangle meshes that locally depends on six vertices which leads to a *discrete bending model*. Alternatively, we make use of the popular *Discrete Shells* model [GHDS03] which depends on two triangles, *i.e.* four vertices, only, and thus represents the smallest possible stencil to realize bending.

Summing up, the appropiate shape space for our purposes is the finite dimensional space of triangle meshes, the so-called *space of discrete shells*. To enable a direct comparison of two different discrete shells, we make use of the common *fixed connectivity constraint*, *i.e.* we postulate a one-to-one correspondence between all nodes and all triangles. The discrete bending model is a core ingredient of a physically sound *dissimilarity measure* on the space of discrete shells, which penalizes variations of the first and second fundamental forms. As explained in the previous paragraph, the designation of a shape space together with the notion of a dissimilarity measure enables a direct application of the time-discrete geodesic calculus. In chapter 5 we present a detailed description as well as an empirical validation of our discrete shell space model.

day 54   *day 69*   *day 83*   *day 96*   *day 109*
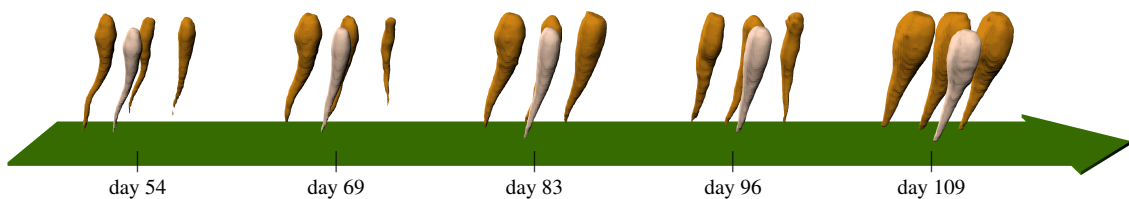
Figure 1.4: *Discrete regression curve (bright) for sugar beet input shapes (dark) at 5 different days in the vegetation period.*

What are relevant applications and desirable extensions?   The time-discrete geodesic calculus applied to the finite dimensional space of discrete shells directly offers solutions to several problems listed above: the interpolation problem between two shapes is solved by computing a time-discrete geodesic (*cf*. Fig. 1.1), extrapolation is performed by means of the time-discrete exponential map and detail transfer can be realized by the notion of a time-discrete parallel transport. In chapter 6, we show numerous numerical simulation results and present a comprehensive qualitative and quantitative evaluation.

Finally, in chapter 7 we discuss three further applications and extensions of the existing calculus:

- **Riemannian splines**. The *multiple interpolation problem*, *i.e.* the computation of a smooth path interpolating more than two keyframes, cannot be solved immediately by existing tools of the geodesic calculus. For example, using piecewise geodesic interpolation generates a continuous path that exhibits discontinuities in the velocity at the keyframes. In Euclidean space, cubic splines minimize the total squared second time-derivative among all curves that pass through a given set of interpolation points—this property is related to the minimization of bending energy. We build on this observation and establish how splines can be variationally defined on general shape spaces where keyframe poses act as interpolation points. To this end we introduce a generalized *spline energy* based on the covariant derivative of the velocity field along the curve—an object which represents a generalization of the second time-derivative. We present a corresponding time-discrete functional that fits perfectly into the time-discrete geodesic calculus, and prove this discretization to be consistent (see chapter 4). Additionally, we show that the optimization of the spline energy—subject to appropiate constraints—can be used to solve the multiple interpolation problem, *e.g.* to realize keyframe animation (*cf*. Fig. 1.2).

- **Regression**. Based on the (time-discrete) spline energy we develop a (time-discrete) *regression model* which generalizes linear regression to shape spaces. To this end, we investigate time-discrete geodesic paths in shape space which best approximate given time indexed input shapes in a least squares sense. Here, we apply the regression model to the space of *viscous fluidic objects* and present numerical simulation results based on real data from anatomy and botany. Fig. 1.4 shows a time-discrete geodesic regression path representing the growth process of sugar beet roots over a vegetation period.

- **Statistical analysis**. Statistical models of the shape or appearance of a class of objects are widely used in computer graphics to model the variability over the object class. Typically, the dimension of the space of observations is orders of magnitude greater than the number of samples in the training set, *i.e.* the underlying shape space is sampled very sparsely. In this scenario, the quality of the model depends on the validity of the structure of the manifold. We aim at performing basic statistical operations on the space of discrete shells. In this setup, the so-called Procrustes analysis, *i.e.* pre-registering shapes and applying the standard Euclidean metric to the vector of nodal positions, fails to capture nonlinear shell deformations appropiately. To account for this inherent nonlinearity we apply the *statistical analysis* of elastic shape spaces presented by Rumpf and Wirth [RW09b, RW11a] to the space of discrete shells and compute for example a principal component analysis of a set of facial expressions.

These applications illustrate in particular that the *numerical methods in shape spaces* developed in this thesis are not only limited to either the space of discrete shells nor to applications in computer graphics and animation. In fact, the geodesic calculus and the corresponding extensions discussed here can be used in various areas, for instance in computer vision and pattern recognition, medical image processing or material sciences, and can be applied to different shape spaces, *e.g.* the space of viscous fluidic objects (*cf*. Fig. 1.4).

Optimizing branching patterns

Mathematical modeling has become an important tool in materials sciences since it provides a useful guide in the search for new functionalities. Important applications include the formation of microstructures and phase transitions *e.g.* in shape memory alloys. Shape memory alloys are metals that are able to recover their original shapes by external stimuli, *e.g.* by a change in temperature, after permanant deformation. The reason for this effect lies in a particular behavior of the atomic lattice, namely a solid-to-solid phase transition, *e.g.* at some specific temperature. If the material is at a high temperature (called austenitic phase), it prefers a cubic lattice structure, whereas at a low temperature (called martensitic phase), there are different preferred lattices with fewer symmetries. Most interesting are, however, intermediate temperatures where both states, *i.e.* martensite and austenite, are present in the material and hence also transition layers between these phases occur. In practice, one often observes complex phase mixtures at these interfaces that lead to characteristic microstructures. By the Hadamard jump condition there is a correspondence between coherent martensite-martensite resp. austenite-martensite interfaces and a rank-one connection between the gradients of the (continuous) macroscopic deformation. However, typical materials do not fulfill such a condition at an austenite-single-martensite interface. In physical experiments, one often observes fine twins of *two* variants of martensite, separated from a uniform region of austenite by a transition layer bearing a certain microstructure. These observations coincide with the mathematical modeling, since a coherent austenite-twinned-martensite transition is possible—in the sense of the Hadamard jump condition—if an average deformation of two variants of martensite is compatible with the austenite.

In this thesis, we focus on a simplified mathematical model describing such a coherent phase transition between a totally rigid austenite and a twinned-martensite phase. Typically, the mathematical analysis of phase transitions proceeds from nonlinear elasticity theory. The central goal is to determine the microstructures and their energetics by studying a suitable energy functional for the transition layers. Although the general situation is described most appropiately by a three-dimensional deformation acting on a three-dimensional material, there exists a well-established reduced model based on a two-dimensional domain and a scalar-valued function [KM92]. This two-dimensional model has proven to be able to capture characteristic geometric properties of the microstructures occuring at an austenite-martensite interface. Although many researchers have investigated this reduced model within the last two decades, a precise description of an *optimal* microstructure, *i.e.* a minimizer of the mathematical model, has not been found so far. However, there are many qualitative and quantitative results one can build on (*cf*. *e.g.* [Con00b, Con06]). Most important, Kohn and Müller [KM94] have proven the existence of such a minimizer and derived an energy scaling law in terms of certain physical parameters. These scaling laws are optimal in the sense that they provide both an upper and a lower bound on the minimal energy, whereas the constants in the bounds still differ. To realize the upper bound, Kohn and Müller constructed an explicit twinned-martensite structure represented by a certain test function. In particular, their microstructure *branches*, *i.e.* refines in a self-similar way, when it approaches the austenite phase.

In chapter 8, we investigate an improvement of the upper bound which is realized by constructing explicit test functions that are energetically advantageous. Based on the insight of a numerical experiment we shall deduce a new branching pattern, that differs both geometrically and topologically from the one considered by Kohn and Müller. In particular, we show numerically and analytically that this new branching pattern produces a better upper constant in the energy bounds.

Reading suggestion Chapter 2 to chapter 7 solely deal with the primary focus of this thesis, *i.e.* numerical methods in shape spaces. A comprehensive description of our investigations of optimal branching patterns is given in chapter 8 in a self-contained way.

Collaborations and publications

The contributions and main results of this thesis are the outcome of various intense collaborations and resulted in a sequence of joint publications.

The results on time-discrete geodesic calculus in the space of shells presented in chapter 6 are joint work with Martin Rumpf, Peter Schröder (Caltech), Max Wardetzky (University of Göttingen) and Benedikt Wirth (University of Münster), and have been published in [HRWW12, HRS$^+$14]. I contributed to the development of the time-discrete geodesic calculus, in particular its application to the space of shells, and investigated the spatial discretization using tools from discrete differential geometry.
Riemannian splines and the application to the space of discrete shells—as presented in Sec. 4.3 resp. Sec. 7.1—were investigated again in joint work with M. Rumpf, P. Schröder, M. Wardetzky and B. Wirth, and resulted in another publication [HRS$^+$16]. I contributed to the mathematical modeling of the nonlinear model and elaborated the simplified $L\Theta A$-model and its efficient implementation. Rigorous aspects of time-discrete Riemannian splines are about to be submitted [HRW16], where I provided the consistency proof as presented in Sec. 4.3.
The work on time-discrete regression presented in Sec. 7.2 was initiated by a collaboration of M. Rumpf and B. Wirth with Thomas Fletcher (University of Utah). I developed a simplification of the original, fully nonlinear model and provided the resulting implementation and numerical experiments—in cooperation with Benjamin Berkels (RWTH Aachen University). The results were published in [BFH$^+$13].
The work concerning the statistical analysis of an elastic shell space, which is presented in Sec. 7.3, is based on a collaboration with William Smith and Chao Zhang (University of York), and has been published in [ZHRS15]. Here, my contribution was the mathematical modeling as well as the preparation of the general framework of the implementation, whereas C. Zhang assembled the corresponding code fractions and performed the quantitative analysis (not shown in this thesis).
The investigation of optimal branching patterns in chapter 8 is joint work with Patrick W. Dondl (University of Freiburg) and M. Rumpf. The basic code structure to perform the subdivision finite element simulations has been provided by P. Dondl, whereas I focussed on the actual numerical experiments as well as on the numerical and analytical optimization of the reduced model. The results of the numerical optimization have been published in [DHR16].

Finally, I contributed to three further publications, that are not considered in this thesis:

- S. Markett, C. Montag, B. Heeren, R. Sariyska, B. Lachmann, B. Weber, and M. Reuter. Voxelwise eigenvector centrality mapping of the human functional connectome reveals an influence of the catechol-o-methyltransferase val158met polymorphism on the default mode and somatomotor network. *Brain Structure and Function*, 221:2755-2765, 2016.

- S. Markett, M. Reuter, B. Heeren, B. Lachmann, B. Weber and C. Montag. Working memory capacity and the functional connectome - insights from resting-state fMRI and voxelwise eigenvector centrality mapping, *Brain Imaging and Behavior*, 2017, *accepted*.

- B. Heeren, B. Wirth, S. Paulus, H. Goldbach, H. Kuhlmann and M. Rumpf. Statistical shape analysis of tuber roots: a methodological case study on laser scanned sugar beets, *in revision*.

2 Related work

2.1 Shape spaces and applications

During the past decades, the notion of *shape spaces* had an increasing impact on the development of new methods in computer vision, graphics and imaging, ranging from shape morphing and modeling, to shape statistics and computational anatomy. A variety of spaces of shapes has been investigated in the literature, some of them are finite-dimensional and consider polygonal curves or triangulated surfaces as shapes, but most approaches deal with infinite-dimensional spaces of shapes. In this section, we provide a summary of related work on shape spaces, with a particular focus on those spaces that can be considered as Riemannian manifolds. Eventually, we gather relevant references concerning applications in shape spaces that are also considered in this thesis, such as interpolation and extrapolation, spline curves, regression analysis and statistical models.

Shape spaces The classical treatment of shape space is due to Kendall [Ken84], where shapes are considered as k-tuples of points in $\mathbb{R}^d$, which can *e.g.* be interpreted as discretized curves or nodes of triangulated surfaces, equipped with a quotient metric which is given by the Euclidean metric modulo translation, rotation and scaling. Linear vector spaces can be considered as shape spaces as well. However, they are usually not a priori invariant with respect to translation or rotation, *i.e.* shape alignment is necessary as a preprocessing step. Examples include the vector space of landmark positions [CTCG95, PMR05, SBYA05] or Lebesgue spaces [LGF00, TYW$^+$03, DRT06]. Further classical shape spaces are induced by the Hausdorff distance or by the Gromov-Hausdorff distance. Although the former one is not invariant with respect to rigid body motion, it has for instance been used to perform shape statistics [CFKM06]. In contrast, the latter one defines an isometrically invariant distance measure between shapes and has been used *e.g.* for shape clustering [MS05] or classification [BBK08]. However, as the lack of isometries is measured globally it is difficult to examine local isometry distortions.

Of particular interest for this work are shape spaces that also have the structure of a Riemannian manifold. The study of spaces of shapes from a Riemannian perspective allows to transfer many important concepts from classical geometry to these usually infinite-dimensional spaces. For example, paths, path lengths and hence shortest paths, *i.e.* geodesics, are generically defined. Further classical geometric quantities, such as exponential map, logarithm, covariant derivative and parallel transport, can be transferred likewise. In the following, we will review works related to three designated groups of shape spaces, namely the space of curves, surfaces and volumetric objects (*e.g.* images).

For planar *curves*, different Riemannian metrics have been devised. In their seminal work, Michor and Mumford [MM06] examined Riemannian metrics on the manifold of closed regular curves. They showed the L^2-metric in tangent space to be pathologic in the sense that it leads to arbitrarily short geodesic paths[1]. To overcome the issue of degenerating geodesic paths they employed a curvature-weighted L^2-metric instead (see also [MM07]). For the same reason, Mennucci *et al.* [MYS08] used Sobolev metrics in the tangent space of planar curves, with applications in image segmentation via active

---

[1]Later, Michor and Mumford [MM05] showed that the vanishing geodesic distance phenomenon for the L^2-metric occurs also in more general shape spaces.

contours [SYM07]. Klassen *et al.* [KSMJ04] proposed a framework for geodesics in the space of arclength parameterized curves and implemented a shooting method to find them. As Riemannian metric, they used the L^2-metric on variations of the direction or curvature functions of the curves. Schmidt *et al.* [SCC06] presented an alternative variational approach for the computation of these geodesics. Srivastava *et al.* [SJJK06, SKJJ11] utilized an elastic string representation where curves can bend and locally stretch. To this end, they assigned different weights to the L^2-metric on stretching and bending variations and obtained an elastic model of curves, which allowed them to define geodesics and distances between curves in a way that is invariant to transformations including reparameterization. In a sequence of papers, Bruveris and co-workers inverstigated properties of the spaces of parametrized and unparametrized curves in $\mathbb{R}^d$, equipped with Sobolev metrics [Bru15, BMM14, BBMM14, BBM16]. For example in [BBM16], the set of Sobolev metrics was divided into three groups: the L^2-metric, which is on the one hand simple and reparametrization invariant, but on the other hand unsuitable for shape analysis (*cf*. [MM06]), the H^1-metric, which was shown to be well suited for numerical computations and therefore useful in applications, and finally higher-order Sobolev metrics, whose theoretical properties make them good candidates for use in shape analysis. In particular, the space of closed plane curves equipped with a second-order Sobolev metric is geodesically complete. Hence Riemannian metrics for spaces of curves obviously benefit from a second-order Sobolev term, which can be considered as a bending term that regularizes curvature changes. This circumstance has also been exploited in physical simulations of viscous or elastic rods, whose centerline is mathematically described by a curve (*cf*. [BWR$^+$08, RW15]).

With regards to the space of *surfaces*, Kurtek *et al.* [**?**, KKDS10] studied L^2-metrics on special representations of parameterized surfaces. To this end, they considered geodesic paths between surfaces parametrized over the unit sphere, using local changes of the area element as a Riemannian metric. As opposed to physics-based approaches, parameterization-based metrics are not intrinsically blind to rigid body motions. Moreover, their induced distance is related to the extrinsic difference between surfaces in ambient space, so that even isometric surfaces might be far apart from one another. A combination of extrinsic and intrinsic distance was presented in [BBK09]. Bauer and co-workers [BHM11, BHM12a, BHM12b, BHM12c] generalized weighted L^2-metrics (introduced in [MM07] for planar curves) to higher dimensions, *i.e.* to the space of surfaces described by embeddings or immersions of a given manifold. They computed geodesic equations and sectional curvatures and showed in particular that these metrics overcome the degeneracy of the L^2-metric; corresponding numerical results were shown in [BB11].

Most relevant for this thesis is the work of Kilian *et al.* [KMP07] who investigated the (finite dimensional) space of triangulated surfaces. To this end, they considered geodesics between consistently triangulated meshes, with respect to a Riemannian metric measuring the stretching of triangle edges. While this metric is invariant to rigid body motions, the lack of a bending term leaves a non-trivial kernel of the metric tensor, including all isometric deformations of the triangular mesh. To avoid the resulting unphysical wrinkling effects, a supplementary (non physical) regularization was incorporated. Liu *et al.* [LSDM10] proposed a metric on a finite simplicial complex that measures resistance of an edge to stretching and compression, quantified by changes in edge length, and bending, which is associated with directional changes. In contrast to the latter examples, we make use of the regularizing effect of a bending energy and stay entirely in a physical simulation framework.

Riemannian spaces have also been considered for *volumetric* shapes, where the metric imitates a physical energy dissipation induced by the deformation of a shape consisting of ductile or viscous material [FJSY09, FW06, WBRS11, RW13]. Such physical approaches tend to yield intuitive paths and allow for a simple and natural time-discretization. For example, Wirth *et al.* [WBRS11] defined time-discrete geodesics as minimizers of a time-discrete path energy. In the context of viscous objects, the path energy consists of a sum of elastic matching energies, whose Hessian at the identity coincides with the rate of

viscous dissipation generated by the shape deformation. This viscous dissipation model can be applied to two- and three-dimensional shapes, where the former ones represent a subset of the space of images.

A different approach to obtain a Riemannian structure on the space of images is using the *metamorphosis approach* [MY01, TY05b, TY05a, HTY09]. This approach generalizes the *flow of diffeomorphism* [DGM98] and considers the temporal change of image intensities *and* image intensity variations (controlled by the so-called material derivative) along motion paths. Physically, the underlying metric describes the viscous dissipation in a multipolar fluid model [NŠ91]. Recently, Berkels *et al.* [BER15] applied the variational time-discretization of geodesics proposed in [WBRS11] to the Riemannian manifold induced by the metamorphosis approach. Moreover, the notion of optimal transport [Mon81, Kan42, Kan48], in particular the formulation proposed by Benamou and Brenier [BB00], can also used to define a Riemannian structure on the space of images, that are considered as measures (*cf*. *e.g*. [PPKC10, PFR12, SS13]).

Only for a few nontrivial Riemannian shape spaces geodesic paths can be computed in closed form (*e.g*. [YMSM08, SMSY11]), else the system of geodesic ODEs has to be solved using numerical time stepping schemes (*e.g*. [KSMJ04, BMTY05]). Alternatively, geodesic paths connecting shapes can also be approximated via the minimization of discretized path length [SCC06] or path energy functionals [FJSY09, WBRS11]. Instead of discretizing the underlying flow the variational discretization proposed by Rumpf and Wirth [WBRS11] is based on the direct minimization of a discrete path energy subject to data given at the initial and the end time. This approach turned out to be very stable and robust, and even for very small numbers of time steps one obtains qualitatively good results [RW13, MRSS15, BER15]. Building on this variational time-discretization, Rumpf and Wirth [RW15] developed a comprehensive discrete geodesic calculus on finite- and on certain infinite-dimensional shape spaces with the structure of a Hilbert manifolds, and presented a corresponding complete convergence analysis.

A main contribution of this thesis is the application of this discrete geodesic calculus to the space of (discrete) shells. In particular, we present features and applications of the geodesic calculus, such as (i) interpolation and extrapolation techniques, (ii) spline curves, (iii) a simple regression model and (iv) a statistical analysis in shape space. In the remainder of this subsection, we report on related work concerning these aspects and distinguish our contributions.

Interpolation and extrapolation   Many shape interpolation schemes in computer graphics are based on the following three-step procedure. First, select a number of geometric quantities or shape descriptors that determine the shape (locally). Then, based on the input shapes, compute the interpolated or extrapolated quantities. Finally, reconstruct the shape or the path in shape space, respectively, that best matches the averaged quantities. The differences between various existing methods lie in the choice of the geometric quantities. Depending on whether the quantities depend linearly or nonlinearly on the vertex positions, the reconstruction is a linear or nonlinear least-squares problem.

Examples of linear reconstruction schemes were given by Sumner *et al.* [SZGP05] and by Lipman *et al.* [LSLCO05]. The method proposed by Sumner *et al.* [SZGP05] uses deformation gradients of the triangles as geometric quantities to be interpolated (*cf*. [SP04]). However, the interpolation is nonlinear since the rotational components of the deformation gradients are extracted and nonlinearly blended by taking the shortest path in the rotation group. Naturally, the blending of the rotations is done separately for each triangle which might lead to undesirable interpolation results (*cf*. [WDAH10] for examples and a discussion of this issue). Instead of treating all triangles individually, Lipman *et al.* [LSLCO05] presented a method that takes the connectivity information of the triangle mesh into account and considers transformations that connect local frames in the mesh (*cf*. also [KG08]). To this end, a local coordinate frame is constructed for each vertex of the mesh and so-called connection map encode the transformation between neighbouring frames. A key property of this ansatz is that it represents the local geometry of a mesh in a rotation-invariant way—in contrast to methods based on deformation gradients. Furthermore,

the reconstruction process is performed in two steps: first the connection maps are used to compute local frames, and based on the local frames, the vertex coordinates are reconstructed. This approach is well-suited to represent deformations with rotational components (*i.e.* twists), but has problems when dealing with deformations that include stretching.

Examples of nonlinear reconstruction schemes were given by Winkler *et al.* [WDAH10] and by Fröhlich and Botsch [FB11]. Winkler *et al.* [WDAH10] used edge lengths and dihedral angles of the triangles of a surface mesh as geometric quantities to be interpolated. In order to find the mesh that best matches the interpolated edge lengths and angles they employed a rather complicated hierarchical shape matching technique. To achieve an improvement in this direction, Fröhlich and Botsch [FB11] introduced a fast reconstruction scheme for the interpolation based on edge lengths and dihedral angles. Their method interpolates between simplified meshes and uses deformation transfer [BSPG06] to map the coarse interpolated shapes to a fine mesh—we will later pick up their method in the context of spline interpolation.

Besides, there are numerous interpolation techniques not depending on a reconstruction step. A classical approach in this direction was presented by Alexa *et al.* [ACOL00]. They proposed a morphing technique that blends the interiors of given two- or three-dimensional shapes in an as rigid as possible manner, *i.e.* their method is locally least-distorting. As already mentioned above, Kilian *et al.* [KMP07] introduced a framework of geometric modeling in the space of triangular meshes that allows for interpolation, extrapolation and even parallel transport. This is closely related to our approach, however, we combine the geometric modeling with a physics-based metric which was not the case in the work by Kilian *et al.* [KMP07]. A more physical approach was considered by Chen *et al.* [CPSS10] which was motivated by a number of physics-like but heuristic algorithms in geometry processing. They advocated a simple geometric model for elasticity, *i.e.* the distance between the differential of a deformation and the rotation group is penalized. Due to its geometric non-linearity, the model does not suffer from linearization artifacts but is computationally almost as efficient as linear elasticity.

Recently, von Tycowisz *et al.* [vTSSH15] introduced a scheme for real-time nonlinear interpolation which exploited the fact that the set of all possible interpolated shapes is a low-dimensional object in a high-dimensional shape space. To this end they constructed a reduced optimization problem that approximates its unreduced counterpart and can be solved very efficiently. We refer to the paper of von Radziewsky *et al.* [vRESH16] for further applications of this very efficient ansatz and in particular to the work by Brandt *et al.* [BvTH16], where the reduction method was used to compute approximations to time-discrete geodesics in the sense of [WBRS11].

Although we are only dealing with the interpolation of triangle meshes embedded in three-dimensional space, we finally refer to [CWKBC13, CCW16] for related work on planar deformation techniques (*cf.* also the review by Alexa [Ale02]).

Riemannian splines In a finite dimensional Riemannian manifold so-called Riemannian cubic polynomials have been introduced first by Noakes *et al.* [NHP89] as smooth curves $y : [0, 1] \rightarrow \mathcal{M}$ that are stationary points of the functional $\mathcal{F}[y] = \int_0^1 g_y \left(\frac{D}{dt} \dot{y}, \frac{D}{dt} \dot{y} \right) dt$ satisfying certain boundary conditions. Here $\frac{D}{dt}$ denotes the covariant derivative along a curve, hence this representation is referred to as *intrinsic* formulation. A necessary condition for optimality of the boundary value problem is given by the Euler–Lagrange equation $\partial_y \mathcal{F}[y] = 0$ which turns out to be a fourth-order differential equation [NHP89]. In particular, Crouch and Silva Leite [CSL95] considered the *multiple interpolation problem* by minimizing $\mathcal{F}[y]$ subject to $y(t_j) = y^j$ for a set of data points $\left((t_j, y^j)_{1 \leq j \leq J} \right) \subset [0, 1] \times \mathcal{M}$.

Trouvé and Vialard [TV12] presented a mathematical framework to perform interpolation on time-indexed sequences of 2D or 3D shapes where they focused on the finite dimensional case of landmarks. They developed a spline interpolation method which is related to the Riemannian cubic polynomials by Noakes *et al.* [NHP89]. However, their approach incorporates a control variable u with respect to the Hamiltonian equations of the geodesics which can be interpreted as $|u|^2 = g_y(\frac{D}{dt}\dot{y}, \frac{D}{dt}\dot{y})$. Hinkle *et al.* [HMFJ12] introduced a family of higher-order Riemannian polynomials defined by $(\frac{D}{dt})^k \dot{y} = 0$

to perform polynomial regression on Riemannian manifolds. Solutions for $k = 3$ are referred to as cubic polynomials. The higher-order covariant differential equation is transferred into a system of first-order covariant differential equations which is solved by a numerical integrator scheme. This method is eventually applied to the shape spaces of 2D image data represented by landmark positions.

Instead of dealing with the *intrinsic* formulation presented above, there are several papers dealing with an *extrinsic* formulation, *i.e.* the minimization of $\int_0^1 \|\ddot{y}\|^2 \, \mathrm{d}t$ in the ambient space. The restriction of the curve to the manifold is then realized as a constraint. Wallner [Wal04] proved existence of minimizers in this setup for finite dimensional manifolds, and Pottmann and Hofer [PH05] showed that these minimizers are C^2. Additionally, Hofer and Pottmann [HP04b] provided a method for the computation of splines on parametric surfaces, level sets, triangle meshes and point set surfaces. Algorithmically, they alternately computed minimizers in the tangent plane and projected them back to the manifold.

Besides the variational formulations there are numerous contributions dealing with *subdivision schemes* to produce smooth interpolating curves on manifolds. Subdivision schemes for curves in linear spaces are well established and mostly based on repeated computations of local (affine) averages (*cf*. *e.g*. [Dyn92, Dyn02]). By replacing the operation of affine averaging either by a geodesic average or by projecting the affine averages onto the manifold one generates a Riemannian extension. Wallner and Dyn [WD05] showed that the Riemannian extension of cubic subdivision actually produces C^1-curves; Wallner proved C^2-smoothness for a certain class of subdivision schemes in [Wal06]. More practically, Rahman *et al*. [RDS$^+$05] proposed a Deslauriers-Dubuc interpolation in the tangent space, where the mapping between tangent space and manifold is realized by means of the exponential and logarithm.

In some applications it might be useful to seek for approximating rather than for interpolating curves with respect to a given set of data points. This can be done by replacing the hard interpolation constraints by soft penalty constraints [Rei67]. Recently, Brandt *et al*. [BvTH16] computed approximating curves in the space of discrete shells by using the path energy $\int_0^1 g_y(\dot{y}, \dot{y}) \, \mathrm{d}t$ as regularizer. A different approach to approximating schemes are Beziér curves. Having the notion of geodesics at hand one can easily transfer this concept to general manifolds. In fact, the Beziér curves are simply generated by applying de Casteljau's algorithm where linear interpolation is replaced by geodesic interpolation [PN07]. This was applied to the shape space of images [ERS$^+$15] resp. to the space of discrete shells [BvTH16]. Finally, Perl [Per15] introduced a Riemannian generalization of B-splines and cardinal splines and showed numerical simulations in the space of shells (represented as subdivision surfaces as in [COS00]).

In this thesis, we focus on a variational formulation based on the intrinsic functional $\mathcal{F}$ to solve the multiple interpolation problem. To this end, we consider general, possibly infinite dimensional manifolds and derive a consistent time-discretization, which is eventually applied to the space of discrete shells.

Regression curves   Time-dependent shape statistics and shape regression has already been investigated in [DFBJ07], where the regression curve is obtained via a simultaneous kernel weighted averaging in time. In the application to brain images the kernel on shape space is linked to the Sobolev metric from the group of diffeomorphisms approach [MTY02]. A variational formulation of geodesic regression was given by Fletcher [Fle11], where for given input shapes $\mathcal{S}_i$ at times t_i the (in a least squares sense) best approximating geodesic is computed as the minimizer of the energy $E[\mathcal{S}, v] = \frac{1}{2} \sum_i \mathrm{dist}^2(\exp_{\mathcal{S}}(t_i v), \mathcal{S}_i)$ over the initial shape $\mathcal{S}$ of the geodesic path and its initial velocity or momentum v. Here, $\mathrm{dist}(\cdot, \cdot)$ is the Riemannian distance and $\exp$ the exponential map. Niethammer *et al*. [NHV11] presented a computationally efficient method in the group of diffeomorphisms shape space which is based on duality calculus in constrained optimization. Hong *et al*. [HJS$^+$12] proposed a generalization allowing for image metamorphosis, *i.e.* a simultaneous diffeomorphic image deformation and image intensity modulation.

In contrast to these approaches, we do not minimize over the initial data of geodesic shooting but directly over the shapes along a time-discrete geodesic. Eventually, this is realized by a penalty approach, *i.e.* we augment the data term by the intrinsic functional $\mathcal{F}$ considered in the context of Riemannian splines.

Statistical models   Statistical models of shape have been used widely in computer vision and graphics. In a 2D setting, PCA-based models such as *active shape* [CTCG95] or *appearance models* [CET01] provide a parametric representation of shape that can be used for segmentation, tracking and recognition. In a 3D setting, they are typically used for fitting to noisy or ambiguous data or for 3D reconstruction via analysis-by-synthesis [BV99, PS09, YWS+11, SHK11, SK15]. For a recent review of statistical shape modeling see [BSBW14]. When doing statistics on manifolds the analysis is performed in a manner that respects the Riemannian geometry of the manifold. This requires Riemannian notions of concepts such as distance, mean value and covariance. In this direction, Pennec [Pen06] showed how to compute these measures for a number of geometric primitives that do not form vector spaces. Fletcher *et al.* [FLPJ04] went further, building statistical models on such manifolds via computation of the principal geodesics of a set of data. Freifeld and Black [FB12] used this principal geodesic analysis to build nonlinear models of human body shape variation. They defined a Lie group characterizing deformations of a triangle mesh and performed statistical analysis on the resulting Riemannian manifold. However, their manifold of deformations was not physically motivated.

Our approach is mostly related to the work presented by Rumpf and Wirth [RW09a, RW09b, RW11a]. They described a statistical analysis which is based on an elastic deformation energy and applied to volumetric shapes represented as boundary contours of elastic objects. We adapt their statistical framework to the space of (discrete) shells by replacing the elastic deformation energy by a suitable shell energy.

2.2 Discrete bending models

There are multiple ways how to represent an embedded surface in the computer. Typically, these approaches are either classified as *explicit* or as *implicit* representations. While implicit models are given by *e.g.* levelset functions or phasefield models, we will focus on explicit representations given by polyhedral surfaces, or more precisely, by triangle meshes. Closely related is the approximation or discretization of functions on surfaces. In this section we discuss different approaches how to discretize curvature related quantites on polyhedral surfaces. Usually the corresponding necessary optimality conditions lead to a fourth-order PDE.

A classical tool for the discretization of variational problems on triangle meshes is the finite element method (FEM), *cf*. *e.g.* [Cia78, Hug87, ZT00, Bra07]. This approach can be divided into three groups, namely (i) conforming, (ii) non-conforming and (iii) mixed methods. As we are dealing with a fourth-order problem, linear C^0-conforming finite elements do not provide the necessary regularity. Instead, one can make use of a standard C^1-conforming finite element method which offers a direct discretization of the fourth-order PDE. However, one introduces additional degrees of freedom—possibly without any geometric meaning—that lead to large linear systems [Cia78]. Alternatively, a H^2-conforming discretization can be build upon basis functions represented as so-called *subdivision surfaces* [COS00, CO01, CSA+02, GKS02], where higher order smoothness is achieved by increasing the support of the basis functions instead of introducing additional degrees of freedom[1]. Of course conformality is not a necessary condition. Hence one might consider a non-conforming finite element method for discretization, *e.g.* an adaption of the *Crouzeix-Raviart* element [WBH+07] or discontinuous Galerkin methods [KMBG09]. Other non-conforming methods seek to replace continuous geometric objects by consistent discrete counterparts instead of discretizing these geometric objects in the first place. This is *e.g.* the spirit of *discrete differential geometry* (DDG), which is used in many well-established approaches in computer graphics—we will also make use of this ansatz in our discretization. In mixed methods the fourth-order PDE problem is split into two second-order PDEs, which are approximated either by linear or by quadratic finite elements [Dzi88, ES10]. A group of fundamental examples is given by the discretization

---

[1] This method will be discussed briefly in Sec. 8.1.

of Willmore's energy [Rus05, BGN07, BGN08, BR12, PPR14]. A variety of approaches discretizing general plate and shell equations build on the *Discrete Kirchhoff Triangle* [BBH80, CB98, Bar13]. However, these splittings are often problem dependent and introduce additional degrees of freedom.

In the remainder of this section we review related works in geometry processing and computer graphics that also deal with deformations of thin shells and curvature approximations on polyhedral surfaces, *i.e. discrete shells*. Various researchers have formulated and discretized separately the membrane and bending effects of a deformation, *cf. e.g.* [TPBF87]. To this end, the treatment of membrane energy for triangulated meshes follows the widely studied models of elasticity in the context of FEM. In contrast, the geometrically *nonlinear* treatment of bending energy, which accounts for change of curvature, is more involved. As mentioned above, numerous approaches in graphics make use of tools from DDG for the treatment of bending energy. Since the leading principle of DDG is "Discretize theory, not equations", a consistent discrete theory is built up from scratch. In the following we consider (i) discrete analogons of curvature related quantities, and (ii) deformation models of discrete shells, *i.e.* polyhedral surfaces. As mentioned above, the majority of these approaches represents a non-conforming method of discretization.

Discrete curvature   Taubin [Tau95] was one of the first authors in computer vision to consider an estimation of the curvature tensor of a surface from a polyhedral approximation. Using the theory of normal cycles Cohen-Steiner and Morvan [CSM03] proved convergence results for integrated mean curvature as well as the integrated second fundamental form. Their discrete notion of (integrated) mean curvature reveals the so-called *dihedral angle* associated with an edge of the mesh which is defined as the angle between the two adjacent triangle normals. However, their assumptions on the mesh are very restrictive and there are no results for pointwise convergence. Wardetzky and co-workers [War06, War08, HPW06] established a convergence analysis for the discrete mean curvature vector in this *integrated* setup and showed that there is in general no convergence for the corresponding *pointwise* mean curvature vector on general meshes. Meyer *et al.* [MDSB02] proposed a set of discrete differential geometry operators for triangular meshes that are supposed to provide flexible tools to approximate important geometric attributes, such as normal vectors or curvatures. They started from the notion of integrated quantities which they consider as local spatial averages and derived a pointwise, discrete definition by dividing by an associated area. Hildebrandt and Polthier [HP04a] introduced a discrete vertex-based shape operator in the context of anisotropic surface filtering, which was derived from the cotangent formula [PP93]. Grinspun *et al.* [GGRZ06] provided a comparison of several discrete shape operators and proposed a new operator by introducing further degrees of freedom. In detail, their matrix-valued shape operator is constant on faces and is based on a normal field associated with edges. Such an edge normal is per definition perpendicular to the corresponding edge, but the angle of rotation about this edge is another degree of freedom. It was shown that this discrete shape operator passes a collection of empirical consistency and convergence tests even if the mesh quality is very poor. A more rigorous approach to introduce a generalized shape operator on polyhedral surfaces was performed by Hildebrandt and Polthier [HP11]. Again, they started from a weak (*i.e.* integrated) definition and derived a pointwise definition by testing with approximations of delta distributions. As in [HPW06] convergence was shown under the assumption of totally normal convergence of the polyhedral surface, whereas here also a pointwise convergence result could be established. Finally, we refer to the work by Vása *et al.* [VVP$^+$16] for a recent review on curvature estimation on meshes.

Discrete shell deformation models   Terzopoulos *et al.* [TPBF87] first introduced the concept of *elastically deformable models* for geometry or surface processing. In detail, they considered a separation of an elastic energy into the sum of a membrane and bending energy measuring variations in first and second fundamental forms, respectively. The entries of the fundamental forms were discretized by using a second-order finite differences scheme on a regular and structured quad-grid. Grinspun *et al.* [GHDS03] introduced their nowadays well-established *Discrete Shells* model based (i) on the dihedral angle representation of integrated mean curvature [CSM03] and (ii) on the reasoning "pointwise notion from spatial averaging" as proposed in [MDSB02]. In particular, the discrete bending energy of their model, which is supposed to measure squared differences of mean curvature, is still widely used in computer graphics, animation and cloth simuations due to its simplicity (*cf.* also [BMF03]). On the other hand, this energy depends on the mesh quality such that there is no convergence of this model to its continuum equivalent as shown by numerical experiments in [GGRZ06]. Wardetzky *et al.* [WBH$^+$07, BWH$^+$06] presentend a family of *discrete isometric bending models* for triangulated surfaces which were derived from an axiomatic treatment of discrete Laplace operators. For flat reference configurations and isometric surface deformations it was shown that the corresponding energies are *quadratic* in vertex positions. Furthermore, if the discrete Laplace operator is obtained by using the non-conforming Crouzeix-Raviart element their discrete isometric bending model agrees with the *Discrete Shells* bending model [GHDS03] up to second-order in the limit of small normal displacements of the plane. The work was extended for *curved* reference configurations in [GGWZ07], where the resulting bending energies were shown to be *cubic* in vertex positions. Botsch *et al.* [BPGK06] proposed a novel framework for 3D shape modeling that achieves intuitive and robust deformations by emulating physically plausible surface behavior. Here, the surface mesh is embedded in a layer of volumetric prisms, which are coupled through nonlinear, elastic forces. To deform the mesh, the prisms are rigidly transformed while minimizing an elastic energy.

Besides the nonlinear approaches mentioned above, there is an abundant literature on deformation models that include a linearization step. Linear methods are attractive for several reasons, *e.g.* they are fast, often simple to implement and robust, *i.e.* the quadratic energy has a unique global minimum (if appropriate boundary conditions are chosen). Following the comprehensive survey by Botsch and Sorkine [BK08], linear deformation approaches can be classified into (i) shell-based techniques (*e.g.* [KCVS98, BK04]) and (ii) methods based on differential coordinates [SP04, LSLCO05, KG08]. Methods of the first kind usually linearize the nonlinear elastic energy by replacing the change of first and second fundamental forms by first and second order partial derivatives of the displacement function. To this end, these methods typically have problems with large rotational deformations, as analyzed in [BS08]. Methods of the second kind manipulate the shape *e.g.* via deformation gradients [SP04] or local frames [LSLCO05, KG08], and are often translation-insensitive (see also [Sor06]).

In order to accelarate simulations that are based on nonlinear bending models one might consider the space of triangular surface descriptors, *i.e.* edge lengths, dihedral angles and triangle areas, instead. This results in an approximation with high computational efficiency since the involved energies are *quadratic* in these variables. Based on a multiscale interpolation method by Winkler *et al.* [WDAH10] this approach was first introduced by Fröhlich and Botsch [FB11]. Alternatively, there are approaches in computer graphics [GKS02] and cloth simulation [TWS06] that build on so-called *subdivision finite element methods*—first introduced in mechanics by Cirak *et al.* [COS00]. Finally, we refer to Thomaszewski and Wacker [TW06] for a review on bending models in engeneering and graphics as well as to Rumpf and Wardetzky [RW14] for a survey of methods in geometry processing related to the mechanics of thin elastic surfaces.

3 Preliminaries

We give a brief summary on topics in both geometry and physics that are related to this thesis.

3.1 Background in differential geometry

In this thesis, we consider the geometric structure of possibly high-dimensional *shape spaces* represented as manifolds as well as the geometry of *shells* represented as embedded surfaces. Naturally, both concepts are associated with a non-Euclidean, *i.e.* a Riemannian, structure and build on notions from differential geometry. To avoid confusion, we examine a careful separation between these two concepts right from the beginning. In the first part of this section, we present a survey on differential geometry and geodesic calculus on *finite* dimensional manifolds based on do Carmo's book [dC92]. These concepts will be used later to derive a consistent generalization in infinite dimensional manifolds [Kli95, Lan95], which are supposed to represent physical shape spaces. In the second part of this section, we introduce characteristic geometric objects on two-dimensional embedded surfaces, such as curvature related quantities, based on [Bär00, dC76]. These findings will later be incorporated in the mathematical modeling of thin shells.

3.1.1 Finite dimensional Riemannian manifolds

We define a differentiable manifold $\mathcal{M}$ of dimension $d < \infty$ in the sense of Definition 2.1 in [dC92, chap. 0], *i.e.* there is a family of injective mappings $x_\alpha : \omega_\alpha \subset \mathbb{R}^d \to \mathcal{M}$ with $\cup_\alpha x_\alpha(\omega_\alpha) = \mathcal{M}$, such that $x_\beta^{-1} \circ x_\alpha$ is differentiable for any pair α, β with $x_\alpha(\omega_\alpha) \cap x_\beta(\omega_\beta) \neq \varnothing$. For convenience, we will assume in the following that there is one global parametrization $x : \omega \subset \mathbb{R}^d \to \mathcal{M}$ with $x(\omega) = \mathcal{M}$. In particular, x is twice differentiable, injective and regular in the sense that Dx has full rank. Furthermore we will often drop the adjective "differentiable" when referring to a *differentiable* manifold $\mathcal{M}$.

Definition 3.1.1 (Tangent space, canonical basis)**.** The tangent space $T_p\mathcal{M}$ of $\mathcal{M}$ at $p \in \mathcal{M}$ is defined as

$$T_p\mathcal{M} = \{\dot{\gamma}(0) \mid \gamma : (-\epsilon, \epsilon) \to \mathcal{M} \text{ is a smooth curve with } \gamma(0) = p, \ \epsilon > 0\}.$$

If $x : \omega \to \mathcal{M}$ is a parametrization with $x(\xi) = p$ for some $\xi = (\xi_1, \dots, \xi_d) \in \omega$, the set $(X_1, \dots, X_d)$ with $X_i = X_i(p) = X_i(\xi) = x_{,i}(\xi) = \frac{\partial x}{\partial \xi_i}(\xi)$ is a basis of $T_p\mathcal{M}$, denoted as *canonical basis*.

Following Definition 2.1 in [dC92, chap. 1] we define:

Definition 3.1.2 (Riemannian metric)**.** A Riemannian metric on $\mathcal{M}$ is a mapping $g : p \mapsto g_p$ such that $g_p : T_p\mathcal{M} \times T_p\mathcal{M} \to \mathbb{R}$ is a bilinear, symmetric and positive-definite form, which varies smoothly in the sense that $\xi \mapsto g_{ij}(\xi) := g_{x(\xi)}(X_i(\xi), X_j(\xi))$ is a differentiable function in ω. A manifold equipped with a Riemannian metric is referred to as Riemannian manifold. As $(g_{ij})_{ij}$ is a regular matrix in $\mathbb{R}^{d,d}$ there is an inverse matrix $g^{-1} \in \mathbb{R}^{d,d}$ which is denoted by $(g^{kl})_{kl}$, *i.e.* $g_{ij}g^{jk} = \delta_{ik}$.

Remark 3.1.3. As mentioned above, we aim at the separation of the geometric structure of a possibly high-dimensional shape space from the geometry of a shell represented as an embedded surface. Since both concepts are associated with the notion of a metric in the sense of Def. 3.1.2, we shall denote the metric associated with generic Riemannian manifolds by *Riemannian metric* and the metric on a two-dimensional embedded surface by *first fundamental form*, *cf.* Sec. 3.1.2.

Definition 3.1.4 (Vector field)**.** A vector field V on $\mathcal{M}$ is a mapping $V : \mathcal{M} \to T\mathcal{M}$, where $T\mathcal{M} = \{(p, W) : p \in \mathcal{M}, W \in T_p\mathcal{M}\}$ is the tangent bundle. For $I \subset \mathbb{R}$, a vector field $V : I \to T\mathcal{M}$ along a curve $\gamma : I \to \mathcal{M}$ fulfills $V(t) = V(\gamma(t)) \in T_{\gamma(t)}\mathcal{M}$. Considering a parametrization $x : \omega \to \mathcal{M}$ we can write $V(x(\xi)) = \sum_{i=1}^{d} v_i(\xi)X_i(\xi)$, with $v_i : \omega \to \mathbb{R}$, $\xi \in \omega$.

(i) We say V is differentiable iff. the functions v_i are differentiable.

(ii) For a differentiable function $f : \mathcal{M} \to \mathbb{R}$ we define $(Vf)(p) := \sum_{i=1}^{d} v_i(p)\frac{\partial f}{\partial \xi_i}(p)$, $p = x(\xi)$.

As in [dC92] we denote the set of all differentiable vector fields on $\mathcal{M}$ by $\mathcal{X}(\mathcal{M})$ and all differentiable functions on $\mathcal{M}$ by $\mathcal{D}(\mathcal{M})$. For $X, Y \in \mathcal{X}(\mathcal{M})$ and $f \in \mathcal{D}(\mathcal{M})$, one can consider functions $X(Yf)$ or $Y(Xf)$. In general, these operations do not produce vector fields (as they involve derivatives of order higher than one), but the following Lemma holds (*cf*. Lemma 5.2 in [dC92, chap. 0]):

Lemma 3.1.5. *Let* $X, Y \in \mathcal{X}(\mathcal{M})$. *Then there exists a unique vector field (*i.e. *the* Lie bracket*) denoted by* $[X, Y]$ *such that* $[X, Y]f = X(Yf) - Y(Xf)$ *for all* $f \in \mathcal{D}(\mathcal{M})$.

A crucial concept in the context of geodesic calculus is the notion of a *covariant derivative*, which is induced by the *affine connection*.

Definition 3.1.6 (Affine connection)**.** An affine connection ∇ on a differentiable manifold $\mathcal{M}$ is a mapping $\nabla : \mathcal{X}(\mathcal{M}) \times \mathcal{X}(\mathcal{M}) \to \mathcal{X}(\mathcal{M})$, $(X, Y) \mapsto \nabla_X Y$, which satisfies the following properties:

(i) $\nabla_{fX+gY} Z = f\nabla_X Z + g\nabla_Y Z$

(ii) $\nabla_X(Y + Z) = \nabla_X Y + \nabla_X Z$

(iii) $\nabla_X(fY) = f\nabla_X Y + X(f)Y$

where $X, Y, Z \in \mathcal{X}(\mathcal{M})$ and $f, g \in \mathcal{D}(\mathcal{M})$.

For a vector field $X \in \mathcal{X}(\mathcal{M})$, the mapping $\nabla_X : \mathcal{X}(\mathcal{M}) \to \mathcal{X}(\mathcal{M})$ with $Y \mapsto \nabla_X Y$ is referred to as *covariant derivative*. Of particular interest is the covariant derivative of a vector field along a curve (*cf*. Prop. 2.2 in [dC92, chap. 2]):

Proposition 3.1.7. *Let* $\mathcal{M}$ *be a differentiable manifold with connection* ∇. *Then there exists a unique correspondence which associates to a vector field* V *along a differentiable curve* $\gamma : I \to \mathcal{M}$ *another vector field* $\frac{D}{dt}V$ *along* γ *such that*

(i) $\frac{D}{dt}(V + W) = \frac{D}{dt}V + \frac{D}{dt}W$, *with* W *being another vector field along* γ

(ii) $\frac{D}{dt}(fV) = \frac{df}{dt}V + f\frac{DV}{dt}$, *with* $f : I \to \mathbb{R}$ *smooth*

(iii) *If* $V(t) = W(\gamma(t))$ *for some* $W \in \mathcal{X}(\mathcal{M})$ *then* $\frac{DV}{dt} = \nabla_{\dot{\gamma}} W$.

The correspondence $V \mapsto \frac{DV}{dt}$ *is called* covariant derivative *of* V *along* γ.

In the following we make use of different notions and notations of variations of the Riemannian metric:

Definition 3.1.8 (Metric derivatives)**.** Let $p \in T_p\mathcal{M}$ and $g_p : T_p\mathcal{M} \times T_p\mathcal{M} \to \mathbb{R}$ be the metric.

(i) For vector fields $V, W, Z \in \mathcal{X}(\mathcal{M})$ we define

$$(D_p g)(Z)(V, W) := Z(p)(g(V, W)) := \frac{d}{dt}\Big(g_{p+tZ}(V, W)\Big)\Big|_{t=0} \qquad (3.1.1)$$

If $V = X_i$, $W = X_j$ and $Z = X_k$ we write $g_{ij,k} = (D_p g)(X_k)(X_i, X_j) = X_k(p)(g(X_i, X_j))$.

(ii) For vector fields $V, W, Z \in \mathcal{X}(\mathcal{M})$ we define

$$\nabla_Z(g_p(V, W)) := (D_p g)(Z)(V, W) - g_p\Big(\nabla_Z V, W\Big) - g_p\Big(V, \nabla_Z W\Big). \tag{3.1.2}$$

(iii) Let $\gamma : I \to \mathcal{M}$ be a curve and V, W vector fields along γ. In local coordinates we write $V(t) = \sum_k v_k(t) X_k(\gamma(t))$ and $\dot{V}(t) = \sum_k \dot{v}_k(t) X_k(\gamma(t))$ with analogous expressions for $W(t)$ and $\dot{W}(t)$. Writing $p = \gamma(t)$ for some $t \in I$ we define

$$\frac{d}{dt}\Big(g_p(V, W)\Big) := (D_p g)(\dot{\gamma})(V, W) + g_p\Big(\dot{V}, W\Big) + g_p\Big(V, \dot{W}\Big). \tag{3.1.3}$$

The fundamental theorem of Riemannian geometry characterizes a particular connection:

Proposition 3.1.9. *On a Riemannian manifold $\mathcal{M}$ there exists a unique affine connection ∇ satisfying*

(i) ∇ is compatible with the Riemannian metric, i.e. $\nabla_Z g(X, Y) = 0$ *for all* $X, Y, Z \in \mathcal{X}(\mathcal{M})$,

(ii) ∇ is symmetric (or torsion-free), i.e. $\nabla_X Y - \nabla_Y X = [X, Y]$ *for any vector fields* X, Y.

Remark 3.1.10. Using the derivatives of the metric defined in Def. (3.1.8) we get from Prop. 3.1.9 (i):

$$(i) \quad (D_p g)(Z)(X, Y) = g_p\Big(\nabla_Z X, Y\Big) + g_p\Big(X, \nabla_Z Y\Big)$$

$$(ii) \quad \frac{d}{dt}(g_p(X, Y)) = g_p\Big(\frac{D}{dt}X, Y\Big) + g_p\Big(X, \frac{D}{dt}Y\Big)$$

for all $p \in \mathcal{M}$ and for all $X, Y, Z \in T_p\mathcal{M}$ (*cf*. Prop. 3.2 and Cor. 3.3 in [dC92, chap. 2]).

Proof of Prop. 3.1.9: As in the proof of Thm. 3.6 in [dC92, chap. 2] one first assumes the existence of such a ∇. Using part (i) of Rem. 3.1.10 and $Z(g(X, Y)) = (D_p g)(Z)(X, Y)$ we get

$$X(g(Y, Z)) + Y(g(Z, X)) - Z(g(Y, X)) \underset{(i)}{=} g(\nabla_X Y + \nabla_Y X, Z) + g(\nabla_X Z - \nabla_Z X, Y) + g(\nabla_Y Z - \nabla_Z Y, X)$$

$$\underset{(ii)}{=} 2g(\nabla_X Y, Z) - g([X, Y], Z) + g([X, Z], Y) + g([Y, Z], X)$$

hence

$$g(\nabla_X Y, Z) = \frac{1}{2}\Big(X(g(Y, Z)) + Y(g(Z, X)) - Z(g(X, Y)) + g([X, Y], Z) - g([Y, Z], X) - g([X, Z], Y)\Big). \tag{3.1.4}$$

Since Z was chosen arbitrarily, this uniquely determines ∇. To prove existence, define ∇ by eq. (3.1.4) and verify the axioms in Def. 3.1.6. $\square$

In the following we assume to deal with the unique connection classified by Prop. 3.1.9. This distinguished connection is called *Levi-Civita connection*. Next, we introduce local coefficients of the Levi-Civita connection in a coordinate basis:

Definition 3.1.11 (Christoffel symbols). Let $x : \omega \subset \mathbb{R}^d \to \mathcal{M}$ be a local parametrization of a neighbourhood of $p \in \mathcal{M}$ and $X_i = x_{,i}$, $i = 1, \ldots, d$, the canonical basis of $T_p\mathcal{M}$. The Christoffel symbols $\Gamma_{ij}^k = \Gamma_{ij}^k[p]$ are defined as the unique coefficients such that

$$\nabla_{X_i} X_j = \sum_{k=1}^d \Gamma_{ij}^k X_k.$$

Remark 3.1.12. Prop. 3.1.9(ii) implies $0 = \nabla_{X_i} X_j - \nabla_{X_j} X_i$, *i.e.*, $\Gamma_{ij}^k = \Gamma_{ji}^k$.

Next, we express the covariant derivative along a curve $\gamma : I \to \mathcal{M}$ by means of the Christoffel symbols. Consider a parametrization $x : \omega \subset \mathbb{R}^d \to \mathcal{M}$ with $\gamma(I) \subset x(\omega)$ and $\gamma_1, \ldots, \gamma_d : I \to \omega$ such that $x(\gamma_1(t), \ldots, \gamma_d(t)) = \gamma(t)$. Furthermore, consider a vector field $V(t) = \sum_k v_k(t) X_k(\gamma(t))$ along γ. In terms of the Christoffel symbols the covariant derivative of V along γ is given by

$$\frac{DV}{dt} = \sum_{k=1}^{d} \left(\dot{v}_k + \sum_{i,j=1}^{d} \Gamma_{ij}^k v_j \dot{\gamma}_i \right) X_k \,, \tag{3.1.5}$$

which follows directly from (i) and (ii) of Prop. 3.1.7 and Def. 3.1.11. Actually, the Christoffel symbols can be represented by the metric:

Proposition 3.1.13. *Let $g^{-1} = (g^{ij})_{ij}$ be the inverse of $g = (g_{ij})_{ij}$, i.e. $g^{ji} g_{ik} = \delta_{jk}$. Then*

$$\Gamma_{ij}^m = \frac{1}{2} \sum_{k=1}^{d} g^{km} \left(g_{jk,i} + g_{ki,j} - g_{ij,k} \right) \,.$$

Proof: Using (3.1.4) with $X = X_i, Y = X_j$ and $Z = X_k$ and $g_{ij,k} = X_k(p)(g(X_i, X_j))$ we get

$$\sum_{l=1}^{d} \Gamma_{ij}^l g_{lk} = g(\nabla_{X_i} X_j, X_k) \underset{(3.1.4)}{=} \frac{1}{2} \left(g_{jk,i} + g_{ki,j} - g_{ij,k} \right). \tag{3.1.6}$$

hence multiplying with g^{km} and summing over k yields the representation. $\square$

Having the notion of a covariant derivative along a curve at hand, one can define the concept of *parallel transport* which eventually leads to geodesic curves. In the following, let $I \subset \mathbb{R}$ and $\gamma : I \to \mathcal{M}$ a curve in $\mathcal{M}$. Then a vector field V along γ is called parallel if $\left(\frac{DV}{dt} \right)(\gamma(t)) = 0$ for all $t \in I$.

Proposition 3.1.14. *Let $t_0 \in I$ and $V_0 \in T_{\gamma(t_0)}\mathcal{M}$. Then there exists a unique parallel vector field $V : I \to T\mathcal{M}$ along γ, i.e. $\frac{DV}{dt} = 0$, with $V(0) = V_0$. The map $\mathrm{P}_{\gamma(t_0) \to \gamma(t)} : T_{\gamma(t_0)}\mathcal{M} \to T_{\gamma(t)}\mathcal{M}$ with $\mathrm{P}_{\gamma(t_0) \to \gamma(t)} V_0 = V(t)$ is a linear isomorphism.*

Proof: Prop. 2.6 in [dC92, chap. 2] or Thm. 3.3 and 3.4 in [Lan95, VIII].

Definition 3.1.15 (Parallel transport). The linear isomorphism $\mathrm{P}_{\gamma(t_0) \to \gamma(t)} : T_{\gamma(t_0)}\mathcal{M} \to T_{\gamma(t)}\mathcal{M}$ with $\mathrm{P}_{\gamma(t_0) \to \gamma(t)} V_0 = V(t)$, where $\frac{DV}{dt} = 0$ and $V(0) = V_0$, is called *parallel transport*.

Definition 3.1.16 (Geodesic). A curve $\gamma : I \to \mathcal{M}$ is called a *geodesic curve* if its velocity vector is transported parallelly, *i.e.*

$$\frac{D}{dt} \dot{\gamma}(t) = 0 \quad \forall t \in I \,. \tag{3.1.7}$$

Since ∇ is compatible with the metric, Rem. 3.1.10 (ii) implies for a geodesic curve $\gamma : I \to \mathcal{M}$:

$$\frac{d}{dt} g_{\gamma(t)} \left(\dot{\gamma}(t), \dot{\gamma}(t) \right) = 2 \, g_{\gamma(t)} \left(\frac{D}{dt} \dot{\gamma}(t), \dot{\gamma}(t) \right) = 0 \,. \tag{3.1.8}$$

That means, the length of the velocity vector $\dot{\gamma}(t)$ is constant.

Definition 3.1.17 (Arc length parametrization). Let $\gamma : [0,1] \to \mathcal{M}$ be a curve. The arc length s of γ is given by $s(t) = \int_0^t \sqrt{g_{\gamma(r)} \left(\dot{\gamma}(r), \dot{\gamma}(r) \right)} \, dr$. We say, that a curve γ is parametrized proportional to arc length if there is a constant $c > 0$ such that $s(t) = c \, t$.

Remark 3.1.18. Eq. (3.1.8) reveals that geodesic curves are parametrized proportional to arc length.

Using local coordinates for γ and $V = \dot{\gamma}$ as in (3.1.5) one can write the geodesic equation (3.1.7) as a system of d second-order differential equations

$$\ddot{\gamma}_k(t) + \sum_{i,j=1}^{d} \Gamma_{ij}^k[\gamma(t)]\,\dot{\gamma}_i(t)\,\dot{\gamma}_j(t) = 0 \quad \text{for } k = 1,\ldots,d\,.$$

Theorem 3.1.19 (Local existence and uniqueness of geodesics). *For any point $p \in \mathcal{M}$ there are numbers $\delta, \epsilon > 0$ such that for all $V \in T_p\mathcal{M}$ with $|V| < \epsilon$ there exists a unique geodesic $\gamma : (-\delta, \delta) \to \mathcal{M}$ with $\gamma(0) = p$ and $\dot{\gamma}(0) = V$. We will denote this unique mapping by $t \mapsto \gamma(t, p, V)$, $t \in (-\delta, \delta)$.*

The proof of this theorem follows from the theory of ordinary differential equations, by noticing that the geodesic equation is a second-order ODE. Existence and uniqueness then follow from the Picard - Lindelöf theorem for the solutions of ODEs with prescribed initial conditions. Note that γ depends smoothly on both p and V.

Using the following rescaling or homogeneity property of geodesic curves (*cf*. Lemma 2.6 in [dC92, chap. 3]), Thm. 3.1.19 implies the existence of an operator on $T_p\mathcal{M}$, that maps an initial velocity V, with $|V|$ sufficiently small, to $\gamma(1, p, V)$.

Lemma 3.1.20 (Homogeneity of geodesics). *Let $t \mapsto \gamma(t, p, V)$, $t \in (-\delta, \delta)$, be the unique geodesic with $\gamma(0) = p$ and $\dot{\gamma}(0) = V$. Then for $\alpha > 0$ the curve $t \mapsto \gamma(t, p, \alpha V)$ is a gedesic on the interval $(-\frac{\delta}{\alpha}, \frac{\delta}{\alpha})$ and $\gamma(t, p, \alpha V) = \gamma(\alpha t, p, V)$.*

Definition 3.1.21 (Exponential map). Let $p \in \mathcal{M}$ and let $\epsilon > 0$ such that for each $V \in T_p\mathcal{M} \cap B_\epsilon(0)$ the evaluation $\gamma(1, p, V)$ is well-defined. We define the exponential map by

$$\exp_p : B_\epsilon(0) \subset T_p\mathcal{M} \to \mathcal{M}\,, \quad \exp_p(V) = \gamma(1, p, V)\,.$$

Note that $\gamma(t, p, V) = \exp_p(tV)$ for $t \in (-\delta, \delta)$. For $\epsilon > 0$ sufficiently small, $\exp_p : B_\epsilon(0) \subset T_p\mathcal{M} \to \mathcal{M}$ is a diffeomorphism. Furthermore, if U is an open neighbourhood of the origin in $T_p\mathcal{M}$ such that $\exp_p$ is a diffeomorphism on U we denote by $\exp_p(U) \subset \mathcal{M}$ the *normal neighbourhood* of p.

Definition 3.1.22 (Logarithm). Let $p \in \mathcal{M}$ and let U_p denote the normal neighbourhood of p. Then the map $\log_p : U_p \to T_p\mathcal{M}$ with $\log_p(q) = (\exp_p^{-1})(q)$ is called *logarithm*.

Geometrically, $\log_p(q)$ is the initial velocity of the unique geodesic connecting p and q. Note that $\log_p(\gamma(t)) = tV$ for $\gamma(t) = \gamma(t, p, V)$ and $t \in (-\delta, \delta)$.

Geodesic curves are often characterized as *locally shortest curves*, which will be specified in the following. The *length* of a curve $\gamma : [0, 1] \to \mathcal{M}$ is defined by

$$\mathcal{L}[\gamma] = \int_0^1 \sqrt{g_{\gamma(t)}\left(\dot{\gamma}(t), \dot{\gamma}(t)\right)}\,\mathrm{d}t\,.$$

Note that $\mathcal{L}$ is invariant under reparametrization. For $p, q \in \mathcal{M}$ the *Riemannian distance* is defined as

$$\text{dist}(p, q) = \inf_{\substack{\gamma:[0,1]\to\mathcal{M}\text{ geodesic} \\ \gamma(0)=p,\,\gamma(1)=q}} \mathcal{L}[\gamma]\,.$$

If q is in the normal neighbourhood of p we have $\text{dist}(p, q) = |\log_p(q)|$ since geodesics are parametrized proportional to arc length. The following two propositions illustrate the length minimizing properties of geodesic curves (*cf*. Prop. 3.6 and Cor. 3.9 in [dC92, chap. 3]).

Proposition 3.1.23. *Let $p \in \mathcal{M}$ and q be in the normal neighbourhood of p. Let $\gamma, \alpha : [0,1] \to \mathcal{M}$ be two piecewise differential curves connecting p and q, where γ is geodesic. Then $\mathcal{L}(\gamma) \leq \mathcal{L}(\alpha)$ with equality iff. $\gamma([0,1]) = \alpha([0,1])$, i.e. γ and α are equal up to reparametrization.*

Proposition 3.1.23 is no longer true if q is not contained in the normal neighbourhood of p.

Proposition 3.1.24. *Let $\gamma : [0,1] \to \mathcal{M}$ be a piecewise differentiable connecting curve of $p, q \in \mathcal{M}$ that is parametrized proportional to arc length. If $\mathcal{L}[\gamma]$ is less or equal to the length of any other piecewise differentiable curve connecting p and q, then γ is a geodesic. In particular, γ is regular.*

3.1.2 Differential geometry on embedded surfaces

As a particular focus of this thesis is on discrete quantities approximating curvature related objects on surfaces embedded in $\mathbb{R}^3$, we will briefly summarize basic notions of these subjects. For further reading we refer to [Bär00, dC76, LR12]. For the remainder of this section let $d = 2$ and $\mathcal{M} \subset \mathbb{R}^3$ is a regular and embedded surface with a (local) parametrization $x : \omega \subset \mathbb{R}^2 \to \mathcal{M}$. Let $\xi \in \omega$ and $p = x(\xi) \in \mathcal{M}$. The canonical basis of $T_p\mathcal{M}$ is given by (X_1, X_2) with $X_i = x_{,i}$, $i = 1, 2$.

Definition 3.1.25 (Normal field). Let $S^2 \subset \mathbb{R}^3$ be the 2-dimensional unit sphere. The (unit) normal field of $\mathcal{M}$ is a mapping $n : \mathcal{M} \to S^2$ with $n(p) \perp T_p\mathcal{M}$ for all $p \in \mathcal{M}$. We say that $\mathcal{M}$ is orientable if there is a continuous normal field[1]. In particular, as $\text{rank}(Dx) = 2$, we will write

$$n(p) = (n \circ x)(\xi) = \frac{x_{,1} \times x_{,2}}{|x_{,1} \times x_{,2}|}(\xi) \,.$$

Definition 3.1.26 (First fundamental form). The first fundamental form in $p \in \mathcal{M}$ is given by

$$g_p : T_p\mathcal{M} \times T_p\mathcal{M} \to \mathbb{R}, \quad g_p(U, V) := \langle U, V \rangle_{\mathbb{R}^3} \,.$$

After choosing a basis of $T_p\mathcal{M}$—here and in the following the canonical basis (X_1, X_2)—we can represent g_p by a symmetric, positive-definite matrix $g = g_\xi \in \mathbb{R}^{2,2}$ with

$$g_{ij} = g_p(X_i, X_j) = \langle X_i, X_j \rangle_{\mathbb{R}^3} \,,$$

i.e. we have $g = Dx^T Dx$. The pull-back of g_p to the parameter domain $\omega \subset \mathbb{R}^2$ is defined as

$$g_\xi(u, v) = g_p(Dx\, u, Dx\, v) = u^T g v \,, \quad u, v \in \omega \,.$$

Geometrically, the first fundamental form is necessary to measure on the surface, *e.g.* to determine lengths of curves or angles between tangent vectors. To simplify notation, we will often drop the index and write $g = g_p$ or $g = g_\xi$, respectively. In particular, g refers to the bilinear form as well as to its representative matrix in $\mathbb{R}^{2,2}$. Note that $g \in \mathbb{R}^{2,2}$ is invertible, since $\mathcal{M} \subset \mathbb{R}^3$ is assumed to be regular.

Next, we introduce the notion of curvature on a regular surface, which is closely related to the differential of the normal field. For a smooth function $f : \mathcal{M} \to \mathbb{R}^3$ and $p \in \mathcal{M}$, the differential $d_p f : T_p\mathcal{M} \to \mathbb{R}^3$ is defined by

$$d_p f(U) := \frac{d}{dt}(f \circ \gamma)\Big|_{t=0} \,,$$

where $\gamma : (-\epsilon, \epsilon) \to \mathcal{M}$ is a smooth curve with $\gamma(0) = p$ and $\dot{\gamma}(0) = U$. In particular, $d_p f$ is independent of the choice of γ, hence $d_p f$ is well defined [Bär00]. Furthermore, $d_p f : T_p\mathcal{M} \to T_{f(p)}f(\mathcal{M})$.

Definition 3.1.27. (Shape operator) Let $\mathcal{M} \subset \mathbb{R}^3$ be regular and orientable, $p \in \mathcal{M}$. The shape operator $S_p : T_p\mathcal{M} \to T_p\mathcal{M}$ at p is the linear mapping defined via $S_p(U) = d_p n(U)$ for $U \in T_p\mathcal{M}$.

---

[1] In this thesis we only consider orientable surfaces.

As $T_{n(p)}S^2 = n(p)^\perp = T_p\mathcal{M}$ the shape operator S_p is indeed an endomorphism on $T_p\mathcal{M}$. Furthermore, S_p is self-adjoint with respect to the first fundamental form [Bär00, dC76], *i.e.* $g_p(S_pU, V) = g_p(U, S_pV)$ for all $U, V \in T_p\mathcal{M}$. As for every self-adjoint endomorphism there is a unique corresponding bilinear form we may define:

Definition 3.1.28. (Second fundamental form) Let $\mathcal{M} \subset \mathbb{R}^3$ be regular and orientable, $p \in \mathcal{M}$. The second fundamental form $h = h_p$ is the unique bilinear form on $T_p\mathcal{M}$ associated with S_p, *i.e.*

$$h_p(U, V) := g_p(S_pU, V)\,, \quad U, V \in T_p\mathcal{M}\,.$$

The corresponding matrix representation $h = h_\xi \in \mathbb{R}^{2,2}$ with respect to the canonical basis is given by

$$h_{ij} = h_p\big(X_i, X_j\big) = g_p\big(S_pX_i, X_j\big) = \left\langle d_p n \cdot \frac{\partial x}{\partial \xi_i}, \frac{\partial x}{\partial \xi_j} \right\rangle_{\mathbb{R}^3} = \left\langle \frac{\partial n(p)}{\partial \xi_i}, \frac{\partial x}{\partial \xi_j} \right\rangle_{\mathbb{R}^3}\,. \tag{3.1.9}$$

Hence we can represent the (symmetric) matrix $h \in \mathbb{R}^{2,2}$ by

$$h = Dn^T Dx\,, \quad Dn = \left[\frac{\partial n(p)}{\partial \xi_1}, \frac{\partial n(p)}{\partial \xi_2}\right] \in \mathbb{R}^{3,2}\,.$$

If we write S_p in the canonical basis (X_1, X_2), *i.e.* $S_p(X_j) = \sum_{i=1}^2 s_{ij}X_i$ for $j = 1, 2$, the coefficient matrix $s = s_\xi \in \mathbb{R}^{2,2}$ is the representation of S_p in the parameter domain. In particular, we have [Bär00]

$$s_\xi = g_\xi^{-1} h_\xi\,. \tag{3.1.10}$$

As S_p is self-adjoint its matrix representation s_ξ is diagonalizable:

Definition 3.1.29. (Curvatures) The eigenvalues κ_1, κ_2 of s_ξ are denoted as principal curvatures of $\mathcal{M}$ in $p = x(\xi)$. The mean curvature in p is defined as the sum $\operatorname{tr} s_\xi = \kappa_1 + \kappa_2$ and the Gaussian curvature in p as the product $\det s_\xi = \kappa_1 \cdot \kappa_2$.

Let us emphasize that g_ξ, h_ξ and hence s_ξ depend on the parametrization x. However, it might be useful to have a (matrix) representation of S_p that is independent of the local parametrization. Such a representation was derived in [LR12] using the pseudo inverse Dx^{-1}, *i.e.* the *curvature tensor* is defined by

$$S_p = Dx s_\xi Dx^{-1}\,, \quad Dx^{-1} = g_\xi^{-1} Dx^T \in \mathbb{R}^{2,3}\,. \tag{3.1.11}$$

Note that $S_p \in \mathbb{R}^{3,3}$ whereas $s_\xi \in \mathbb{R}^{2,2}$. Again, we will often drop the index in S_p and s_ξ, respectively, and $S = S_p$ refers to a bilinear form on $T_p\mathcal{M}$ or the corresponding matrix in $\mathbb{R}^{3,3}$.

Remark 3.1.30. For $u_1, u_2 \in T_\xi\omega = \mathbb{R}^2$, *i.e.* $U_i = Dx\, u_i \in T_p\mathcal{M}$, we have $U_i^T S_p U_j = u_i^T s_\xi u_j$. Furthermore, $U_i^T S_p n = 0$. Hence the eigenvalues of S_p are given exactly by κ_1, κ_2 and 0.

3.2 A spotlight on physics

In this section we briefly summarize important prerequisites from continuum mechanics that are relevant for the definition of physically motivated dissimilarity measures on the space of thin shells and viscous fluidic objects, respectively.

Elasticity theory First, we give a survey on the theory of elastic deformations; for further reading we refer to [Cia88, MH94, Bra07]. Let $\mathcal{O} \subset \mathbb{R}^3$ be a homogenous[1] and solid object with boundary and $\phi \in W^{1,2}(\mathcal{O}; \mathbb{R}^3)$ a potentially large and nonlinear deformation. Typically, one assumes that ϕ is orientation preserving, *i.e.* $\det D\phi(x) > 0$ for all $x \in \mathcal{O}$, and injective (*i.e.*, no interpenetration of matter occurs). We postulate the existence of an *elastic deformation energy* $\mathcal{W}[\phi, \mathcal{O}]$ associated with the deformation ϕ. By definition, *elastic* means that $\mathcal{W}$ solely depends on the Jacobian $D\phi$ of ϕ. Furthermore, for so-called *hyperelastic* materials, $\mathcal{W}[\phi, \mathcal{O}]$ is the integral of an elastic energy density $W = W(D\phi)$, *i.e.*

$$\mathcal{W}[\phi, \mathcal{O}] = \int_{\mathcal{O}} W(D\phi) \; \mathrm{d}x \,. \tag{3.2.1}$$

A fundamental axiom of continuum mechanics is *frame indifference*, *i.e.* the invariance of the deformation energy with respect to rigid body motions. Hence, any coordinate transform $x \mapsto Qx + b$ for a rotation $Q \in SO(3)$ and a shift $b \in \mathbb{R}^3$ does not change the energy, *i.e.*

$$W(D\phi) = W(Q^{\mathrm{T}} D\phi Q) \quad \forall Q \in SO(3) \,.$$

A direct consequence is that W only depends on the so-called right Cauchy–Green strain tensor $C[\phi] = D\phi^{\mathrm{T}} D\phi$, which geometrically represents the metric measuring the deformed length in the undeformed reference configuration. Furthermore, we might assume $\mathcal{O}$ to be an *isotropic* material, *i.e.* a rotation of the material before applying a deformation yields the same energy as before, *i.e.*

$$W(D\phi) = W(D\phi Q) \quad \forall Q \in SO(3) \,.$$

It follows from the Rivlin-Erikson-Theorem [RE55] that the above two conditions lead to the fact that the energy density W only depends on the singular values $\lambda_1, \lambda_2, \lambda_3$ of $D\phi$, the so-called principal stretches. Instead of the principal stretches, one can equivalently describe the local deformation using the so-called invariants of the deformation gradient,

$$I_1 = \|D\phi\|_F = \sqrt{\lambda_1^2 + \lambda_2^2 + \lambda_3^2} \,,$$
$$I_2 = \|\mathrm{cof} \, D\phi\|_F = \sqrt{\lambda_1^2 \lambda_2^2 + \lambda_1^2 \lambda_3^2 + \lambda_2^2 \lambda_3^2} \,,$$
$$I_3 = \det D\phi = \lambda_1 \lambda_2 \lambda_3 \,,$$

where $\|A\|_F = \sqrt{\mathrm{tr}\,(A^{\mathrm{T}} A)}$ for $A \in \mathbb{R}^{d,d}$ and the cofactor matrix is given by $\mathrm{cof}\, A = \det A A^{-\mathrm{T}}$ for $A \in GL(d)$. Hence there is a function $\hat{W} : \mathbb{R}^3 \to \mathbb{R}$ with $W(D\phi) = \hat{W}(I_1, I_2, I_3)$, where $I_1, I_2,$ and I_3 can be interpreted as the locally averaged change of an infinitesimal length, area, and volume during the deformation, respectively.

We shall furthermore assume that isometries, *i.e.* deformations with $D\phi^{\mathrm{T}} D\phi = \mathbb{1}$, are local minimizers with $W(D\phi) = 0$ [Cia88]. Typical energy densities in this class are given by

$$W(D\phi) = \hat{W}(I_1, I_2, I_3) = a_1 I_1^p + a_2 I_2^q + \Gamma(I_3) \,, \tag{3.2.2}$$

---

[1] This will later result in energy densities that do not depend on $x \in \mathcal{O}$.

for $a_1, a_2 > 0$ and a convex function $\Gamma : [0, \infty) \to \mathbb{R}$ with $\Gamma(I_3) \to \infty$ for $I_3 \to 0$ or $I_3 \to \infty$. In this work we focus on $p = q = 2$ which corresponds to the Mooney–Rivlin model [Cia88]. The built-in penalization of volume shrinkage, *i.e.* $\hat{W}(I_1, I_2, I_3) \to \infty$ for $\det D\phi \to 0$, enables us to control local injectivity. Incorporation of such a nonlinear elastic energy allows to describe large deformations with strong material and geometric nonlinearities, which cannot be treated by a linear elastic approach.

If we assume the Hessian of the energy density W at the identity to be given by

$$W_{,FF}(\mathbb{1})(G, G) = \lambda(\operatorname{tr} G)^2 + \frac{\mu}{2}\operatorname{tr}\left((G + G^T)^2\right), \qquad (3.2.3)$$

which can be realized in (3.2.2) for a particular choice of a_1, a_2, and Γ, then by the ansatz $\phi_\tau(x) = x + \tau u(x)$ and a second order Taylor expansion we obtain [RW11b]

$$W(D\phi_\tau) = W(\mathbb{1}) + \tau W_{,F}(\mathbb{1})(Du) + \frac{\tau^2}{2}W_{,FF}(\mathbb{1})(Du, Du) + O(\tau^3)$$

$$= 0 + 0 + \tau^2\left(\frac{\lambda}{2}(\operatorname{tr} Du)^2 + \frac{\mu}{4}\operatorname{tr}\left(\left(Du + Du^T\right)^2\right)\right) + O(\tau^3).$$

That means for small deformations, the Hessian of the nonlinear elastic energy density W leads to the typical energy density in linearized, isotropic elasticity

$$W^{\text{lin}}(D\phi) = \frac{\lambda}{2}\left(\operatorname{tr}\epsilon[u]\right)^2 + \mu\operatorname{tr}\left(\epsilon[u]^2\right) \qquad (3.2.4)$$

for displacements u with $u(x) = \phi(x) - x$ and $\epsilon[u] = \frac{1}{2}(Du + Du^T)$. A particular choice for a nonlinear elastic energy density satisfying (3.2.3) was introduced in [Wir09] (*cf.* appendix A.1 of [WBRS11]) as

$$W(D\phi) = \frac{\mu}{2}\|D\phi\|_F^2 + \frac{\lambda}{4}(\det D\phi)^2 - \left(\mu + \frac{\lambda}{2}\right)\log\det D\phi - \frac{d\mu}{2} - \frac{\lambda}{4} \qquad (3.2.5)$$

for $d = 2, 3$.

Remark 3.2.1. The nonlinear elastic density (3.2.5) is invariant with respect to rigid body motions, *i.e.* $W(D\phi) = 0$ iff. $\phi(x) = Qx + b$ with $Q \in SO(3)$. However, this is true for the linear elastic density (3.2.4) only in an infinitesimal sense. In detail, W^{lin} is invariant with respect to linearized rigid body motions, *i.e.* $W^{\text{lin}}(D\phi) = 0$ iff. $\phi(x) = Ax + b$ with $A \in \mathbb{R}^{3,3}$ skew-symmetric.

In elasticity theory one typically considers variational problems $\min_\phi(\mathcal{W}[\phi, \mathcal{O}] - \mathcal{F}[\phi, \partial\mathcal{O}])$, where $\mathcal{F}$ represents a force acting on (some part of) the boundary $\partial\mathcal{O}$ of $\mathcal{O}$. An existence theory for hyperelastic materials whose corresponding energy density W fulfills certain properties was established by John Ball [Bal77]. In a slightly different fashion, we will utilize $\mathcal{W}$ to define an elastic *dissimilarity measure* between *shapes*. That means, given two shapes $\mathcal{S}_A$ and $\mathcal{S}_B$ which are supposed to describe two elastic materials $\mathcal{O}_A$ and $\mathcal{O}_B$, we aim in minimizing $\phi \mapsto \mathcal{W}[\phi, \mathcal{S}_A]$ subject to the constraint[1] $\phi(\mathcal{S}_A) = \mathcal{S}_B$. The dissimilarity measure is then given by (*cf.* eq. (6) in [RW11b])

$$d_{\text{elast}}(\mathcal{S}_A, \mathcal{S}_B) = \min_{\phi:\phi(\mathcal{S}_A)=\mathcal{S}_B}\sqrt{\mathcal{W}[\phi, \mathcal{S}_A]}.$$

However, d_{elast} does not induce a notion of distance on the space of shapes. Indeed, neither a symmetry property nor the triangle inequality hold in general [RW11b]. Furthermore, the axiom of elasticity implies that $\mathcal{W}[\phi, \mathcal{S}_A]$ does not depend on the path from $\mathcal{S}_A$ to $\mathcal{S}_B$. Since we want to study paths in shape spaces this so called stated-based elastic concept might not be satisfying. In the following we will introduce a different physical setup that allows for the notion of paths in shape space. For a detailed discussion of the differences of the state-based and path-based approach we refer to [RW11b].

---

[1]In practice the hard constraint is realized by a penalty approach.

Viscous fluidic objects   We summarize the physical background on the continuum mechanics of viscous fluid transport and review the fundamental concept of viscous dissipation in a Newtonian fluid. This summary is based on corresponding sections in [Wir09, WBRS11, RW11b].

In contrast to the elastic model presented above the viscous model for shapes allows for the notion of a *path* between two given shapes $\mathcal{S}_A$ and $\mathcal{S}_B$. We regard a path $\mathcal{S}(t)$, $t \in [0,1]$, as a time-continuous deformation of $\mathcal{S}(0) = \mathcal{S}_A$ into $\mathcal{S}(1) = \mathcal{S}_B$. Here, $\mathcal{S}(t)$ is generated by a motion field $v(t) : \mathcal{S}(t) \to \mathbb{R}^d$, which represents the time derivative or the velocity field of the deformation. Formally, if $\phi : [0,1] \times \mathcal{S}(0) \to \mathbb{R}^d$ describes a deformation path with $\mathcal{S}(t) = \phi(t, \mathcal{S}(0))$, we have $v(t) = \dot{\phi}(t, \cdot) \circ \phi(t, \cdot)^{-1}$ in the Eulerian description[1]. Different from above, $\mathcal{S}(t)$ is here considered to be made of a *viscous material*. This means, internal friction will occur during the deformation which results in so-called *viscous dissipation*, that is, conversion of mechanical energy into heat. The viscous dissipation depends on the motion field $v(t)$, and will later induce a Riemannian metric on the space of shapes. This viscous flow model is supposed to capture at least some characteristics of the usually much more complex underlying physical processes one aims to represent (*e.g.* plant growth [BFH$^+$13]).

Based on the common continuum assumption one studies the macroscopic behavior of a fluid via governing partial differential equations which describe the transport of fluid material. *Viscosity* describes the internal resistance in a fluid and may be thought of as a macroscopic measure of the friction between fluid particles. Mathematically, the friction is described in terms of the Cauchy stress tensor $\sigma = (\sigma_{ij})_{i,j=1,...,d}$, whose entries describe a force per area element. By definition, σ_{ij} is the force component along the ith coordinate direction acting on the area element with a normal pointing in the jth coordinate direction (*cf.* sketch on the right taken from [Wir09]). Hence, the diagonal entries of the stress tensor σ refer to normal stresses, *e.g.* due to compression, and the off-diagonal entries represent tangential (shear) stresses. The Cauchy stress law states that due to the preservation of angular momentum the stress tensor σ is symmetric [Cia88].
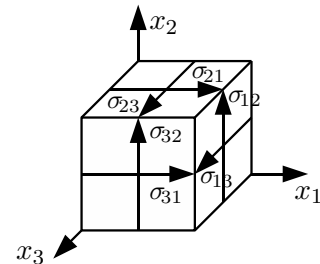
In a *Newtonian fluid* the stress tensor is assumed to depend linearly on the velocity gradient Dv. Since the stress is supposed to vanish for rigid body motions (*i.e.* rotations and translations) and a rotational component of the local motion is generated by the antisymmetric part $\frac{1}{2}(Dv - Dv^T)$ of Dv, the stress only depends on the symmetric part $\epsilon[v] = \frac{1}{2}(Dv + Dv^T)$ of the velocity gradient. If we separate compressive stresses, reflected by the trace of the velocity gradient, from shear stresses depending solely on the trace-free part of the velocity gradient, we obtain the representation of an isotropic Newtonian fluid in matrix form [CM90], *i.e.*

$$\sigma = \lambda \operatorname{tr}(\epsilon[v])\mathbb{1} + 2\mu\,\epsilon[v].$$

The physical parameters $\lambda, \mu > 0$ are denoted Lamé coefficients [Bra07]. The local rate of viscous dissipation—the rate at which mechanical energy is locally converted into heat due to friction—can now be computed as

$$\operatorname{diss}[v] = \frac{\lambda}{2}\operatorname{tr}(\epsilon[v])^2 + \mu \operatorname{tr}(\epsilon[v]^2). \tag{3.2.6}$$

This corresponds directly to the mechanical definition of the stress tensor σ as the first variation of the local dissipation rate with respect to the velocity gradient [WBRS11, RW11b]. Here $\operatorname{tr}(\epsilon[v]^2)$ measures the averaged local change of length and $\operatorname{tr}(\epsilon[v])^2$ the local change of volume induced by the deformation. If each point $x \in \mathcal{S}(t)$ at time $t \in [0,1]$ moves at the velocity $v(t,x)$ the total deformation of $\mathcal{S}(0)$ into

---

[1] In contrast to a Lagrangian description, where all quantities (*e.g.* stresses) are evaluated in an undeformed reference configuration, in a Eulerian description we work on the defomed configuration. Hence, the concatenation with the inverse of ϕ is needed to obtain a proper Eulerian description of the motion field v.

$\mathcal{S}(t)$ can be obtained by integrating the velocity field v in time. Then the accumulated global dissipation of the motion field v in the time interval $[0,1]$ takes the form

$$\mathbf{Diss}\left((v(t))_{t\in[0,1]}\right) = \int_0^1 \int_{\mathcal{S}(t)} \operatorname{diss}[v(t)]\,\mathrm{d}x\,\mathrm{d}t\,. \tag{3.2.7}$$

Later we will seek for a path with prescribed end points $\mathcal{S}(0) = \mathcal{S}_A$ and $\mathcal{S}(1) = \mathcal{S}_B$, that minimizes its global dissipation.

Remark 3.2.2. Even though the dissipation rate (3.2.6) looks like the energy density from linearized elasticity (3.2.4), if the velocity v is replaced by the displacement u, the underlying physics is only related in the sense that an infinitisimal displacement in the fluid leads to stresses caused by viscous friction, and these stresses are immediately absorbed via dissipation, which reflects a local heating. This connection is sometimes referred to as *Rayleigh's paradigm* [Ray96], *i.e.* one derives a viscous dissipation model from an elastic energy by replacing the elastic strain $u \sim \phi - \mathrm{id}$ by *strain rates* $v \sim \dot{\phi}$.

4 Time-discrete geodesic calculus

A starting point of this thesis is the development of a robust interpolation method in the space of (discrete) shells with direct applications in computer graphics *e.g.* for morphing or keyframe animation. To this end, we consider the shape space of (discrete) shells as Riemannian manifold. We aim at combining a physically sound model of thin shells with a geometric description of locally shortest path, which are *geodesics* in the Riemannian framework. Continuous geodesics are minimizers of the so-called path energy. One way to approximate geodesic paths connecting two points in a generic manifold is via the minimization of a discretized path energy. Instead of discretizing the underlying flow, the *variational time-discretization* proposed by Rumpf and Wirth [WBRS11] is based on the direct minimization of this discrete path energy subject to the prescribed data given at the initial and the end time. When applied to the space of viscous fluidic, *i.e. volumetric* objects, this approach has proven to be be very stable and robust, and even for very small numbers of time steps one obtains qualitatively good results [Wir09, WBRS09, WBRS11]. Hence, the initial idea of the present work is to apply the variational time-discretization to the space of shells in order to compute geodesics, *i.e.* interpolating paths between two points in shell space.

Building on the variational time-discretization of geodesic paths, Rumpf and Wirth [RW13] developed a comprehensive discrete geodesic calculus on the space of viscous fluidic objects and presented in [RW15] a corresponding complete convergence analysis on general finite- and on certain infinite-dimensional shape spaces with the structure of a Banach manifold. The generic definitions of several discrete geometric objects, such as exponential map, logarithm and parallel transport, are appropiate to be transferred directly to other shape spaces. To this end, we apply exactly this discrete geodesic calculus to the space of shells to obtain useful and robust tools for applications in computer graphics such as extrapolation or detail transfer.

Rumpf and Wirth [RW15] have already provided a glimpse in the direction of a time-discrete covariant derivative along a curve via the notion of a discrete connection. Here, we propose a pointwise evaluation of the time-discrete covariant derivative along a curve by means of the local construction of a so-called discrete geodesic parallelogram and prove consistency of this definition. The notion of a time-discrete covariant derivative eventually leads to the definition of a generalized spline energy which can be used to tackle the multiple interpolation problem—a crucial task in keyframe animation and other related issues in computer graphics. Although the main application of the geodesic calculus considered in this thesis is the finite dimensional space of discrete shells, the theoretical results on the spline energy presented in this chapter are in particular valid in general infinite dimensional manifolds.

This chapter is organized as follows: In Sec. 4.1, we define geodesics and related geometric quantities in the generic framework of infinite dimensional manifolds. In Sec. 4.2, we review the variational time-discretization and the corresponding convergence analysis. Finally, in Sec. 4.3, we derive a time-discrete spline energy and prove consistency of this definition.

Remark 4.0.1. The main ideas as well as the convergence analysis presented in Sec. 4.1 and Sec. 4.2 were developed by Rumpf and Wirth in a sequence of papers [Wir09, WBRS09, WBRS11, RW13, RW15, Rum15]. The work on Riemannian splines in Sec. 4.3 is joint work with Martin Rumpf and Benedikt Wirth and will be presented in a forthcoming paper [HRW16].

4.1 Geodesic calculus on a Riemannian manifold

Geodesics are usually defined as curves that transport their velocity vector parallely or equivalently, that are solutions of the geodesic equation (*cf*. Sec. 3.1). Both definitions are based on the notion of a covariant derivative. Alternatively, one can make use of the characteristic length minimizing properties of geodesic curves in the sense of Prop. 3.1.23 and Prop. 3.1.24 to come up with an equivalent definition. Fortunately, these properties literally hold for general manifolds, *cf*. *e.g.* Thm. 6.2 in [Lan95, VIII] and the Corollary thereof. That means one can define geodesics by reparameterizing a minimizer of the length functional such that it has constant speed. To avoid this reparameterization step as well as the minimization of the non-convex length functional we make use of the *path energy* instead. We shall see that minimizers of this path energy are in fact constant speed geodesics that also minimize the length functional and fulfill the geodesic equation. Once a notion of geodesics is at hand, one can easily deduce further geometric quantities, such as exponential map, parallel transport and covariant derivative.

In Sec. 4.1.1, we define geodesic curves on a general Riemannian manifold by a variational formulation. We import existence and uniqueness results from [RW15] to show that this definition yields well-defined geodesics. In Sec. 4.1.2, we define a covariant derivative and parallel transport and show that geodesics defined by the variational framework are actually solutions of the geodesic equation. Finally, we derive the exponential map from the initial value problem given by the geodesic equation, and its inverse operator, the logarithm.

4.1.1 Path energy and geodesics

Given a smooth path $(y(t))_{t \in [0,1]}$ on a Riemannian manifold $(\mathcal{M}, g)$, the length of this path is defined as

$$\mathcal{L}[(y(t))_{t \in [0,1]}] = \int_0^1 \sqrt{g_{y(t)}(\dot{y}(t), \dot{y}(t))} \, \mathrm{d}t \,. \tag{4.1.1}$$

Note that the path length is independent of reparameterization. This geometrically nice property leads to analytical complications when dealing with the existence theory of shortest paths as well as to computational difficulties when optimizing this non-convex functional. The path energy is defined as

$$\mathcal{E}[(y(t))_{t \in [0,1]}] = \int_0^1 g_{y(t)}(\dot{y}(t), \dot{y}(t)) \, \mathrm{d}t \,. \tag{4.1.2}$$

In contrast to $\mathcal{L}$, the path energy is *not* independent of reparameterization. A direct application of the Cauchy-Schwarz inequality shows that

$$\mathcal{L}[(y(t))_{t \in [0,1]}] \leq \sqrt{\mathcal{E}[(y(t))_{t \in [0,1]}]}$$

and equality holds if and only if $g_{y(t)}(\dot{y}(t), \dot{y}(t)) = \text{const.}$ We will see that minimizers of $\mathcal{E}$ will have this *constant speed property*. Thus, to identify shortest paths for fixed boundary data $y(0) = y_A$ and $y(1) = y_B$ with $y_A, y_B \in \mathcal{M}$ we will seek for minimizers of the path energy and minimizers will be paths with constant speed.

Definition 4.1.1 (Geodesic path). For $y_A, y_B \in \mathcal{M}$ a minimizer of the path energy among all path $y : [0,1] \to \mathcal{M}$ with $y(0) = y_A$ and $y(1) = y_B$ is denoted as geodesic path connecting y_A and y_B.

Rumpf and Wirth have shown in [RW15] that this variational definition is indeed well-defined, *i.e.* a minimizer of $\mathcal{E}$ exists and is unique under suitable assumptions. We will summarize these theoretical results here to maintain the self-containedness.

To state existence and uniqueness results from [RW15] we need a precise technical setup. Let $\mathbf{V}$ be a separable, reflexive Banach space that is compactly embedded in a Banach space $\mathbf{Y}$. Let $\mathcal{M}$ be the closure of an open connected subset of $\mathbf{V}$ and hence a Banach manifold, potentially with boundary (in which case we assume the boundary $\partial\mathcal{M}$ to be smooth). We assume $\mathcal{M}$ to be path-connected. Let $g : \mathcal{M} \times \mathbf{V} \times \mathbf{V} \to \mathbb{R}$ be a Riemannian metric, which satisfies the following hypotheses:

(H1) $\begin{cases} g \text{ is uniformly bounded and } \mathbf{V}\text{-coercive in the sense } c^* \|v\|_{\mathbf{V}}^2 \leq g_y(v,v) \leq C^* \|v\|_{\mathbf{V}}^2 . \\[1mm] g \text{ is continuous in the sense } |g_y(v,v) - g_{\tilde{y}}(v,v)| \leq \beta(\|y - \tilde{y}\|_{\mathbf{Y}}) \|v\|_{\mathbf{V}}^2 \\ \text{for a strictly increasing, continuous function } \beta \text{ with } \beta(0) = 0. \end{cases}$

Hypothesis (H1) is globally fulfilled only for quite special Riemannian manifolds. However, the setup is also adequate to analyze general, possibly infinite-dimensional manifolds locally, where the linear space $\mathbf{V}$ or its subset $\mathcal{M}$ have to be interpreted as a chart of the considered manifold.

For y_A, $y_B \in \mathcal{M}$, the next theorem states the existence of a connecting path with least energy. The key point in the proof is the weak lower semi-continuity of the continuous path energy (4.1.2) using the compact embedding of $\mathbf{V}$ into $\mathbf{Y}$.

Theorem 4.1.2 (Existence of continuous geodesics, [RW15]). *Let $(\mathcal{M}, g)$ be a Riemannian manifold satisfying assumption* (H1). *For y_A, $y_B \in \mathcal{M}$ there exists a classical geodesic connecting y_A and y_B, i.e. a minimizer of $\mathcal{E}$ in the space of all paths $(y(t))_{t\in[0,1]} \in W^{1,2}((0,1);\mathcal{M})$ with $y(0) = y_A$ and $y(1) = y_B$. In particular, y is Hölder continuous in the $\mathbf{V}$-topology.*

As in finite-dimensional Riemannian geometry the shortest geodesic between close points is unique as stated in the next theorem (*cf*. also Cor. 5.2 in [Lan95, VIII]).

Theorem 4.1.3 (Uniqueness of short continuous geodesics, [RW15]). *Under the assumptions of Theorem 4.1.2, for the metric g being $C^2(\mathcal{M}; \mathbf{V}' \otimes \mathbf{V}')$-smooth, classical geodesics are unique locally.*

Once we have existence and uniqueness of geodesics, we can define a Riemannian distance of two points y_A, $y_B \in \mathcal{M}$ in the usual way, *i.e.*

$$\text{dist}(y_A, y_B) = \min_{y(0)=y_A, y(1)=y_B} \mathcal{L}[(y(t))_{t\in[0,1]}] = \sqrt{\min_{y(0)=y_A, y(1)=y_B} \mathcal{E}[(y(t))_{t\in[0,1]}]}. \tag{4.1.3}$$

Remark 4.1.4. One can verify the axioms of a metric and show that the induced topology is equivalent to the $\mathbf{V}$-topology, *i.e.* $\sqrt{c^*}\|y_B - y_A\|_{\mathbf{V}} \leq \text{dist}(y_A, y_B) \leq \sqrt{C^*}\|y_B - y_A\|_{\mathbf{V}}$.

4.1.2 Covariant derivative and parallel transport

Next, we derive a notion of a covariant derivative along a curve in a general manifold which is *e.g.* necessary to obtain a concept of parallel transport. To this end, we first revisit the definition and formulation by means of the Christoffel symbols used in the finite dimensional setup in Sec. 3.1. In particular, we formulate a coordinate-free representation which can be transferred directly to the infinite dimensional setup. Consistency is ensured as (i) the finite dimensional case appears as a special case of the general setup and (ii) geodesics are precisely the solutions of the geodesic equations. For further reading we refer to [Lan95] as well as to [Rum15].

As a motivation, we first consider a d-dimensional setup ($d < \infty$) using coordinates as in Sec. 3.1. The Christoffel symbols were defined in Def. 3.1.11 by $\nabla_{X_i} X_j = \sum_{k=1}^{d} \Gamma_{ij}^k X_k$. To obtain a *coordinate-free* formulation, we first define an operator $\Gamma = \Gamma_p : T_p\mathcal{M} \times T_p\mathcal{M} \to T_p\mathcal{M}$ by

$$\Gamma(U, V) = \sum_{i,j=1}^{d} u_i v_j \nabla_{X_i} X_j = \sum_{i,j,k=1}^{d} u_i \, v_j \, \Gamma_{ij}^k X_k$$

and get for tangent vectors $U = \sum_i u_i X_i$, $V = \sum_j v_j X_j$ and $W = \sum_k w_k X_k$:

$$g_p(\Gamma(U,V),W) = \sum_{i,j,k,l=1}^{d} u_i\, v_j\, w_k\, \Gamma_{ij}^l g_{kl}\,. \tag{4.1.4}$$

On the other hand, from (3.1.6) we get

$$\frac{1}{2}\Big(U(g_p(V,W)) + V(g_p(W,U)) - W(g_p(U,V))\Big) = \sum_{i,j,k=1}^{d} u_i v_j w_k \underbrace{g_p(\nabla_{X_i} X_j, X_k)}_{=\sum_l \Gamma_{ij}^l g_{lk}}\,. \tag{4.1.5}$$

Comparing (4.1.4) and (4.1.5), we can define Γ implicitly without using coordinates by

$$g_p(\Gamma(U,V),W) = \frac{1}{2}\Big((D_p g)\,(V)(U,W) + (D_p g)\,(U)(V,W) - (D_p g)\,(W)(U,V) \Big)\,.$$

Definition 4.1.5 (Christoffel operator). For $p \in \mathcal{M}$ the Christoffel operator $\Gamma = \Gamma_p$ is a mapping $\Gamma_p : T_p\mathcal{M} \times T_p\mathcal{M} \to T_p\mathcal{M}$. For $U,V \in T_p\mathcal{M}$ the evaluation $\Gamma_p(U,V)$ is defined implicitly by

$$g_p(\Gamma_p(U,V),W) = \frac{1}{2}\Big((D_p g)\,(V)(U,W) + (D_p g)\,(U)(V,W) - (D_p g)\,(W)(U,V) \Big) \quad \forall W \in T_p\mathcal{M}\,. \tag{4.1.6}$$

Note that the symmetry of the metric implies the symmetry of the Christoffel operator. Existence of such an operator is shown in Thm. 4.2 of [Lan95, VIII]. Furthermore, if we assume g to be coercive (*e.g.* in the sense of (H1)) existence of Γ_p can be proved by means of the Riesz representation theorem. Indeed, if $(T_p\mathcal{M}, g_p)$, with $T_p\mathcal{M} = \mathbf{V}$, is a Hilbert space the mapping $\mathscr{R} : \mathbf{V} \to \mathbf{V}'$ defined by $\mathscr{R}(v) : w \mapsto g_p(v,w)$ is an isometric isomorphism.

Next, we define a covariant derivative along a curve by means of the Christoffel operator as in Sec. 3.1. Again, we start in a finite dimensional setup working with coordinates. Using (3.1.5) with the vector field $V(t) = \sum_k v_k(t) X_k(\gamma(t))$ along the curve $\gamma : I \to \mathcal{M}$, we get for $W = \sum_l w_l X_l \in T_p\mathcal{M}$

$$g_p\Big(\frac{D}{dt}V, W\Big) = \sum_{k,l=1}^{d} \Big(\dot{v}_k + \sum_{i,j=1}^{d} \Gamma_{ij}^k \dot{\gamma}_j v_i\Big) w_l g_{kl} = g_p\Big(\dot{V} + \Gamma_p(V,\dot{\gamma}), W\Big)\,, \tag{4.1.7}$$

where $\dot{V}(t) = \sum_k \dot{v}_k(t) X_k(\gamma(t))$ and Γ_p as in Def. 4.1.5. As above, we make use of (4.1.7) to define a covariant derivative along a curve *without* using coordinates:

Definition 4.1.6 (Covariant derivative). Let $\gamma : I \to \mathcal{M}$ be a curve and $V : I \to T\mathcal{M}$ a vector field along γ. We define the covariant derivative $\frac{D}{dt}V$ of V along γ at $p = \gamma(t)$ for $t \in I$ implicitly by

$$g_{\gamma(t)}\Big(\frac{D}{dt}V(t), W\Big) = g_{\gamma(t)}\Big(\dot{V}(t) + \Gamma_p\left(V(t), \dot{\gamma}(t)\right), W\Big) \quad \forall W \in T_{\gamma(t)}\mathcal{M}\,. \tag{4.1.8}$$

Remark 4.1.7. This is exactly the same formulation as in Thm. 3.1 in [Lan95, VIII]. As for the Christoffel operator one can show existence by means of the Riesz representation theorem if g is coercive.

With a notion of a covariant derivative along a curve we can define parallel transport such as in the finite dimensional setup (*cf.* Def. 3.1.15), which is indeed well-defined due to Thm. 3.3/3.4 in [Lan95, VIII]:

Proposition 4.1.8 (Parallel transport). *Let $\gamma : I \to \mathcal{M}$ be a curve. A vector field $V : I \to T\mathcal{M}$ along γ is called* parallel *if $\frac{D}{dt}V(t) = 0$ for all $t \in I$. For $t_0 \in I$, $V_0 \in T_{\gamma(t_0)}\mathcal{M}$, there is a unique parallel vector field $V : I \to T\mathcal{M}$ with $V(t_0) = V_0$. Furthermore, the map $\mathrm{P}_{\gamma(t_0)\to\gamma(t)} : T_{\gamma(t_0)}\mathcal{M} \to T_{\gamma(t)}\mathcal{M}$, $\mathrm{P}_{\gamma(t_0)\to\gamma(t)} V_0 = V(t)$ is a linear isomorphism.*

For a given vector $V_0 \in T_{\gamma(t_0)}\mathcal{M}$ one can solve $\frac{D}{dt}V(t) = 0$ with $V(t_0) = V_0$ as an ordinary differential equation to perform the (unique) parallel transport of V_0 along the path. The next theorem states that geodesics as defined in Def. 4.1.1 are solutions of the geodesic equation (*cf.* eq. (3.1.7) in Sec. 3.1):

Theorem 4.1.9. *If $y : [0,1] \to \mathcal{M}$ is a geodesic connecting $y(0)$ and $y(1)$, then $\frac{D}{dt}\dot{y} = 0$.*

Proof. Consider the Euler–Lagrange equation of the path energy and apply integration by parts to obtain

$$
\begin{aligned}
0 &= \partial_y \mathcal{E}[y](\vartheta) = \int_0^1 (D_y g_y)(\vartheta)(\dot{y}, \dot{y}) + 2g_y(\dot{y}, \dot{\vartheta}) \, dt \\
&= \int_0^1 (D_y g_y)(\vartheta)(\dot{y}, \dot{y}) - 2(D_y g_y)(\dot{y})(\dot{y}, \vartheta) - 2g_y(\ddot{y}, \vartheta) \, dt
\end{aligned}
$$

for all smooth test vector fields ϑ along the path y. By the fundamental lemma we achieve

$$
0 = g_y(\ddot{y}, \vartheta) + (D_y g_y)(\dot{y})(\dot{y}, \vartheta) - \frac{1}{2}(D_y g_y)(\vartheta)(\dot{y}, \dot{y}) = g_y(\ddot{y} + \Gamma(\dot{y}, \dot{y}), \vartheta) = g_y(\frac{D}{dt}\dot{y}, \vartheta). \quad \square
$$

In particular, minimizers of the path energy satisfy the constant speed property; *cf.* Rem. 3.1.10 (ii).

Remark 4.1.10. If $V : I \to T\mathcal{M}$ is a parallel vector field along a *geodesic* path $y : I \to \mathcal{M}$ the angle $\alpha(t)$ between the velocity field $\dot{y}(t)$ and $V(t)$ is fixed:

$$
\frac{d}{dt}\cos\alpha(t) = \frac{d}{dt}\left(\frac{g_y(V, \dot{y})}{\sqrt{g(V,V)}\sqrt{g(\dot{y}, \dot{y})}}\right) = \frac{g_y\left(\frac{D}{dt}V, \dot{y}\right) + g_y\left(V, \frac{D}{dt}\dot{y}\right)}{\sqrt{g(V,V)}\sqrt{g(\dot{y}, \dot{y})}} = 0.
$$

Finally, we define the exponential map for a general manifold (*cf.* Def. 3.1.21):

Definition 4.1.11 (Exponential map)**.** Let $y = y(t, p, V)$ be the solution of $\frac{D}{dt}\dot{y}(t) = 0$ for initial data $y(0) = p$ and $\dot{y}(0) = V$. The (geometric) exponential map $\exp_p : T_p\mathcal{M} = \mathbf{V} \to \mathcal{M}$ is defined as $\exp_p(V) = y(1, p, V)$.

To see that this definition is well-defined we refer to Prop. 4.2 in [Lan95, IV]. Obviously, we have the scaling property $y(t, p, V) = \exp_p(tV)$, which implies that $y(1, p, V)$ is well-defined if $\|V\|$ is sufficiently small (*cf.* Lemma 3.1.20). From the local uniqueness of short geodesic paths we deduce that there exists $\delta > 0$, such that $\exp_p : B_\delta(0) \to \exp_p(B_\delta(0))$ is a bijection. In this case, we define $U_p = \exp_p(B_\delta(0))$ to be the *normal neighbourhood* of p. Hence the notion of an inverse mapping is locally well-defined (*cf.* Def. 3.1.22):

Definition 4.1.12 (Logarithm)**.** The inverse operator of the exponential map is called the (geometric) logarithm $\log_p : U_p \to T_p\mathcal{M}$, where U_p denotes the normal neighbourhood of p.

4.2 Variational time-discretization of the geodesic calculus

In a sequence of papers, Rumpf and Wirth [Wir09, WBRS09, RW13, RW15, Rum15] have introduced a time-discrete analogon of the continuous geodesic calculus presented in the previous section. The resulting time-discrete geodesic calculus has already been applied to several Riemannian manifolds or shape spaces, *e.g.* in [HRWW12, HRS⁺14, BER15, MRSS15, Per15]. In this section, we provide a survey of the time-discrete geodesic calculus proposed by Rumpf and Wirth and summarize important convergence results that will later be validated numerically on the space of (discrete) shells. As before, we start with a variational formulation of *discrete* geodesics, defined via minimizers of a *discrete* path energy[1].

---

[1] Since we do not consider spatial discretization at all in this chapter, we will often omit the prefix "time" when referring to a time-discrete object.

However, different from the continuous setting, the notion of a discrete geodesic will then serve as the core ingredient of the entire discrete calculus. Hence, the name *geodesic calculus* is in particular justified in the discrete setting.

In the continuous setting the starting point of a geometric calculus on a Riemannian manifold is usually the definition of a Riemannian metric. However, as we will see, the discrete geodesic calculus is solely based on the notion of a (squared) Riemannian distance resp. a local approximation thereof. Obviously, a Riemannian distance is induced by the metric (*cf.* eq. (4.1.3)). On the other hand, given the Riemannian distance dist, one can recover the Riemannian metric g_p at some point $p \in \mathcal{M}$ by

$$g_p(V, W) = \frac{1}{2} \partial_2^2 \operatorname{dist}^2(p, p)(V, W) \,, \quad V, W \in T_p\mathcal{M} \,. \tag{4.2.1}$$

For many applications, *e.g.* when dealing with physical shape spaces, it is difficult to define a Riemannian metric a priori. On the other hand, it is often much easier to come up with the notion of a distance, *e.g.* by using a physically sound dissimilarity measure. To account for this circumstance as well as for the fact that Riemannian distances are in practice hard to compute (as they require solving an optimization problem), the discrete geodesic calculus is actually based on an *approximation* of the squared Riemannian distance which is easy to evaluate and consistent with the metric by definition due to (4.2.1).

4.2.1 Time-discrete path energy

In the following, we denote an ordered set of points $Y^K = (y_0, \ldots, y_K)$ in the manifold $\mathcal{M}$ as a time-discrete K-path. Often we interpret this discrete path as a uniform sampling of a smooth curve $y : [0, 1] \to \mathcal{M}$, *i.e.* we have $y_k = y(t_k)$ with $t_k = k\tau$ for $k = 0, \ldots, K$ where $\tau = K^{-1}$ and $K \in \mathbb{N}$ denotes the sample size. Instead of using a straightforward time-discretization of the continuous path energy (4.1.2) we first consider the following estimates

$$\mathcal{L}[(y(t))_{t\in[0,1]}] \geq \sum_{k=1}^{K} \operatorname{dist}(y_{k-1}, y_k) \,, \qquad \mathcal{E}[(y(t))_{t\in[0,1]}] \geq \frac{1}{\tau} \sum_{k=1}^{K} \operatorname{dist}^2(y_{k-1}, y_k) \,, \tag{4.2.2}$$

where equality holds for geodesic paths due to the constant speed property. The first estimate is straightforward, and the second estimate follows with the Cauchy-Schwarz inequality, *i.e.*

$$\sum_{k=1}^{K} \operatorname{dist}^2(y_{k-1}, y_k) \leq \sum_{k=1}^{K} \left(\int_{(k-1)\tau}^{k\tau} \sqrt{g_{y(t)}(\dot{y}(t), \dot{y}(t))} \, \mathrm{d}t \right)^2 \leq \sum_{k=1}^{K} \tau \int_{(k-1)\tau}^{k\tau} g_{y(t)}(\dot{y}(t), \dot{y}(t)) \, \mathrm{d}t \,,$$

since the expression on the right hand side is exactly $\tau \, \mathcal{E}[(y(t))_{t\in[0,1]}]$.

Remark 4.2.1. In the appendix (Lemma A.1.4 resp. A.1.5) we show a lower bound on the rightmost sum in (4.2.2). In detail, let $(y_0, \ldots, y_K) \subset \mathcal{M}$ be an arbitrary time-discrete K-path. Then we have

$$\operatorname{dist}^2(y_0, y_K) \leq K \sum_{k=1}^{K} \operatorname{dist}^2(y_{k-1}, y_k) \,,$$

with equality iff. there is a geodesic $y : [0, 1] \to \mathcal{M}$ such that $y(k\tau) = y_k$ for $k = 0, \ldots, K$.

The estimate on the path energy in (4.2.2) as well as Rem. 4.2.1 suggest that the sum on the right hand side might be a reasonable approximation of $\mathcal{E}$. However, as already mentioned in the beginning, the squared Riemannian distance dist^2 is often difficult to compute in practice. Therefore we assume there is a smooth functional $\mathcal{W} : \mathcal{M} \times \mathcal{M} \to \mathbb{R}$, such that for $y, \tilde{y} \in \mathcal{M}$

$$\mathcal{W}[y, \tilde{y}] = \operatorname{dist}^2(y, \tilde{y}) + O(\operatorname{dist}^3(y, \tilde{y})) \,. \tag{4.2.3}$$

Note that $\mathcal{W}$ is not required to be symmetric. For g smooth enough, a valid approximation of dist^2 is *e.g.* given by $\mathcal{W}[y,\tilde{y}] = \frac{1}{2}g_y(\tilde{y}-y,\tilde{y}-y)$. In general, we will see later that $g_y = \frac{1}{2}\mathcal{W}_{,22}[y,y]$ implies (4.2.3) for smooth g and $\mathcal{W}$.

We arrive at the following definition of a *discrete path energy* and a *discrete path length* (see [RW15]):

Definition 4.2.2 (Discrete length and energy). For a discrete K-path $Y^K = (y_0,\ldots,y_K)$ with $y_k \in \mathcal{M}$ for $k = 0,\ldots,K$ we define the *discrete length* L^K and the *discrete energy* E^K by

$$L^K[Y^K] = \sum_{k=1}^{K} \sqrt{\mathcal{W}[y_{k-1},y_k]}\,, \qquad E^K[Y^K] = K\sum_{k=1}^{K}\mathcal{W}[y_{k-1},y_k]\,. \tag{4.2.4}$$

Then a *discrete geodesic* (of order K) is defined as a minimizer of $E^K[Y^K]$ for fixed end points y_0, y_K.

In the remainder of this section we gather important theorems from [RW15], *e.g.* on the existence and uniqueness of discrete geodesics (*cf.* also [Rum15]). These results will provide a solid ground for the definition of further discrete geometric objects in the next section, which are based on discrete geodesics. First of all, one needs to introduce a rigorous functional analytic setup. Let $\mathcal{W} : \mathcal{M} \times \mathcal{M} \to \mathbb{R}$ be a local approximation of the squared Riemannian distance dist^2. In detail, it is supposed that $\mathcal{W}$ is weakly lower semi-continuous and that it satisfies the following hypotheses:

(H2)
$$\begin{cases} \text{There exist } \varepsilon, C > 0 \text{ such that for all } y, \tilde{y} \in \mathcal{M}: \\ \mathrm{dist}(y,\tilde{y}) \le \varepsilon \;\Rightarrow\; |\mathcal{W}[y,\tilde{y}] - \mathrm{dist}^2(y,\tilde{y})| \le C\mathrm{dist}^3(y,\tilde{y}) \\ \mathcal{W} \text{ is coercive in the sense } \mathcal{W}[y,\tilde{y}] \ge \gamma(\mathrm{dist}(y,\tilde{y})) \\ \text{for a strictly increasing, continuous function } \gamma \text{ with } \gamma(0) = 0 \text{ and } \lim_{d\to\infty}\gamma(d) = \infty. \end{cases}$$

Theorem 4.2.3 (Existence of discrete geodesics, [RW15]). *Given $y_A, y_B \in \mathcal{M}$, there is a discrete geodesic path $(y_0,\ldots,y_K)$ which minimizes the discrete energy E^K over all discrete paths $(\tilde{y}_0,\ldots,\tilde{y}_K)$ with $\tilde{y}_0 = y_A$ and $\tilde{y}_K = y_B$.*

Theorem 4.2.4 (Convergence of path energy, [RW15]). *Under hypothesis (H2) there exists $\delta > 0$ such that $\mathrm{dist}(y_A, y_B) < \sqrt{K}\delta$ implies*

$$\left| \min_{\substack{(y_0,\ldots,y_K) \\ y_0=y_A, y_K=y_B}} E^K[(y_0,\ldots,y_K)] - \mathrm{dist}^2(y_A, y_B) \right| = O(\tau)$$

Theorem 4.2.5 (Equidistribution of points along discrete geodesics, [RW15]). *Under hypothesis (H2) there exists $\delta > 0$ such that if $\mathrm{dist}(y_A, y_B) < \sqrt{K}\delta$, then discrete geodesics satisfy $\mathrm{dist}(y_{k-1}, y_k) \le C\tau$ for all $k = 1,\ldots,K$ with the constant $C > 0$ only depending on $\mathrm{dist}(y_A, y_B)$.*

Theorem 4.2.6 (Consistency conditions, [RW15]). *Unter hypothesis (H1), if $\mathcal{W}$ is twice Gâteaux-differentiable on $\mathcal{M} \times \mathcal{M}$ with bounded second Gâteaux derivative, then $\mathcal{W}[y,\tilde{y}] = \mathrm{dist}^2(y,\tilde{y}) + O(\mathrm{dist}^3(y,\tilde{y}))$ for $\tilde{y}$ close to $y \in \mathring{\mathcal{M}}$ implies*

$$\mathcal{W}[y,y] = 0\,, \quad \mathcal{W}_{,2}[y,y](V) = 0\,, \quad \mathcal{W}_{,22}[y,y](V,W) = 2g_y(V,W)$$

for any $V, W \in \mathbf{V}$. Furthermore, $\mathcal{W}_{,1}[y,y](V) = 0$ and

$$\mathcal{W}_{,11}[y,y](V,W) = -\mathcal{W}_{,12}[y,y](V,W) = -\mathcal{W}_{,21}[y,y](V,W) = \mathcal{W}_{,22}[y,y](V,W)\,.$$

If $\mathcal{W}$ is even three times Fréchet-differentiable, the implication becomes an equivalence.

Theorem 4.2.7 (Uniqueness of discrete geodesics, [RW15]). *Let (H1) and (H2) hold and assume $\mathcal{W}$ to be twice Fréchet-differentiable on $\mathcal{M} \times \mathcal{M}$. For all $y_A \in \mathring{\mathcal{M}}$ and $K \in \mathbb{N}$ there exists $\varepsilon > 0$ such that there exists a unique discrete geodesic $(y_0,\ldots,y_K)$ with $y_0 = y_A$ and $y_K = y_B$ for all y_B with $\|y_A - y_B\|_{\mathbf{V}} < \varepsilon$.*

4.2.2 Time-discrete geometric objects

Let $p, q \in \mathcal{M}$ such that there is a unique geodesic $y : [0,1] \to \mathcal{M}$ with $y(0) = p$ and $y(1) = q$. Then, by Def. 4.1.12, the logarithm of q with respect to p is the initial velocity $\dot{y}(0) \in T_p\mathcal{M}$, *i.e.* $\log_p(q) = \dot{y}(0)$. The initial velocity $\dot{y}(0)$ can be approximated by a difference quotient in time,

$$\dot{y}(0) = \frac{y(\tau) - y(0)}{\tau} + O(\tau)\,.$$

Thus, we obtain

$$\tau \log_p(q) = y(\tau) - y(0) + O(\tau^2)\,.$$

This gives rise to a consistent definition of a time-discrete logarithm (see [RW15]):

Definition 4.2.8 (Discrete logarithm)**.** Suppose the discrete geodesic $(y_0, \ldots, y_K)$ is the unique minimizer of the discrete path energy (4.2.4) with $y_0 = p$ and $y_K = q$. Then we define the *discrete logarithm* $\left(\frac{1}{K}\text{LOG}\right)_p(q) = y_1 - y_0$. Note that $\frac{1}{K}$ is part of the symbol and not a factor.

We consider the difference $y_1 - y_0$ as a tangent vector at $p = y_0$. In the special case $K = 1$ we have $\left(\frac{1}{1}\text{LOG}\right)_p(q) = q - p$. As in the continuous case, the discrete logarithm can be considered as a representation of the nonlinear variation q of p in the (linear) tangent space of *displacements*[1] on p.

In the continuous setting, the exponential map $\exp_p$ maps tangent vectors $V \in T_p\mathcal{M}$ onto the end point $y(1)$ of the unique geodesic $(y(t))_{t \in [0,1]}$ with $y(0) = p$ and $\dot{y}(0) = V$. That means, we have $\exp_p(V) = y(1)$ and, via a simple scaling argument, $\exp_p(t_k V) = y(t_k)$, for $k = 0, \ldots, K$, where $t_k = k\tau$ and $\tau = K^{-1}$. Let us again consider a discrete geodesic $(y_0, \ldots, y_K)$ with $y_0 = p$ and $y_K = q$. Since $V = \left(\frac{1}{K}\text{LOG}\right)_p(q) = y_1 - y_0$ is the discrete logarithm in the tangent space $T_p\mathcal{M}$, we aim at defining a discrete power k exponential map EXP_p^k such that

$$\text{EXP}_p^k(V) = \text{EXP}_p(kV) = y_k\,.$$

This notation is motivated by the observation that $\exp(ks) = \exp^k(s)$ on $\mathbb{R}$ or more general matrix groups. Furthermore, we would like to have the following recursive property, which holds in the continuous setup:

$$y(t_k) = \exp_p(kV) = \exp_{y(t_{k-2})}(2V_{k-1})\,, \quad V_{k-1} := \log_{y(t_{k-2})} y(t_{k-1})\,, \quad k \geq 2\,. \tag{4.2.5}$$

That means, once we have defined a discrete version EXP_p^2 corresponding to $\exp_p(2\cdot)$, we can use the recursive relation (4.2.5) to define EXP_p^k for $k \geq 2$ by

$$y_k = \text{EXP}_p^k(V_1) = \text{EXP}_{y_{k-2}}^2(V_{k-1})\,, \quad V_{k-1} = y_{k-1} - y_{k-2}\,, \tag{4.2.6}$$

for given $y_0 = p$ and $y_1 = y_0 + V_1$, as shown in Fig. 4.1.
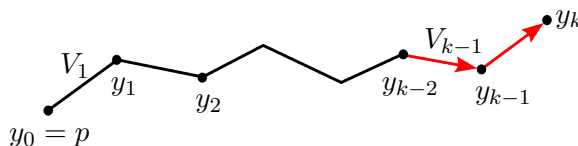
Figure 4.1: *A sketch of the polygonal path associated with the computation of* $\text{EXP}_p^k(V_1)$.

---

[1]Note that these displacements are indeed well-defined, as we assumed that $\mathcal{M}$ embeds into a Banach space.

Note that the discrete analogon of V_{k-1} is exactly $V_{k-1} = (\frac{1}{1}\mathrm{LOG})_{y_{k-2}} y_{k-1} = y_{k-1} - y_{k-2}$.

It remains to define a discrete version EXP_p^2 corresponding to $\exp_p(2\cdot)$. Formally, we have the identity $\frac{1}{2}\log_p\left(\exp_p(2V)\right) = V$, *i.e.* we can define $\mathrm{EXP}_{y_0}^2(y_1 - y_0)$ as the root of the function

$$z \mapsto (\tfrac{1}{2}\mathrm{LOG})_{y_0}(z) - (y_1 - y_0)$$

for given $y_0, y_1 \in \mathcal{M}$. In fact, we are seeking for a third point $y_2 \in \mathcal{M}$, such that (y_0, y_1, y_2) is a time-discrete geodesic for $K = 2$. Using Def. 4.2.2, a necessary condition of this is given by

$$0 = \partial_2 \mathcal{W}[y_0, y_1](\psi) + \partial_1 \mathcal{W}[y_1, y_2](\psi) \quad \forall \psi \in \mathbf{V},$$

where $\partial_i \mathcal{W}$ denotes the Gâteaux derivative with respect to the ith argument of $\mathcal{W}$. Hence we define:

Definition 4.2.9 (Discrete exponential map)**.** For given points $y_0, y_1 \in \mathcal{M}$, $V_1 = y_1 - y_0$, we define $\mathrm{EXP}_{y_0}^2(V_1)$ as the solution of

$$\partial_2 \mathcal{W}[y_0, y_1](\psi) + \partial_1 \mathcal{W}[y_1, y](\psi) = 0 \quad \forall \psi \in \mathbf{V},$$

and hence $\mathrm{EXP}_{y_0}^k(V_1) = \mathrm{EXP}_{y_{k-2}}^2(V_{k-1})$ for $V_{k-1} = y_{k-1} - y_{k-2}$ and $k \geq 2$.

Remark 4.2.10. It is straightforward to verify that $\mathrm{EXP}_p^K = (\frac{1}{K}\mathrm{LOG})_p^{-1}$ as long as the discrete logarithm is invertible. In fact, the Euler–Lagrange equations for $(y_0, \ldots, y_K)$ being a discrete geodesic with fixed end points y_0 and y_K are given by the $K - 1$ nonlinear equations

$$0 = \partial_2 \mathcal{W}[y_{k-1}, y_k](\psi) + \partial_1 \mathcal{W}[y_k, y_{k+1}](\psi) \quad \forall \psi \in \mathbf{V}, \quad k = 1, \ldots, K-1, \tag{4.2.7}$$

which have to be solved *simultaneously*. On the other hand, if we compute $\mathrm{EXP}_{y_0}^k(y_1 - y_0)$ for given $y_0, y_1 \in \mathcal{M}$ and $k = 2, \ldots, K$, we get exactly the same system (4.2.7). However, in this case the system can be solved *sequentially*.

Finally, we introduce a time-discrete notion of parallel transport along a discrete path as proposed in [RW15]. In the continuous setting, given a path $y : [0,1] \to \mathcal{M}$ and a vector $V_0 \in T_{y(0)}\mathcal{M}$, parallel transport $\mathrm{P}_{y(0) \to y(\tau)} V_0$ of V_0 along the path y is defined as the solution of the initial value problem $\frac{D}{dt} V(t) = 0$ for $t \in [0, \tau]$ and $V(0) = V_0$.
There is a well-known first-order approximation of parallel transport called Schild's ladder (*cf.* [EPS72, KMN00]), which is based on the construction of a sequence of so-called *geodesic parallelograms*; this method has been used *e.g.* by Lorenzi *et al.* [LAP11] to perform parallel transport of deformations along time series of images (see also [PL11]). We once more use the notation $y_k = y(t_k)$, $t_k = k\tau$, for samples of the path $y : [0,1] \to \mathcal{M}$. Given a tangent vector $V_{k-1} \in T_{y_{k-1}}\mathcal{M}$, the approximation $V_k \in T_{y_k}\mathcal{M}$ of the parallely transported vector $\mathrm{P}_{y_{k-1} \to y_k} V_{k-1}$ via a geodesic parallelogram is illustrated in Fig. 4.2.
The scheme in Fig. 4.2 can be easily transferred to the time-discrete setup by replacing y by a discrete path $(y_0, \ldots, y_K)$ and the geodesics that define the geodesic parallelogram by time-discrete geodesics, *e.g.* of length 3. Conceptually, we will again replace tangent or velocity vectors V by displacements ζ of points.

Definition 4.2.11 (Discrete geodesic parallelogram)**.** Let $p_0, p_1, p_2 \in \mathcal{M}$. We define $\hat{p} = \hat{p}(p_0, p_1, p_2)$ such that (p_0, p^c, p_2) and $(p_1, p^c, \hat{p})$ are discrete geodesics for some $p^c \in \mathcal{M}$. Then $(p_0, p_1, p_2, \hat{p})$ defines a discrete geodesic parallelogram, p^c is refered to as center point of the parallelogram.

Figure 4.2: *A sketch of the parallel transport of $V_{k-1} \in T_{y_{k-1}}\mathcal{M}$ from y_{k-1} to y_k along y via Schild's ladder. Here, y_k^c is the midpoint of the two diagonals of the geodesic parallelogramm, i.e. (y_{k-1}^p, y_k^c, y_k) and (y_{k-1}, y_k^c, y_k^p), which are both geodesic curves.*
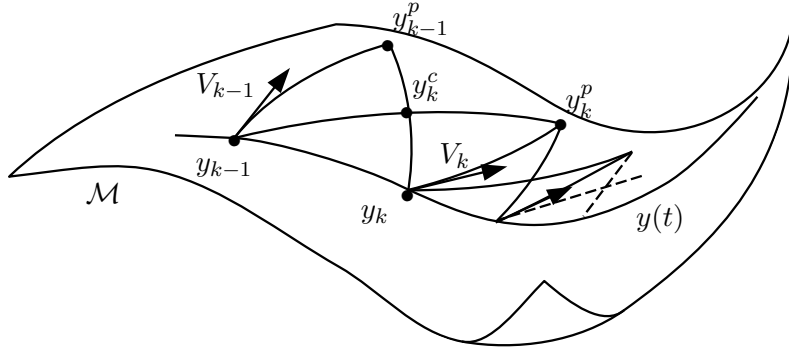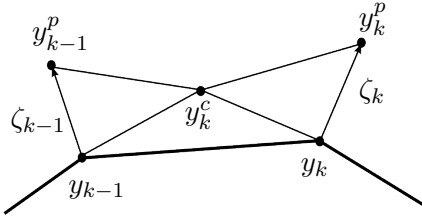
$$y_{k-1}^p = \exp_{y_{k-1}}(V_{k-1})$$

$$y_k^c = \exp_{y_{k-1}^p}\left(\tfrac{1}{2}\log_{y_{k-1}^p}(y_k)\right)$$

$$y_k^p = \exp_{y_{k-1}}\left(2\log_{y_{k-1}}(y_k^c)\right)$$

$$V_k = \log_{y_k}(y_k^p)$$

Definition 4.2.12 (Discrete parallel transport). Let $(y_0, \dots, y_K)$ be a discrete path in $\overset{\circ}{\mathcal{M}}$ with $y_k - y_{k-1}$ sufficiently small for $k = 1, \dots, K$ and ζ_0 a sufficiently small displacement of y_0, given as $y_0^p = y_0 + \zeta_0$. Then the *discrete parallel transport* of ζ_0 along $(y_0, \dots, y_K)$ is defined for $k = 1, \dots, K$ via the iteration

$$y_k^c = y_{k-1}^p + \left((\tfrac{1}{2}\mathrm{LOG})_{y_{k-1}^p}(y_k)\right),$$

$$y_k^p = \mathrm{EXP}^2_{y_{k-1}}\left(y_k^c - y_{k-1}\right),$$

where $\zeta_k = y_k^p - y_k$ is the transported displacement at y_k. We define

$$\mathbf{P}_{y_K,\dots,y_0}(y_0^p - y_0) = y_K^p - y_K.$$

The notation is chosen such that $\mathbf{P}_{y_K,\dots,y_0}\mathbf{P}_{\tilde{y}_K,\dots,\tilde{y}_0} = \mathbf{P}_{y_K,\dots,y_0,\tilde{y}_K,\dots,\tilde{y}_0}$.

Remark 4.2.13. In the kth step of the discrete parallel transport the Euler–Lagrange equations to determine y_k^c and $y_k^p = y_k + \zeta_k$ for given $y_{k-1}^p = y_{k-1} + \zeta_{k-1}$ and discrete path $(y_0, \dots, y_K)$ are

$$\mathcal{W}_{,2}[y_{k-1}^p, y_k^c](\psi) + \mathcal{W}_{,1}[y_k^c, y_k](\psi) = 0 \quad \forall \psi \in \mathbf{V},$$
$$\mathcal{W}_{,2}[y_{k-1}, y_k^c](\psi) + \mathcal{W}_{,1}[y_k^c, y_k^p](\psi) = 0 \quad \forall \psi \in \mathbf{V}.$$

If $\mathcal{W}$ is symmetric, these conditions are the same as the Euler–Lagrange equations for inverse parallel transport, so that $\mathbf{P}_{y_K,\dots,y_0}^{-1} = \mathbf{P}_{y_0,\dots,y_K}$. However, if $\mathcal{W}$ is not symmetric this is not true in general.

In the remainder of this section we gather important theorems from [RW15], which examine the convergence properties of the discrete geometric calculus as the time step size $\tau = \frac{1}{K}$ tends to 0.

First, we state that sequences of successively refined discrete geodesic paths converge to a continuous geodesic path. To this end, one considers continuous paths $(y(t))_{t\in[0,1]}$ on $\mathcal{M}$ which are composed of shortest geodesic segments. This means, $(y(t))_{t\in[\frac{k-1}{K},\frac{k}{K}]}$ is a (possibly non-unique) shortest geodesic path connecting $y(\frac{k-1}{K})$ and $y(\frac{k}{K})$ for all $k = 1, \dots, K$. We define an energy $\tilde{E}^K : L^2((0,1); \mathbf{Y}) \to \mathbb{R}$ via

$$\tilde{E}^K[(y(t))_{t\in[0,1]}] = \begin{cases} E^K\left[(y(0), y(\tfrac{1}{K}), \dots, y(\tfrac{K-1}{K}), y(1))\right], & \text{if } (y(t))_{t\in[0,1]} \text{ is a pw. geodesic path} \\ \infty, & \text{else} \end{cases}.$$

where E^K denotes the discrete path energy in (4.2.4). Based on these notational preliminaries one obtains the following convergence result:

Theorem 4.2.14 (Γ-convergence of the discrete energy, [RW15]). *Assuming* (H1) *and* (H2)*, the Γ-limit of $\tilde{E}^K$ for $K \to \infty$ in the $L^2((0,1); \mathbf{Y})$-topology is $\mathcal{E}$.*

We refer to [DGDM83, Bra02] for an introduction to the concept of Γ-convergence. It is a fundamental implication of the Γ-convergence $\tilde{E}^K \to \mathcal{E}$, that minimizers of $\tilde{E}^K$ converge to minimizers of $\mathcal{E}$, *i.e.* one has actually shown convergence of time-discrete geodesic to continuous geodesics:

Corollary 4.2.15 (Convergence of discrete geodesics, [RW15]). *Under* (H1) *and* (H2)*, any sequence of minimizers of $\tilde{E}^K$ contains a $C^0([0,1]; \mathbf{Y})$-convergent subsequence, and the limit is a minimizer of $\mathcal{E}$.*

Remark 4.2.16. Taking into account the equivalence of the $\mathbf{V}$ topology and the manifold topology mentioned in Remark 4.1.4, a similar argument can be given for the piecewise linear interpolation of discrete geodesics $(y_0, \ldots, y_K)$ instead of piecewise geodesic interpolations.

Note that discrete minimizers of the discrete path length L^K are in general unrelated to continuous geodesics. Let us consider the case $\mathcal{M} = \mathbb{R}^2 \setminus B_r$, where $B_r = \{x : |x| < r\}$, and $\mathcal{W}[y, \tilde{y}] = \|y - \tilde{y}\|^2$, as depicted in Fig. 4.3. Then a discrete path $(y_0, \ldots, y_K)$ connecting $y_A = (-\alpha r, 0)$ and $y_B = (\alpha r, 0)$, $\alpha > 1$, that minimizes the time-discrete path energy tend to distribute uniformly along the connecting curve, as stated in Thm. 4.2.5. If $r \gg \text{dist}(y_A, y_B)/K$ this is not realizable along a straight line connecting y_A and y_B, *cf.* Fig. 4.3. However, the distribution of points representing a discrete minimizer of L^K is arbitrary, since moving points along the connecting line does not alter the length.
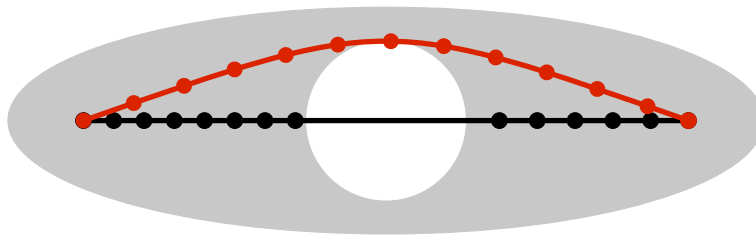
Figure 4.3: *In general, minimizers of the discrete path length do not converge to continuous geodesics.*

For convergence of discrete logarithm, exponential map, and parallel transport, the following smoothness hypotheses are required (in addition to (H1) and (H2)):

(H3) The metric g is $C^2(\mathbf{Y}; \mathbf{V}' \otimes \mathbf{V}')$-smooth.

(H4) The energy $\mathcal{W}$ is $C^4(\mathcal{M} \times \mathcal{M}; \mathbb{R})$-smooth with bounded derivatives.

In [RW15] it is shown that under hypotheses (H1) - (H4) one can expect local uniqueness of $(\frac{1}{2}\text{LOG})$ and local existence of (EXP^2). Moreover, Rumpf and Wirth have proven that all time-discrete geometric objects introduced above converge to their continuous counterparts:

Theorem 4.2.17 (Convergence of discrete logarithm, [RW15]). *Given $y, \tilde{y} \in \mathring{\mathcal{M}}$, assume that hypotheses* (H1) - (H4) *hold, that the continuous and discrete geodesics between $y, \tilde{y}$ are unique, and that the continuous geodesic lies in $\mathring{\mathcal{M}}$. Then $K(\frac{1}{K}\text{LOG})_y \tilde{y} \to \log_y \tilde{y}$ weakly in $\mathbf{V}$ (and thus strongly in $\mathbf{Y}$) as $K \to \infty$.*

Theorem 4.2.18 (Existence and convergence of discrete exponential, [RW15]). *Let $y : [0,1] \to \mathring{\mathcal{M}}$ be a smooth geodesic. Under the hypotheses* (H1) - (H4)*, $\text{EXP}^K_{y(0)}(\frac{\dot{y}(0)}{K})$ exists for K large enough, and for $\tau = \frac{1}{K}$ one obtains*

$$\left\| \text{EXP}^K_{y(0)}\big(\tfrac{\dot{y}(0)}{K}\big) - y(1) \right\|_{\mathbf{V}} = O(\tau).$$

Theorem 4.2.19 (Convergence of discrete parallel transport, [RW15])**.** *Let $y : [0,1] \to \mathcal{M}$ be a smooth path and $\zeta : [0,1] \to \mathbf{V}$ a parallel vector field along y. For $K \in \mathbb{N}$ and $\tau = K^{-1}$ we set $y_k = y(k\tau)$, $k = 0, \ldots, K$. Then under the hypotheses* (H1) - (H4)*, we have*

$$\left\| K\mathbf{P}_{y_K,\ldots,y_0}\left(\frac{\zeta(0)}{K}\right) - \zeta(1)\right\|_{\mathbf{V}} = O(\tau)\,.$$

More generally, if the sequence $(y_k)_k$ only satisfies $\|y_k - y(k\tau)\|_{\mathbf{V}} \leq \epsilon$, $k = 0, \ldots, K$, we still get

$$\left\| K\mathbf{P}_{y_K,\ldots,y_0}\left(\frac{\zeta(0)}{K}\right) - \zeta(1)\right\|_{\mathbf{V}} = O(\tau + \epsilon)\,.$$

4.3 Riemannian splines

For two points $p_0, p_1 \in \mathcal{M}$ a smooth interpolation $y : [0,1] \to \mathcal{M}$ with $y(0) = p_0$ and $y(1) = p_1$ is given by the connecting geodesic path. However, for a sequence $0 = t_1 < t_2 < \ldots < t_J = 1$ and corresponding points $p_1, \ldots, p_J \in \mathcal{M}$, there is in general no geodesic curve $y : [0,1] \to \mathcal{M}$ that fulfills the *interpolation constraints*, i.e. $y(t_j) = p_j$ for $j = 1, \ldots, J$. In particular, a curve y satisfying the interpolation constraints does in general not comply with the geodesic equation $\frac{D}{dt}\dot{y} = 0$. For example, a piecewise geodesic curve connecting $p_1, \ldots, p_J$ fulfills $\frac{D}{dt}\dot{y} = 0$ on each segment (t_j, t_{j+1}), $j = 1, \ldots, J-1$, but exhibits discontinuities in $\dot{y}$ at the interpolation points. Nevertheless, if one is interested in a curve that on the one hand satisfies the interpolation constraints *exactly* and on the other hand is *as smooth as possible*, one might consider the geodesic equation as a *penalty term*. This motivation leads to the functional

$$\mathcal{F}[(y(t))_{t\in[0,1]}] = \int_0^1 g_{y(t)}\left(\frac{D}{dt}\dot{y}(t), \frac{D}{dt}\dot{y}(t)\right)\, \mathrm{d}t\,, \tag{4.3.1}$$

where $\frac{D}{dt}$ denotes the covariant derivative along y as defined by Def. 4.1.6.

In the finite dimensional Euclidean setting, *i.e.* $\mathcal{M} = \mathbb{R}^d$ and g_p denotes the standard Euclidean product, the covariant derivative of $\dot{y}$ is simply given by the second time derivative $\ddot{y}$, *i.e.* we have

$$\mathcal{F}_{\mathrm{Euc}}[(y(t))_{t\in[0,1]}] = \int_0^1 \|\ddot{y}(t)\|^2\, \mathrm{d}t\,. \tag{4.3.2}$$

Consider a discretization of the unit interval $I = [0,1]$ with nodes $I_h = \{0 = z_0 < z_2 < \ldots < z_N = 1\}$. A spline function of degree k on I_h is a function $s \in C^{k-1}(I, \mathbb{R}^d)$ such that s is a polynomial of degree $\leq k$ on each interval $[z_{n-1}, z_n]$, $n = 1, \ldots, N$. The following theorem is often refered to as Schoenberg's theorem although it has been proved first by de Boor[1]:

Theorem 4.3.1 (de Boor, 1963)**.** *For $0 = t_1 < t_2 < \ldots < t_J = 1$ and $p_1, \ldots, p_J \in \mathbb{R}^d$ there is a unique minimizer $y \in C^2([0,1], \mathbb{R}^d)$ of $\mathcal{F}_{\mathrm{Euc}}$ that satisfies the interpolation constraints $y(t_j) = p_j$ for $j = 1, \ldots, J$ as well as one of the boundary conditions*

$$\ddot{y}(0) = \ddot{y}(1) = 0\,, \qquad\qquad\qquad\qquad\qquad \textit{(natural b.c.)}$$

$$\dot{y}(0) = v_0\,, \quad \dot{y}(1) = v_1 \quad \textit{for given } v_0, v_1 \in \mathbb{R}^d,\ or \qquad \textit{(Hermite b.c.)}$$

$$y(0) = y(1)\,, \quad \dot{y}(0) = \dot{y}(1)\,, \quad \ddot{y}(0) = \ddot{y}(1)\,. \qquad\qquad \textit{(periodic b.c.)}$$

The minimizer is given by the unique cubic spline, i.e. *a spline of degree 3, satisfying the interpolation constraints and boundary conditions.*

---

[1] Actually, Schoenberg cites de Boor's paper [dB63] when referring to this result in [Sch64b]. For further reading on this we refer to [Sch73, Sch64a], a simple proof is given *e.g.* in [DH02, 7.4].

As (4.3.1) can be seen as a generalization of (4.3.2) to Riemannian manifolds, we refer to $\mathcal{F}$ as *spline energy* and we denote minimizers of $\mathcal{F}$ as *Riemannian (cubic) splines*.

Remark 4.3.2. We refer to our forthcoming paper [HRW16] for a detailed discussion of existence of such interpolating splines, which is beyond the scope of this thesis. However, on general manifolds there may be situations where global minimizers of the spline energy $\mathcal{F}$ do not exist. To ensure well-posedness one can regularize the problem and consider minimizers of the augmented functional $y \mapsto \mathcal{F}[y] + \sigma \mathcal{E}[y]$ with $\sigma > 0$. Here $\mathcal{E}$ denotes the path energy as defined in (4.1.2). Under certain additional assumptions on $\mathcal{M}$ and g one can then show existence of minimizers of $\mathcal{F} + \sigma \mathcal{E}$ (see [HRS$^+$16, Sec. 9] and [HRW16]). Minimizers of a linear combination of path energy and spline energy are often referred to as *splines in tension*, *cf. e.g.* [Sch66].

4.3.1 Variational time-discretization

In this section, we derive a consistent time-discretization of the spline energy (4.3.1) that fits into the framework of time-discrete geodesic calculus presented in Sec. 4.2. As a motivation we start taking a look at the Euclidean setup, *i.e.* $\mathcal{M} = \mathbb{R}^d$. We consider a curve $y : [0, 1] \to \mathcal{M}$ and for some stepsize $\tau = K^{-1}$ a uniform sampling $y_k = y(t_k)$ with $t_k = k\tau$ for $k = 0, \ldots, K$. In the following, we focus on the local configuration around some interior point y_k, $0 < k < K$. The continuous spline energy is given by (4.3.2), *i.e.* the covariant derivative of $\dot{y}$ is simply the second time derivative $\ddot{y}$. Approximating the integrand $\|\ddot{y}(t_k)\|^2$ by a second order finite difference quotient yields

$$\|\ddot{y}(t_k)\|^2 \approx \left\| \frac{2\, y_k - y_{k-1} - y_{k+1}}{\tau^2} \right\|^2 = 4\tau^{-4} \left\| y_k - \frac{y_{k-1} + y_{k+1}}{2} \right\|^2 .$$

The key insight is to interprete the local average $\frac{1}{2}(y_{k-1} + y_{k+1})$ as the midpoint of a geodesic in the Euclidean space connecting y_{k-1} and y_{k+1}, where a geodesic is given by the straight connecting line. Replacing the Euclidean metric by a general Riemannian metric, *i.e.* the squared Euclidean distance $\mathrm{dist}^2_{\mathrm{euc}}(p, q) = \|p - q\|^2$ by the squared Riemannian distance dist^2, and the local average by the midpoint $\tilde{y}_k$ of a short geodesic connecting y_{k-1} and y_{k+1}, one obtains

$$g_{y(t_k)} \left(\frac{D}{dt} \dot{y}(t_k), \frac{D}{dt} \dot{y}(t_k) \right) \approx 4\tau^{-4} \, \mathrm{dist}^2(y_k, \tilde{y}_k) .$$

If we finally substitute the squared Riemannian distance by the local approximation $\mathcal{W}$, we arrive at

$$g_{y(t_k)} \left(\frac{D}{dt} \dot{y}(t_k), \frac{D}{dt} \dot{y}(t_k) \right) \approx 4\tau^{-4} \, \mathcal{W}[y_k, \tilde{y}_k] , \tag{4.3.3}$$

$\tilde{y}_k$ is midpoint of the geodesic connecting y_{k-1} and y_{k+1}.

Using the simple numerical quadrature $\int_0^1 f(t) \, \mathrm{d}t \approx \tau \sum_{k=1}^{K-1} f(t_k)$ to integrate (4.3.3) we arrive at the definition of a *time-discrete spline energy*:

Definition 4.3.3 (Time-discrete spline energy)**.** For $K \in \mathbb{N}$ let $Y^K = (y_0, \ldots, y_K)$ be a discrete K-path in $\mathcal{M}$. We define the time-discrete spline energy by

$$F^K[Y^K] = 4K^3 \sum_{k=1}^{K-1} \mathcal{W}[y_k, \tilde{y}_k] , \tag{4.3.4}$$

subject to the constraint that $(y_{k-1}, \tilde{y}_k, y_{k+1})$ is a discrete geodesic for $k = 1, \ldots, K-1$, *i.e.*

$$\tilde{y}_k = \arg\min_{y \in \mathcal{M}} \left(\mathcal{W}[y_{k-1}, y] + \mathcal{W}[y, y_{k+1}] \right), \text{ for } k = 1, \ldots, K-1 . \tag{4.3.5}$$

Remark 4.3.4. Boundedness of the discrete spline energy does not necessarily imply boundedness of the discrete path energy in general. Indeed, a discrete geodesic has zero discrete spline energy but positive discrete path energy. As a consequence, minimizing the discrete spline energy might not be a well-posed problem. However, one can consider the functional $F^K + \sigma E^K$ instead (*cf*. Rem. 4.3.2). Again, one can show existence of discrete minimizers for every $\sigma > 0$ subject to the interpolation conditions as well as the Γ-convergence of $F^K + \sigma E^K$ to $\mathcal{F}^K + \sigma \mathcal{E}^K$ (*cf*. [HRW16]). In what follows, however, we stick to F^K (without adding the path energy) since we never observed numerical instabilities in practice.

Definition 4.3.5 (Time-discrete spline). For $K \in \mathbb{N}$ let $Y^K = (y_0, \dots, y_K)$ be a discrete K-path in $\mathcal{M}$. Let $0 = i_1 < i_2 < \dots < i_J = K$ be an index set ($J \geq 2$). We say that Y^K is a time-discrete spline interpolating $y_{i_1}, \dots, y_{i_J}$ if it minimizes (4.3.4) while fixing y_{i_j} for $j = 1, \dots, J$.

Remark 4.3.6. If $J = 2$, *i.e.* we only fix y_0 and y_K, the time-discrete spline is precisely the time-discrete geodesic connecting y_0 and y_K.

Before proving consistency of the time-discrete spline energy, we will comment on the boundary conditions. In the following, we formulate three types of boundary conditions, analogously to the Euclidean case in Thm. 4.3.1. Therefore we temporarily consider a generalization of Def. 4.3.3 by introducing *ghost points* y_{-1} and y_{K+1}, which are supposed to extend the discrete path $(y_0, \dots, y_K)$ in both directions. We derive the boundary conditions in the generalized setting and eventually see that we do not need the ghost points at all, *i.e.* end up with Def. 4.3.3 again. The generalized time-discrete spline energy is defined by

$$\tilde{F}^K[y_0, \dots, y_K] = F^K[y_{-1}, y_0, \dots, y_K, y_{K+1}] = 4K^3 \sum_{k=0}^K \mathcal{W}[y_k, \tilde{y}_k],$$

$$\text{s.t. } \tilde{y}_k = \arg\min_{y \in \mathcal{M}} \left(\mathcal{W}[y_{k-1}, y] + \mathcal{W}[y, y_{k+1}] \right), \text{ for } k = 0, \dots, K.$$

Different to Def. 4.3.3 the index in the sum as well as in the constraint equations now runs from $k = 0$ to $k = K$. The constraint equations can be expressed as the following necessary conditions which have to hold for all test functions $\psi \in \mathbf{V}$:

$$[0] \quad 0 = \partial_2 \mathcal{W}[y_{-1}, \tilde{y}_0](\psi) + \partial_1 \mathcal{W}[\tilde{y}_0, y_1](\psi)$$

$$[1] \quad 0 = \partial_2 \mathcal{W}[y_0, \tilde{y}_1](\psi) + \partial_1 \mathcal{W}[\tilde{y}_1, y_2](\psi)$$

$$\vdots$$

$$[K-1] \quad 0 = \partial_2 \mathcal{W}[y_{K-2}, \tilde{y}_{K-1}](\psi) + \partial_1 \mathcal{W}[\tilde{y}_{K-1}, y_K](\psi)$$

$$[K] \quad 0 = \partial_2 \mathcal{W}[y_{K-1}, \tilde{y}_K](\psi) + \partial_1 \mathcal{W}[\tilde{y}_K, y_{K+1}](\psi)$$

Natural boundary conditions The condition $\ddot{y}(0) = 0$ resp. $\ddot{y}(1) = 0$ is given by enforcing $\tilde{y}_0 := y_0$ resp. $\tilde{y}_K := y_K$, *i.e.* we have $\mathcal{W}[y_0, \tilde{y}_0] = 0$ resp. $\mathcal{W}[y_K, \tilde{y}_K] = 0$. Obviously, the summation in $\tilde{F}^K$ will then run from $k = 1$ to $k = K-1$ again. Furthermore, if we formally define

$$y_{-1} := \text{EXP}_{y_1}^2(y_0 - y_1), \quad y_{K+1} := \text{EXP}_{y_{K-1}}^2(y_K - y_{K-1}), \tag{4.3.6}$$

condition [0] and [K] are fulfilled by definition, hence we end up with the setting in Def. 4.3.3.

Hermite boundary conditions Instead of prescribing first derivatives at $t = 0$ and $t = 1$ we will prescribe y_1 and y_{K-1} (note that y_0 and y_K are always fixed). Again we set $\tilde{y}_0 := y_0$ and $\tilde{y}_K := y_K$ and use (4.3.6) to get back the setting in Def. 4.3.3 (fixing at least y_0, y_1 and y_{K-1}, y_K).

Periodic boundary conditions We set $y_0 = y_K$ to have a closed curve. In order to ensure higher regularity we additionally postulate $y_{K+1} := y_1$ and $y_{-1} := y_{K-1}$. Plugging this into condtion [0] and [K] we see that these two equations coincide, *i.e.* we have $\tilde{y}_K = \tilde{y}_0$. Due to the periodic identification summation runs from $k = 0$ to $k = K-1$ and we end up having K conditions for $\tilde{y}_0, \dots, \tilde{y}_{K-1}$.

4.3.2 Consistency of the time-discrete spline energy

In this section we prove consistency for the time-discrete spline energy (4.3.4), which is based on a quantitative consistency error analysis of the approximation in (4.3.3).

Due to the variational constraint in the definition of F^K, we have to ensure that the objects $\tilde{y}_k$ in (4.3.5), $k = 1, \ldots, K-1$, are indeed well-defined:

Definition 4.3.7 (Admissible path)**.** A discrete path $(y_0, \ldots, y_K)$ is admissible, if $\epsilon = 2 \max_k \|y_k - y_{k-1}\|_{\mathbf{V}}$ is small enough, s.t. for each $0 < k < K$ any two points in $B_\epsilon(y_k) = \{y \in \mathcal{M} : \|y - y_k\|_{\mathbf{V}} < \epsilon\}$ can be uniquely connected by a discrete geodesic.

Remark 4.3.8. Let $y : [0,1] \to \mathcal{M}$ be a curve with $y_k = y(k\tau)$ for $k = 0, \ldots, K$ and $\tau = K^{-1}$. Then we have $\max_k \|y_k - y_{k-1}\| \leq \tau \|\dot{y}\|_\infty$. Hence for any $\epsilon > 0$ there is a $K \in \mathbb{N}$ such that $\max_k \|y_k - y_{k-1}\|_{\mathbf{V}} < \epsilon$. This means that $(y_0, \ldots, y_K)$ is *admissible* if K is large enough.

Furthermore it follows directly from Remark 4.3.8:

Proposition 4.3.9. *For $y \in C^1([0,1], \mathcal{M})$, $y_k = y(k\tau)$, $\tau = K^{-1}$ and $K \in \mathbb{N}$ we have*

$$\max_{k=1,\ldots,K} \|y_k - y_{k-1}\|_{\mathbf{V}} = O(\tau) \,.$$

Our main result will be proved at the end of this section:

Theorem 4.3.10. *We assume* (H1) - (H4) *to hold. Let $y : [0,1] \to \mathcal{M}$ be a smooth path with $y_k = y(t_k)$ for $t_k = \tau k$, $\tau = K^{-1}$ and $K \in \mathbb{N}$. We assume that K is large enough such that $(y_0, \ldots, y_K)$ is admissible in the sense of Def. 4.3.7. We define $\tilde{y}_k$ for $k = 1, \ldots, K-1$ such that $(y_{k-1}, \tilde{y}_k, y_{k+1})$ is a discrete geodesic. Then*

$$g_{y(t_k)}\Big(\frac{D}{dt}\dot{y}(t_k), \, \frac{D}{dt}\dot{y}(t_k)\Big) = 4K^4 \, \mathcal{W}[y_k, \tilde{y}_k] + O(\tau) \,.$$

Using the first order consistency of the numerical quadrature rule $\int_0^1 f(t)\,\mathrm{d}t = \tau \sum_{k=1}^{K-1} f(t_k) + O(\tau)$ then results directly in the consistency of the time-discrete spline energy (4.3.4):

Theorem 4.3.11 (Consistency of time-discrete spline energy)**.** *We assume* (H1) - (H4) *to hold. Let $y : [0,1] \to \mathcal{M}$ be a path with $y_k = y(t_k)$ for $t_k = \tau k$, $\tau = K^{-1}$ and $K \in \mathbb{N}$. We assume that K is large enough such that $(y_0, \ldots, y_K)$ is admissible in the sense of Def. 4.3.7. Then we have for the spline energy $\mathcal{F}$ defined in (4.3.1) and the discrete spline energy defined in (4.3.4), respectively:*

$$\left|F^K[y_0, \ldots, y_K] - \mathcal{F}[(y(t))_{t \in [0,1]}]\right| = O(\tau) \,.$$

To prove Thm. 4.3.10 we will proceed as follows. In Thm. 4.3.12 we will first introduce a consistent approximation of the covariant derivative based on the geodesic parallelogram construction shown in Fig. 4.4. In particular, we will see in Cor. 4.3.13 that the geodesic parallelogram is actually flat, *i.e.* all edge lengths are of order $O(\tau)$, whereas the length of the *short* diagonal connecting y_k and $\hat{y}_k$ is of order $O(\tau^2)$. Then we will show in Thm. 4.3.14 that the evaluation of the covariant derivative in the metric can be approximated by the (properly scaled) squared distance of y_k and $\hat{y}_k$. Finally, the rather technical Lemma 4.3.16 reveals that this quantity is proportional to the squared

Figure 4.4: *Geodesic parallelogram,* i.e. $(y_{k-1}, \tilde{y}_k, y_{k+1})$ and $(y_k, \tilde{y}_k, \hat{y}_k)$ are discrete geodesics.

distance of y_k and $\tilde{y}_k$, where the latter is the geodesic midpoint of the geodesic parallelogram. Then the consistency statement in Thm. 4.3.10 is a direct consequence.

We start with an approximation of the covariant derivative based on the geodesic parallelogram construction in Fig. 4.4.

Theorem 4.3.12. *We assume* (H1) - (H4) *to hold. Let* $y : [0,1] \to \mathcal{M}$ *be a smooth curve and* $K \in \mathbb{N}$ *large enough such that* $(y_0, \ldots, y_K)$ *is admissible in the sense of Def. 4.3.7, where* $y_k = y(k\tau)$ *for* $\tau = K^{-1}$ *and* $K \in \mathbb{N}$. *For* $0 < k < K$ *we define* $\hat{y}_k$ *such that* $(y_{k-1}, y_k, y_{k+1}, \hat{y}_k)$ *is a discrete geodesic parallelogram. Then we have*

$$\left\| \frac{D}{dt}\dot{y}(t_k) - K^2(\hat{y}_k - y_k) \right\|_{\mathbf{V}} = O(\tau) \,.$$

Proof. The proof consists of three parts. First, we consider $\frac{D}{dt}\dot{y}(t_k)$ based on the implicit definition of the covariant derivative in Def. 4.1.6. Second, we investigate the equations defining the discrete geodesic parallelogram depicted in Fig. 4.4. The last part combines the first two parts to obtain the final result. Let us mention that the first two parts of the proof are similar to the proof of Thm. 5.10 in [RW15]. We fix one $t_k = k\tau$ and write $y_k = y(t_k)$ and $\dot{y}_k = \dot{y}(t_k)$.

I. Covariant derivative. The evaluation of the covariant derivative $\frac{D}{dt}\zeta$ along y is defined by Def. 4.1.6:

$$g_{y_k}((\tfrac{D}{dt}\zeta)(t_k), \psi) = g_{y_k}(\dot{\zeta}(t_k), \psi) + g_{y_k}(\Gamma(\dot{y}(t_k), \zeta(t_k)), \psi) \,, \quad \forall \psi \in \mathbf{V} \,. \tag{4.3.7}$$

The consistency conditions in Thm. 4.2.6 imply $g_y = \frac{1}{2}\mathcal{W}_{,22}[y,y]$. Differentiation yields:

$$(D_y g_y)(\psi)(v,w) = \frac{1}{2}\left(\mathcal{W}_{,221}[y,y](v,w,\psi) + \mathcal{W}_{,222}[y,y](v,w,\psi)\right) \,, \quad \psi, v, w \in \mathbf{V} \,.$$

Using this, Def. 4.1.5 of the Christoffel operator $\Gamma : \mathbf{V} \times \mathbf{V} \to \mathbf{V}$ implies that we have for all $\psi \in \mathbf{V}$:

$$
\begin{aligned}
g_{y_k}(\Gamma(\dot{y}_k, \dot{y}_k), \psi) ={}& \tfrac{1}{2}\left[(D_y g_{y_k})(\dot{y}_k)(\psi, \dot{y}_k) + (D_y g_y)(\dot{y}_k)(\psi, \dot{y}_k) - (D_y g_y)(\psi)(\dot{y}_k, \dot{y}_k)\right] \\
={}& \tfrac{1}{4}\Big[2\,\mathcal{W}_{,221}[y_k, y_k](\psi, \dot{y}_k, \dot{y}_k) + 2\,\mathcal{W}_{,222}[y_k, y_k](\psi, \dot{y}_k, \dot{y}_k) \\
& - \mathcal{W}_{,221}[y_k, y_k](\dot{y}_k, \dot{y}_k, \psi) - \mathcal{W}_{,222}[y_k, y_k](\dot{y}_k, \dot{y}_k, \psi)\Big] \\
={}& \tfrac{1}{4}\Big[2\,\mathcal{W}_{,221}[y_k, y_k](\psi, \dot{y}_k, \dot{y}_k) + \mathcal{W}_{,222}[y_k, y_k](\psi, \dot{y}_k, \dot{y}_k) - \mathcal{W}_{,221}[y_k, y_k](\dot{y}_k, \dot{y}_k, \psi)\Big] \\
={}& \tfrac{1}{4}\Big[\mathcal{W}_{,221}[y_k, y_k](\psi, \dot{y}_k, \dot{y}_k) - \mathcal{W}_{,211}[y_k, y_k](\psi, \dot{y}_k, \dot{y}_k) \\
& - \mathcal{W}_{,212}[y_k, y_k](\psi, \dot{y}_k, \dot{y}_k) - \mathcal{W}_{,221}[y_k, y_k](\dot{y}_k, \dot{y}_k, \psi)\Big] \\
={}& -\tfrac{1}{4}\Big[\mathcal{W}_{,211}[y_k, y_k](\psi, \dot{y}_k, \dot{y}_k) + \mathcal{W}_{,221}[y_k, y_k](\dot{y}_k, \dot{y}_k, \psi)\Big] \\
={}& -\tfrac{1}{4}\Big[\mathcal{W}_{,112}[y_k, y_k](\dot{y}_k, \dot{y}_k, \psi) + \mathcal{W}_{,221}[y_k, y_k](\dot{y}_k, \dot{y}_k, \psi)\Big] \,, \tag{4.3.8}
\end{aligned}
$$

where we have used (*cf.* derivation of eq. (5.9) in [RW15]) Schwarz's theorem and the identity

$$\mathcal{W}_{,221}[y,y] + \mathcal{W}_{,222}[y,y] = -\mathcal{W}_{,211}[y,y] - \mathcal{W}_{,212}[y,y] \,,$$

which is obtained by differentiating $\mathcal{W}_{,11}[y,y] = \mathcal{W}_{,22}[y,y] = -\mathcal{W}_{,21}[y,y] = -\mathcal{W}_{,12}[y,y]$, *cf.* Thm. 4.2.6.

Next, we insert (4.3.8) and $\ddot{y}_k = \ddot{y}(t_k) = -\frac{2y_k - y_{k-1} - y_{k+1}}{\tau^2} + O(\tau^2)$ into (4.3.7), using $g_y = \frac{1}{2}\mathcal{W}_{,22}[y,y]$:

$$
\begin{aligned}
\mathcal{W}_{,22}[y_k, y_k]\left((\tfrac{D}{dt}\dot{y})(t_k), \psi\right) ={}& K^2\,\mathcal{W}_{,22}[y_k, y_k](y_{k-1} + y_{k+1} - 2y_k, \psi) \\
& - \tfrac{1}{2}\left(\mathcal{W}_{,112}[y_k, y_k] + \mathcal{W}_{,221}[y_k, y_k]\right)(\dot{y}_k, \dot{y}_k, \psi) + O\Big[\tau\|\psi\|_{\mathbf{V}}\Big] \,. \tag{4.3.9}
\end{aligned}
$$

By the continuity of $\mathcal{W}$ and its derivatives we can move the base point in (4.3.9) from y_k to y_k^c and get:

$$
\begin{aligned}
\mathcal{W}_{,22}[y_k^c, y_k^c]\left(\tfrac{D}{dt}\dot{y}(t_k), \psi\right) ={}& K^2\,\mathcal{W}_{,22}[y_k^c, y_k^c](y_{k-1} + y_{k+1} - 2y_k, \psi) \\
& - \tfrac{1}{2}\left(\mathcal{W}_{,112}[y_k^c, y_k^c] + \mathcal{W}_{,221}[y_k^c, y_k^c]\right)(\dot{y}(t_k), \dot{y}(t_k), \psi) \tag{4.3.10} \\
& + O\Big[\left(\|\tfrac{D}{dt}\dot{y}(t_k)\|_{\mathbf{V}} + \|\ddot{y}_k\|_{\mathbf{V}} + \|\dot{y}_k\|_{\mathbf{V}}^2\right)\|y_k - y_k^c\|_{\mathbf{V}}\|\psi\|_{\mathbf{V}} + \tau\|\psi\|_{\mathbf{V}}\Big] \,.
\end{aligned}
$$

II. Discrete geodesic parallelogram. Next, we derive equations from the discrete geodesic parallelogram in Fig. 4.4, *i.e.* we define $\hat{y}_k$ and y_k^c such that for all $\psi \in \mathbf{V}$

$$\mathcal{W}_{,2}[y_{k-1}, y_k^c](\psi) + \mathcal{W}_{,1}[y_k^c, y_{k+1}](\psi) = 0 \,, \tag{4.3.11}$$

$$\mathcal{W}_{,2}[y_k, y_k^c](\psi) + \mathcal{W}_{,1}[y_k^c, \hat{y}_k](\psi) = 0 \,, \tag{4.3.12}$$

which for the moment we assume to be uniquely solvable. As these are exactly the necessary conditions for one step of discrete parallel transport via Schild's ladder, we can write $\hat{y}_k$ as

$$\hat{y}_k - y_{k+1} = \mathbf{P}_{y_{k+1}, y_k}(y_{k-1} - y_k) \,.$$

As in the proof of Thm. 5.10 in [RW15], we compute Taylor expansions of $\mathcal{W}$ about (y_k^c, y_k^c):

$$\mathcal{W}[y_{k-1}, y_k^c] = \int_0^1 (1-s)\, \mathcal{W}_{,11}[y_k^c + s(y_{k-1} - y_k^c), y_k^c](y_{k-1} - y_k^c, y_{k-1} - y_k^c)\, \mathrm{d}s \,,$$

$$\mathcal{W}[y_k^c, y_{k+1}] = \int_0^1 (1-s)\, \mathcal{W}_{,22}[y_k^c, y_k^c + s(y_{k+1} - y_k^c)](y_{k+1} - y_k^c, y_{k+1} - y_k^c)\, \mathrm{d}s \,,$$

$$\mathcal{W}[y_k, y_k^c] = \int_0^1 (1-s)\, \mathcal{W}_{,11}[y_k^c + s(y_k - y_k^c), y_k^c](y_k - y_k^c, y_k - y_k^c)\, \mathrm{d}s \,,$$

$$\mathcal{W}[y_k^c, \hat{y}_k] = \int_0^1 (1-s)\, \mathcal{W}_{,22}[y_k^c, y_k^c + s(\hat{y}_k - y_k^c)](\hat{y}_k - y_k^c, \hat{y}_k - y_k^c)\, \mathrm{d}s \,.$$

Next, we differentiate these expressions with respect to y_k^c, *e.g.* for the term $\mathcal{W}[y_k, y_k^c]$ we obtain:

$$\partial_{y_k^c} \mathcal{W}[y_k, y_k^c](\psi) = \int_0^1 (1-s) \Big(-2\,\mathcal{W}_{,11}[y_k^c + s(y_k - y_k^c), y_k^c](y_k - y_k^c, \psi)$$

$$+ \mathcal{W}_{,111}[y_k^c + s(y_k - y_k^c), y_k^c](y_k - y_k^c, y_k - y_k^c, (1-s)\,\psi)$$

$$+ \mathcal{W}_{,112}[y_k^c + s(y_k - y_k^c), y_k^c](y_k - y_k^c, y_k - y_k^c, \psi) \Big)\, \mathrm{d}s$$

$$= \int_0^1 (1-s) \Big(-2\,\mathcal{W}_{,11}[y_k^c, y_k^c](y_k - y_k^c, \psi)$$

$$- 2 \int_0^1 \mathcal{W}_{,111}[y_k^c + rs(y_k - y_k^c), y_k^c](y_k - y_k^c, \psi, s(y_k - y_k^c))\, \mathrm{d}r$$

$$+ \mathcal{W}_{,111}[y_k^c + s(y_k - y_k^c), y_k^c](y_k - y_k^c, y_k - y_k^c, (1-s)\,\psi)$$

$$+ \mathcal{W}_{,112}[y_k^c + s(y_k - y_k^c), y_k^c](y_k - y_k^c, y_k - y_k^c, \psi) \Big)\, \mathrm{d}s$$

$$= -1 \cdot \mathcal{W}_{,11}[y_k^c, y_k^c](y_k - y_k^c, \psi)$$

$$+ \int_0^1 (1-s) \int_0^1 \Big(-2\,\mathcal{W}_{,111}[y_k^c + rs(y_k - y_k^c), y_k^c](y_k - y_k^c, \psi, s(y_k - y_k^c))$$

$$+ \mathcal{W}_{,111}[y_k^c + s(y_k - y_k^c), y_k^c](y_k - y_k^c, y_k - y_k^c, (1-s)\,\psi) \Big)\, \mathrm{d}r\, \mathrm{d}s$$

$$+ \int_0^1 (1-s)\, \mathcal{W}_{,112}[y_k^c + s(y_k - y_k^c), y_k^c](y_k - y_k^c, y_k - y_k^c, \psi)\, \mathrm{d}s$$

$$= -1 \cdot \mathcal{W}_{,11}[y_k^c, y_k^c](y_k - y_k^c, \psi)$$

$$+ \int_0^1 (1-s)\mathcal{W}_{,111}[y_k^c, y_k^c]((1-3s)\psi, y_k - y_k^c, y_k - y_k^c) + O(\|v\|_{\mathbf{V}}^3\, \|\psi\|_{\mathbf{V}})\, \mathrm{d}s$$

$$+ \frac{1}{2}\mathcal{W}_{,112}[y_k^c, y_k^c](y_k - y_k^c, y_k - y_k^c, \psi) + \int_0^1 (1-s)\, O(s\, \|y_k - y_k^c\|_{\mathbf{V}}^3\, \|\psi\|_{\mathbf{V}})\, \mathrm{d}s$$

$$= -\mathcal{W}_{,11}[y_k^c, y_k^c](y_k - y_k^c, \psi) + \frac{1}{2}\mathcal{W}_{,112}[y_k^c, y_k^c](y_k - y_k^c, y_k - y_k^c, \psi)$$

$$+ O(\|y_k - y_k^c\|_{\mathbf{V}}^3\, \|\psi\|_{\mathbf{V}}) \,.$$

Here we made use of the fundamental theorem of calculus, *i.e.* $g(1) = g(0) + \int_0^1 g'(r)\,\mathrm{d}r$ for a function $g : [0,1] \to \mathbb{R}$, which was applied to $g(s) = \mathcal{W}_{,11}[y_k^c + s(y_k - y_k^c), y_k^c](y_k - y_k^c, \psi)$. As in [RW15] we use the fact that for a spatially differentiable trilinear form f we have for $0 \le r, s \le 1$:

$$-2s\, f[a, a + rsv](\psi, v, v) + (1 - s)\, f[a, a + sv](\psi, v, v) = (1 - 3s)\, f[a, a](\psi, v, v) + O(\|v\|^3 \|\psi\|),$$

which after multiplication with $(1 - s)$ integrates up to $O(\|v\|^3 \|\psi\|)$ since $\int_0^1 (1 - s)(1 - 3s)\,\mathrm{d}s = 0$. The differentiation of the other three terms obtained by the Taylor expansions above works analogously:

$$
\begin{aligned}
\partial_{y_k^c} \mathcal{W}[y_k^c, \hat{y}_k](\psi) ={}& -\mathcal{W}_{,22}[y_k^c, y_k^c](\hat{y}_k - y_k^c, \psi) \\
&+ \frac{1}{2}\mathcal{W}_{,221}[y_k^c, y_k^c](\hat{y}_k - y_k^c, \hat{y}_k - y_k^c, \psi) + O(\|\hat{y}_k - y_k^c\|_{\mathbf{V}}^3 \|\psi\|_{\mathbf{V}}), \\
\partial_{y_k^c} \mathcal{W}[y_{k-1}, y_k^c](\psi) ={}& -\mathcal{W}_{,11}[y_k^c, y_k^c](y_{k-1} - y_k^c, \psi) \\
&+ \frac{1}{2}\mathcal{W}_{,112}[y_k^c, y_k^c](y_{k-1} - y_k^c, y_{k-1} - y_k^c, \psi) + O(\|y_{k-1} - y_k^c\|_{\mathbf{V}}^3 \|\psi\|_{\mathbf{V}}), \\
\partial_{y_k^c} \mathcal{W}[y_k^c, y_{k+1}](\psi) ={}& -\mathcal{W}_{,22}[y_k^c, y_k^c](y_{k+1} - y_k^c, \psi) \\
&+ \frac{1}{2}\mathcal{W}_{,221}[y_k^c, y_k^c](y_{k+1} - y_k^c, y_{k+1} - y_k^c, \psi) + O(\|y_{k+1} - y_k^c\|_{\mathbf{V}}^3 \|\psi\|_{\mathbf{V}}).
\end{aligned}
$$

Next, we insert these four derivatives into (4.3.11) resp. (4.3.12). Then we subtract (4.3.11) from (4.3.12), use $\mathcal{W}_{,11}[y_k^c, y_k^c] = \mathcal{W}_{,22}[y_k^c, y_k^c]$ (*cf.* Thm. 4.2.6) and get:

$$
\begin{aligned}
0 ={}& \mathcal{W}_{,22}[y_k^c, y_k^c](y_k - y_k^c, \psi) - \frac{1}{2}\mathcal{W}_{,112}[y_k^c, y_k^c](y_k - y_k^c, y_k - y_k^c, \psi) + O(\|y_k - y_k^c\|_{\mathbf{V}}^3 \|\psi\|_{\mathbf{V}}) \\
&+ \mathcal{W}_{,22}[y_k^c, y_k^c](\hat{y}_k - y_k^c, \psi) - \frac{1}{2}\mathcal{W}_{,221}[y_k^c, y_k^c](\hat{y}_k - y_k^c, \hat{y}_k - y_k^c, \psi) + O(\|\hat{y}_k - y_k^c\|_{\mathbf{V}}^3 \|\psi\|_{\mathbf{V}}) \\
&- \mathcal{W}_{,22}[y_k^c, y_k^c](y_{k-1} - y_k^c, \psi) + \frac{1}{2}\mathcal{W}_{,112}[y_k^c, y_k^c](y_{k-1} - y_k^c, y_{k-1} - y_k^c, \psi) + O(\|y_{k-1} - y_k^c\|_{\mathbf{V}}^3 \|\psi\|_{\mathbf{V}}) \\
&- \mathcal{W}_{,22}[y_k^c, y_k^c](y_{k+1} - y_k^c, \psi) + \frac{1}{2}\mathcal{W}_{,221}[y_k^c, y_k^c](y_{k+1} - y_k^c, y_{k+1} - y_k^c, \psi) + O(\|y_{k+1} - y_k^c\|_{\mathbf{V}}^3 \|\psi\|_{\mathbf{V}}) \\
={}& \mathcal{W}_{,22}[y_k^c, y_k^c](y_k + \hat{y}_k - y_{k-1} - y_{k+1}, \psi) \\
&- \frac{1}{2}\Big(\mathcal{W}_{,112}[y_k^c, y_k^c](y_k - y_k^c, y_k - y_k^c, \psi) - \mathcal{W}_{,112}[y_k^c, y_k^c](y_{k-1} - y_k^c, y_{k-1} - y_k^c, \psi)\Big) \\
&- \frac{1}{2}\Big(\mathcal{W}_{,221}[y_k^c, y_k^c](\hat{y}_k - y_k^c, \hat{y}_k - y_k^c, \psi) - \mathcal{W}_{,221}[y_k^c, y_k^c](y_{k+1} - y_k^c, y_{k+1} - y_k^c, \psi)\Big) \\
&+ O\Big((\|y_k - y_k^c\|_{\mathbf{V}}^3 + \|\hat{y}_k - y_k^c\|_{\mathbf{V}}^3 + \|y_{k-1} - y_k^c\|_{\mathbf{V}}^3 + \|y_{k+1} - y_k^c\|_{\mathbf{V}}^3) \|\psi\|_{\mathbf{V}}\Big) \\
={}& \mathcal{W}_{,22}[y_k^c, y_k^c](y_k + \hat{y}_k - y_{k-1} - y_{k+1}, \psi) \\
&- \frac{1}{2}\Big(\mathcal{W}_{,112}[y_k^c, y_k^c](y_k + y_{k-1} - 2y_k^c, y_k - y_{k-1}, \psi) + \mathcal{W}_{,221}[y_k^c, y_k^c](\hat{y}_k + y_{k+1} - 2y_k^c, \hat{y}_k - y_{k+1}, \psi)\Big) \\
&+ O\Big((\|y_k - y_k^c\|_{\mathbf{V}}^3 + \|\hat{y}_k - y_k^c\|_{\mathbf{V}}^3 + \|y_{k-1} - y_k^c\|_{\mathbf{V}}^3 + \|y_{k+1} - y_k^c\|_{\mathbf{V}}^3) \|\psi\|_{\mathbf{V}}\Big).
\end{aligned}
$$
$$\tag{4.3.13}$$

In the last step, we have used that for the bilinear, symmetric form $(v, w) \mapsto F(v, w)$ we obtain:

$$
\begin{aligned}
& F(v - x, v - x) - F(w - x, w - x) \\
={}& F(w + v - x, v - x) - F(v + w - x, w - x) - F(w, v - x) + F(v, w - x) \\
={}& F(w + v - x, v - w) - F(w, w + v - x) + F(v, v + w - x) + F(w, w) - F(v, v) \\
={}& 2\,F(w + v - x, v - w) + F(w, w + v) - F(v, v + w) - F(w.v) + F(v, w) \\
={}& F(w + v - 2x, v - w),
\end{aligned}
$$

which was applied for $x = y_k^c$ to $F(v, w) = \mathcal{W}_{,112}[y_k^c, y_k^c](v, w, \psi)$ with $v = y_k$ and $w = y_{k-1}$, as well as to $F(v, w) = \mathcal{W}_{,221}[y_k^c, y_k^c](v, w, \psi)$ with $v = \hat{y}_k$ and $w = y_{k+1}$.

III. Combination. Finally, we add (4.3.10) to $K^2 \cdot$ (4.3.13). To this end, we use

$$\dot{y}(t_k) = \frac{y_{k+1} - y_k}{\tau} + O(\tau), \quad \dot{y}(t_k) = \frac{y_k - y_{k-1}}{\tau} + O(\tau),$$

as well as the consistency with the metric (*cf.* Thm. 4.2.6), *i.e.* $g_{y_k^c} = \frac{1}{2} \mathcal{W}[y_k^c, y_k^c]$:

$$
\begin{aligned}
g_{y_k^c}\left(\left(\tfrac{D}{\mathrm{d}t}\dot{y}\right)(t_k), \psi\right) &= K^2 \, g_{y_k^c}(\hat{y}_k - y_k, \psi) \\
&\quad - \frac{K^2}{4} \Big(\mathcal{W}_{,112}[y_k^c, y_k^c](y_k - y_{k-1}, y_k + y_{k-1} - 2y_k^c, \psi) \\
&\qquad\qquad + \mathcal{W}_{,221}[y_k^c, y_k^c](\hat{y}_k - y_{k+1}, \hat{y}_k + y_{k+1} - 2y_k^c, \psi)\Big) \\
&\quad - \frac{K^2}{4} \Big(\mathcal{W}_{,112}[y_k^c, y_k^c](y_k - y_{k-1}, y_k - y_{k-1}, \psi) \\
&\qquad\qquad + \mathcal{W}_{,221}[y_k^c, y_k^c](y_{k+1} - y_k, y_{k+1} - y_k, \psi)\Big) \\
&\quad + O\Big(\big(\|(\tfrac{D}{\mathrm{d}t}\dot{y})(t_k)\|_{\mathbf{V}} + \|\ddot{y}_k\|_{\mathbf{V}} + \|\dot{y}_k\|_{\mathbf{V}}^2\big) \|y_k - y_k^c\|_{\mathbf{V}} \, \|\psi\|_{\mathbf{V}} + \tau \|\psi\|_{\mathbf{V}} \Big) \\
&\quad + O\Big(K^2 \big(\|y_k - y_k^c\|_{\mathbf{V}}^3 + \|\hat{y}_k - y_k^c\|_{\mathbf{V}}^3 + \|y_{k-1} - y_k^c\|_{\mathbf{V}}^3 + \|y_{k+1} - y_k^c\|_{\mathbf{V}}^3\big) \|\psi\|_{\mathbf{V}} \Big).
\end{aligned}
$$

To estimate the $\mathcal{W}_{,112}$ terms, we consider the bilinear, symmetric form $F(v, w) = \mathcal{W}_{,112}[y_k^c, y_k^c](v, w, \psi)$:

$$
\begin{aligned}
F(y_k - y_{k-1}, y_k + y_{k-1} - 2y_k^c) + F(y_k - y_{k-1}, y_k - y_{k-1}) &= F(y_k - y_{k-1}, 2y_k - 2y_k^c) \\
&= O(\|y_k - y_{k-1}\|_{\mathbf{V}} \, \|y_k - y_k^c\|_{\mathbf{V}} \, \|\psi\|_{\mathbf{V}}).
\end{aligned}
$$

To estimate the $\mathcal{W}_{,221}$ terms, we consider the bilinear, symmetric form $F(v, w) = \mathcal{W}_{,221}[y_k^c, y_k^c](v, w, \psi)$:

$$
\begin{aligned}
&F(\hat{y}_k - y_{k+1}, \hat{y}_k + y_{k+1} - 2y_k^c) + F(y_{k+1} - y_k, y_{k+1} - y_k) \\
&= F(\hat{y}_k - y_k, \hat{y}_k + y_{k+1} - 2y_k^c) + F(y_k - y_{k+1}, \hat{y}_k + y_{k+1} - 2y_k^c) + F(y_k - y_{k+1}, y_k - y_{k+1}) \\
&= F(\hat{y}_k - y_k, \hat{y}_k + y_{k+1} - 2y_k^c) + F(y_k - y_{k+1}, \hat{y}_k + y_k - 2y_k^c) \\
&= O\Big(\big(\|\hat{y}_k - y_k\|_{\mathbf{V}} (\|\hat{y}_k - y_k^c\|_{\mathbf{V}} + \|y_{k+1} - y_k^c\|_{\mathbf{V}}) + \|y_k - y_{k+1}\|_{\mathbf{V}} (\|\hat{y}_k - y_k^c\|_{\mathbf{V}} + \|y_k - y_k^c\|_{\mathbf{V}})\big) \|\psi\|_{\mathbf{V}} \Big).
\end{aligned}
$$

Now we insert these estimates using $\|(\tfrac{D}{\mathrm{d}t}\dot{y})(t_k)\|_{\mathbf{V}}, \|\ddot{y}_k\|_{\mathbf{V}}, \|\dot{y}_k\|_{\mathbf{V}} = O(1)$:

$$
\begin{aligned}
g_{y_k^c}\left(\left(\tfrac{D}{\mathrm{d}t}\dot{y}\right)(t_k), \psi\right) &= K^2 \, g_{y_k^c}(\hat{y}_k - y_k, \psi) \\
&\quad + O\Big(K^2 \|\hat{y}_k - y_k\|_{\mathbf{V}} (\|\hat{y}_k - y_k^c\|_{\mathbf{V}} + \|y_{k+1} - y_k^c\|_{\mathbf{V}}) \|\psi\|_{\mathbf{V}} \Big) \\
&\quad + O\Big(K^2 \|y_k - y_{k+1}\|_{\mathbf{V}} (\|\hat{y}_k - y_k^c\|_{\mathbf{V}} + \|y_k - y_k^c\|_{\mathbf{V}}) \|\psi\|_{\mathbf{V}} \Big) \\
&\quad + O\Big(K^2 \|y_{k-1} - y_k\|_{\mathbf{V}} \|y_k^c - y_k\|_{\mathbf{V}} \|\psi\|_{\mathbf{V}} \Big) \\
&\quad + O\Big(\|y_k - y_k^c\|_{\mathbf{V}} \|\psi\|_{\mathbf{V}} + \tau \|\psi\|_{\mathbf{V}} \Big) \\
&\quad + O\Big(K^2 \big(\|y_k - y_k^c\|_{\mathbf{V}}^3 + \|\hat{y}_k - y_k^c\|_{\mathbf{V}}^3 + \|y_{k-1} - y_k^c\|_{\mathbf{V}}^3 + \|y_{k+1} - y_k^c\|_{\mathbf{V}}^3\big) \|\psi\|_{\mathbf{V}} \Big) \\
&= K^2 \, g_{y_k^c}(\hat{y}_k - y_k, \psi) + O\Big(K \|\hat{y}_k - y_k\|_{\mathbf{V}} \|\psi\|_{\mathbf{V}} + \tau \|\psi\|_{\mathbf{V}} \Big),
\end{aligned}
$$

where we used that for $j \in \{k-1, k+1\}$ we have

$$\|y_j - y_k\|_{\mathbf{V}} = O(\tau), \qquad \|y_j - y_k^c\|_{\mathbf{V}} = O(\tau), \qquad \|y_j - \hat{y}_k\|_{\mathbf{V}} = O(\tau).$$

Furthermore, since $(y_k, y_k^c, \hat{y}_k)$ is a short discrete geodesic, Lemma 4.3.16 below implies:

$$\|y_k - y_k^c\|_{\mathbf{V}} + \|y_k^c - \hat{y}_k\|_{\mathbf{V}} = O(\|y_k - \hat{y}_k\|_{\mathbf{V}}) = O(\tau)\,,$$

which we used in the last step. Using the coercivity of the metric, we finally arrive at:

$$(\tfrac{D}{dt}\dot{y})(t_k) = K^2(\hat{y}_k - y_k) + O(K\,\|\hat{y}_k - y_k\|_{\mathbf{V}} + \tau) = K^2(\hat{y}_k - y_k) + O(\tau)\,,$$

where the last step is due to the fact that $\|(\tfrac{D}{dt}\dot{y})(t_k)\|_{\mathbf{V}} = O(1)$. $\square$

Indeed, the geodesic parallelogram is flat:

Corollary 4.3.13. *Under the assumptions above we have*

$$\|\hat{y}_k - y_k\|_{\mathbf{V}} = O(\tau^2)\,.$$

Proof: Thm. 4.3.12 implies $\tau^2 \| \left(\tfrac{D}{dt}\dot{y}\right)_{y_k} \|_{\mathbf{V}} = \|\hat{y}_k - y_k\|_{\mathbf{V}} + O(\tau^3)$, where $\left(\tfrac{D}{dt}\dot{y}\right)_{y_k} = O(1)$. $\square$

Next, we show that the evaluation of the covariant derivative in the metric can be approximated by the (properly scaled) squared distance of two opposite points in the geodesic parallelogram (*cf*. Fig. 4.4):

Theorem 4.3.14. *We assume* (H1) - (H4) *to hold. Let* $y : [0,1] \to \mathcal{M}$ *be a path with* $y_k = y(t_k)$ *for* $t_k = \tau k$, $\tau = K^{-1}$ *and* $K \in \mathbb{N}$. *We assume that* K *is large enough such that* $(y_0, \ldots, y_K)$ *is admissible in the sense of Def. 4.3.7. Fr* $0 < k < K$, *let* $(y_{k-1}, y_k, y_{k+1}, \hat{y}_k)$ *be a discrete geodesic parallogram. Then*

$$g_{y_k}\left(\frac{D}{dt}\dot{y}(t_k), \frac{D}{dt}\dot{y}(t_k)\right) = K^4\,\mathcal{W}[y_k, \hat{y}_k] + O(\tau)\,.$$

In the proof we make use of the following lemma, which is proved in the appendix (*cf*. Lemma A.1.1):

Lemma 4.3.15. *For* $y_0, y_1 \in \mathcal{M}$ *with* $\|y_0 - y_1\|_{\mathbf{V}}$ *sufficiently small we get*

$$
\begin{aligned}
(i) \quad \mathcal{W}[y_0, y_1] &= \mathcal{W}[y_1, y_0] + O(\|y_0 - y_1\|_{\mathbf{V}}^3) \\
(ii) \quad \mathcal{W}[y_0, y_1] &= g_{y_1}(y_0 - y_1, y_0 - y_1) + O(\|y_0 - y_1\|_{\mathbf{V}}^3) \\
&= g_{y_0}(y_0 - y_1, y_0 - y_1) + O(\|y_0 - y_1\|_{\mathbf{V}}^3)\,.
\end{aligned}
$$

Proof of Thm. 4.3.14: Using Thm. 4.3.12, Corollary 4.3.13 and the boundedness of the metric we get

$$g_{y_k}\left(\frac{D}{dt}\dot{y}(t_k), \frac{D}{dt}\dot{y}(t_k)\right) = K^4 g_{y_k}(\hat{y}_k - y_k, \hat{y}_k - y_k) + K^2 \underbrace{\|\hat{y}_k - y_k\|_{\mathbf{V}}}_{=O(\tau^2)} O(\tau) + O(\tau^2)\,.$$

Using Lemma 4.3.15 and Corollary 4.3.13 we get

$$\mathcal{W}[y_k, \hat{y}_k] = g_{y_k}(\hat{y}_k - y_k, \hat{y}_k - y_k) + O(\|\hat{y}_k - y_k\|_{\mathbf{V}}^3) = g_{y_k}(\hat{y}_k - y_k, \hat{y}_k - y_k) + O(\tau^6)\,. \square$$

Note that the evaluation of $\mathcal{W}[y_k, \hat{y}_k]$ requires the construction of an entire geodesic parallelogram. In practice, however, it might be reasonable to avoid computing $\hat{y}_k$ explicitly. Fortunately, we can use $\mathcal{W}[y_k, \tilde{y}_k]$ instead, which is a direct consequence of the following equidistribution property of a short time-discrete geodesic, which is also proved in the appendix (*cf*. Lemma A.1.2):

Lemma 4.3.16. *Let* (y_0, y_1, y_2) *be a discrete geodesic. Then*

$$
\begin{aligned}
(i) \quad & \mathcal{W}[y_0, y_2] = 4\mathcal{W}[y_0, y_1] + O(\max\{\|y_0 - y_1\|_{\mathbf{V}}, \|y_1 - y_2\|_{\mathbf{V}}\}^3)\,, \\
(ii) \quad & \mathcal{W}[y_0, y_1] = \mathcal{W}[y_1, y_2] + O(\max\{\|y_0 - y_1\|_{\mathbf{V}}, \|y_1 - y_2\|_{\mathbf{V}}\}^3)\,.
\end{aligned}
$$

Note that Lemma 4.3.16 corresponds to an arclength parametrization result for continuous geodesics $(y(t))_{t \in [0,1]}$ connecting $y(0) = y_0$ and $y(1) = y_2$, where we have for $y_1 = y(\frac{1}{2})$:

$$\mathrm{dist}^2(y_0, y_2) = 4 \, \mathrm{dist}^2(y_0, y_1) = 4 \, \mathrm{dist}^2(y_1, y_2) \,.$$

Collecting all results from this section we are finally able to prove our main result in Thm. 4.3.10:

Proof of Thm. 4.3.10: Lemma 4.3.16 and Corollary 4.3.13 imply

$$\mathcal{W}[y_k, \hat{y}_k] = 4 \mathcal{W}[y_k, \tilde{y}_k] + O(\max\{\|y_k - \tilde{y}_k\|_{\mathbf{V}}, \|\hat{y}_k - \tilde{y}_k\|_{\mathbf{V}}\}^3) = 4 \mathcal{W}[y_k, \tilde{y}_k] + O(\tau^6) \,.$$

Plugging this into Thm. 4.3.14 proves the claim. $\square$

4.3.3 Discussion and an open question

We have presented a consistent time-discretization of the covariant derivative along a curve that leads to a time-discrete spline energy which is also first-order consistent. The evaluation of the discrete co-variant derivative is based on the local construction of a discrete geodesic parallelogram. However, due to Lemma 4.3.15 we can avoid constructing the geodesic parallelogram, *i.e.* computing the node $\hat{y}_k$ explicitly, when evaluating the discrete spline energy. This is realized by replacing the evaluation of $\mathcal{W}[y_k, \hat{y}_k]$ by $4 \mathcal{W}[y_k, \tilde{y}_k]$. Nevertheless, we are still dealing with a constrained optimization problem, since the geodesic midpoint $\tilde{y}_k$ is defined variationally. In particular, the constraint equations are non-linear. That means, if the spline energy is optimized within a numerical simulation, *e.g.* via a gradient descent scheme, one has to solve several nonlinear optimization problems for each energy or gradient evaluation[1]. Moreover, since the constraints contain an optimality condition in terms of $\mathcal{W}$, an overall numerical optimization of the spline energy by a second-order approach, *e.g.* by a Newton-type method, requires second derivatives of the objective functional and hence third derivatives of the functional $\mathcal{W}$, which are in practice hard to compute.

Hence, an ultimate goal would be to get rid of the variational constraints and find a closed form of the time-discrete spline energy (4.3.4). If Fig. 4.4 represents a flat geodesic parallelogram in $\mathbb{R}^2$, the *parallelogram law* reads

$$2 \|y_{k-1} - y_k\|^2 + 2 \|y_k - y_{k+1}\|^2 = \|y_{k-1} - y_{k+1}\|^2 + \|y_k - \hat{y}_k\|^2 \,,$$

which yields a closed formula for $\|y_k - \hat{y}_k\|^2$. Although the parallelogram law is only valid in normed vector spaces, the following proposition quantifies the error when being transferred to a generic manifold, where the squared Riemannian distance is locally approximated by a functional $\mathcal{W}$:

Proposition 4.3.17. *Let $\delta > 0$ and $y \in \mathcal{M}$ such that for any two points $y_a, y_b \in B_\delta(y)$ there is a unique discrete geodesic connecting y_a and y_b. Let $(y_0, y_1, y_2, y_3) \subset B_\delta(y)$ be a discrete geodesic parallelogram,* i.e. *there is y^c such that (y_0, y^c, y_2) and (y_1, y^c, y_3) are discrete geodesics. If $\epsilon = \max\{\|y_0 - y_1\|_{\mathbf{V}}, \|y_1 - y_2\|_{\mathbf{V}}\}$ we have*

$$2 \mathcal{W}[y_0, y_1] + 2 \mathcal{W}[y_1, y_2] = \mathcal{W}[y_0, y_2] + \mathcal{W}[y_1, y_3] + O(\epsilon^3) \,.$$

---

[1] We will see in Sec. 7.1 that this results in severe efficiency problems in practice.

We shall use a result on short time-discrete geodesics which is proved in the appendix (*cf*. Lemma A.1.3):

Lemma 4.3.18. *Let* (y_0, y_1, y_2) *a discrete geodesic. Then*

$$\left\| y_1 - \frac{y_0 + y_2}{2} \right\|_{\mathbf{V}} = \max\{ \|y_1 - y_0\|_{\mathbf{V}}, \|y_2 - y_1\|_{\mathbf{V}} \}^2 .$$

Proof of Prop. 4.3.17: From Thm. 4.3.16 (i) and (ii) we know

$$\mathcal{W}[y_1, y_3] = 4\,\mathcal{W}[y_1, y^c] + O(\epsilon^3) ,$$
$$\mathcal{W}[y_0, y_2] = 4\,\mathcal{W}[y_0, y^c] + O(\epsilon^3) = 2\,\mathcal{W}[y_0, y^c] + 2\,\mathcal{W}[y^c, y_2] + O(\epsilon^3) .$$

Furthermore, we have

$$
\begin{aligned}
2\,\mathcal{W}[y_0, y_1] &= 2\,g_{y_1}(y_1 - y_0, y_1 - y_0) + O(\epsilon^3) \\
&= 2\,\mathcal{W}[y_0, y^c] + 2\,\mathcal{W}[y^c, y_1] - 4\,g_{y_1}(y^c - y_0, y^c - y_1) + O(\epsilon^3) , \\
2\,\mathcal{W}[y_1, y_2] &= 2\,g_{y_1}(y_1 - y_2, y_1 - y_2) + O(\epsilon^3) \\
&= 2\,\mathcal{W}[y_1, y^c] + 2\,\mathcal{W}[y^c, y_2] - 4\,g_{y_1}(y^c - y_2, y^c - y_1) + O(\epsilon^3) ,
\end{aligned}
$$

and hence with Lemma 4.3.18 we get

$$
\begin{aligned}
\mathcal{W}[y_0, y_2] &+ \mathcal{W}[y_1, y_3] - 2\,\mathcal{W}[y_0, y_1] - 2\,\mathcal{W}[y_1, y_2] \\
&= 4\,g_{y_1}(y^c - y_0, y^c - y_1) + 4\,g_{y_1}(y^c - y_2, y^c - y_1) + O(\epsilon^3) \\
&= 8\,g_{y_1}\!\left(y^c - \frac{y_0 + y_2}{2}, y^c - y_1\right) + O(\epsilon^3) \\
&= O(\underbrace{\|y^c - \frac{y_0 + y_2}{2}\|_{\mathbf{V}}}_{=O(\epsilon^2)} \cdot \|y^c - y_1\|_{\mathbf{V}}) + O(\epsilon^3) . \qquad \square
\end{aligned}
$$

We aim at using this result to find another representation of Thm. 4.3.14, *i.e.* by writing

$$\mathcal{W}[y_k, \hat{y}_k] = 2\,\mathcal{W}[y_{k-1}, y_k] + 2\,\mathcal{W}[y_k, y_{k+1}] - \mathcal{W}[y_{k-1}, y_{k+1}] + O(\tau^3)$$

and deduce a different definition of the time-discrete spline energy without additional constraints, *i.e.* by

$$\tilde{F}^K[y_0, \ldots, y_K] = 4K^3 \sum_{k=1}^{K-1} \Big(2\,\mathcal{W}[y_{k-1}, y_k] + 2\,\mathcal{W}[y_k, y_{k+1}] - \mathcal{W}[y_{k-1}, y_{k+1}] \Big) . \qquad (4.3.14)$$

However, as $\mathcal{W}[y_k, \hat{y}_k]$ is scaled by K^4 in Thm. 4.3.14, we have not been able to derive a consistent approximation in (4.3.14). Furthermore, (4.3.14) is only ensured to be strictly positive if $\mathcal{W}$ obeys the triangle inequality, which is rarely the case in practice. Indeed, we observe certain terms in the sum in (4.3.14) to become negative, in particular along flat segments, *i.e.* where y_k does not differ a lot from the geodesic midpoint of y_{k-1} and y_{k+1}. Eventually, these negative terms induce numerical instabilities and artefacts in the solution. Nevertheless, we will see in Sec. 7.1.4 that the minimization of (4.3.14) (subject to the usual interpolation constraints) can result in reasonable approximations of time-discrete splines in special cases.

5 Thin shell modeling

In the previous chapter we introduced a time-discrete geodesic calculus for a generic Riemannian manifold $\mathcal{M}$ which was solely based on a suitable approximation of the squared Riemannian distance, *i.e.* a (smooth) functional $\mathcal{W} : \mathcal{M} \times \mathcal{M} \to \mathbb{R}$. Now we consider the specific case where $\mathcal{M}$ represents the space of thin elastic shells. Physically, shells are deformable materials in three-dimensional space with a high ratio from width to thickness, *i.e.* one of three spatial directions is orders of magnitude smaller than the other two. Mathematically, these objects are described by compact, regular, embedded surfaces in $\mathbb{R}^3$ which are supposed to represent the material's middle layer. In the following, we derive a dissimilarity measure on the space of thin shells based on elastic deformations and introduce a suitable spatial discretization.

We start in Sec. 5.1 with the mathematical modeling of thin shells and deformations thereof which are built on concepts from 3D elasticity. Given two shells $\mathcal{S}, \tilde{\mathcal{S}} \in \mathcal{M}$ and an elastic deformation energy $\phi \mapsto \mathcal{W}[\mathcal{S}, \phi]$, a physically sound dissimilarity measure can then be defined via

$$\mathcal{W}[\mathcal{S}, \tilde{\mathcal{S}}] = \min_{\phi:\phi(\mathcal{S})=\tilde{\mathcal{S}}} \mathcal{W}[\mathcal{S}, \phi] \, . \tag{5.0.1}$$

In Sec. 5.2 we introduce a spatial discretization of shells based on triangular meshes and define corresponding discrete deformation energies in Sec. 5.3. A particular focus is on the definition of discrete curvature functionals, thus we give a detailed numerical validation of our discrete bending model in Sec. 5.4.

Remark 5.0.1. Foundations of the discrete membrane and bending model have already been discussed in the author's diploma thesis [Hee11] and were published partly in [HRWW12]. However, the formal mathematical derivation, the relation and comparison to other existing bending models and an experimental validation of the proposed discrete shape operator are new contributions of this thesis.

5.1 Physics of thin elastic shells

In this section we derive a physically sound model for thin shells based on concepts from 3D elasticity (*cf*. Sec. 3.2). Since the main focus of this work is on the geodesic calculus in the space of *discrete* shells, *i.e.* triangular meshes, we will only give a short and often informal summary of *smooth* shell theory. This summary is based on the comprehensive and detailed descriptions found in several works by Ciarlet and co-workers [Cia00, Cia05, CM08].

5.1.1 Derivation of a two-dimensional shell model

The main objective of shell theory is to predict the stress and the displacement arising in an elastic shell in response to given forces [CM08]. Such a prediction is made either by solving a system of partial differential equations or by minimizing a functional, *cf*. Sec. 3.2. Formally, the Euler–Lagrange equations of the variational problem represent a weak formulation of the corresponding differential equations, although different regularity assumptions are made. We will stick to the variational formulation and show how an elastic shell can be modeled by equations defined on a two-dimensional domain which is an

abstract idealization of the physical shell when its thickness is "small". These equations may be viewed as a simplification of the equations of three-dimensional elasticity, obtained by eliminating some of the terms of lesser order of magnitude with respect to the thickness of the shell. This simplification is done by exploiting the special geometry of the shell, and especially, the assumed "smallness" of the thickness of the shell.

First, we introduce the mathematical description of the reference configuration of an elastic shell. Let $\omega \subset \mathbb{R}^2$ be a domain in the plane, $\delta > 0$, and $\omega_\delta = \omega \times (-\frac{\delta}{2}, \frac{\delta}{2}) \subset \mathbb{R}^3$. Let $\theta : \omega \to \mathbb{R}^3$ be an immersion and a (local) parametrization of a regular surface $\mathcal{S} \subset \mathbb{R}^3$, *i.e.* $\mathcal{S} = \theta(\omega)$. Then the mapping $\theta_\delta : \omega_\delta \to \mathbb{R}^3$ with

$$\theta_\delta(\xi, z) = \theta(\xi) + z\,(n \circ \theta)(\xi)\,, \quad \xi = (\xi_1, \xi_2) \in \omega\,, \quad z \in (-\tfrac{\delta}{2}, \tfrac{\delta}{2})\,, \tag{5.1.1}$$

is globally injective on ω_δ if the immersion θ is globally injective on ω and $\delta > 0$ is small enough [Cia05]. In this case, the set $\bar{\mathcal{S}}_\delta = \theta_\delta(\omega_\delta)$ is defined as the *reference configuration* of an elastic shell with thickness δ and midsurface $\mathcal{S}$, *cf*. Fig. 5.1. The more general case of shells with variable thickness or with a midsurface described by several charts can also be dealt with. The coordinates (ξ_1, ξ_2, z) of an arbitrary point $x_\delta \in \omega_\delta$ are referred to as *curvilinear coordinates* of the point $\bar{x}_\delta = \theta_\delta(x_\delta)$ of the reference configuration of the shell. A shell problem can now be modeled by means of a minimization problem which is expressed in 3D Cartesian coordinates of a point $\bar{x}_\delta = \theta_\delta(x_\delta)$ in the reference configuration of the shell. To this end, a deformation $\phi_\delta \in W^{1,2}(\bar{\mathcal{S}}_\delta, \mathbb{R}^3)$ is characterized by a stored energy function $\mathcal{W}$ as in (3.2.1), *i.e.*

$$\mathcal{W}[\bar{\mathcal{S}}_\delta, \phi_\delta] = \int_{\bar{\mathcal{S}}_\delta} W(D\phi_\delta)\,\mathrm{d}\bar{x}_\delta\,, \tag{5.1.2}$$

and the functional $\mathcal{W}[\bar{\mathcal{S}}_\delta, \phi_\delta]$ is optimized subject to forces and boundary conditions. The natural point of departure for the two-dimensional approach to shell theory is then to recast this problem in terms of the curvilinear coordinates $x_\delta = (\xi_1, \xi_2, z)$ describing the reference configuration of the same shell [CM08]. Due to the regularity of θ_δ this is a simple application of the transformation formula on (5.1.2). The resulting equations are referred to as the three-dimensional model of the shell problem.

In the *two-dimensional approach to shell theory* [Cia05], the above minimization problem is replaced by a (presumably simpler) two-dimensional problem, which is eventually posed over the middle surface $\mathcal{S}$ of the shell. The two-dimensional approach to shell theory yields a variety of different shell models, which can be classified into two categories [Cia05]:

(i) The first category of models is obtained from the three-dimensional problem formulation by letting the thickness $\delta > 0$ of the shell go to zero. This can be formulated rigorously by means of Γ-convergence [DGDM83, Bra02]. Depending on the scaling, boundary conditions and applied forces one obtains either a so-called *membrane* shell model [LDR95, LDR96], or a flexural or *bending* shell model [FJM02a, FJM02b, FJMM03].

(ii) The second category of models are obtained from the three-dimensional model by restricting the range of admissible deformations by means of specific a priori assumptions that are supposed to take into account the smallness of the thickness. For example, the (geometric) Kirchhoff-Love assumptions [Kir50, Lov88], combined with mechanical assumption by John [Joh65], lead to Koiter's shell model [Koi66] (see also [RS10]). More general models of this category are of the Middlin-Reissner type, *e.g.* the Cosserat model, which does not postulate the Kirchhoff-Love assumption.

In the following, we derive our shell model in the spirit of the first category.

5.1.2 Membrane and bending energies

In this section we briefly summarize the main results of a two-dimensional approach to shell theory derived by means of Γ-convergence[1]. However, this will be done in a rather informal and strongly abridged way, for a comprehensive and detailed discussion we refer *e.g.* to [Cia05, CM08] and the references below.
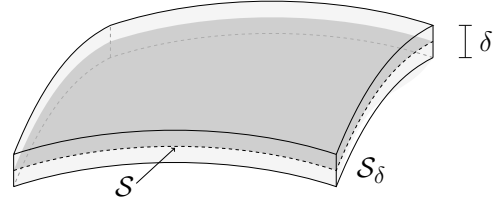
Figure 5.1: *Elastic shell $\mathcal{S}_\delta \subset \mathbb{R}^3$ with finite thickness $\delta > 0$ and midsurface $\mathcal{S}$.*

Remark 5.1.1. Let us emphasize in particular that we focus on the *qualitative* understanding of the rigorous derivations, *i.e.* we are interested in which objects the limit depends on. These objects will then be used to define a physically sound dissimilarity measure between two thin shells. Hence we neglect *quantitative* aspects, *e.g.* the detailed shape of limit integrands or values of physical constants in the limit, as these will later be chosen individually for different applications.

We assume the shell $\bar{\mathcal{S}}_\delta \subset \mathbb{R}^3$ to be made of a homogeneous hyperelastic material, thus a deformation $\phi_\delta : \bar{\mathcal{S}}_\delta \to \mathbb{R}^3$ is characterized by the stored energy functional (5.1.2). Furthermore, we postulate that the material is isotropic (*cf.* Sec. 3.2), *i.e.* the corresponding elastic energy density $W : \mathbb{R}^{3,3} \to \mathbb{R}^+$ satisfies (3.2.3). In particular, the stored energy density is minimized exactly on $SO(3)$. For example, one can think of a standard *St Venant-Kirchhoff* material whose corresponding energy density is given by

$$W^{\text{StVK}}(F) = \frac{\lambda}{8}(\text{tr}\,(F^T F - \mathbb{1}))^2 + \frac{\mu}{4}\text{tr}\,(F^T F - \mathbb{1})^2\,. \tag{5.1.3}$$

Note that $W^{\text{StVK}}(D\phi) = \frac{\lambda}{2}(\text{tr}\,E)^2 + \mu\,\text{tr}\,E^2$, with $E = \frac{1}{2}(D\phi^T D\phi - \mathbb{1})$, hence W^{StVK} is deduced from W^{lin} in (3.2.4) by replacing the linearized argument $\epsilon[u]$ by its nonlinear counterpart E.

Membrane model Le Dret and Raoult [LDR95, LDR96] established that the properly scaled three-dimensional elastic energy (5.1.2) Γ-converges with respect to the weak $W^{1,p}$-topology as $\delta \to 0$. In detail, they showed that a subsequence of deformations that minimize $\frac{1}{\delta}\mathcal{W}$ weakly converges in $W^{1,p}$ as $\delta \to 0$. The weak limit deformation minimizes a so-called *membrane* shell energy that is precisely given by the Γ-limit. The number $p > 1$ is governed by certain growth properties of the stored energy density W. These growth conditions are fulfilled by typical energy densities representing isotropic materials, *e.g.* by (5.1.3). Furthermore, if the original density W was frame-indifferent, then the limit density is also frame-indifferent and depends on the metric of the deformed middle surface only [LDR96]. If additionally $W(F) \geq W(\mathbb{1})$ for all $F \in \mathbb{R}^{3,3}$, which is always the case in our examples as we assume $W(\mathbb{1}) = 0$ and $W \geq 0$, the corresponding membrane shell energy is constant under compression, *i.e.* the shell offers no resistance to crumpling [LDR96]. Although a closed formula for the integrand of the limit model induced by a St Venant-Kirchhoff material is given in Prop. 16 in [LDR96], we will focus on the qualitative description according to Rem. 5.1.1.

Indeed, for frame-indifferent and isotropic densities the limit membrane energy can be written as an integral over the midsurface $\mathcal{S}$ whose integrand depends on the principal invariants of the right Cauchy-Green strain tensor $C[\phi] = D\phi^T D\phi$ only (*cf.* Sec. 3.2), where $\phi : \mathcal{S} \to \mathbb{R}^3$ is a deformation of the midsurface $\mathcal{S}$ to $\mathcal{S}^\phi = \phi(\mathcal{S})$. In detail, the pointwise linear operator $C[\phi]$ measures the distortion of tangent vectors which are mapped from $T_p\mathcal{S}$ to $T_{\phi(p)}\mathcal{S}^\phi$ for some arbitrary point $p \in \mathcal{S}$, *i.e.*

$$g_p(C[\phi]V, W) = g_{\phi(p)}(D\phi V, D\phi W)\,, \quad V, W \in T_p\mathcal{S}\,. \tag{5.1.4}$$

---

[1]For an introduction to the concepts of Γ-convergence we refer to [DGDM83, Bra02].

If we assume that a local neighborhood of p and $\phi(p)$, respectively, are parametrized over the same domain $\omega \subset \mathbb{R}^2$ by immersions $x, x^\phi : \omega \to \mathbb{R}^3$, we can formally write $\phi = x^\phi \circ x^{-1}$. This concatenation property has been used in [CLR04, LDRS05] to derive a two-dimensional representation of $C[\phi] \in \mathbb{R}^{3,3}$ by a distortion tensor $\mathcal{G}[\phi] \in \mathbb{R}^{2,2}$; we refer to [Hee11] for details. In particular, we can write

$$\mathcal{G}[\phi] = g^{-1} g_\phi \tag{5.1.5}$$

with $g = Dx^T Dx$ and $g_\phi = (Dx^\phi)^T (Dx^\phi)$ denoting the first fundamental form of the undeformed and deformed configuration, respectively. Note that $\mathcal{G}[\phi]$ as well as g and g_ϕ are defined pointwise.

From the considerations above we deduce a membrane shell energy $\mathcal{W}_{\text{mem}}$ which is supposed to measure the dissimilarity in terms of tangential stretching and shearing induced by a deformation ϕ of the undeformed (reference) shell $\mathcal{S}$, *i.e.*

$$\mathcal{W}_{\text{mem}}[\mathcal{S}, \phi] = \int_\mathcal{S} W_{\text{mem}}(\mathcal{G}[\phi]) \, da \,. \tag{5.1.6}$$

We shall make use of the polyconvex density defined in (3.2.5) with $d = 2$. In particular, we have $W_{\text{mem}}(\mathcal{G}[\phi]) = W_{\text{mem}}(\operatorname{tr} \mathcal{G}[\phi], \det \mathcal{G}[\phi])$ as well as $W_{\text{mem}}(\mathbb{1}) = 0$ and $dW_{\text{mem}}(\mathbb{1}) = 0$.

Bending model (plate) Now we consider the functional (5.1.2) for a thin *plate*, *i.e.* $\theta = \operatorname{id}$ and $n \parallel e_3$ in (5.1.1). If we set $\omega = (-1, 1)^2$ and apply compressive boundary conditions, we have

$$\bar{\mathcal{S}}_\delta = (-1, 1)^2 \times (-\frac{\delta}{2}, \frac{\delta}{2}) \,, \quad \phi_\delta(x)\Big|_{x_1 = \pm 1} = x \mp (a, 0, 0) \,,$$

for some $a \in (0, 1)$. The corresponding elastic energy (5.1.2) scales like δ^3, *i.e.* the plate will accommodate the boundary conditions by bending while keeping its midsurface unstretched [FJM02b]. However, as the volume of $\bar{\mathcal{S}}_\delta$ scales like δ the integrand $W(D\phi_\delta)$ approaches zero much faster. That means, since W is assumed to be minimized exactly on $SO(3)$, the Jacobian $D\phi_\delta \in \mathbb{R}^{3,3}$ tends in a certain sense to $SO(3)$. Friesecke, James and Müller [FJM02b] came up with a rigorous derivation of the thin-plate limit of three-dimensional nonlinear elasticity theory, not just under the special compressive boundary conditions considered above but under any boundary condition that does not induce tangential distortion of the midsurface. As for the derivation of the membrane model, the mathematical setting in which these results are formulated is that of Γ-convergence. However, due to the scaling mentioned above, for the derivation of the bending model the limit process of $\frac{1}{\delta^3}\mathcal{W}$ is considered for $\delta \to 0$. Although the approaches are similar, the bending model is more difficult to derive since the limit functional contains higher derivatives and one is thus dealing with a singular perturbation problem.

A special case of the convergence result in [FJM02b] is to consider (5.1.2) with an *isotropic* energy density fulfilling (3.2.3), *i.e.* $W_{,FF}(\mathbb{1})(G, G) = 2\mu \operatorname{tr}(E^2) + \lambda(\operatorname{tr} E)^2$ with $E = \frac{1}{2}(G + G^T)$. Then it is shown that $\frac{1}{\delta^3}\mathcal{W}$ converges in the sense of Γ-convergence with respect to the $W^{1,2}$-topology to a two-dimensional limit functional given by

$$\mathcal{W}^0_{\text{iso}}[\phi] = \begin{cases} \frac{1}{24} \int_\omega \left(2\mu \operatorname{tr}(h[\phi]^2) + \frac{\lambda\mu}{\mu + \lambda/2}(\operatorname{tr} h[\phi])^2 \right) \sqrt{\det g_\phi} \, d\xi & , \text{on isometries } \phi : \omega \to \mathbb{R}^3 \\ +\infty & , \text{otherwise} \end{cases} \,.$$

The limiting energy thus depends on the second fundamental form $h[\phi] = Dn^T D\phi$, where ϕ can be thought of being a parametrization of the deformed plate $\phi(\omega)$, *i.e.* $n \parallel (\phi_{,1} \times \phi_{,2})$. Note that $\phi : \omega \to \mathbb{R}^3$ is an isometry iff. $(g_\phi)_{ij} = \phi_{,i} \cdot \phi_{,j} = \delta_{ij}$, *i.e.* in particular $\det g_\phi = 1$.

Bending model (shell) More general, the two-dimensional midsurface $\mathcal{S} \subset \mathbb{R}^3$ of the reference configuration $\bar{\mathcal{S}}_\delta = \{x + z\, n(x) \,|\, x \in \mathcal{S}, |2z| < \delta\}$ is already curved. Under similar assumptions as above, Friesecke *et al.* [FJMM03] showed that the scaled energy $\frac{1}{\delta^3}\mathcal{W}$ converges in the sense of Γ-convergence with respect to the $W^{1,2}$-topology to a two-dimensional limit functional given by

$$\mathcal{W}^0[\phi] = \begin{cases} \frac{1}{24} \int_\mathcal{S} \min_{v \in \mathbb{R}^3} Q(S_\phi^{\mathrm{rel}}(x) + v \otimes n(x))\, \mathrm{d}a & , \phi \in \mathcal{A} \\ +\infty & , \text{otherwise} \end{cases},$$

with the quadratic form $Q(G) = W_{,FF}(\mathbb{1})(G, G)$ and the admissible set of isometric deformations

$$\mathcal{A} = \{\phi \in W^{2,2}(\mathcal{S}, \mathbb{R}^3) \,|\, (D_{\tan}\phi)^T(D_{\tan}\phi) = \mathbb{1} \text{ a.e. on } \mathcal{S}\}\,.$$

Here the tangential derivative $D_{\tan}\phi \in \mathbb{R}^{3,2}$ can be extended to a proper rotation $Q(x) = Q[\phi](x) \in SO(3)$ if ϕ is isometric. The two-dimensional limit energy density depends on the *relative shape operator* $S_\phi^{\mathrm{rel}}(x) : T_x\mathcal{S} \to T_x\mathcal{S}$ defined pointwise by

$$S_\phi^{\mathrm{rel}}(x) = S(x) - Q(x)^T S_\phi(\phi(x))\, Q(x)\,, \tag{5.1.7}$$

where $S(x) : T_x\mathcal{S} \to T_x\mathcal{S}$ and $S_\phi(y) : T_y\mathcal{S}^\phi \to T_y\mathcal{S}^\phi$ are the shape operators on the undeformed and deformed configuration, respectively, where we have used the notation $\mathcal{S}^\phi = \phi(\mathcal{S})$ and $y = \phi(x)$ for $x \in \mathcal{S}$. The relative shape operator is supposed to measure the (pointwise) difference between the shape operators on $\mathcal{S}$ and $\mathcal{S}^\phi$, respectively. However, as these operators live on different tangent spaces, *i.e.* rotated planes in $\mathbb{R}^3$, we must include proper rotations to ensure well-definedness of the pointwise difference. Hence $Q(x)$ and $Q(x)^T$ denote the linear mappings between the two different tangent spaces, as illustrated in the following diagram:

$$
\begin{array}{ccc}
T_x\mathcal{S} & \xrightarrow{\;\;S(x)\;\;} & T_x\mathcal{S} \\
{\scriptstyle Q(x)}\Big\downarrow & & \Big\uparrow{\scriptstyle Q(x)^T} \\
T_{\phi(x)}\phi(\mathcal{S}) & \xrightarrow[\;S_\phi(\phi(x))\;]{} & T_{\phi(x)}\phi(\mathcal{S})
\end{array}
$$

The limit bending energy $\mathcal{W}^0[\phi]$ is only finite for deformations $\phi \in \mathcal{A}$, hence we will assume in the remainder of this section that we are dealing with isometric deformations. In particular, we have $Q(x) = D\phi(x) \in SO(3)$ and $D\phi(x)n(x) = n^\phi(\phi(x))$, where n^ϕ denotes the normal on the deformed surface. To this end, we can think of $Q^T(S_\phi \circ \phi)Q$ as being a *pulled-back* representation of the shape operator S_ϕ on the deformed configuration. This pulled-back linear operator $S_\phi^* : T_x\mathcal{S} \to T_x\mathcal{S}$ is then implicitly defined by

$$g_x\left(S_\phi^*(x)V, W\right) = h_{\phi(x)}\left(D\phi V, D\phi W\right)\,, \quad V, W \in T_x\mathcal{S}\,, \tag{5.1.8}$$

where g and h denote the first and second fundamental form, respectively. If we compare (5.1.8) with (5.1.7) we get $S_\phi^{\mathrm{rel}} = S - S_\phi^*$ which coincides with the notation used in [HRWW12, HRS$^+$14].

As for the membrane shell energy we use the analytic results presented above to extract a generic bending shell energy in the spirit of Rem. 5.1.1 by setting

$$\mathcal{W}_{\mathrm{bend}}[\mathcal{S}, \phi] = \int_\mathcal{S} W_{\mathrm{bend}}(S_\phi^{\mathrm{rel}})\, \mathrm{d}a\,. \tag{5.1.9}$$

In general, we make use of the density

$$W_{\text{bend}}(A) = \alpha(\operatorname{tr} A)^2 + (1 - \alpha) \|A\|_F^2, \quad \alpha \in \{0, 1\}. \tag{5.1.10}$$

In particular, for $\alpha = 1$ we recover an adapted form of the Willmore energy measuring differences in mean curvature, as it was used *e.g.* in [CLR04, LDRS05] for surface matching. Next, we introduce a representation $s^{\text{rel}} = s^{\text{rel}}(\xi) \in \mathbb{R}^{2,2}$ of $S^{\text{rel}}(x) = S^{\text{rel}}(x(\xi))$ in the parameter domain defined by

$$s^{\text{rel}} = g^{-1}(h - h_\phi) = s - \mathcal{G}[\phi]s_\phi = s - s_\phi, \tag{5.1.11}$$

with $s, s_\phi \in \mathbb{R}^{2,2}$ being the matrix representations of the two shape operators in a common reference domain $\omega \subset \mathbb{R}^2$ (*cf.* Sec. 3.1). Note that we have $\mathcal{G}[\phi] = \mathbb{1}$ since we are dealing with isometric deformations ϕ. We prove in Lemma A.1.6 in the appendix that for $\alpha = 0$ we get

$$\mathcal{W}_{\text{bend}}[\mathcal{S}, \phi] = \int_{\mathcal{S}} \|S_\phi^{\text{rel}}\|_F^2 \, da = \int_\omega \operatorname{tr}\left((s - s_\phi)^2\right) \sqrt{\det g} \, d\xi, \tag{5.1.12}$$

and for $\alpha = 1$ we get

$$\mathcal{W}_{\text{bend}}[\mathcal{S}, \phi] = \int_{\mathcal{S}} \left(\operatorname{tr} S_\phi^{\text{rel}}\right)^2 da = \int_\omega \left(\operatorname{tr}(s - s_\phi)\right)^2 \sqrt{\det g} \, d\xi. \tag{5.1.13}$$

Note that one can deduce already from (3.1.11) that $\|S\|_F^2 = \operatorname{tr} s^2 \neq \operatorname{tr}(s^T s) = \|s\|_F^2$. Hence the integrand on the right hand side in (5.1.12) is *not* given by $\|s - s_\phi\|_F^2$ which was used in [Hee11].

Full elastic model Given a surface $\mathcal{S} \in \mathcal{M}$ representing a physical shell with thickness $\delta > 0$ and a deformation $\phi : \mathcal{S} \to \mathbb{R}^3$, a generic elastic deformation energy is given by

$$\int_{\mathcal{S}} \delta \, W_{\text{mem}}(\mathcal{G}[\phi]) + \delta^3 \, W_{\text{bend}}(S_\phi^{\text{rel}}) \, da, \tag{5.1.14}$$

with $W_{\text{mem}}(A) = W_{\text{mem}}(\operatorname{tr} A, \det A)$ as defined in (3.2.5) for $d = 2$ and W_{bend} as defined in (5.1.10). Nevertheless, for convenience we shall consider in the following a rescaled version of (5.1.14), namely

$$\mathcal{W}_{\mathcal{S}}[\phi] = \int_{\mathcal{S}} W_{\text{mem}}(\mathcal{G}[\phi]) + \eta \, W_{\text{bend}}(S_\phi^{\text{rel}}) \, da, \tag{5.1.15}$$

where the bending weight η represents the squared thickness of the shell. Note that (5.1.15) is invariant with respect to rigid body motions by construction, *i.e.* $\mathcal{W}_{\mathcal{S}}[\phi] = 0$ and $d\mathcal{W}_{\mathcal{S}}[\phi] = 0$ if $\phi(x) = Qx + b$ with $Q \in SO(3)$ and $b \in \mathbb{R}^3$. In particular, we have

$$\mathcal{W}_{\mathcal{S}}[\text{id}] = 0, \quad d\mathcal{W}_{\mathcal{S}}[\text{id}] = 0. \tag{5.1.16}$$

Remark 5.1.2. Using (5.0.1), we can derive a dissimilarity measure $\mathcal{W} : \mathcal{M} \times \mathcal{M} \to \mathbb{R}$ for two given shells $\mathcal{S}, \tilde{\mathcal{S}} \in \mathcal{M}$ by minimizing (5.1.15) over all deformations satisfying $\phi(\mathcal{S}) = \tilde{\mathcal{S}}$. However, we do not discuss whether this definition is actually well-defined, *i.e.* if there exists such a minimizer. Physically, one might regard the second shell $\tilde{\mathcal{S}}$ as a deformed version of the first shell $\mathcal{S}$, *i.e.*, the corresponding material of $\tilde{\mathcal{S}}$ is just in a deformed configuration compared to its configuration in $\mathcal{S}$. Since every material point has a well-defined position, one can view this correspondence as *a priori* information. In this setup, one can then assume the dissimilarity measure $\mathcal{W}[\mathcal{S}, \tilde{\mathcal{S}}]$ to be well-defined. However, we will see in the next section that the well-posedness of the corresponding discrete dissimilarity measure is trivial by construction of the discrete shell space.

5.2 Discrete shells and discrete shell space

The geodesic calculus introduced in chapter 4 is by construction in a *time-discrete* setup. In the previous section we derived a thin shell deformation energy that induces a notion of a dissimilarity measure on the space of shells represented as regular embedded surfaces. In this section we spatially discretize these surfaces and corresponding energies to be able to actually compute *e.g.* time-discrete geodesics in the space of *discrete shells*. In particular, we will derive a discrete deformation energy that can be used as dissimilarity measure on this discrete shell space. By the introduction of a spatial discretization the corresponding Riemannian manifold reduces to a finite dimensional space that can be represented as a submanifold of $\mathbb{R}^d$ for a suitable $d \gg 1$. Although there are multiple ways how to discretize an embedded surface, *e.g.* by levelset functions or phasefield models, we focus on polyhedral surfaces, or more precisely, on triangle meshes.

5.2.1 Structure of discrete shells

As mentioned above, we discretize thin shells resp. embedded surfaces by triangle meshes. A triangular mesh is uniquely determined by its *geometry* and its *connectivity*. The geometry is described by the embedding, *i.e.* the set of nodal positions of the vertices

$$\mathcal{N} = \{X_i \in \mathbb{R}^3 : i = 0, \ldots, n-1\} \,,$$

where $n \in \mathbb{N}$ is the number of nodes of the mesh. We often identify a vertex $X_i \in \mathcal{N}$ with its global index $i \in \{0, \ldots, n-1\}$ hence we may also write $\mathcal{N} = \{0, \ldots, n-1\}$. The connectivity is encoded in a mapping defined on the set of faces $\mathcal{T}$, *i.e.*

$$\pi_{\mathcal{T}} : \mathcal{T} \to \mathcal{N}^3 \,,$$

that assigns each face three vertex indices. If $m \in \mathbb{N}$ denotes the number of faces in the mesh, we often identify a face $T_j \in \mathcal{T}$ with its global index $j \in \{0, \ldots, m-1\}$ and write $\mathcal{T} = \{0, \ldots, m-1\}$. Moreover, we might represent a face by its image under $\pi_{\mathcal{T}}$, *i.e.* $T_j = \pi_{\mathcal{T}}(j) =: (j_0, j_1, j_2)$ or $T_j = (X_{j_0}, X_{j_1}, X_{j_2})$, respectively. Note that all further structural properties of the mesh, such as neighboring relationships, boundary etc., can be derived from $\mathcal{T}$ or $\pi_{\mathcal{T}}$, respectively. In particular, the set of edges

$$\mathcal{E} = \{(i,j) \in \mathcal{N}^2 : \exists k \in \mathcal{T} : i, j \in \pi_{\mathcal{T}}(k)\}$$

is also determined by the mapping $\pi_{\mathcal{T}}$.

Definition 5.2.1 (Discrete shell). A discrete shell $\mathbf{S}$ is given as the collection of a set of nodes $\mathcal{N} \subset \mathbb{R}^3$, a set of triangles $\mathcal{T}$ and possibly a set of edges $\mathcal{E}$. We write $\mathbf{S} = (\mathcal{N}, \mathcal{T})$ or $\mathbf{S} = (\mathcal{N}, \mathcal{T}, \mathcal{E})$.

Topology We assume that each mesh is a *two-dimensional discrete manifold* in the sense of Sec. 3.1 in [DKT08]. That means, that any pair of triangles either shares one edge or one node or that their intersection is empty. In particular, we do not allow for hanging nodes, *i.e.* nodes that do not belong to any face, or degenerated faces, *i.e.* faces with less than three different nodes.

Local structure As described above, each vertex $X = X_i$ has a global index $i \in \{0, \ldots, n-1\}$. Furthermore, as X_i belongs to at least one face T it has an additional local index $j \in \{0, 1, 2\}$ with respect to T. Analogously, each edge E of a mesh belongs to at least one face and hence it also has a local index $j \in \{0, 1, 2\}$ with respect to T. Moreover, we make use of the convention that an edge with local index j (wrt. face T) connects the nodes with local indices $j-1$ and $j+1$ (wrt. face T), where the notation is modulo 3, *i.e.*

$$E_j = X_{j-1} - X_{j+1} \,, \quad j \in \{0, 1, 2\} \bmod 3 \,.$$

That means E_j is opposite X_j in face T, if j is the local index wrt. face T. In the following, it will be clear from the context if we are referring to the global or local index of a vertex or edge, respectively.

Orientation   The order of the local indices of nodes within one face determines the orientation of the face and hence of the mesh. Since we only consider (approximations of) orientable surfaces we assume that all local indices are ordered consistently.

Local parametrizations   We assume that each discrete shell $\mathbf{S}$ is parametrized over a reference or parameter domain Ω. Yet different from the continuous setting this reference domain is not a connected subset of $\mathbb{R}^2$ but rather an abstract collection of multiple reference triangles as it is often used in the context of subdivision surfaces (*cf*. [Rei95]). Thus each triangle $T \in \mathcal{T}$ of $\mathbf{S}$, with $T = (X_0(T), X_1(T), X_2(T))$, is parametrized over a reference triangle given by the *unit triangle*

$$\omega := (\begin{pmatrix} 0 \\ 0 \end{pmatrix}, \begin{pmatrix} 1 \\ 0 \end{pmatrix}, \begin{pmatrix} 0 \\ 1 \end{pmatrix}) \subset \mathbb{R}^2$$

via an affine mapping $X_T : \omega \to T$, which is defined by

$$X_T(\xi) := X_T(\xi_1, \xi_2) := \xi_1 X_1(T) + \xi_2 X_2(T) + (1 - \xi_1 - \xi_2)X_0(T) \tag{5.2.1}$$

for the barycentric coordinates $\xi \in \omega$, *i.e.* $\xi = (\xi_1, \xi_2)$ with $0 \leq \xi_1, \xi_2 \leq 1$ and $\xi_1 + \xi_2 \leq 1$.

Formally, the reference domain is given by $\Omega = \omega \times \mathcal{T}$, a global parametrization via $X : (\xi, i) \mapsto X_{T_i}(\xi)$. Wherever it is possible, we drop the dependence of the local parametrization X on the face T_j in the following and write $X = X_{T_j}$. Finally, we define the unit face normal N_T on a triangle $T = (X_0, X_1, X_2)$ by

$$N_T = \frac{(X_1 - X_0) \times (X_2 - X_0)}{\|(X_1 - X_0) \times (X_2 - X_0)\|} .$$

5.2.2 Structure of discrete shell space

As pointed out in the previous section a discrete shell is uniquely determined by its geometry and connectivity. Following Kilian *et al.* [KMP07] we will fix the connectivity and consider the geometry, *i.e.* the nodal positions of the vertices, as only degress of freedom.

Definition 5.2.2 (Fixed connectivity constraint)**.** We say that two triangular meshes $\mathbf{S}_A = (\mathcal{N}_A, \mathcal{T}_A)$ and $\mathbf{S}_B = (\mathcal{N}_B, \mathcal{T}_B)$ are in *dense correspondence* if there is a 1-to-1-correspondence between all nodes and all triangles. In particular, we have $|\mathcal{N}_A| = |\mathcal{N}_B|$, $|\mathcal{T}_A| = |\mathcal{T}_B|$ and $\pi_{\mathcal{T}_A} = \pi_{\mathcal{T}_B}$. A set of triangular meshes obeys the *fixed-connectivity constraint* if all elements are pairwise in dense correspondence.

We postulate that the dissimilarity between $\mathbf{S}_A$ and $\mathbf{S}_B$ is infinite if $\mathbf{S}_A$ and $\mathbf{S}_B$ are *not* in dense correspondence. Hence we assume that we are dealing with an arbitrary but fixed component of the set of all triangular meshes, where the component obeys the fixed connectivity constraint. Although this assumption is very restrictive it is widely used in computer graphics [KMP07, FB11, vTSSH15]. There are two important implications of this assumption:

1. The minimization problem in (5.0.1) is trivial, since for two given discrete shells $\mathbf{S}, \tilde{\mathbf{S}}$ having the same connectivity, a piecewise affine deformation $\Phi : \mathbf{S} \to \tilde{\mathbf{S}}$ is uniquely determined.

2. The discrete shell space can be identified with $\mathbb{R}^{3n}$, where n is the number of nodes.

In particular, it follows from the first point that we do not have to care about existence of optimal matching deformations.

Definition 5.2.3 (Discrete shell space). Given a discrete shell $\bar{\mathbf{S}} = (\bar{\mathcal{N}}, \bar{\mathcal{T}})$, the corresponding discrete shell space $\mathcal{M}[\bar{\mathbf{S}}]$ is defined as an equivalence class, where the equivalence relation is given by the notion of dense correspondence, *i.e.*

$$\mathcal{M}[\bar{\mathbf{S}}] = \{(\mathcal{N}, \mathcal{T}) \,:\, |\bar{\mathcal{N}}| = |\mathcal{N}|, \ \pi_{\bar{\mathcal{T}}} = \pi_{\mathcal{T}} \}\,.$$

If $n = |\bar{\mathcal{N}}|$ we identify $\mathcal{M} = \mathcal{M}[\bar{\mathbf{S}}] = \mathbb{R}^{3n}$, in particular we drop the dependence on the representative shell $\bar{\mathbf{S}}$ in the notation.

5.3 Discrete deformation energies

In this section we derive a discrete membrane model and a discrete bending model that reflect the structural properties of the corresponding continuous models introduced in Sec. 5.1.2. In particular, we introduce a discrete analogon of the (relative) shape operator, which is based on unpublished work by Wardetzky [War11], *cf.* also [Hee11].

5.3.1 Discrete membrane model

Let $\mathcal{S} \subset \mathbb{R}^3$ be a regular embedded surface with (local) parametrization $x : \omega \to \mathcal{S}$ and $\xi \in \omega$. Following Def. 3.1.26 we can represent the first fundamental form g at some point $x(\xi)$ by the matrix $g_{\xi} = Dx(\xi)^T Dx(\xi)$. According to (5.2.1), the local parametrization X of a a discrete shell $\mathbf{S}$ is affine, hence its derivative is constant on each triangle $T \in \mathbf{S}$, *i.e.*

$$DX|_T = \left(\frac{\partial X_T}{\partial \xi_1}, \frac{\partial X_T}{\partial \xi_2} \right) = \left[X_1(T) - X_0(T) \,\Big|\, X_2(T) - X_0(T) \right] \in \mathbb{R}^{3,2}\,.$$

Hence the definition of a discrete first fundamental form is straightforward:

Definition 5.3.1 (Discrete first fundamental form). For a discrete shell $\mathbf{S} = (\mathcal{N}, \mathcal{T})$ the elementwise constant discrete first fundamental form is defined by

$$G_T = (DX|_T)^T DX|_T \in \mathbb{R}^{2,2}\,, \quad T \in \mathcal{T}\,. \tag{5.3.1}$$

To simplify notation we will often drop the dependence on T and write $G = G_T$. Note that $\det G_T = 0$ iff. T has parallel edges, which is not admissible due to the assumption that $\mathbf{S}$ is a discrete manifold. Hence G_T is invertible for each $T \in \mathcal{T}$.

Next we consider *two* discrete shells $\mathbf{S} = (\mathcal{N}, \mathcal{T})$ and $\tilde{\mathbf{S}} = (\tilde{\mathcal{N}}, \tilde{\mathcal{T}})$ that are in dense correspondence. On the one hand, we have elementwise constant first fundamental forms and a unique correspondence between all faces, *i.e.* for each face $T \in \mathcal{T}$ there is a corresponding face $\tilde{T} \in \tilde{\mathcal{T}}$. On the other hand, we want to make use of the membrane model derived in Sec. 5.1.2 and in particular of the representation of the distortion tensor (5.1.5). Hence to describe membrane distortions induced by a discrete deformation $\Phi : \mathbf{S} \to \tilde{\mathbf{S}}$ we arrive at an elementwise constant, discrete distortion tensor

$$\mathcal{G}[\Phi]|_T = (G_T)^{-1} G_{T_{\Phi}} \in \mathbb{R}^{2,2}\,, \quad T \in \mathcal{T}\,, \quad T_{\Phi} = \tilde{T} \in \tilde{\mathcal{T}}\,. \tag{5.3.2}$$

Again using the continuous membrane model in Sec. 5.1.2 and in particular the generic membrane energy in (5.1.6) we define the *discrete membrane energy* by

$$\mathbf{W}_{\text{mem}}[\mathbf{S}, \tilde{\mathbf{S}}] = \int_{\mathbf{S}} W_{\text{mem}}(\mathcal{G}[\Phi]) \, \mathrm{d}a = \sum_{T \in \mathcal{T}} |T| \cdot W_{\text{mem}}(\mathcal{G}[\Phi]|_T)\,, \quad \tilde{\mathbf{S}} = \Phi(\mathbf{S})\,. \tag{5.3.3}$$

Note that a one point quadrature is sufficient as we are dealing with an elementwise constant discrete distortion tensor. Different from (5.1.6), the discrete membrane energy directly depends on the undeformed and deformed discrete shell, since the discrete deformation in uniqely determined, as described above. For the membrane energy density W_{mem} we can use exactly the same density as in (5.1.6). In the applications we make use of an adapted form of the polyconvex density (3.2.5), *i.e.*

$$W_{\mathrm{mem}}(\mathcal{G}[\Phi]|_T) = \frac{\mu}{2}\operatorname{tr}\mathcal{G}[\Phi]|_T + \frac{\lambda}{4}\det\mathcal{G}[\Phi]|_T - \left(\frac{\mu}{2} + \frac{\lambda}{4}\right)\log\det\mathcal{G}[\Phi]|_T - \mu - \frac{\lambda}{4}\,.$$

Note that $\operatorname{tr}\mathcal{G}[\Phi]|_T$ controls the local change of length, *i.e.* the change of edge lengths, whereas $\det\mathcal{G}[\Phi]|_T$ controls the local change of volume, *i.e.* the change of triangle volumes. In particular, the density grows quadratically for $\det G|_{T_\Phi} \to \infty$ but due to the log-term it grows even faster for $\det G|_{T_\Phi} \to 0$. This prevents a local interpenetration of matter, *i.e.* the degeneration of triangles. Finally, we have $W_{\mathrm{mem}}(\mathbb{1}) = 0$ and $dW_{\mathrm{mem}}(\mathbb{1}) = 0$ for the identity matrix $\mathbb{1} \in \mathbb{R}^{2,2}$.

5.3.2 Discrete shape operator

In the previous section we have derived a matrix representation $\mathcal{G} \in \mathbb{R}^{2,2}$ of the discrete distortion tensor that lives in the reference domain. Furthermore, $\mathcal{G} = \mathcal{G}[\Phi]|_T$ is constant on each triangle T. Hence we aim at defining a matrix representation of a discrete shape operator B that also lives in the reference domain and is elementwise constant, *i.e.* we have $B = B_T \in \mathbb{R}^{2,2}$. If we make use of (3.1.10) we can write $B_T = G_T^{-1}H_T$ and as G_T has been defined in Def. 5.3.1 we just have to provide a matrix representation $H = H_T \in \mathbb{R}^{2,2}$ of a discrete second fundamental form that is constant on faces.

Let $T \in \mathcal{T}$ be an arbitrary triangle of a discrete shell **S** with a local parametrization $X = X_T$ as defined in (5.2.1). Note that we have

$$\frac{\partial X}{\partial \xi_1} = X_1 - X_0 = E_2\,, \qquad \frac{\partial X}{\partial \xi_2} = X_2 - X_0 = -E_1\,. \tag{5.3.4}$$

Plugging this into (3.1.9) yields for the entries of $H = H_T$:

$$H_{11} = \left\langle dN(E_2), E_2 \right\rangle_{\mathbb{R}^3} \qquad H_{12} = -\left\langle dN(E_2), E_1 \right\rangle_{\mathbb{R}^3}$$
$$H_{21} = -\left\langle dN(E_1), E_2 \right\rangle_{\mathbb{R}^3} \qquad H_{22} = \left\langle dN(E_1), E_1 \right\rangle_{\mathbb{R}^3}$$

Using concepts from discrete differential geometry we associate the discrete normal field N on **S** with edges (*cf*. [GGRZ06, DKT08]). More precisely, for an edge $E \in$ **S** the corresponding edge normal N_E lives at the edge midpoint and is defined as the normalized sum of the unit face normals belonging to the two adjacent faces. For boundary edges, we take the respective triangle normal. With normals associated to edge midpoints, the (discrete) 1-form dN acts on line segments connecting these midpoints[1]. For a triangle T with edges E_0, E_1, E_2 we denote the corresponding edge normals by N_0, N_1, N_2 and the connecting line segments by E_{ij}, *i.e.* E_{ij} connects the midpoint of E_i with that of E_j, *cf*. Fig. 5.2. In particular, we have the vector identity $E_k = -2\,E_{ij}$, where k is the complementary index to i and j in T. Using this notation, the fundamental theorem of calculus implies

$$dN(E_k) = -2\,dN(E_{ij}) = -2\int_{E_{ij}} dN = -2\,(N_j - N_i) = 2\,(N_i - N_j)\,. \tag{5.3.5}$$

---

[1] A continuous 1-form ω on a manifold $\mathcal{M}$ is a mapping with $\omega(p) \in T_p^*\mathcal{M}$ for all $p \in \mathcal{M}$, where $T_p^*\mathcal{M}$ is the dual space of $T_p\mathcal{M}$. Continuous 1-forms are naturally evaluated as integrals along piecewise differentiable curves $\gamma : [a, b] \to \mathcal{M}$. An important example is given by $\omega = df$, where $f : \mathcal{M} \to \mathbb{R}$ is a differentiable function. Here we have $\int_\gamma \omega = f(b) - f(a)$. The concept of *Discrete Exterior Calculus (DEC)* aims at deriving a consistent theory of discrete forms on discrete manifolds, *i.e.* polygonal surfaces with certain properties. Analogously to the continuous setup, discrete 1-forms (*e.g.* given as a differential of a discrete function on a discrete manifold) are evaluated as integrals along discrete curves, *i.e.* polygonal chains. For further information and a comprehensice introduction on DEC we refer to [Hir03, DHLM05, DKT08].

We can use (5.3.5) to simplify the entries of $H = H_T$ further, *i.e.*

$$H_{11} = \langle dN(E_2), E_2 \rangle = 2 \langle N_0 - N_1, E_2 \rangle = 2 \langle N_0, E_2 \rangle + 2 \langle N_1, E_0 \rangle$$
$$H_{12} = -\langle dN(E_2), E_1 \rangle = -2 \langle N_0 - N_1, E_1 \rangle = 2 \langle N_0, -E_1 \rangle = 2 \langle N_0, E_2 \rangle$$
$$H_{21} = -\langle dN(E_1), E_2 \rangle = -2 \langle N_2 - N_0, E_2 \rangle = 2 \langle N_0, E_2 \rangle$$
$$H_{22} = \langle dN(E_1), E_1 \rangle = 2 \langle N_2 - N_0, E_1 \rangle = 2 \langle N_0, E_2 \rangle + 2 \langle N_2, E_1 \rangle$$

where we have used $\langle N_i, E_i \rangle = 0$ and $E_0 + E_1 + E_2 = 0$. Hence we get the representation

$$H = H_T = 2 \sum_{i=0}^{2} \langle N_i, E_{i-1} \rangle \, M_i \,,$$

with a basis (M_0, M_1, M_2) of symmetric 2×2 - matrices given by

$$M_0 = \begin{pmatrix} 1 & 1 \\ 1 & 1 \end{pmatrix}, \quad M_1 = \begin{pmatrix} 1 & 0 \\ 0 & 0 \end{pmatrix}, \quad M_2 = \begin{pmatrix} 0 & 0 \\ 0 & 1 \end{pmatrix}.$$

In the following, we will interpret the terms $\langle N_i, E_{i-1} \rangle$ geometrically. We refer to the height in T with base E_i by h_i, the neighboring triangle is denoted by T_i, *i.e.* $T \cap T_i = E_i$, *cf.* Fig. 5.2. Then the angle α_i at E_i between T and T_i is given by two times the angle between h_i and N_i, since N_i is the angle bisector of α_i by definition. We further use $h_i = -E_{i-1} + \beta E_i$ for some $\beta \in \mathbb{R}$ and obtain

$$\cos \frac{\alpha_i}{2} = \langle N_i, \frac{h_i}{|h_i|} \rangle = -\frac{1}{|h_i|} \langle N_i, E_{i-1} \rangle + \beta \underbrace{\langle N_i, E_i \rangle}_{=0}.$$

Since $a_T := |T| = \frac{1}{2} |h_i| \, |E_i|$ we have $\langle N_i, E_{i-1} \rangle = -2 \frac{a_T}{|E_i|} \cos \frac{\alpha_i}{2}$, hence

$$H_T = -4 \, a_T \sum_{i=0}^{2} \frac{\cos \frac{\alpha_i}{2}}{|E_i|} M_i = -4 \, a_T \sum_{i=0}^{2} \frac{\cos \frac{\pi+\theta_i}{2}}{|E_i|} M_i \,, \tag{5.3.6}$$

where θ_i denotes the dihedral angle at edge E_i, *i.e.* the angle between the face normals of T and T_i.
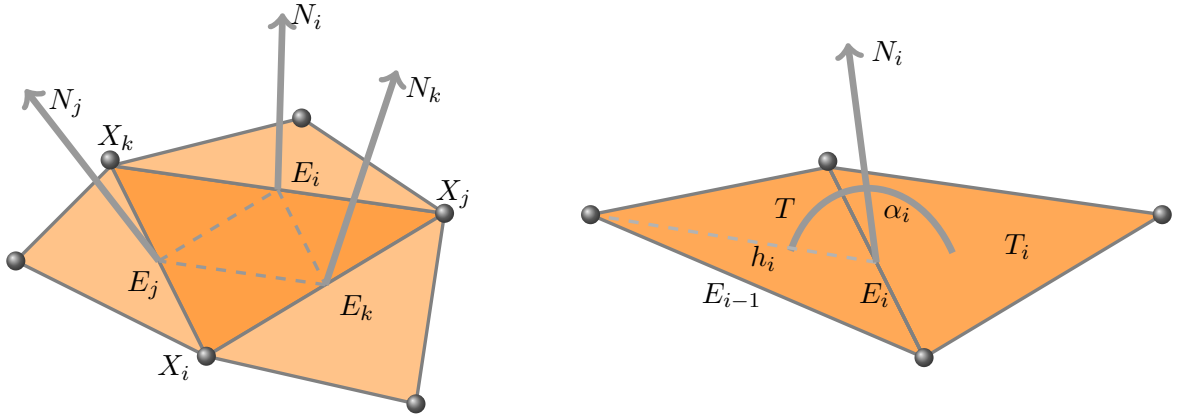
Figure 5.2: *Support of discrete shape operator (left) and geometric interpretation of coefficients (right).*

Finally, using (5.3.1), (5.3.6) and (3.1.10), we get a matrix representation of our discrete shape operator

$$B_T = G_T^{-1} H_T \in \mathbb{R}^{2,2} \,. \tag{5.3.7}$$

Since N is the outer unit normal field we want to have positive curvature for convex shapes. Indeed, convex shapes have dihedral angles $0 < \theta < \pi$, hence $-\cos \frac{\pi+\theta}{2} > 0$.

Remark 5.3.2. In the appendix A.2 we derive a formula for the *embedded* discrete shape operator. This representation coincides with the one proposed in eq. (15) in [HRWW12].

5.3.3 Discrete bending model

Having a notion of a discrete shape operator given by (5.3.7) at hand, we can translate the general representation of a bending energy given in (5.1.9) (with the density (5.1.10) and $\alpha \in \{0,1\}$) directly into the discrete setup. Setting $\alpha = 0$, as in (5.1.12), we can define a discrete bending energy via

$$\mathbf{W}_{\text{bend}}[\mathbf{S}, \tilde{\mathbf{S}}] = \sum_{T \in \mathcal{T}} a_T \cdot \text{tr}\left((B_T - B_{\Phi(T)})^2\right), \quad \tilde{\mathbf{S}} = \Phi(\mathbf{S}), \tag{5.3.8}$$

with $a_T = |T|$ as above. Alternatively, by choosing $\alpha = 1$, as in (5.1.13), we can derive a discrete version of the Willmore energy:

$$\tilde{\mathbf{W}}_{\text{bend}}[\mathbf{S}, \tilde{\mathbf{S}}] = \sum_{T \in \mathcal{T}} a_T \cdot \left(\text{tr}\left(B_T - B_{\Phi(T)}\right)\right)^2, \quad \tilde{\mathbf{S}} = \Phi(\mathbf{S}). \tag{5.3.9}$$

Note that a one point quadrature is again sufficient as we are integrating over an elementwise constant density. In the remainder of this section we investigate another definition of a discrete Willmore energy and derive a representation that corresponds to a non-conforming FEM approach. Furthermore, after some simplifications, we obtain the *Discrete Shells* bending model [GHDS03] as a special case.

First of all, we derive a representation of discrete mean curvature. Let $T \in \mathbf{S}$ be an arbitrary triangle of the discrete shell $\mathbf{S}$. Analogously to the continous setting, the discrete mean curvature is defined as $\text{tr}\, B_T$, hence it is also constant on faces. From (5.3.7) we know $B_T = G_T^{-1} H_T$. Using (5.3.1) and (5.3.4) we get

$$G_T^{-1} = \frac{1}{\det G_T}\left(\begin{array}{cc} |E_1|^2 & \langle E_1, E_2\rangle \\ \langle E_1, E_2\rangle & |E_2|^2 \end{array}\right)$$

and hence, since $\det G_T = 4\, a_T^2$, we have

$$\text{tr}\,(G_T^{-1} M_0) = \frac{1}{\det G_T}\left(|E_1|^2 + |E_2|^2 + 2\,\langle E_1, E_2\rangle\right) = \frac{|E_0|}{4\, a_T^2}$$

$$\text{tr}\,(G_T^{-1} M_1) = \frac{1}{\det G_T}(|E_1|^2) = \frac{|E_1|}{4\, a_T^2}$$

$$\text{tr}\,(G_T^{-1} M_2) = \frac{1}{\det G_T}(|E_2|^2) = \frac{|E_2|}{4\, a_T^2}$$

which implies

$$\text{tr}\, B_T = \text{tr}\,(G_T^{-1} H_T) = -\sum_{i=0}^{2} \frac{\cos(\frac{\pi+\theta_i}{2})}{a_T}|E_i|. \tag{5.3.10}$$

Now we consider the discrete mean curvature functional which can be written as a sum over edges:

$$\int_{\mathbf{S}} \text{tr}\, B\, \mathrm{d}a = \sum_{T \in \mathcal{T}} a_T \cdot \text{tr}\, B_T = \sum_{T \in \mathcal{T}} \sum_{i=0}^{2} -\cos\left(\frac{\pi+\theta_i}{2}\right)|E_i| = -2\sum_{E \in \mathcal{E}} \cos\left(\frac{\pi+\theta_E}{2}\right)|E|.$$

We introduce an area $d_E \in \mathbb{R}$ corresponding to an edge E, such that $|\mathbf{S}| = \sum_{T \in \mathcal{T}} a_T = \sum_{E \in \mathcal{E}} d_E$; a suitable choice is given *e.g.* by $d_E = \frac{1}{3}(T_i + T_j)$ if $E = T_i \cap T_j$, *cf.* Fig. 5.3. Furthermore, we make use of the notation $l_E = |E|$. Then we rewrite the discrete mean curvature functional by introducing a mean curvature density at edges:

$$\int_{\mathbf{S}} \text{tr}\, B\, \mathrm{d}a = \sum_{E \in \mathcal{E}} d_E \cdot \left(\frac{-2\cos(\frac{\pi+\theta_E}{2})}{d_E} l_E\right).$$

In the spirit of [MDSB02] an approximative discrete Willmore energy can be deduced by squaring the mean curvature edge density, *i.e.*

$$\int_{\mathbf{S}} (\operatorname{tr} B)^2 \, \mathrm{d}a \approx \sum_{E \in \mathcal{E}} d_E \cdot \left(\frac{-2 \cos(\frac{\pi + \theta_E}{2})}{d_E} l_E \right)^2 = \sum_{E \in \mathcal{E}} \frac{4 \cos^2(\frac{\pi + \theta_E}{2})}{d_E} l_E^2. \qquad (5.3.11)$$

Remark 5.3.3. Wardetzky *et al.* [WBH+07] present a discretization of the Willmore functional using the non-conforming Crouzeix-Raviart element. The corresponding discrete Willmore energy (*i.e.* eq. (7) in [WBH+07]) coincides exactly with the right hand side of (5.3.11). This underlines the fact that models derived by principles of *Discrete Differential Geometry* often correspond to non-conforming FEM approaches.

Now we further simplify (5.3.11) to derive the *Discrete Shells* bending model proposed in [GHDS03]. A Taylor expansion of the function $f(\theta) = -2 \cos \frac{\theta + \pi}{2}$ about $\theta = 0$ yields $f(\theta) = \theta + O(\theta^3)$. Let $\mathbf{S}$ be a reference shell, *i.e.* the undeformed configuration. If we assume that we have an isometric[1] deformation $\Phi : \mathbf{S} \to \mathbb{R}^3$, *i.e.* $l_{\Phi(E)} = l_E$ and $d_{\Phi(E)} = d_E$, we obtain up to higher order terms

$$\int_{\mathbf{S}} \operatorname{tr} (B - B_\Phi \circ \Phi) \, \mathrm{d}a = \sum_{E \in \mathcal{E}} d_E \left(\frac{\theta_E - \theta_{\Phi(E)}}{d_E} l_E \right).$$

Again in the spirit of [MDSB02], one arrives at the *Discrete Shells* bending model by squaring the discrete density, *i.e.*

$$\mathbf{W}_{\mathrm{bend}}^{\mathrm{DS}}[\mathbf{S}, \tilde{\mathbf{S}}] = \sum_{E \in \mathcal{E}} \frac{(\theta_E - \theta_{\Phi(E)})^2}{d_E} l_E^2, \quad \tilde{\mathbf{S}} = \Phi(\mathbf{S}). \qquad (5.3.12)$$

Intuitively, $\mathbf{W}_{\mathrm{bend}}^{\mathrm{DS}}$ can be considered as a simplification of (5.3.9). Although (5.3.12) coincides exactly with the *Discrete Shells* bending energy introduced in [GHDS03], the authors in [GHDS03] derive their discrete bending energy by using results from [CSM03].
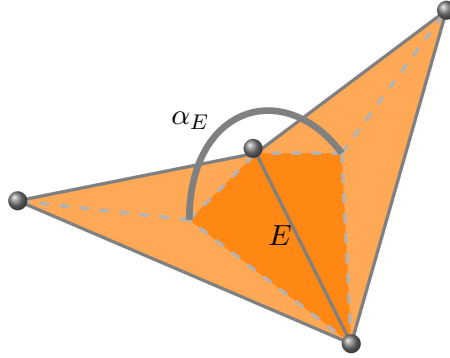
Figure 5.3: *Support of the* Discrete Shells *bending energy [GHDS03]; the dihedral angle $\theta_E = \alpha_E - \pi$ at an edge E is defined as the angle between adjacent triangle normals, where α_E is the angle between the two faces. The darker region represents the area d_E associated with E.*

---

[1] When deriving (discrete) bending models, one typically assumes to deal with *inextensible* materials which are characterized by mostly isometric deformations, *cf*. *e.g.* [GHDS03, BWH+06]. This corresponds to the analytic results presented in Sec. 5.1.2, where bending modes are of higher order and hence only decisive when the present deformation is (almost) isometric.

5.4 Numerical validation of discrete curvature functionals

In this section we validate our discrete shape operator and corresponding discrete curvature quantities empirically. Recall, that the mean curvature is defined as the trace of the shape operator.

What can be expected? In their work on discrete minimal surfaces Pinkall and Polthier [PP93] introduced the nowadays well-established *cotangent formula* that provides a discrete representation of the (integrated) mean curvature vector sitting at a vertex of the mesh (*cf.* also [Dzi88, Dzi91, DMSB99]). Their formula is derived from the discretization of the Dirichlet energy by linear FEM and employs the fact that the Laplace-Beltrami operator of the embedding represents the mean curvature vector. Following these lines, Wardetzky and co-workers [War06, War08, HPW06] established a convergence analysis for the discrete mean curvature vector in this *integrated* (functional) setup and show that there is in general no convergence for the corresponding *pointwise* mean curvature vector on general meshes. Indeed, pointwise convergence of curvatures cannot be expected in general: If normals could be approximated to order $O(h^2)$ then curvatures (corresponding to normal derivatives) could be approximated to order $O(h)$. However, unless one imposes extra assumptions on the underlying discrete data, normals are in general only known to order $O(h)$. In [HPW06] the authors provide conditions for convergence of polyhedral surfaces and their discrete geometric properties to smooth surfaces embedded in $\mathbb{R}^3$ in an appropriately chosen norm. For instance, it is shown that so-called *totally normal convergence*, *i.e.* convergence of surfaces in Hausdorff distance together with convergence of their normals in L^∞, suffices to ensure convergence of curvature operators, *e.g.* the mean curvature vector, in the H^{-1} norm, *i.e.* in an integrated or weak sense. Due to the famous *Schwarz lantern* example it is obvious that convergence of surfaces in Hausdorff distance is in general not sufficient and a notion of normal convergence is indeed required. Our empirical validation underlines these results as we observe convergence only in an integrated sense.

We validate our discrete shape operator and corresponding discrete curvature quantities on a discretization of the standard torus $\mathcal{S} = \mathcal{S}(a, b) \subset \mathbb{R}^3$ with radii $0 < a < b$, *i.e.* we use $b = 1$ and $a = 0.2$ in all examples below. The torus is parametrized by some parametrization $X : \Omega = [0, 2\pi]^2 \to \mathbb{R}^3$ with

$$X(u, v) = \begin{pmatrix} (b + a \cos v) \cos u \\ (b + a \cos v) \sin u \\ a \sin v \end{pmatrix}, \quad (u, v) \in \Omega. \tag{5.4.1}$$

Hence v parametrizes the inner circle of radius a and u parametrizes the outer circle with radius b. Furthermore, for the principal curvatures κ_1, κ_2 we have the expressions

$$\kappa_1(u, v) = \kappa_1(X(u, v)) = \frac{1}{a}, \quad \kappa_2(u, v) = \kappa_2(X(u, v)) = \frac{\cos v}{b + a \cos v}, \quad (u, v) \in \Omega,$$

as well as $\sqrt{\det g(u, v)} = a \, (b + a \cos v)$. In this section we denote the mean curvature by $h = \kappa_1 + \kappa_2$.

We consider different tesselations of Ω, see Fig. 5.4. Let $\mathbf{S} \subset \mathbb{R}^3$ be the discrete shell representing an approximation of the corresponding embedding, *i.e.* for a triangle $t \subset \Omega$ with nodes $(u_k, v_k) \in \Omega$, $k = 0, 1, 2$ the corresponding triangle $T \subset \mathbf{S}$ has nodes $X(u_k, v_k) \in \mathbf{S}$, $k = 0, 1, 2$. We define the curvature functional $\mathcal{C}(A)$ and the Willmore functional $\mathcal{W}(A)$, respectively, for some area $A \subset \Omega$ by

$$\mathcal{C}_\kappa(A) = \int_A \kappa(u, v) \sqrt{\det g(u, v)} \, du \, dv, \quad \mathcal{W}_\kappa(A) = \int_A h(u, v)^2 \sqrt{\det g(u, v)} \, du \, dv,$$

for $\kappa \in \{\kappa_1, \kappa_2, h\}$, where $h = \kappa_1 + \kappa_2$ denotes the mean curvature. Note that $\mathcal{C}_\kappa(A)$ and $\mathcal{W}_\kappa(A)$ can be computed explicitly.

Energy based on our triangle-averaged shape operator   The discrete curvature functional $\mathbf{C}(\mathbf{A})$ for some area $\mathbf{A} \subset \mathbf{S}$ is defined by

$$\mathbf{C}_\kappa^{\text{our}}(\mathbf{A}) = \int_\mathbf{A} \kappa \, \mathrm{d}x = \sum_{T \in \mathbf{A}} a_T \, \kappa_T \,,$$

$$\mathbf{W}_\kappa^{\text{our}}(\mathbf{A}) = \int_\mathbf{A} \mathrm{tr}\,(B)^2 \, \mathrm{d}x = \sum_{T \in \mathbf{A}} a_T \, h_T^2 \,,$$

where κ_T is induced by the elementwise constant discrete shape operator B_T as defined in (5.3.7). That means κ_T denotes the eigenvalues, *i.e.* the principal curvatures, or the mean curvature $h_T = \mathrm{tr}\,(B_T)$, respectively.

Hinge energy   The integrated curvature measures derived in [CSM03] were used in [GHDS03] to introduce a simple hinge-based bending energy, *cf*. Sec. 5.3.3. For comparison we will consider

$$\mathbf{C}_h^{\text{DS}}(\mathbf{S}) = \sum_{E \in \mathcal{E}} \theta_E \, l_E \,, \quad \mathbf{W}_h^{\text{DS}}(\mathbf{S}) = \sum_{E \in \mathcal{E}} \frac{\theta_E^2}{d_E} \, l_E^2 \,,$$

where $\mathbf{C}_h^{\text{DS}}$ is obtained by $\mathbf{C}_h^{\text{our}}$ by a Taylor expansion, *cf*. Sec. 5.3.3, and $\mathbf{W}_h^{\text{DS}}$ corresponds to the *Discrete Shells* bending energy as in (5.3.12).

Cotangent formula vertex energy   A notion of discrete mean curvature can be derived by FEM discretizations of the Laplace-Beltrami operator, which leads to the well-established *cotangent formula* [PP93, DMSB99]. Let $\{\phi_i\}_{1 \le i \le n}$ denote the standard piecewise linear FEM basis (*i.e.* hat functions) which are defined by $\phi_i(X_j) = \delta_{ij}$ and linear interpolation on triangles. The mass matrix $M \in \mathbb{R}^{n,n}$ is defined by $M_{ij} = \int \phi_i \phi_j \, \mathrm{d}x$ and the stiffness matrix $L \in \mathbb{R}^{n,n}$ by $L_{ij} = \int \nabla \phi_i \cdot \nabla \phi_j \, \mathrm{d}x$. Then one can write

$$L_{ij} = \frac{1}{2}\,(\cot \alpha_{ij} + \cot \beta_{ij})\,, \quad \text{for } i \sim j\,, \qquad L_{ii} = \sum_{j \sim i} L_{ij}\,,$$

where $j \sim i$ means that X_i and X_j share one edge $E = (i,j)$ and α_{ij} and β_{ij} denote the vertex angles opposite to the edge (i,j) in the two triangles adjacent to (i,j). The *integrated* mean curvature vector associated with a vertex $X_i \in \mathbf{S} \subset \mathbb{R}^{3n}$ is hence given by

$$\int_\mathbf{S} h N \phi_i \, \mathrm{d}x = (L\mathbf{S})_i = \frac{1}{2} \sum_{j \sim i} (\cot \alpha_{ij} + \cot \beta_{ij})(X_j - X_i)\,.$$

If one uses a lumped mass matrix, *i.e.* a diagonal matrix with diagonal entries a_i equal to the ith row sum of M, one can deduce a mean curvature vector $h_i N_i \in \mathbb{R}^3$ associated with vertex X_i and furthermore a notion of mean curvature $h_i = \|h_i N_i\|$ by

$$h_i^{\text{cot}} = \|h_i N_i\| = \|(M^{-1} L \mathbf{S})_i\| = \frac{1}{2 a_i} \left\| \sum_{j \sim i} (\cot \alpha_{ij} + \cot \beta_{ij})(X_j - X_i) \right\|\,.$$

In general, a_i can be any area associated with the node X_i, see [MDSB02] for several possible definitions. Based on the findings above one defines

$$\mathbf{C}_h^{\text{cot}}(\mathbf{S}) = \frac{1}{2} \sum_{i \in \mathcal{N}} \left\| \sum_{j \sim i} (\cot \alpha_{ij} + \cot \beta_{ij})(X_j - X_i) \right\|\,,$$

$$\mathbf{W}_h^{\text{cot}}(\mathbf{S}) = \sum_{i \in \mathcal{N}} a_i \left\| \frac{1}{2 a_i} \sum_{j \sim i} (\cot \alpha_{ij} + \cot \beta_{ij})(X_j - X_i) \right\|^2\,.$$

Note that the representation of the approximative Willmore energies $\mathbf{W}_h$ coincides with the different energies considered in [GGRZ06].

To prescribe the nodal positions on the torus we discretize $\Omega = [0, 2\pi]^2$ by a regular grid

$$\Omega_\delta = \{(i\delta_u, j\delta_v) : 0 \le i \le M, \, 0 \le j \le N\}$$

with gridsizes $\delta_u = 2\pi M^{-1}$ and $\delta_v = 2\pi N^{-1}$ for integers $M, N > 0$. In the default setting we want to obtain a triangulation of the torus with aspect ratio about 1 for all triangles. To this end we postulate $aM = bN$, if not stated otherwise. As we have chosen $a = 0.2$ and $b = 1$ in the torus parametrization (5.4.1), we get $M = b/a\, N = 5N$.

We might add noise to the grid, *i.e.* we distort the gridpoints by setting $((i + \sigma_i(\beta))\delta_u, (j + \sigma_j(\beta))\delta_v)$, where $\sigma(\beta)$ is a random number in $(-\beta, \beta)$. Since we add noise in the parameter domain it is always guaranteed that we are dealing with *inscribed* approximations, *i.e.* all nodes of the discrete shell lie on the (continuous) embedded torus. Hence this kind of distortion is referred to as *tangential* distortion resp. *tangential* noise in the following.
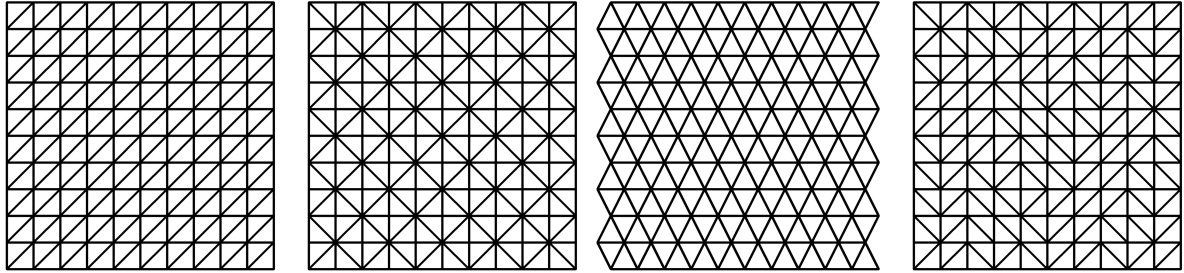
Figure 5.4: *Tesselations (with valences): regular (6), criss-cross (4+8), equilateral (6) and mixed (4-8) from left to right. Here we have used $M = N = 10$ and periodic boundary.*

The set of nodal positions of Ω_δ is triangulated in four different manners, as depicted in Fig. 5.4. In detail, we make use of a

- regular tesselation: all triangles are right-angled and all vertices have valence 6,
- criss-cross tesselation: all triangles are right-angled and vertices have either valence 4 or 8,
- equilateral tesselation: all triangles are equilateral and all vertices have valence 6,
- mixed tesselation: all triangles are right-angled and vertices have valences between 4 and 8.

Of course, the property of right-angled and equilateral triangles is lost as soon as one applies tangential distortion to the regular grid Ω_δ. The equilateral tesselation is also known as Schwartz lantern, if $X : \Omega \to \mathbb{R}^3$ is the parametrization of a cylinder. In particular, if $M/N^2 > c$ for a constant $c > 0$ and $M, N \to \infty$ the area (resp. the normals) of the discrete shell does not converge to the area (resp. the normals) of the continuous cylinder. The same phenomenon applies for the torus.

Our numerical convergence tests suggest that the eigenvalues of the elementwise constant, discrete shape operator $B = B_T$, *i.e.* the principal curvatures κ_1, κ_1, and therefore the mean curvature $h = \operatorname{tr} B = \kappa_1 + \kappa_2$, converge weakly to their continuous counterparts (*cf.* Fig. 5.5). Indeed, for all four tesselations and for $\kappa \in \{\kappa_1, \kappa_2, h\}$ we have

$$\epsilon_{\text{loc}}^{\text{our}} = \max_{t \subset \Omega} \left| \frac{\mathcal{C}_\kappa(t) - \mathbf{C}_\kappa^{\text{our}}(X(t))}{\mathcal{C}_\kappa(t)} \right| \to 0, \quad \text{if } M, N \to \infty,$$
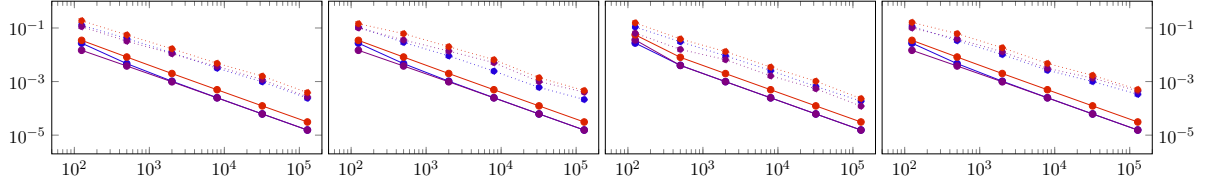
Figure 5.5: *Maximum local error ϵ_{loc}^{our} for integrated eigenvalues (blue and violet) as well as trace (red) of discrete shape operator. Left to right: Regular, criss-cross, equilateral and mixed tesselation of torus ($M = 5N$); dotted lines with tangential noise ($\beta = 0.5$).*

even if one applies a substantial amount of tangential noise (up to $\beta = 0.5$). Note that for $\beta > 0.5$ triangles are no longer guaranteed to be non-degenerated as gridpoints might overlap.

This represents the common results on convergence analysis of discrete curvatures as reported *e.g.* in [CSM03, HPW06], where one has shown convergence only in an integrated (*i.e.* weak) sense. For comparison, we also consider the relative error of the mean curvature functional, *i.e.*
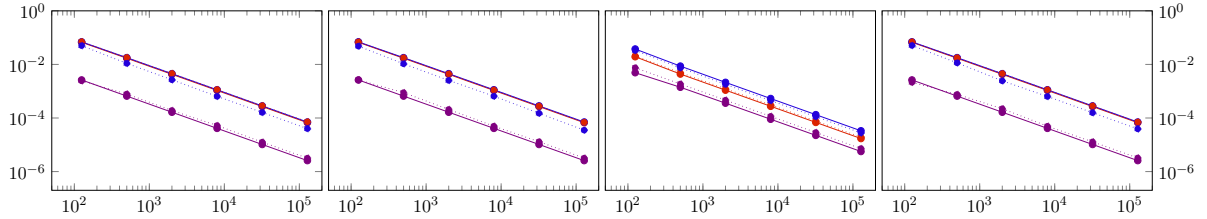
$$\epsilon^{\diamond} = \left| \frac{\mathcal{C}_h(\Omega) - \mathbf{C}_h^{\diamond}(\mathbf{S})}{\mathcal{C}_h(\Omega)} \right|$$

for all models $\diamond \in \{\text{our}, \text{DS}, \text{cot}\}$. In Fig. 5.6 we see that $\epsilon^{\diamond} \to 0$ if the number of vertices, which is of order $O(M \cdot N) = O(N^2)$, goes to infinity. This result holds for all four different tesselations and for tangential noise (up to $\beta = 0.5$).

Figure 5.6: *Relative error in mean curvature functional $\epsilon^{\diamond}$ with increasing number of vertices. Discrete shape operator (red), hinge energy (violet) and cotangent formula (blue); no tangential noise (solid lines) vs. tangential noise ($\beta = 0.5$, dotted lines). Left to right: Regular, criss-cross, equilateral and mixed tesselation of torus ($M = 5N$).*

Furthermore, the empirical (weak) convergence still holds if we deviate from the condition $M = 5N$, which corresponds to a moderate aspect ratio. Indeed, if we choose $M = 50N$ resp. $M = N/2$, which results in a very high aspect ratio, we still observe $\epsilon^{\diamond} \to 0$ as $M, N \to \infty$ for all models and for different tesselations, as shown in Fig. 5.7 resp. Fig. 5.8 (solid lines). If we additionally add tangential noise (Fig. 5.7 and Fig. 5.8, dotted lines) our energy and the hinge based energy outperfrom the energy based on the cotangent formula (if $M = N/2$).

Finally, we show by some further numerical experiments that one cannot aspect (strong) convergence of mean curvature in L^2 or even in L^{∞} in general. First, we consider the L^2-error of discrete mean curvatures $\kappa \in \{\kappa_1, \kappa_2, h\}$ induced by our discrete shape operator $B = B_T$, with $T = X(t)$ for some $t \subset \Omega$, *i.e.*

$$\epsilon_{L^2}^{\text{our}} = \sum_{t \subset \Omega} \int_t (\kappa(u,v) - \kappa_{X(t)})^2 \sqrt{\det g(u,v)} \, \mathrm{d}u \, \mathrm{d}v \,.$$

Fig. 5.9 reveals numerical convergence for $\kappa \in \{\kappa_1, \kappa_2, h\}$ and for all four different tesselations in the absence of tangential noise (solid lines). However, this is probably due to the fact that we have used very

Figure 5.7: *Relative error in mean curvature functional $\epsilon^{\diamond}$ with increasing number of vertices. Discrete shape operator (red), hinge energy (violet) and cotangent formula (blue). Left to right: Regular, crisscross, equilateral and mixed tesselation of torus ($M = 0.5N$), dotted line with tangential noise ($\beta = 0.5$), as depicted in bottom row.*
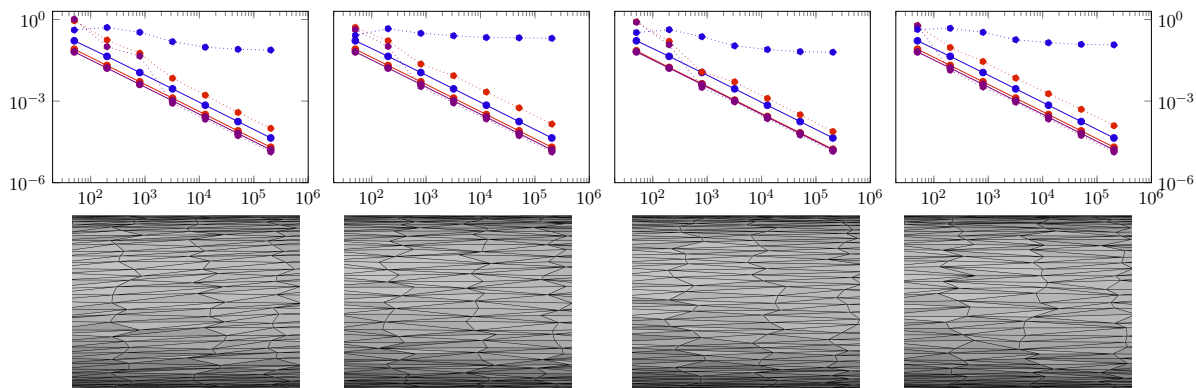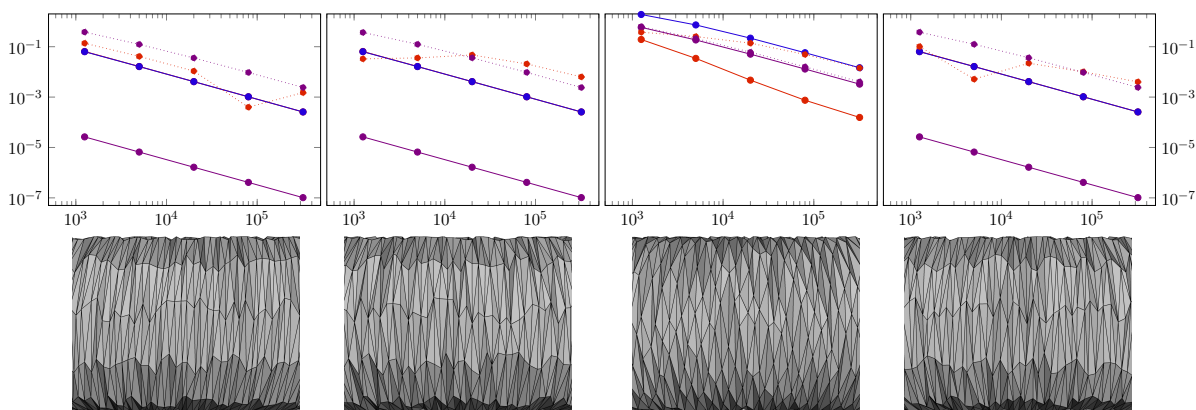

Figure 5.8: *Relative error in mean curvature functional $\epsilon^{\diamond}$ with increasing number of vertices. Discrete shape operator (red), hinge energy (violet) and cotangent formula (blue). Left to right: Regular, crisscross, equilateral and mixed tesselation of torus ($M = 50N$), dotted line with tangential noise ($\beta = 0.5$), as depicted in bottom row.*

regular tesselations, which is emphasized by the failure of convergence already for very little tangential noise (Fig. 5.9, dotted lines). This reproduces the results in the form of counterexamples given *e.g.* in [HPW06].

The same behaviour can be observed if one computes the relative error of the discrete Willmore functional, *i.e.*

$$\epsilon_{\mathcal{W}}^{\diamond} = \left| \frac{\mathcal{W}_h(\Omega) - \mathbf{W}_h^{\diamond}(\mathbf{S})}{\mathcal{W}_h(\Omega)} \right| ,$$

as shown in Fig. 5.10. Again, in the absence of tangential noise we observe numerical convergence for all three models (solid lines). However, the convergence fails already for very little tangential distortion (dotted lines). Here we have used the torus (equilateral tesselation, $M = 5N$) as well as an inscribed approximation of the unit sphere (*cf*. Fig. 5.10, right).
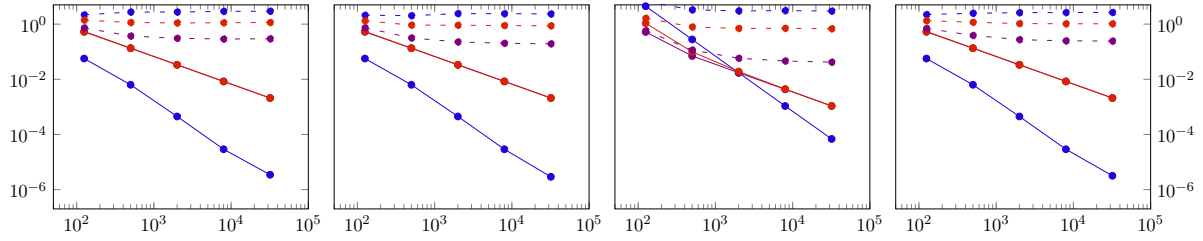
Figure 5.9: L^2-error for eigenvalues (blue and violet) as well as trace (red) of discrete shape operator with increasing number of vertices, subject to no tangential noise (solid) and tangential noise ($\beta = 0.1$, dashed). Left to right: Regular, criss-cross, equilateral and mixed tesselation of torus.
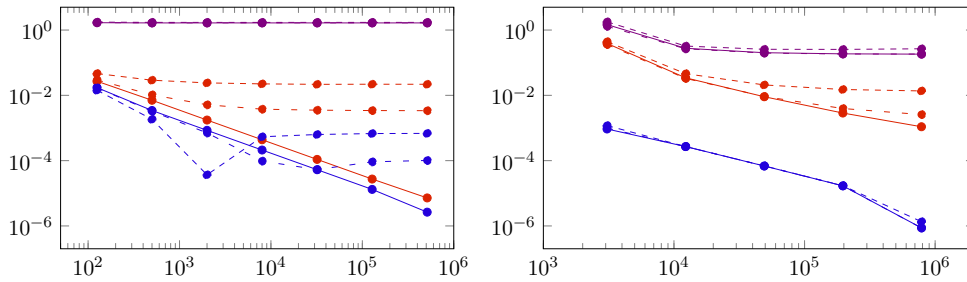
Figure 5.10: Relative error $\epsilon_{\mathcal{W}}^{\diamond}$ for Willmore energy with increasing number of vertices based on discrete shape operator (red), hinge energy (violet) and cotan formula (blue). Computations were performed on torus (left; equilateral, $M = 5N$) and unit sphere (right) and with different amount of tangential noise, i.e. $\beta = 0$ (solid), $\beta = 0.1$ (loosely dashed), $\beta = 0.25$ (densely dashed). The relative error for the hinge energy is less than 3%.

The failure of convergence, or less dramatically the dependence on the mesh, has also been studied in [GGRZ06]. In detail, Grinspun *et al.* [GGRZ06] investigate several different notions of discrete mean curvature, including the three models considered here. In particular, they propose an extended and improved version of our discrete shape operator, that is not based on edge normals defined as averaged triangle normals, *cf.* Sec. 5.3.2. Indeed, one can admit the angle of rotation of an edge normal N_E about the edge E as an additional degree of freedom, whereas this angle is prescribed in our definition. Allowing these additional degrees of freedom induces a discrete shape operator and a notion of discrete mean curvature, respectively, that seems to result in a consistent approximation of the Willmore functional.

6 Time-discrete geodesic calculus in the space of discrete shells

Based on the work by Rumpf and Wirth [Wir09, WBRS11, RW15], we have presented a comprehensive time-discrete geodesic calculus for generic Riemannian manifolds in chapter 4. In particular, this calculus is built on a dissimilarity measure that is supposed to approximate the squared Riemannian distance locally. Furthermore, we have deduced a physically sound dissimilarity measure for the space of shells given by the combination of a *membrane energy* and a *bending energy* in chapter 5. While the former one was easy to translate to a spatially discretized setting, the spatial discretization of the latter one required a non-conforming approach and incorporates ideas from *Discrete Differential Geometry*.

In this chapter we apply the time-discrete geodesic calculus to the space of discrete shells represented as triangle meshes with fixed connectivity. The dissimilarity measure, *i.e.* the core ingredient of the calculus, is precisely given by the sum of the discrete membrane and the discrete bending energy. Time-discrete geodesics are then obtained by transferring the notion of the discrete path energy to the discrete shell space. The definition of further discrete geometric objects are obtained analogously.

The chapter is organized as follows. In Sec. 6.1 we comment on the physical interpretation of the variational time-discretization, *i.e.* the optimization of the time-discrete path energy, which is built on elastic energies. Additionally, we prove that the Hessian of generic elastic shell energies induces indeed a Riemannian metric on the space of shells. In Sec. 6.2 we show applications of time-discrete geodesic calculus in the space of discrete shells, *e.g.* for shape interpolation and extrapolation and for detail transfer. In particular, we investigate the convergence behaviour empirically, which has been predicted by analytical results in Sec. 4.2.2. We report on several issues concerning an efficient implementation and optimization in Sec. 6.3 and give a final discussion as well as an outlook for future work in Sec. 6.4.

To keep this section self-contained, we state the definition of time-discrete geodesics in shell space:

Definition 6.0.1 (Time-discrete geodesic in the space of shells). Given two shells $\mathcal{S}_A$ and $\mathcal{S}_B$ we refer to the minimizer $(\mathcal{S}_0, \mathcal{S}_1, \ldots, \mathcal{S}_K)$ of the *time-discrete path energy*

$$E^K[\mathcal{S}_0, \ldots, \mathcal{S}_K] = K \sum_{k=1}^{K} \mathcal{W}[\mathcal{S}_{k-1}, \mathcal{S}_k], \quad \mathcal{W}[\mathcal{S}, \tilde{\mathcal{S}}] = \min_{\phi : \phi(\mathcal{S}) = \tilde{\mathcal{S}}} \mathcal{W}_{\mathcal{S}}[\phi], \qquad (6.0.1)$$

with $\mathcal{S}_0 = \mathcal{S}_A$ and $\mathcal{S}_K = \mathcal{S}_B$ as a *time-discrete geodesic*, where $\mathcal{W}_{\mathcal{S}}$ has been defined in (5.1.15).

We refer to Rem. 5.1.2 for a comment on the well-definedness of $\mathcal{W}[\mathcal{S}, \tilde{\mathcal{S}}]$. Next, we recall the discrete deformation energies derived in Sec. 5.3 to define a dissimilarity measure on the space of discrete shells:

Definition 6.0.2 (Discrete energies). Given two discrete shells $\mathbf{S} = (\mathcal{N}, \mathcal{T}, \mathcal{E})$ and $\tilde{\mathbf{S}} = (\tilde{\mathcal{N}}, \tilde{\mathcal{T}}, \tilde{\mathcal{E}})$ that are in dense correspondence, *i.e.* there is a unique affine deformation Φ with $\tilde{\mathbf{S}} = \Phi(\mathbf{S})$. The *discrete deformation energy* $\mathbf{W} = \mathbf{W}_{\mathbf{S}}[\Phi] = \mathbf{W}[\mathbf{S}, \tilde{\mathbf{S}}]$ is defined by

$$\mathbf{W}[\mathbf{S}, \tilde{\mathbf{S}}] = \mathbf{W}_{\text{mem}}[\mathbf{S}, \tilde{\mathbf{S}}] + \eta \, \mathbf{W}_{\text{bend}}[\mathbf{S}, \tilde{\mathbf{S}}],$$

where the *bending weight* $\eta = \delta^2$ represents the squared thickness of the shell. The *discrete membrane energy* and the *discrete bending energy*, respectively, are given by

$$\mathbf{W}_{\text{mem}}[\mathbf{S}, \tilde{\mathbf{S}}] = \sum_{T \in \mathcal{T}} a_T \cdot W_{\text{mem}}(\mathcal{G}[\Phi]|_T) \,,$$

$$\mathbf{W}_{\text{bend}}[\mathbf{S}, \tilde{\mathbf{S}}] = \sum_{T \in \mathcal{T}} a_T \cdot W_{\text{bend}}(B_T - B_{\Phi(T)}) \,,$$

where $\mathcal{G}[\Phi] \in \mathbb{R}^{2,2}$ denotes the discrete distortion tensor defined in (5.3.2) and $B \in \mathbb{R}^{2,2}$ the matrix representation of the discrete shape operator defined in (5.3.7). The membrane density W_{mem} and the bending density W_{bend}, respectively, are defined as

$$W_{\text{mem}}(A) = \frac{\mu}{2} \operatorname{tr} A + \frac{\lambda}{4} \det A - \left(\mu + \frac{\lambda}{2} \right) \log \det A - \mu - \frac{\lambda}{4} \,,$$

$$W_{\text{bend}}(A) = \alpha (\operatorname{tr} A)^2 + (1 - \alpha) \operatorname{tr} (A^2) \,, \quad \alpha \in \{0, 1\} \,.$$

For $\alpha = 1$, a simplification leads to the *Discrete Shells* bending energy [GHDS03], *cf.* Sec. 5.3.3, *i.e.*

$$\mathbf{W}_{\text{bend}}^{\text{DS}}[\mathbf{S}, \tilde{\mathbf{S}}] = \sum_{E \in \mathcal{E}} \frac{(\theta_E - \theta_{\Phi(E)})^2}{d_E} l_E^2 \,.$$

In analogy to Def. 6.0.1 this leads to the notion of time-discrete geodesics in the space of *discrete* shells:

Definition 6.0.3 (Time-discrete geodesic in the space of discrete shells)**.** Given two discrete shells $\mathbf{S}_A, \mathbf{S}_B \in \mathcal{M} = \mathbb{R}^{3n}$ we refer to the minimizer $(\mathbf{S}_0, \mathbf{S}_1, \ldots, \mathbf{S}_K)$ of the *time-discrete path energy*

$$\mathbf{E}^K[\mathbf{S}_0, \ldots, \mathbf{S}_K] = K \sum_{k=1}^{K} \mathbf{W}[\mathbf{S}_{k-1}, \mathbf{S}_k] \,, \tag{6.0.2}$$

with $\mathbf{S}_0 = \mathbf{S}_A$ and $\mathbf{S}_K = \mathbf{S}_B$, as a *time-discrete geodesic*.

The variational formulation of the time-discrete geodesics leads to the following necessary optimality conditions:

$$0 = \partial_{\mathbf{S}_k} \mathbf{E}^K[\mathbf{S}_0, \ldots, \mathbf{S}_K] \,, \quad k = 1, \ldots, K - 1 \,,$$

$$\Longleftrightarrow \quad 0 = \partial_2 \mathbf{W}[\mathbf{S}_{k-1}, \mathbf{S}_k] + \partial_1 \mathbf{W}[\mathbf{S}_k, \mathbf{S}_{k+1}] \,, \quad k = 1, \ldots, K - 1 \,, \tag{6.0.3}$$

where $\partial_i \mathbf{W}$ refers to the variation with respect to the ith argument of $\mathbf{W}$. Note that for a functional $F = F[X]$ we make use of the notation

$$0 = \partial_X F[X] \quad :\Leftrightarrow \quad 0 = \frac{d}{dt} (F[X + tV]) \Big|_{t=0} \quad \forall V \in \mathcal{X} \,,$$

where the test directions V live in a suitable test space $\mathcal{X}$, which is simply $\mathcal{X} = \mathbb{R}^{3n}$ if we consider variations of discrete shell energies. To compute time-discrete geodesics we have to solve the system of nonlinear equations (6.0.3) simultaneously, where we fix the two end shapes $\mathbf{S}_0$ and $\mathbf{S}_K$.

6.1 Physics and geometry

In the previous chapter we have introduced elastic energies induced by a thin shell deformation. Here we discuss the connection to a *viscous dissipation model*, *cf*. Sec. 3.2. While nonlinear elasticity is based on the stored potential energy of reversible deformations, viscous dissipation models depend on irreversible energy conversion into heat during a deformation. Despite this conceptual difference, a viscous deformation may be seen as the limit of many infinitesimally small elastic deformations with subsequent stress relaxation [Wir09]. The coupling of both concepts is the motivation of the variational time-discretization from a physical point of view. Furthermore, it leads to a physical justification of deformation paths based on consecutive elastic deformations despite the fundamental axiom of elasticity which prevents the notion of paths. In particular, this resulting formulation coincides with Rayleigh's paradigm [Ray96], where the dissipation density is given by the second derivative of an elastic energy density at the identity. According to this, we eventually show that the Hessian of the (discrete) elastic energy defined above induce a well-defined Riemannian metric on the space of (discrete) shells.

6.1.1 Elastic vs. viscous formulation

Here we report on an interpretation of the variational time-discretization of geodesics from a physical point of view (see [Wir09, WBRS09, WBRS11, RW11b] for details). The framework of elastic deformations does not provide a natural notion of paths between two shapes: due to the fundamental axiom of elasticity, the state and energy of an elastically deformed object is completely independent of the path along which this final configuration was reached. Moreover, a nonlinear elastic deformation energy is in general neither symmetric nor does it satisfy the triangle inequality, hence it will not induce a metric distance[1].

A physically different concept is the approach of viscous deformations (*cf*. Sec. 3.2). To this end, the distance between two shapes is based on viscous dissipation, *i.e.* the conversion of energy into heat due to internal friction between particles, induced by the deformation of one into the other.

From a physical point of view, shells are three-dimensional materials which are only described mathematically by a two-dimensional surface. Hence the viscous dissipation model (*cf*. Sec. 3.2) can also be applied to the space of shells $\mathcal{M}$. Let $\mathcal{S}$ be a smooth surface embedded into $\mathbb{R}^3$ and let $\mathcal{S}^\delta$ denote the corresponding material around $\mathcal{S}$, where δ denotes a scale parameter that reflects the physical thickness of the shell. Consider now a family $(\psi_t)_{0 \leq t \leq 1} : \mathcal{S}^\delta \to \mathbb{R}^3$ of diffeomorphisms with $\psi_0 = \mathrm{Id}$. Then ψ_t generates a deformation path $\psi_t(\mathcal{S}^\delta)$ of an initial shell $\mathcal{S}^\delta$. If we suppose that shells were made of a *viscous* material, then such a deformation would lead to viscous friction within the shell's volume. The density of this viscous friction—which represents precisely the viscous dissipation—can be described as a *quadratic* function $\mathrm{diss}[v_t] = \mathrm{diss}(\epsilon[v_t])$ of the symmetrized gradient $\epsilon[v_t]$ of the corresponding Eulerian flow field $v_t = \dot{\psi}_t \circ \psi_t^{-1}$. For instance, in a Newtonian fluid, the local dissipation rate reads

$$\mathrm{diss}[v] = \frac{\lambda}{2} (\mathrm{tr}\,(\varepsilon[v]))^2 + \mu \mathrm{tr}\,((\varepsilon[v])^2)\,,$$

as seen in Sec. 3.2. This approach imposes a Riemannian structure on $\mathcal{M}$ where the metric g at a point $\mathcal{S}^\delta$ is given by the viscous dissipation rate

$$g_{\mathcal{S}^\delta}(v, v) = \int_{\mathcal{S}^\delta} \mathrm{diss}[v]\, \mathrm{d}x\,. \tag{6.1.1}$$

---

[1] Nevertheless, the elastic setup is particularly appropriate when we are interested in unidirectional comparisons of a number of shapes with one single distinguished shape, for instance when computing an elastic average of a whole set of input shapes as it will be done in Sec. 7.3.

Here the velocity field v represents a tangent vector at $\mathcal{S}^\delta$. This leads to a natural setting to find (optimal) paths between shapes, *i.e.* geodesics with respect to the metric (6.1.1), by minimizing

$$\mathcal{E}[(\psi_t)_{0 \le t \le 1}] = \int_0^1 \int_{\psi_t(\mathcal{S}^\delta)} \operatorname{diss}[v_t] \, \mathrm{d}x \, \mathrm{d}t \,, \qquad (6.1.2)$$

which represents exactly the path energy. Furthermore, a distance between any two shapes is then defined as the minimum path length of a connecting geodesic, which in particular fulfills characteristic properties such as symmetry and triangle inequality.

The missing concepts of *paths*—and hence the lack of measurable path length—in the elasticity-based shape space has the effect that the shape space is in general not metrisable. Moreover, an elastic deformation energy is neither symmetric nor does it satisfy the triangle inequality. Both properties only hold in the limit of infinitesimal deformations, the regime of linearized elasticity, where the elastic energy is essentially quadratic. However, this fact provides a hint to the connection between the elastic and the viscous perspective: a viscous deformation may be seen as the limit of many infinitesimally small elastic deformations with subsequent stress relaxation. This relation describes the physical motivation of the variational time-discretization of geodesic paths in an elastic shape space, where a geodesic is discretized by minimizing a sum of elastic energies between consecutive shapes along a time-discrete path, *cf*. Def. 6.0.1. To this end, we illustrate in the following that the resulting *discrete* geodesics are indeed a consistent approximation within a viscous dissipation model (*cf*. [Wir09]). In particular, one can recover the viscous fluid model for vanishing time step size. Additionally, this connection recovers Rayleigh's paradigm [Ray96], where one derives viscous dissipation models from elastic energies by replacing elastic strains by *strain rates*.

We make use of the notation $\mathcal{S}_k^\delta = \psi_{t_k}(\mathcal{S}^\delta)$ with $t_k = k\tau$ for $k = 0, \ldots, K$ and $\tau = K^{-1}$. Moreover, let $\phi_k : \mathcal{S}_{k-1}^\delta \to \mathcal{S}_k^\delta$ be a matching deformation and $\mathcal{W}_{\mathcal{S}_{k-1}^\delta}[\phi_k] = \int_{\mathcal{S}_{k-1}^\delta} W(D\phi_k) \, \mathrm{d}x$ the corresponding elastic energy. It has been shown in [Wir09, Sec.6.2.3], that the time-discrete path energy $E^K = K \sum_{k=1}^K \mathcal{W}_{\mathcal{S}_{k-1}^\delta}[\phi_k]$ is consistent, *i.e.* it turns into the time-continuous dissipation functional

$$\mathbf{Diss}[(v_t)_{0 \le t \le 1}] = \int_0^1 \int_{\psi_t(\mathcal{S}^\delta)} \frac{1}{2}\lambda(\operatorname{tr}\epsilon[v_t])^2 + \mu\operatorname{tr}\left(\epsilon[v_t]^2\right) \, \mathrm{d}x \, \mathrm{d}t \,, \qquad (6.1.3)$$

for $K \to \infty$. We set $v_k = \frac{1}{\tau}(\phi_k - \mathrm{id})$ and apply a second order Taylor expansion:

$$W(D\phi_k) = W(\mathbb{1} + \tau Dv_k) = W(\mathbb{1}) + \tau W_{,A}(\mathbb{1}) : Dv_k + \frac{\tau^2}{2}W_{,AA}(\mathbb{1})Dv_k : Dv_k + O(\tau^3) \,.$$

Note that the energy density W attains its minimum 0 at the identity, hence $W_{,A}(\mathbb{1}) = 0$. Furthermore, the rigid body motion invariance of W implies $W_{,AA}(\mathbb{1})A = 0$ for all skew-symmetric matrices $A \in \mathbb{R}^{d \times d}$ and thus $W_{,AA}(\mathbb{1})Dv : Dv = W_{,AA}(\mathbb{1})\epsilon[v] : \epsilon[v]$. According to Sec. 3.2 we may now choose the deformation energy density W in such a way that we obtain

$$W_{,AA}(\mathbb{1})\epsilon[v] : \epsilon[v] = \lambda(\operatorname{tr}\epsilon[v])^2 + 2\mu\operatorname{tr}\left(\epsilon[v]^2\right)$$

for given parameters λ and μ. Collecting the results above we finally obtain

$$E^K = K\sum_{k=1}^K \int_{\mathcal{S}_{k-1}^\delta} W(D\phi_k) \, \mathrm{d}x = \left(K\sum_{k=1}^K \int_{\mathcal{S}_{k-1}^\delta} \frac{\tau^2}{2}W_{,AA}(\mathbb{1})Dv_k : Dv_k \, \mathrm{d}x\right) + O(\tau) \,,$$

i.e. in the limit $K \to \infty$ (*i.e.* $\tau \to 0$) we recover the desired dissipation integral (6.1.3). Furthermore, the resulting Riemannian metric, given by the dissipation rate (6.1.1), is associated with the Hessian of

the nonlinear deformation energy. This representation coincides with Rayleigh's formulation [Ray96], where the dissipation density is given by the second derivative of an elastic energy density at the identity.

Hence one may conclude that the variational time-discretization is indeed consistent with the time-continuous viscous dissipation model of geodesic paths. The total energy dissipation (6.1.3), *i.e.* the *accumulated* viscous friction along the deformation path, is exactly given by (6.1.2) and properly approximated by the discrete path energy $K \sum_{k=1}^{K} \mathcal{W}_{\mathcal{S}_{k-1}^{\delta}}[\phi_k]$, *i.e.* the sum of elastic deformation energies. In particular, geodesics in shell space correspond to paths of *least energy dissipation*.

Remark 6.1.1. As already shown in [Wir09, WBRS11, RW11b], the variational time-discretization fulfills a series of desired properties. For example, a rigid body motion invariance is inherited from the elastic matching problems. In contrast, a straightforward linear time-discretization of the motion field v_t in (6.1.2) does not ensure such an invariance; we refer to [Wir09, Sec.6.2] for a comprehensible illustration. Furthermore, the variational time-discretization allows to approximate geodesics with only few intermediate shapes and is particularly usefull to be combined with an efficient multiscale approach.

6.1.2 On the metric

From Sec. 4.2.2 we know that one can expect convergence of a time-discrete geodesic to a continuous geodesic with respect to a particular metric. However, the convergence result is subject to strong assumptions on the manifold and the underlying metric and we do not show that these assumptions hold for the space of shells. Nevertheless, we will show that the Hessian of the elastic deformation energy induces a Riemannian metric on the space of shells, both in the (spatially) smooth and discrete setup.

Metric on the space of smooth shells   First, we state the theorem on the non-degeneracy of the smooth Hessian, which has been proved in [HRS$^+$14][1]. For the Theorem we consider a slight modification of the elastic energy (5.1.15), *i.e.* we define

$$\mathcal{W}_{\mathcal{S}}[\phi] = \int_{\mathcal{S}} W(g - g_\phi^*) + \eta \, W(h - h_\phi^*) \, \mathrm{d}a \,,$$

with g, h being the first and second fundamental forms, respectively, of the undeformed surface, and g_ϕ^*, h_ϕ^* being the pulled back forms of the deformed surface (see [HRS$^+$14] for details). For the density W we require that (i) $W(0) = 0$, (ii) $dW = 0$ at the zero matrix, and (iii) d^2W is positive definite at the zero matrix. These requirements correspond to the fact that if the shell is in a stress free configuration, then the deformation id is a minimizer of $\mathcal{W}_{\mathcal{S}}$ and thus (i) $\mathcal{W}_{\mathcal{S}}[\mathrm{id}] = 0$ and (ii) $d\mathcal{W}_{\mathcal{S}}[\mathrm{id}] = 0$. Additionally, we assume (iii) that the energy is strictly convex (modulo rigid body motions) in a neighbourhood of a minimizer. These assumptions capture most thin elastic materials [Cia00] and a typical choice is the squared Frobenius norm $W(A) = \|A\|_F^2$.

Theorem 6.1.2 (Non-degeneracy of smooth Hessian)**.** *Let $\mathcal{M}$ denote the space of smooth shells. For V a tangent vector field to $\mathcal{M}$ at some smooth $\mathcal{S} \in \mathcal{M}$, $\mathrm{Hess}(\mathcal{W}_{\mathcal{S}})(V, V) = 0$ if and only if V induces an infinitesimal rigid motion. Consequently, $g_{\mathcal{S}}(V, W) = \frac{1}{2}\mathrm{Hess}(\mathcal{W}_{\mathcal{S}})(V, W)$ is indeed a Riemannian metric on the space of smooth shells modulo infinitesimal rigid body motions.*

For the proof we refer to the appendix of [HRS$^+$14]. Note that in general the Hessian $\mathrm{Hess}(f) = \nabla(df)$ of a function $f : \mathcal{M} \to \mathbb{R}$ depends on the choice of a Riemannian metric through the covariant derivative ∇. Thus in general it is meaningless to define a Riemannian metric as the Hessian of a function without presuming such a metric to be given. However, at a critical point of a function (*i.e.* a point where $df = 0$), the Hessian $\mathrm{Hess}(f)$ is *independent* of the choice of metric [Mil63]. This is our setting since a given shell is the minimizer of its elastic energy.

---

[1] The proof was essentially done by Max Wardetzky and Benedikt Wirth.

Metric on the space of discrete shells   Now we consider the space of discrete shells $\mathcal{M} = \mathbb{R}^{3n}$ given by triangulated surfaces. Then for $\mathbf{S} \in \mathcal{M}$ we have $T_{\mathbf{S}}\mathcal{M} = \mathbb{R}^{3n}$. According to Def. 6.0.2, we define $\mathbf{W}_{\mathbf{S}}[\tilde{\mathbf{S}}] = \mathbf{W}_{\mathrm{mem}}[\mathbf{S}, \tilde{\mathbf{S}}] + \eta\,\mathbf{W}_{\mathrm{bend}}^{\mathrm{DS}}[\mathbf{S}, \tilde{\mathbf{S}}]$, for $\mathbf{S}, \tilde{\mathbf{S}} \in \mathcal{M}$, where $\mathbf{W}_{\mathrm{bend}}^{\mathrm{DS}}$ denotes the *Discrete Shells* bending energy [GHDS03]. We have shown in [HRS$^+$14]:

Theorem 6.1.3 (Non-degeneracy of discrete Hessian). *Let* $\mathbf{S} \in \mathcal{M}$, *with* $\mathcal{M} = \mathbb{R}^{3n}$, *and* $\mathbf{V} \in T_{\mathbf{S}}\mathcal{M}$. *Then* $\mathrm{Hess}\mathbf{W}_{\mathbf{S}}[\mathbf{S}](\mathbf{V}, \mathbf{V}) = 0$ *if and only if* $\mathbf{V}$ *induces an infinitesimal rigid motion. Consequently,* $g_{\mathbf{S}}(\mathbf{V}, \mathbf{W}) = \frac{1}{2}\mathrm{Hess}\mathbf{W}_{\mathbf{S}}[\mathbf{S}](\mathbf{V}, \mathbf{W})$ *is a Riemannian metric on the space of discrete shells modulo rigid body motions.*

Proof. Suppose that $\mathrm{Hess}\mathbf{W}_{\mathbf{S}}[\mathbf{S}](\mathbf{V}, \mathbf{V}) = 0$ for some vector field $\mathbf{V}$ sitting at the vertices. Then $\mathbf{V}$ is both in the kernel of the Hessian of discrete membrane energy and the Hessian of discrete bending energy since both are positive semi-definite operators. Consider two adjacent triangles T_1 and T_2. After subtracting global translations induced by $\mathbf{V}$, for $\mathbf{V}$ to be in the kernel of the Hessian of membrane energy implies that $\mathbf{V}$ induces an infinitesimal rotation of T_1 since the edge lengths of T_1 must not change. The same holds for T_2. Since $\mathbf{V}$ is also in the kernel of the Hessian of bending energy, it follows that $\mathbf{V}$ must not induce a change of the dihedral angle between T_1 and T_2. Hence $\mathbf{V}$ induces a single infinitesimal rotation of the hinge $T_1 \cup T_2$. Iterating this argument over the entire mesh proves the claim. $\square$

6.2 Exploring the geometry of the space of shells

In this section we show results of the time-discrete geodesic calculus applied to the space of discrete shells. In Sec. 6.2.1 and Sec. 6.2.2, respectively, we discuss the impact of the physical model parameters and report on features such as a lack of symmetry and non-uniqueness of geodesic paths. Furthermore, we apply the definition of other time-discrete geometric objects—such as a discrete notion of logarithm, exponential map and parallel transport—as derived in Sec. 4.2.2 on generic Riemannian manifolds, to the space of discrete shells. In Sec. 6.2.3 resp. Sec. 6.2.4, we show their usefulness in applications as *e.g.* extrapolation method or tool to realize a nonlinear detail transfer. Finally, we report on empirical convergence tests in Sec. 6.2.5.

Remark 6.2.1. The results of this section are partly joint work with Martin Rumpf, Peter Schröder, Max Wardetzky and Benedikt Wirth, and have been published in [HRWW12] and [HRS$^+$14].

6.2.1 Natural regularization and physical tuning

First, we discuss the physical parameters of our model and point out that our framework effortlessly allows a physically based tuning of "best" paths between shells. The choice of physics-based deformation energies offers several advantages. Due to everyday experience, physical models come close to human intuition so that our framework tends to lead to intuitive discrete geodesic paths. In particular, along a discrete path one can separate bending from stretching effects. The former especially play an important role for near-isometric deformations (see Fig. 6.1), an ubiquitous case in applications. Here, the energy dissipation due to bending serves as the proper path selection mechanism. In the following, we discuss the impact of the physical parameters in detail. Obviously, the parameters η, λ, μ in our deformation energy have a physical interpretation and can be adjusted to change the typical behavior of shells.
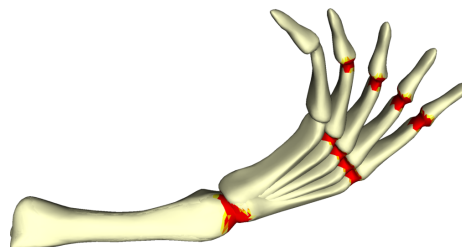
Figure 6.1: *Discrete geodesic* ($\eta = 10^{-4}$) *representing the motion of a finger (all shells superimposed), color-coded by dissipation rate (low ▬ high).*

Figure 6.2: Almost isometric geodesic between two hemispheres with fixed rim ($\eta = 10^{-4}$).

As discussed previously, the bending weight η represents the approximate squared thickness δ^2 of the shell, a measure of resistance against bending: On the one hand geodesics with low η allow for crumpling (Fig. 6.2), and if the initial and final shell are near-isometric, this property is approximately maintained for intermediate shells during the deformation.
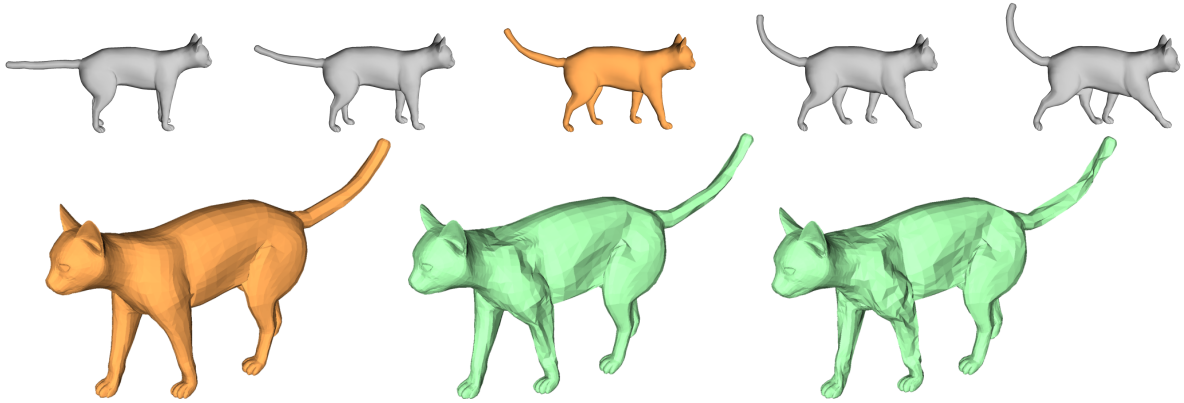
Figure 6.3: The bending term serves as a natural regularization; there is no need for artificial regularizers as in [KMP07] (top row, $\eta = 0.8$). Decreasing η leads to the occurance of creases until the underlying matching deformations are finally only as-isometric-as-possible (bottom, left to right: intermediate shape of a geodesic with $\eta = 0.8, 0.01, 0.0001$).

On the other hand, a larger value of η prevents crumpling (Fig. 6.3), which is especially desired in applications where one expects smooth intermediate shapes if the end poses are smooth. Hence the parameter η may also be seen as the *natural regularization* parameter and there is no need for artificial regularizers as it was used in [KMP07]. The parameters λ and μ represent the respective resistance against area and length changes, whose relative magnitudes also influence the appearance of discrete geodesics: In the previous examples we have pointed out that area compression can be avoided by out-of-plane buckling (*i.e.* crumpling) for sufficiently small bending resistance. This can also be seen in Fig. 6.4 (bottom) where a high ratio $\mu/\lambda = 20$ of shear to dilation resistance leads to the formation of loops. An alternative effect occurs for a low ratio $\mu/\lambda = 1/20$ between shearing and dilation resistance, which allows for a simultaneous shell contraction in one and extension in the opposite direction (Fig. 6.4 top). Note that the central constriction of the intermediate shells is found as a means to reduce the bending resistance locally. However, the tuning of the parameters λ and μ is rather of theoretical interest, hence we will set $\lambda = \mu = 1$ in all subsequent experiments.
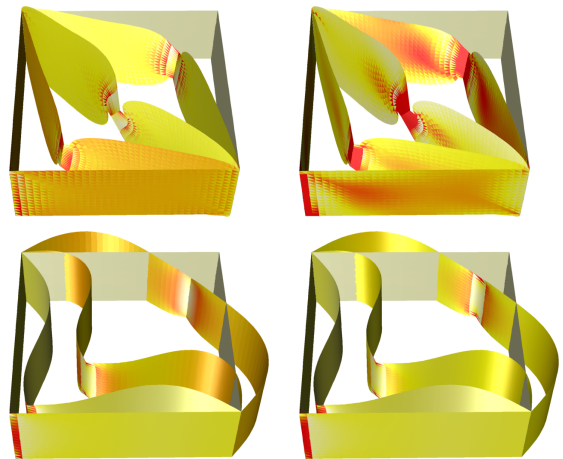
Figure 6.4: Discrete geodesics between two bracket shapes with fixed rim (all shapes superimposed), color-coded by $\det \mathcal{G}[\Phi]$ (left, $0 \blacksquare 1.5$) and $\operatorname{tr} \mathcal{G}[\Phi]$ (right, $0 \blacksquare 2.5$).

Finally, we show that the bending parameter η is not only a regularization weight but can also be used to manipulate the visual appearance of the deformation path. In particular, it can be used to simulate different physical materials, such as paper, aluminum foil, rubber, cloth or metal and corresponding optimal deformation paths, *i.e.* geodesics, are perfectly consistent with the intuitively optimal way to deform such a material. As already discussed above, a low bending parameter η induces almost isometric deformation paths. In Fig. 6.5 (top) this leads to the effect that the handle is folded in order to be pushed through the outer frame. On the other hand, a larger η prevents folding at the cost of involving a fair amount of tangential stretching of the outer frame resp. compression of the handle (Fig. 6.5, bottom). Hence the physical behaviour of the deformation reminds either of a thin metal sheet (Fig. 6.5, top) or of a material made of rubber (Fig. 6.5, bottom).
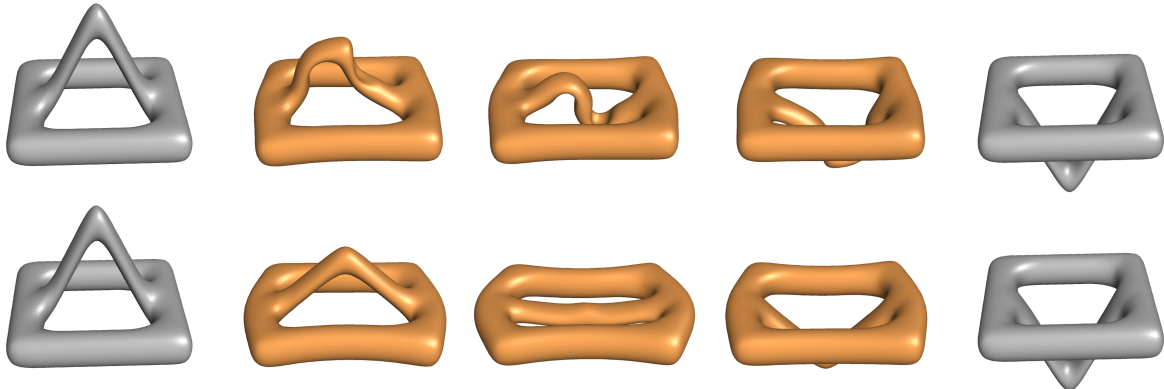
Figure 6.5: *Discrete geodesic for low (top, $\eta = 0.005$) and high (bottom, $\eta = 0.1$) bending resistance. Stiff materials prefer the handle being folded (inducing bending dissipation) whereas soft materials stretch the outer frame (i.e. induce membrane distortion) to avoid folding.*

Another example is given in Fig. 6.6, where a low bending weight η essentially represents a flat sheet of paper or aluminum foil, that is rolled up in two orthogonal directions (top). Again, this deformation path is almost isometric as tangential distortion is highly expensive. On the other hand, if η is increased the optimal path no longer stays in the submanifold of isometric deformations but rather prefers a "shortcut" by introducing a little bit of tangential distortion (Fig. 6.6, bottom). Visually, this represents the behaviour of a piece of cloth that is not very stiff at all. Note that in both examples in Fig. 6.5 and Fig. 6.6 a simple rotation of the end poses is not allowed due to the dense correspondence assumption. For instance, if the four boundary edges of the plate in Fig. 6.6 are labeled clockwise by A, B, C and D, then in the first pose A is supposed to be aligned with C, whereas in the last pose B is supposed to be aligned with D, which cannot be resolved by a global rotation.
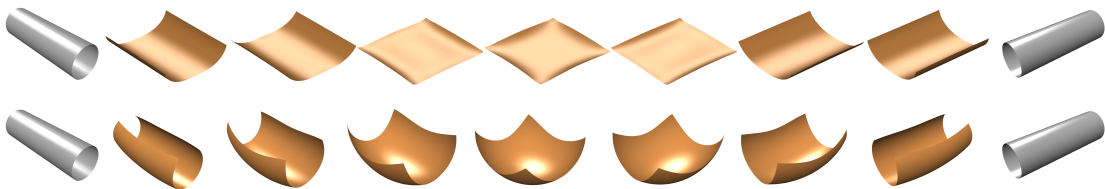
Figure 6.6: *Discrete geodesic for low (top, $\eta = 10^{-6}$) and high (bottom, $\eta = 10^{-1}$) bending resistance.*

6.2.2 Features of time-discrete geodesic paths

In this section we discuss two features of time-discrete geodesics: lack of symmetry and non-uniqueness.

Lack of symmetry Time-discrete geodesics are in general not symmetric, that means a path from A to B will be (slightly) different from a path from B to A. In particular, the approximation of the Riemannian distance given by the square root of the optimal path energy $\mathbf{E}^K$, is not symmetric either. This is due to the fact that the dissimilarity measure $\mathbf{W}$ in Def. 6.0.2 is not symmetric in its arguments, as the density is integrated over the *undeformed* shell. However, the lack of symmetry of $\min \mathbf{E}^K$ decreases with increasing K, as will be shown numerically in Sec. 6.2.5. Furthermore, already for a very low number K the lack of symmetry in the time-discrete geodesic is visually not perceptible: in Fig. 6.7 we show a time-discrete geodesic between two hand poses A and B, where the top row shows results from computations of $A{\rightarrow}B$ and the bottom row shows (reversed) results from $B{\rightarrow}A$. Note, that both
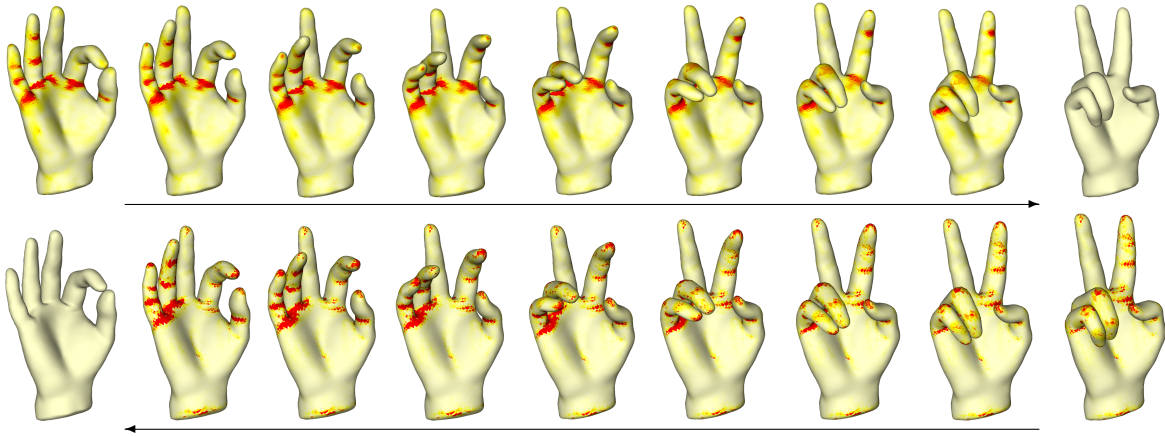
Figure 6.7: *Time-discrete geodesics $A\rightarrow B$ (top) vs. $B\rightarrow A$ (bottom) between two hand poses (both $\eta = 10^{-4}$). The underlying dissipation is represented by the two energy densities,* i.e. W_{mem} *(top row, 0 ▱ 0.01) and W_{bend} (bottom row, 0 ▱ 10).*

energies are mainly concentrated at the joints, where dissipation due to bending is significantly larger than dissipation due to tangential distortion (*cf*. also Fig. 6.1). The relative difference between path energies of the two sequences is 3%. The deformation energy $\mathbf{W}$ between two corresponding shapes in the two sequences is less than 0.01% of the deformation energy from the first to the final shell.

The issue of missing symmetry in our model has also been investigated in [BvTH16]. The authors conclude that a straightforward symmetrization of the deformation energy by using $\mathbf{W}[A, B]+\mathbf{W}[B, A]$, does not lead to significantly different results but slows down the numerical simulation instead.

Non-uniqueness Geodesic paths need not be unique, and in particular buckling modes might lead to multiple (shortest) geodesic paths between two input shells (*cf*. Fig. 6.8). The flat plate as an intermediate shape is avoided since it would induce high tangential distortion. Therefore the bumps flip to the other side succesively, while the order of flipping does not effect the accumulated dissipation. Different paths are induced by different initializations. Note that the example shown in Fig. 6.5 (top) also leads to a non-unique geodesic, as the left part of the handle could have been pushed through the frame first as well.
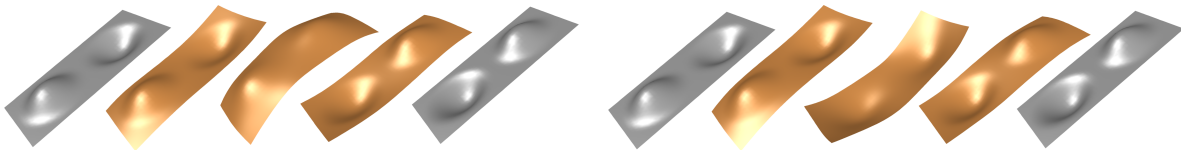
Figure 6.8: *Symmetric setups can lead to non-unique geodesic paths.*

6.2.3 Geodesic interpolation and extrapolation

Obviously, time-discrete geodesics provide a natural *interpolation* tool in discrete shell space. Now we apply the notion of a time-discrete exponential map as introduced in Sec. 4.2.2 to the space of discrete shells in order to generate a consistent *extrapolation* tool.

Following Def. 4.2.9 the time-discrete exponential map is built on an iterative scheme computing single *shooting steps* sequentially. The setup of such a single shooting step is considering the necessary conditions for a discrete path $(\mathbf{S}_0, \mathbf{S}_1, \mathbf{S}_2)$ to be a time-discrete geodesic connecting $\mathbf{S}_0$ and $\mathbf{S}_2$. Due to the variational definition, this is the case iff. $\mathbf{S}_1$ is a solution of the necessary condtion (6.0.3), *i.e.* a root of the mapping

$$\mathbf{S} \mapsto \partial_2 \mathbf{W}[\mathbf{S}_0, \mathbf{S}] + \partial_1 \mathbf{W}[\mathbf{S}, \mathbf{S}_2].$$

Analogously, $(\mathbf{S}_0, \mathbf{S}_1, \mathbf{S}_2)$ is a time-discrete geodesic starting with $\mathbf{S}_0$ and $\mathbf{S}_1$ iff. $\mathbf{S}_2$ is a solution of the *same* necessary condtion (6.0.3), *i.e.* a root of the mapping

$$\mathbf{S} \mapsto \partial_2 \mathbf{W}[\mathbf{S}_0, \mathbf{S}_1] + \partial_1 \mathbf{W}[\mathbf{S}_1, \mathbf{S}].$$

Note that existence is ensured if $\|\mathbf{S}_1 - \mathbf{S}_0\|$ is sufficiently small [RW15]. By Def. 4.2.9 the root of this map is defined to be the discrete exponential map $\mathrm{EXP}^2_{\mathbf{S}_0}(\mathbf{S}_1 - \mathbf{S}_0)$, which is thought of as a one-step *geodesic extrapolation* starting at $\mathbf{S}_0$ in direction $\mathbf{S}_1 - \mathbf{S}_0$. To further extrapolate the sequence this shooting step is repeated iteratively, *i.e.* we solve

$$0 = \partial_2 \mathbf{W}[\mathbf{S}_{k-2}, \mathbf{S}_{k-1}] + \partial_1 \mathbf{W}[\mathbf{S}_{k-1}, \mathbf{S}_k], \quad k = 2, \ldots, K, \tag{6.2.1}$$

sequentially for $\mathbf{S}_k$, where the initial shapes $\mathbf{S}_0$ and $\mathbf{S}_1$ are given. Note that (6.2.1) coincides exactly with the $K - 1$ necessary conditions (6.0.3) for $(\mathbf{S}_0, \ldots, \mathbf{S}_K)$ to be a discrete geodesic. In particular, the interpolated geodesic $(\mathbf{S}_0, \ldots, \mathbf{S}_K)$ and the geodesic extrapolation from $\mathbf{S}_0$ in direction $\mathbf{S}_1 - \mathbf{S}_0$ coincide because the defining system of Euler–Lagrange equations is the same and the minimizer of the variational problem is unique. For discrete shells $\mathbf{S}_0, \mathbf{S}_K$ close to each other, the latter is guaranteed due to the non-degeneracy of the Hessian, which implies local strict convexity. Geodesic interpolation can

0.0   0.05   0.25   0.50   0.75   1.0   t
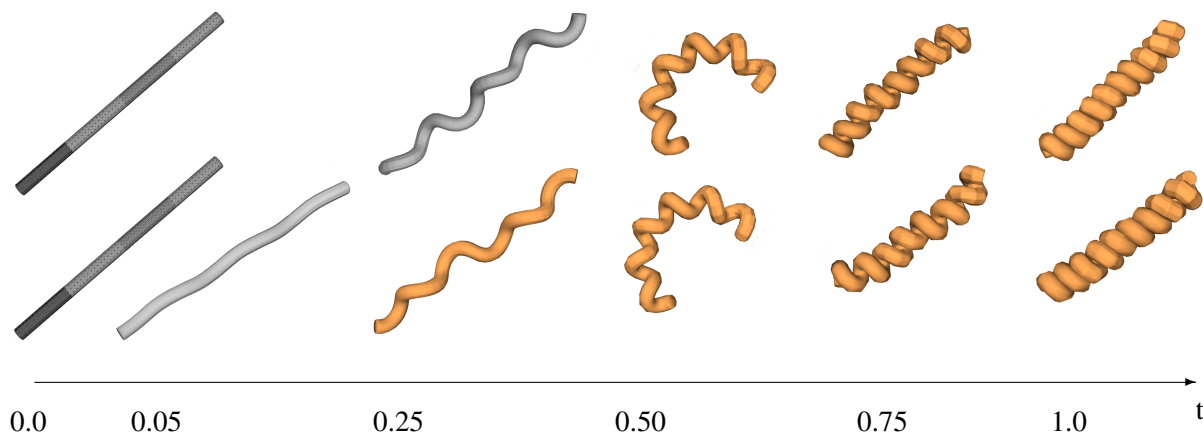
Figure 6.9: *Shape extrapolation is applied to generate a strong twisting of a helix with $\eta = 10^{-5}$.*

be considered as a map from a geodesic path $(\mathbf{S}_0, \ldots, \mathbf{S}_K)$ to a difference vector $\mathbf{S}_1 - \mathbf{S}_0$, while geodesic extrapolation can be seen as a map from a difference vector $\mathbf{S}_1 - \mathbf{S}_0$ to a geodesic path connecting $\mathbf{S}_0$ to $\mathbf{S}_K$. Due to the consistency of the variational definition these operations are exactly the discrete counterparts of the smooth *logarithm map*, which maps a geodesic path to an initial velocity vector, and the smooth *exponential map* which maps an initial velocity to a geodesic path.

Remark 6.2.2. Above we have made use of a difference vector $\mathbf{V} = \tilde{\mathbf{S}} - \mathbf{S}$ which is *physically* thought of as a displacement of $\mathbf{S}$ or *geometrically* considered as a tangent vector in shell space at the point $\mathbf{S}$. However, this notion is ambiguous due to the inherent rigid body motion invariance of our model. Imagine Φ is a rigid body motion, *e.g.* a large translation, then $\Phi(\tilde{\mathbf{S}})$ equals $\tilde{\mathbf{S}}$ in shell space but $\Phi(\tilde{\mathbf{S}}) - \mathbf{S}$ is not comparable to $\mathbf{V}$ any longer. Although the displacement formulation is used formally in the notation of the discrete exponential map, we actually never compute displacements when performing geodesic shooting, since they are not present in the variational formulation (6.2.1).

In Fig. 6.9 we show an example of geodesic extrapolation based on initial data taken from the computational results in [FB11] (*cf.* Fig. 6). The generation of the strongly twisted helix demonstrates the robustness of the time-discrete geodesic extrapolation, both for large time steps and large nonlinear initial variation (Fig. 6.9, top) as well as for many small time steps and small initial offset (Fig. 6.9, bottom).
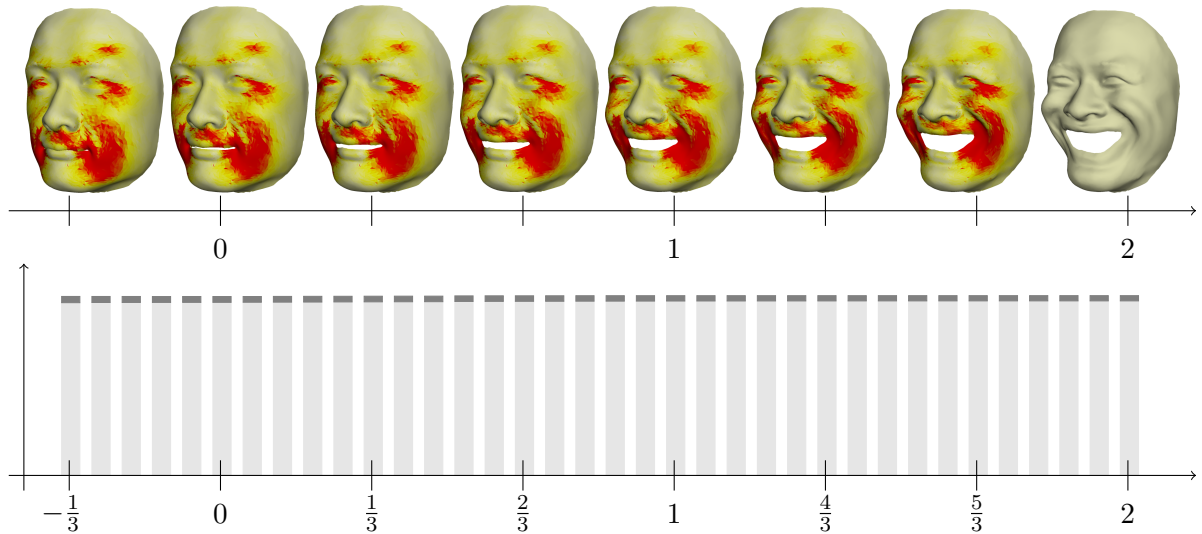
Figure 6.10: *Top: Geodesic interpolation for $0 \leq t \leq 1$ of given shells at time 0 and 1, geodesic extrapolation for $t < 0$ and $t > 1$ (local dissipation rate is color coded as 0 ▮▮▮ 1; bending weight $\eta = 1$). Bottom: The total dissipation rate (membrane contribution in light gray, bending contribution in dark gray) stays constant along the path.*

Geodesic inter- and extrapolation can naturally be combined by *e.g.* first interpolating between two given end poses and then extrapolating the motion in both directions. This is illustrated in Fig. 6.10, where the shapes at times $t = 0$ and $t = 1$ were given as input shapes. Another striking feature of computing (approximative) geodesic paths are constant dissipation rates along the path (Fig. 6.10, bottom), which corresponds geometrically to the property $g_y(\dot{y}, \dot{y}) = \text{const}$ that holds for geodesic paths. This property of equidistribution of dissipation is in particular visible when comparing to other approaches: the two gray elephant poses in Fig. 6.11 are connected via a discrete geodesic with $K = 4$ and for $\eta = 10^{-5}$. The geodesic is extended using geodesic extrapolation. On the right the corresponding rate of viscous dissipation is plotted for the 6 time steps. Furthermore, black lines indicate the dissipation rates for the corresponding sequence from Fig. 11 in [WDAH10].
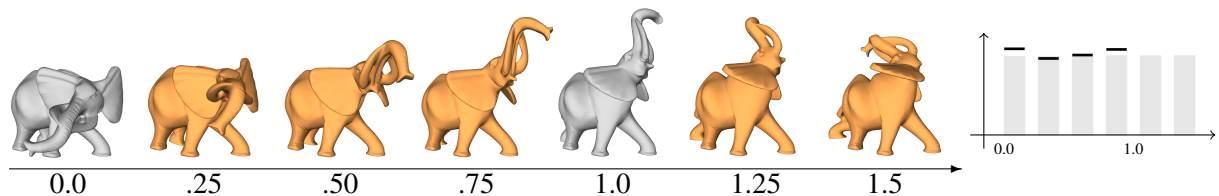
Figure 6.11: *Geodesic interpolation and extrapolation of the two gray poses (left) revealing constant dissipation rates (right, gray) opposed to the interpolation method by [WDAH10] (right, black lines).*

In animation applications geodesic shooting can further be used to generate natural motions of three-dimensional models without much user interaction. Given a particular shell $\mathbf{S}$, one can compute eigenmodes of the Hessian of the elastic deformation energy $\partial_2^2 \mathbf{W}[\mathbf{S}, \mathbf{S}]$ corresponding to the lowest eigenvalues *e.g.* by a standard inverse power iteration. Due to Thm. 6.1.3, the first 6 eigenvalues are trivial, representing the translations and rotations, respectively, in 3D space. Computing eigenvectors of the Hessian of an elastic energy to launch natural animations has also been done to perform *physical simulations* based on Newton's law of motion [HSTP11, vTSSH13]. Slightly different to these physical simulations, moving $\mathbf{S}$ in the direction of eigenmodes—corresponding to low but non-trivial eigenvalues—by means of geodesic shooting represents a deformation of $\mathbf{S}$ in a direction with *least energy dissipation*. Hence the motion along these so-called *dissipation modes* induces energetically preferred deformations that look very natural. In particular, the dissipation rates are again constant which is not the case for physical simulations as in [HSTP11, vTSSH13]. In Fig. 6.12 we demonstrate geodesic extrapolation of a shell $\mathbf{S}$ along two different dissipation modes, given by the second and fourth non-trivial eigenmode of $\partial_2^2 \mathbf{W}[\mathbf{S}, \mathbf{S}]$ with eigenvalues $\lambda = 4.85$ (left) and $\lambda = 5.91$ (right), respectively. Shown are the initial shell with the corresponding eigenmode scaled by ± 5 and the extrapolated shells based on 10, 20 and 30 iterations of the time-discrete extrapolation. As mentioned above, the dissipation rates are constant up to numerical errors (Fig. 6.12, bottom).
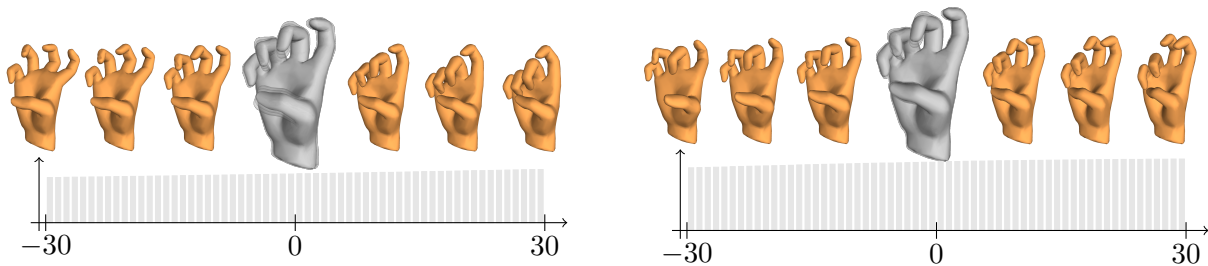
Figure 6.12: *Geodesic extrapolation along low dissipation modes (bending weight $\eta = 10^{-3}$).*

6.2.4 Parallel transport and curvature

In Sec. 4.2.2 we have introduced a well-known first order approximation of continuous parallel transport named Schild's ladder. In the continuous setting it is based on a Riemannian parallelogram construction (*cf*. Fig. 4.2), whose building elements are local geodesic interpolation and extrapoltion operations. To obtain a fully time-discrete scheme we have simply replaced these geometric operations by their time-discrete counterparts. In this section we apply the idea of time-discrete parallel transport to the space of discrete shells and show applications in animation *e.g.* for detail transfer.

The construction of a (time-discrete) Riemannian parallelogram is illustrated in Fig. 6.13. Given three shells $\mathbf{S}_A$, $\mathbf{S}_B$, and $\mathbf{S}_C$, we can construct a fourth shell $\mathbf{S}_D$, such that the (time-discrete) geodesics $\mathbf{S}_C \leftrightarrow \mathbf{S}_B$ and $\mathbf{S}_A \leftrightarrow \mathbf{S}_D$ share the same midpoint $\mathbf{S}^\times$. To compute $\mathbf{S}_D$ we proceed as follows:

   (i) compute the (time-discrete) geodesic from $\mathbf{S}_C$ to $\mathbf{S}_B$ and mark its midpoint $\mathbf{S}^\times$,

   (ii) compute $\mathbf{S}_D$ through (time-discrete) extrapolation starting from $\mathbf{S}_A$ in direction $\mathbf{S}^\times$.
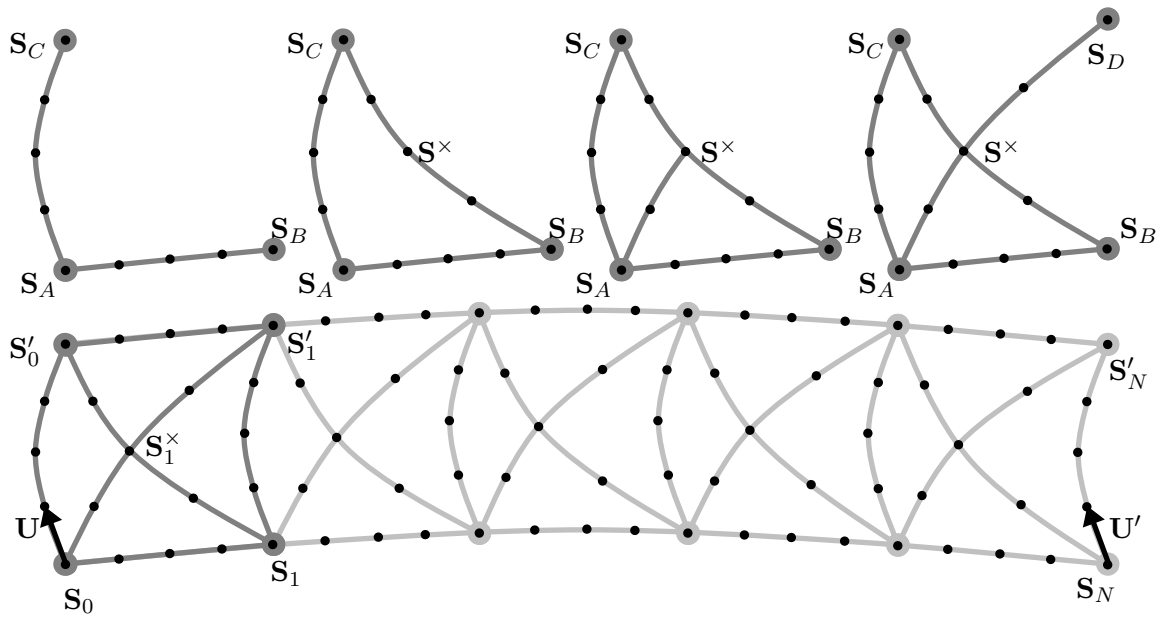
Figure 6.13: *Top: Stepwise construction of a single (discrete) geodesic parallelogram. Bottom: Iterative construction for the time-discrete parallel transport of* $\mathbf{U}$ *along* $(\mathbf{S}_0, \ldots, \mathbf{S}_N)$ *to* $\mathbf{U}'$.

Let $\mathbf{U}$ be a variation of $\mathbf{S}_0$ towards some shell $\mathbf{S}'_0$ represented by the (time-discrete) logarithm. A sequence of N such parallelograms then transports $\mathbf{U}$ along the path from $\mathbf{S}_0$ to $\mathbf{S}_N$ and one obtains a variation $\mathbf{U}'$ of $\mathbf{S}_N$ in the direction $\mathbf{S}'_N$ represented again by the (time-discrete) logarithm. In Fig. 6.13 we show a schematic example for $N = 5$, where the curved lines correspond to smooth geodesic segments, whereas the dots represent the corresponding time-discrete geodesics with $K = 4$. Fig. 6.14 uses such a concatenation of geodesic parallelograms to transport a smile along a path from a neutral to a disgusted facial expression. Note that in practice the (discrete) logarithms $\mathbf{U}$ resp. $\mathbf{U}'$ are not computed explicitly, since the algorithm is based on the corresponding shapes $\mathbf{S}'_0$ resp. $\mathbf{S}'_N$ only.
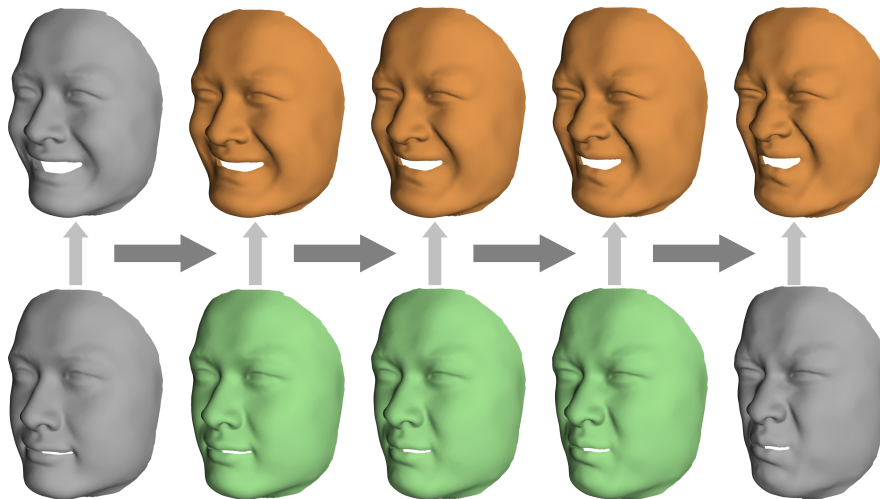
Figure 6.14: *Time-discrete parallel transport of the difference between a smiling (upper left) and a neutral face (lower left) along a path (bottom row) towards a disgusted face (bottom right), resulting in a smile with a frown (upper right).*

However, given a shell surface $\mathbf{S}$ and two variants $\mathbf{S}'$ and $\mathbf{S}''$ of this shell, there are different ways to combine these two nonlinear shell variations in a new shell $\mathbf{S}'''$ (*cf*. Fig. 6.15):

(A) construct a single geodesic parallelogram $\mathbf{S}, \mathbf{S}', \mathbf{S}'', \mathbf{S}'''$,

(B) transport $(\mathbf{S}, \mathbf{S}'')$ along a discrete geodesic from $\mathbf{S}$ to $\mathbf{S}'$ via a sequence of parallelograms, or

(C) transport $(\mathbf{S}, \mathbf{S}')$ along a discrete geodesic from $\mathbf{S}$ to $\mathbf{S}''$ via a sequence of parallelograms.

Due to the holonomy in Riemannian manifolds with non-zero curvature, the results will differ (Fig. 6.15).
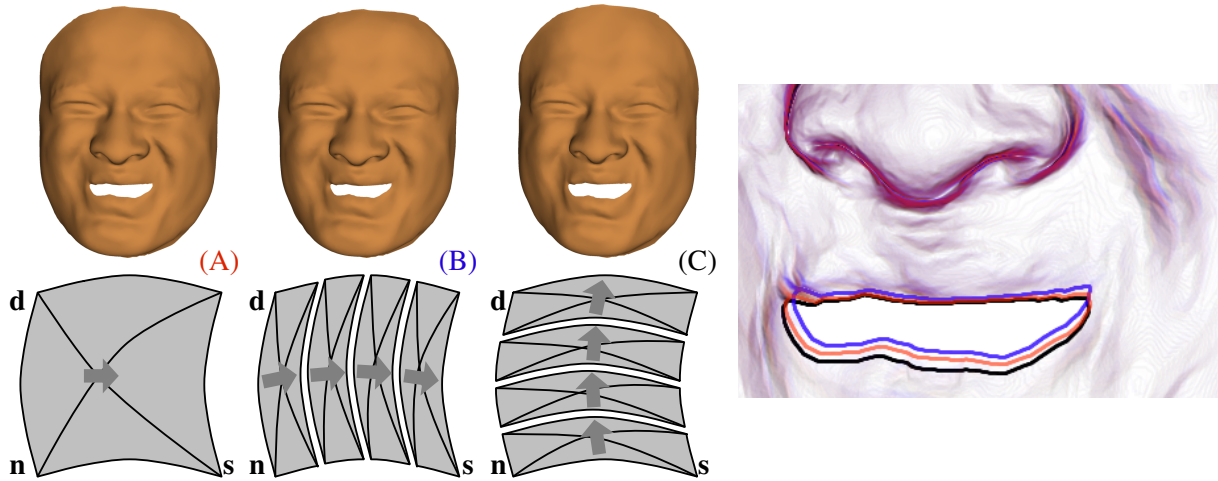
Figure 6.15: *Different results $\mathbf{S}'''$ of combining an expression of disgust ($\mathbf{S}' = \boldsymbol{d}$) with a smile ($\mathbf{S}'' = \boldsymbol{s}$), starting from a neutral face ($\mathbf{S} = \boldsymbol{n}$). The colored contours on the right show differences due to holonomy.*

In particular, that means the space of shells is not flat, but curved. Another example of holonomy is shown in Fig. 6.16: if a tangent vector is parallely transported along a closed curve, it will in general not return to its initial direction. Theoretically, this poses limitations on the extent to which parallel transport can robustly be used for deformation transfer. However, practically the example in Fig. 6.16 indicates that parallel transport still remains a very robust and useful tool: even though there is a numerical difference between the starting and end point due to holonomy, it is hardly perceptible visually.
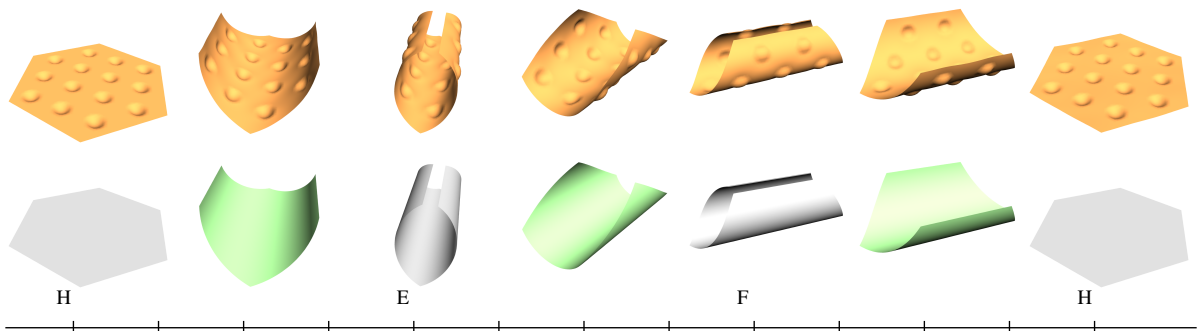
Figure 6.16: *A bump map (as a variation of the flat hexagon H) is transported along a closed curve $(H \to E \to F \to H)$ in shell space ($\eta = 10^{-5}$). The $L^2(H)$-distance between the initial and the final bump map on the shell H due to holonomy is 0.0125.*

For shell space, a rough understanding of its curvature has yet to be developed. However, Fig. 6.17 provides a further glimpse into this direction. Here, a triangle of three time-discrete geodesics with $K = 17$ is computed between three given shells D, E, and F. On the geodesic edge from D ($t = 0$) to E ($t = 1$) intermediate shells are displayed for $t = \frac{1}{4}$ (d, d'), $t = \frac{1}{2}$ (e, e'), and $t = \frac{3}{4}$ (f, f'). Furthermore, the associated geodesic barycenters (the point with the least average geodesic distance to the vertices), M and M' respectively, are shown. Note that the points on the edges of the geodesic triangles are positioned such that the length of solid line segments connecting the barycenter reflects the geodesic distance between the end points. However, these lengths are slightly larger than they would be in a flat Riemannian space, indicating a positive sectional curvature. The curvature is more pronounced for smaller nominal shape thickness δ. Note that $\eta = \delta^2$ can be interpreted as the relative weight between bending and membrane dissipation. Intuitively, the bending term prefers paths along which the local shell curvature at each point transitions uniformly in time from the initial to the final value. However, since this cannot happen isometrically, the membrane term prevents such a uniform transition, resulting in a more curved shell space. Note that the shell space curvature is not uniform. Indeed, if in Fig. 6.17 the shell M is replaced by a flat hexagon, the distance relations even indicate a very slight negative curvature (not displayed here).
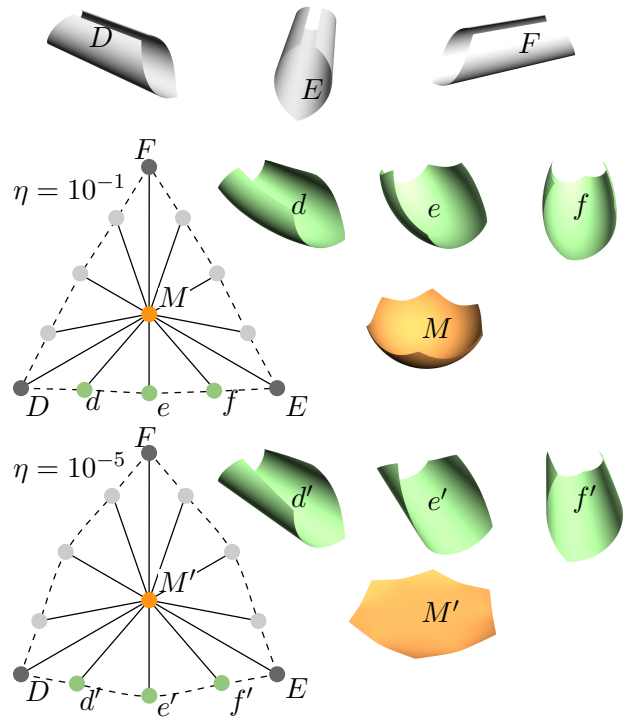
Figure 6.17: *Geodesic triangles indicate positive curvature of shell space.*

6.2.5 Empirical convergence

In this section we investigate the empirical convergence of the time-discrete geodesic calculus applied to the space of discrete shells. In particular, we compare the experimental results to the analytical results predicted in Sec. 4.2.2. Recall that the convergence analysis provided in [RW15] is based on restrictive (smoothness) assumptions on the manifold as well as on the metric and the approximating functional $\mathcal{W}$. In particular, the assumptions are not fulfilled for the space of (continuous) shells equipped with a metric as considered in Sec. 6.1.2. Nevertheless, we will show that the empirical convergence rates coincide with the analytical ones for several geometric objects living in the finite dimensional space of discrete shells.

Let u_τ be the approximative solution to a generic problem depending on a stepsize $\tau > 0$. To quantify the numerical error for a sequence of decreasing stepsizes $(\tau_k)_{k \geq 0}$, we make use of the so-called experimental order of convergence (eoc). If the exact solution u is not known one chooses a large $M > 0$ and defines $u_M = u_{\tau_m}$, *i.e.* the numerical solution corresponding to the stepsize τ_M, as *ground truth*. Then the error e_k induced by the solution u_k resulting from a stepsize τ_k is defined as $e_k = \|u_k - u_M\|$, measured in some suitable error norm. Assuming there are constants $p, C > 0$ with $e_k = C\tau_k^p$ for all k, the experimental order of convergence *eoc* (which is supposed to approximate p) is defined as

$$eoc = \frac{\log(e_{k-1}/e_k)}{\log(\tau_{k-1}/\tau_k)} \, .$$

In the following, we make use of the sequence $\tau_k = 2^{-k}$ for $k = 0, \dots, M$ with $M \in \{6, 7\}$.

First, we investigate the convergence of the optimal time-discrete path energy $\mathbf{E}^K$, which is according to Thm. 4.2.4 of first order. To this end we consider the energy of multiple geodesic paths computed pairwise between different face expressions shown in Fig. 6.18. In Tab. 6.1 we show convergence of $\min \mathbf{E}^K$ as well as a decreasing lack of symmetry of the "distance" measure $\mathrm{dist}(\mathbf{S}_A, \mathbf{S}_B) = \sqrt{\min_{Y^K} \mathbf{E}^K[Y^K]}$, for a curve $Y^K = (\mathbf{S}_0, \dots, \mathbf{S}_K)$ with $\mathbf{S}_0 = \mathbf{S}_A$ and $\mathbf{S}_K = \mathbf{S}_B$ (*cf.* also Sec. 6.2.2).

neutral   smile   disgust   surprise
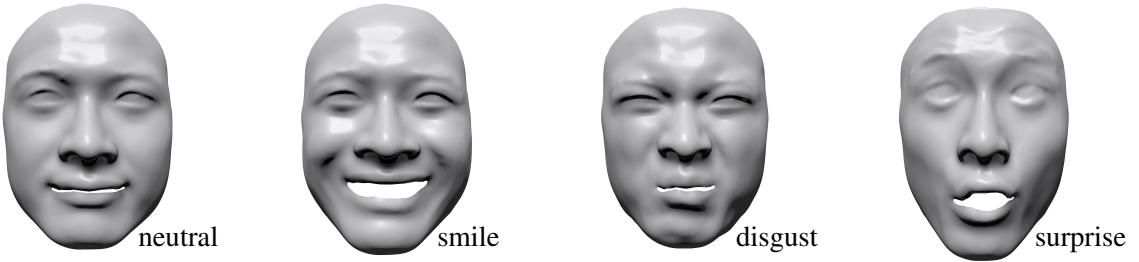
***Figure 6.18:** Face expressions used in convergence experiments.*

We also observe first order convergence of the path energy when considering a large nonlinear deformation as shown in Tab. 6.2. Note that the lack of the triangle inequality for the dissimilarity measure $\sqrt{\mathbf{W}(.,.)}$ implies the fact that we might have *decreasing* sequences $\min_{Y^K} \mathbf{E}^K[Y^K]$ for increasing K. In fact, $\sqrt{\mathbf{W}(\mathbf{S}_A, \mathbf{S}_B)} \leq \sqrt{\mathbf{W}[\mathbf{S}_A, \mathbf{S}_C]} + \sqrt{\mathbf{W}[\mathbf{S}_C, \mathbf{S}_B]}$ would imply

$$\mathbf{E}^1[\mathbf{S}_A, \mathbf{S}_B] = \mathbf{W}[\mathbf{S}_A, \mathbf{S}_B] \leq \min_{\mathbf{S}} 2\left(\mathbf{W}[\mathbf{S}_A, \mathbf{S}] + \mathbf{W}[\mathbf{S}, \mathbf{S}_B]\right) = \min_{\mathbf{S}} \mathbf{E}^2[\mathbf{S}_A, \mathbf{S}, \mathbf{S}_B] \, ,$$

which obviously does not hold.

K	neutral to smile min $\mathbf{E}^K$	eoc	smile to neutral min $\mathbf{E}^K$	eoc
1	1.529		1.530	
2	1.520		1.520	
4	1.518	1.59	1.518	1.59
8	1.517	/	1.517	/
16	1.517	/	1.517	/
32	1.517		1.517	

K	neutral to disgust min $\mathbf{E}^K$	eoc	disgust to neutral min $\mathbf{E}^K$	eoc
1	1.941		2.024	
2	1.947		1.988	
4	1.954	0.91	1.974	1.26
8	1.958	1.00	1.968	1.32
16	1.961	2.00	1.966	1.00
32	1.962		1.964	

K	neutral to surprise min $\mathbf{E}^K$	eoc	surprise to neutral min $\mathbf{E}^K$	eoc
1	5.395		5.627	
2	5.348		5.459	
4	5.350	0.17	5.405	1.40
8	5.357	0.83	5.385	1.34
16	5.363	1.59	5.376	1.70
32	5.366		5.372	

K	smile to disgust min $\mathbf{E}^K$	eoc	disgust to smile min $\mathbf{E}^K$	eoc
1	2.670		2.786	
2	2.667		2.723	
4	2.673	0.68	2.701	1.30
8	2.678	1.00	2.692	1.32
16	2.681	1.32	2.688	1.59
32	2.683		2.686	

K	smile to surprise min $\mathbf{E}^K$	eoc	surprise to smile min $\mathbf{E}^K$	eoc
1	8.406		8.586	
2	8.242		8.316	
4	8.200	2.09	8.245	1.66
8	8.205	1.42	8.223	1.59
16	8.207	1.59	8.216	1.46
32	8.208		8.212	

K	disgust to surprise min $\mathbf{E}^K$	eoc	surprise to disgust min $\mathbf{E}^K$	eoc
1	6.730		6.550	
2	6.491		6.406	
4	6.423	1.59	6.371	0.76
8	6.401	1.51	6.380	1.70
16	6.393	1.59	6.383	2.00
32	6.389		6.384	

Table 6.1: *Experimental order of convergence (eoc) for the (minimal) discrete path energy* $\min \mathbf{E}^K$ *computed pairwise for the face expressions as shown in Fig. 6.18,* $\eta = 1.0$*. Note that the first example (top, left) has already converged for* $K = 8$*. The lack of symmetry (computed as relative error, not shown in the table) decreases linearly in* K *and is about* 0.1% *for* $K = 32$ *in all examples.*

K	$\mathbf{S}_A \to \mathbf{S}_B$ $\mathbf{E}^K$	eoc	$\mathbf{S}_B \to \mathbf{S}_A$ $\mathbf{E}^K$	eoc
1	4.906		5.466	
2	4.898		5.139	
4	4.922	0.66	5.038	1.31
8	4.941	0.90	4.999	1.23
16	4.953	1.14	4.982	1.27
32	4.960	1.74	4.974	1.59
64	4.963		4.970	
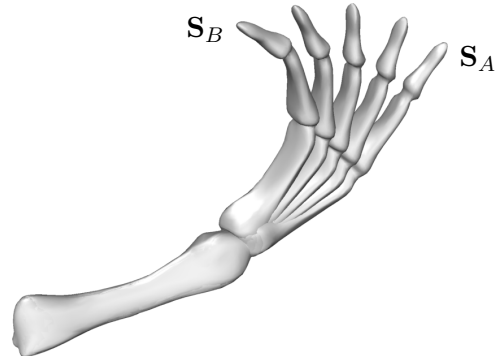
Table 6.2: *Experimental order of convergence (eoc) for the (minimal) discrete path energy* $\mathbf{E}^K$ *in both directions* $\mathbf{S}_A \to \mathbf{S}_B$ *and* $\mathbf{S}_B \to \mathbf{S}_A$ *using* $\eta = 10^{-4}$*. The input data* $\mathbf{S}_A$ *and* $\mathbf{S}_B$ *is depicted on the right (here with a time-discrete geodesic with* $K = 4$*).*

In Tab. 6.3 we further show convergence of time-discrete geodesics, measured in $L^\infty(\|.\|_{L^2})$ resp. $L^\infty(\sqrt{\mathbf{W}})$. Note that the analytical results do not provide a convergence order for discrete geodesics.

K	$L^\infty(\sqrt{\mathbf{W}})$	eoc	$L^\infty(\|\ \|_{L^2})$	eoc	K	$L^\infty(\sqrt{\mathbf{W}})$	eoc	$L^\infty(\|\ \|_{L^2})$	eoc
2	13.20		85.95		2	19.62		74.40	
4	6.67	0.98	40.07	1.10	4	8.74	1.17	37.94	0.97
8	3.29	1.02	18.43	1.12	8	3.85	1.18	17,98	1.08
16	1.47	1.16	7.85	1.23	16	1.60	1.27	7.75	1.21
32	0.51	1.53	2.61	1.58	32	0.54	1.57	2.59	1.58

Table 6.3: *Experimental order of convergence (eoc) for time-discrete geodesics in both directions $\mathbf{S}_A \to \mathbf{S}_B$ (left) and $\mathbf{S}_B \to \mathbf{S}_A$ (right) for the input data shown in Tab. 6.2; $\eta = 10^{-4}$. The error is measured in two different "norms", i.e. $L^\infty(\sqrt{\mathbf{W}})$ and $L^\infty(\|\ \|_{L^2})$, respectively.*

Furthermore, we investigate the experimental convergence of the discrete exponential map, which is supposed to be of first order as stated in Thm. 4.2.18. Again, we observe the same order in terms of *eoc* as shown in Tab. 6.4 for two different "norms". Finally, we confirm the first order convergence of the time-discrete parallel transport which corresponds to the results in Thm. 4.2.19, *cf*. Tab. 6.5 where we show two different examples again measured in two different norms.

K	$\sqrt{\mathbf{W}}$	eoc	$\|\ \|_{L^2}$	eoc	K	$\sqrt{\mathbf{W}}$	eoc	$\|\ \|_{L^2}$	eoc
2	0.575		8.34		2	0.637		0.374	
4	0.303	0.92	3.93	1.08	4	0.338	0.91	0.186	1.01
8	0.145	1.06	1.84	1.08	8	0.163	1.06	0.090	1.05
16	0.063	1.21	0.89	1.00	16	0.070	1.21	0.046	0.97
32	0.021	1.58	0.51	0.65	32	0.024	1.58	0.030	0.60

Table 6.4: *Experimental order of convergence (eoc) of the discrete exponential map based on input data $\mathbf{S}_A$ and $\mathbf{S}_B$ as in Tab. 6.2; $\eta = 10^{-4}$. Left: for $\zeta \approx \log_{\mathbf{S}_A}(\mathbf{S}_B)$ we measured the error between $\mathrm{EXP}^K_{\mathbf{S}_A}(\zeta/K)$ and $\mathbf{S}_B$ in two different "norms"; right: switching $\mathbf{S}_A$ and $\mathbf{S}_B$.*

K	$\sqrt{\mathbf{W}}$	eoc	$\|\ \|_{L^2}$	eoc	K	$\sqrt{\mathbf{W}}$	eoc	$\|\ \|_{L^2}$	eoc
1	2.224		51.708		1	2.842		118.551	
2	1.044	1.09	22.232	1.22	2	1.434	0.99	49.118	1.28
4	0.544	0.94	9.832	1.18	4	0.732	0.97	21.072	1.22
8	0.344	0.66	4.104	1.26	8	0.408	0.85	8.680	1.28
16	0.304	0.21	1.376	1.58	16	0.320	0.34	2.848	1.61

Table 6.5: *Experimental order of convergence (eoc) for the discrete parallel transport based on face expressions in Fig. 6.18 and measured in two different "norms" ($\eta = 1$). Left: transported variation "disgust" along path from "neutral" to "smile"; right: transported variation "smile" along path from "neutral" to "disgust" (as shown in Fig. 6.14 for $K = 4$).*

6.3 Implementation

The minimization of the discrete path energy is a nonlinear optimization problem in $\mathbb{R}^{3\,n\,(K-1)}$, where n is the number of vertices of the triangulated shells, $K+1$ the number of shapes. On the other hand, computing a single shooting step is a nonlinear optimization problem in $\mathbb{R}^{3\,n}$, but in order to generate a sequence of $K+1$ shapes this has to be solved $K-1$ times.

We apply a standard Newton's method to solve the necessary conditions (6.0.3) resp. (6.2.1) combined with an inexact line search method subject to either Armijo's rule or the strong Wolfe conditions. The stopping criterion is based on a threshold of $\epsilon K n$ in the squared l^2-norm for the energy gradient (with *e.g.* $\epsilon \sim 10^{-8}$). Implementation details of the minimization methods can be found in [NW99]; we give explicit formulas for the energy gradient and the energy Hessian in the appendix A.5.

It is well-known that Newton's method converges quadratically to the solution if one starts the iteration in the convergence radius, *i.e.* "close" to the optimum. Otherwise, convergence might be very slow or the method might even get stuck in (undesired) local minima. In Sec. 6.3.1 we discuss the impact of a suitable initialization as well as the benefit of a cascadic scheme in time in order to handle high temporal resolutions. Furthermore, we discuss the issue of the inherent rigid body motion invariance in the numerical optimization in Sec. 6.3.2. Finally, we describe how an efficient hierachical scheme in space is used to accelerate convergence in Sec. 6.3.3.

6.3.1 Initialization

For the geodesic shooting problem we only have to solve (a couple of) relatively small problems. Hence we focus on the efficient optimization of the time-discrete path energy $\mathbf{E}^K$ (with K fairly large) to compute time-discrete geodesics here. Let us assume we are given two (discrete) input shells $\mathbf{S}_A, \mathbf{S}_B \in \mathbb{R}^{3n}$ and some integer $K \gg 1$ and we want to compute a time-discrete geodesic of length $K+1$, *i.e.* a discrete path $(\mathbf{S}_0, \mathbf{S}_1, \ldots, \mathbf{S}_K)$ with $\mathbf{S}_0 = \mathbf{S}_A$ and $\mathbf{S}_K = \mathbf{S}_B$ that satisfies the system of necessary conditions (6.0.3).

As mentioned above, the performance of Newton's method depends on the initialization. A straightforward choice for the initialization is the nodalwise linear interpolation of the two input shells. However, if the input shapes differ by a large nonlinear deformation the linear interpolation might introduce self-intersections, degenerated triangles and odd angles (*cf*. Fig. 4.4 in [Hee11]). These artefacts often hamper the numerical optimization substantially, in the worst case the iteration does not converge.

Alternatively, one might initialize the sequence by the "trivial" path $(\mathbf{S}_A, \mathbf{S}_A, \ldots, \mathbf{S}_A, \mathbf{S}_B)$. However, that means, the initialization is far apart from the final solution and in particular shapes $\mathbf{S}_k$ with $0 \ll k < K$ have to be deformed significantly. These large deformations are computationally hard to resolve, hence we make use of an approach proposed in [Per15]: We consider the weighted average functional

$$\mathbf{S} \mapsto (K-k)\,\mathbf{W}[\mathbf{S}_0, \mathbf{S}] + k\,\mathbf{W}[\mathbf{S}, \mathbf{S}_K]\,, \tag{6.3.1}$$

and iteratively minimize (6.3.1) for $k = 1, \ldots, K-1$ to get $\mathbf{S}_k$, starting the kth iteration with the initilization $\mathbf{S} = \mathbf{S}_{k-1}$. This procedure benefits from the fact that in each iteration the start value $\mathbf{S}_{k-1}$ is close to the optimum $\mathbf{S}_k$ due to the different scaling of the two terms in (6.3.1). Hence we solve a sequence of $K-1$ smaller problems sequentially which results in a good approximation to the actual time-discrete geodesic. In practice, it is often reasonable to make use of this iteration first and then initialize the optimization of the full time-discrete path energy with the resulting sequence than starting with the latter one with a bad initialization.

Finally, we report on two further strategies to create good initialiations that can be used alternatively or additionally to the iterative scheme proposed above.

Cascadic scheme If $K = 2^L$ for some integer $L > 1$ one might make use of the cascadic scheme described in Sec. 4.3.3 in [Hee11]:

```
1  for l = 0, . . . , L − 1 do
2      // in parallel
3      for m = 1, . . . , 2^l do
4          compute S as midpoint of a short geodesic (S_{(m−1)·2^{L−l}}, S, S_{m·2^{L−l}});
5          set S_{(2m−1)·2^{L−l−1}} = S;
6      end
7  end
```

Odd-even-scheme If $K = 2L$ for some integer $L > 0$ one might apply M iterations of the so-called *odd-even-scheme*, which optimizes alternately all odd resp. all even shapes, while fixing the other ones:

```
1   for m = 1, . . . , M do
2       // update odd shapes (in parallel)
3       for l = 1, . . . , L do
4           compute S as midpoint of a short geodesic (S_{2(l−1)}, S, S_{2l});
5           set S_{2l−1} = S;
6       end
7       // update even shapes (in parallel)
8       for l = 1, . . . , L − 1 do
9           compute S as midpoint of a short geodesic (S_{2l−1}, S, S_{2l+1});
10          set S_{2l} = S;
11      end
12  end
```

6.3.2 Dealing with rigid body motions

Our shell model is invariant with respect to rigid body motions. That means if $\mathbf{S}$ denotes a (discrete) shell and $\Phi(x) = Qx + b$, $Q \in SO(3)$, $b \in \mathbb{R}^3$, is a rigid body motion, we have $\mathbf{W}[\mathbf{S}, \Phi(\mathbf{S})] = 0$. For computing a three-point interpolating geodesic between two discrete shells $\mathbf{S}_0$ and $\mathbf{S}_2$ one has to find a root of

$$F_{\text{int}} : \mathbf{S} \mapsto \partial_2 \mathbf{W}[\mathbf{S}_0, \mathbf{S}] + \partial_1 \mathbf{W}[\mathbf{S}, \mathbf{S}_2],$$

whereas for a single step of geodesic shooting from $\mathbf{S}_0$ in direction $\mathbf{S}_1 - \mathbf{S}_0$ one has to find a root of

$$F_{\text{ext}} : \mathbf{S} \mapsto \partial_2 \mathbf{W}[\mathbf{S}_0, \mathbf{S}_1] + \partial_1 \mathbf{W}[\mathbf{S}_1, \mathbf{S}].$$

Solving $F[\mathbf{S}] = 0$ in both cases could be done by means of Newton's method, *i.e.* for a given initial value $\mathbf{S}^0$ we compute $\mathbf{S}^k$ iteratively for $k > 0$ by computing

$$DF[\mathbf{S}^{k-1}] \Delta \mathbf{S} = -F[\mathbf{S}^{k-1}], \tag{6.3.2}$$
$$\mathbf{S}^k = \mathbf{S}^{k-1} + \tau_k \Delta \mathbf{S},$$

where the stepsize $\tau_k \in [\tau_{\min}, \tau_{\max}]$ is found by an inexact line search using *e.g.* Armijos rule [NW99]. However, DF is not invertible due to the rigid body motion invariance, *i.e.* it has a six-dimensional kernel (*cf*. Thm. 6.1.2 resp. Thm. 6.1.3). In the following, we describe two different possibilities how to resolve this problem.

Dirichlet conditions An elementary and popular approach to handle the singularity of the system matrix (here induced by the rigid body motion invariance) is to impose Dirichlet boundary conditions, *i.e.* fix a certain region of the (discrete) shell while minimizing. This is valid due to the embedding $H^2 \hookrightarrow C^0$ resp. the trace theorem. In practice this is realized by manipulating the linear system (6.3.2): if the kth node is supposed to be fixed, one sets $DF_{ik} = DF_{ki} = \delta_{ik}$ as well as $(\Delta \mathbf{S})^l_k = 0$ for $l = 0, 1, 2$ in the solution $\Delta \mathbf{S} = (\Delta \mathbf{S}^0, \Delta \mathbf{S}^1, \Delta \mathbf{S}^2)$, where $\Delta \mathbf{S}^l \in \mathbb{R}^n$. Theoretically, it suffices to fix *two* nodes since we have six degrees of freedom representing the rigid body motion invariance. However, one usually prescribes a whole (connected) region of vertices, depending on the application [BK04]. For instance, in Fig. 6.1 we fixed the longest phalanx and in Fig. 6.7 or Fig. 6.12 we fixed the entire wrist region.

Lagrange ansatz As a motivation, let us consider a generic functional $\mathcal{F} = \mathcal{F}[\mathbf{S}]$. The necessary condition of the *unconstrained optimization* problem $\min_{\mathbf{S}} \mathcal{F}[\mathbf{S}]$ reads $D_{\mathbf{S}} \mathcal{F} = 0$. For a family of (constraint) functionals $\mathcal{G}_l = \mathcal{G}_l[\mathbf{S}]$, $l = 1, \dots, L$, the corresponding *constrained* optimization problem is given by solving

$$ D_{\mathbf{S}} \mathcal{F} = 0 \,, \quad \text{subject to} \quad \mathcal{G}_l[\mathbf{S}] = 0 \,, \quad \text{for } l = 1, \dots, L \,. \tag{6.3.3} $$

For some $\alpha \in \mathbb{R}^L$, an equivalent formulation of (6.3.3) is derived by defining the Lagrange functional

$$ \mathcal{L}[\mathbf{S}, \alpha] = \mathcal{F}[\mathbf{S}] + \sum_{l=1}^{L} \alpha_l \, \mathcal{G}_l[\mathbf{S}] $$

and solving $D_{(\mathbf{S}, \alpha)} \mathcal{L}[\mathbf{S}, \alpha] = 0$, which is again equivalent to solving the system

$$ \begin{cases} D_{\mathbf{S}} \mathcal{F}[\mathbf{S}] + \sum_l \alpha_l D_{\mathbf{S}} \mathcal{G}_l[\mathbf{S}] &= 0 \,, \\ \mathcal{G}_l[\mathbf{S}] &= 0 \,, \quad l = 1, \dots, L \,. \end{cases} \tag{6.3.4} $$

In particular, the solution of (6.3.3) does not require an explicit formulation of the functional $\mathcal{F}$ but only of the gradient $D_{\mathbf{S}} \mathcal{F}$. Hence we shall use the identification $F = D_{\mathbf{S}} \mathcal{F}$ and solve $D_{(\mathbf{S}, \alpha)} \mathcal{L}[\mathbf{S}, \alpha] = 0$ for appropiate constraint functionals.

In our setup, the constraint functionals are supposed to prescribe the six degrees of freedom corresponding to the rigid body motion invariance. This is done by postulating that the zeroth and first momentum of the solution $\mathbf{S}$ of $F[\mathbf{S}] = 0$ coincides with the zeroth and first momentum of a particular *reference shell* $\hat{\mathbf{S}}$. We define (linear) functions $\hat{\mathcal{T}}_i = \mathcal{T}_i[\hat{\mathbf{S}}]$, $\hat{\mathcal{R}}_i = \mathcal{R}_i[\hat{\mathbf{S}}]$, $i = 0, 1, 2$, such that $\hat{\mathcal{T}}_i(\mathbf{S}) = 0$ and $\hat{\mathcal{R}}_i(\mathbf{S}) = 0$ iff. the zeroth and first momentums of $\hat{\mathbf{S}}$ and $\mathbf{S}$, respectively, coincide. Let $\Phi = (\Phi^0, \Phi^1, \Phi^2) : \hat{\mathbf{S}} \to \mathbb{R}^3$ denote a deformation with $\Phi(\hat{\mathbf{S}}) = \mathbf{S}$. Using the dense correspondence between $\hat{\mathbf{S}}$ and $\mathbf{S}$ we can define the displacement $\mathbf{U}(\hat{x}) = \Phi(\hat{x}) - \hat{x} = x - \hat{x}$, with $\mathbf{U} = (\mathbf{U}^0, \mathbf{U}^1, \mathbf{U}^2)$ and $\hat{x} = (\hat{x}^0, \hat{x}^1, \hat{x}^2) \in \hat{\mathbf{S}}$. To fix the zeroth momentum, we postulate that the integral average of $\hat{x} \mapsto \mathbf{U}(\hat{x})$ vanishes, *i.e.* we set

$$ \hat{\mathcal{T}}_i(\mathbf{S}) := \mathcal{T}_i[\hat{\mathbf{S}}](\mathbf{U}) := \int_{\hat{\mathbf{S}}} \mathbf{U}^i(\hat{x}) \, \mathrm{d}a = \int_{\hat{\mathbf{S}}} x^i - \hat{x}^i \, \mathrm{d}a $$

for $i = 0, 1, 2$ (modulo 3). To fix the first momentum, we postulate that the integral average of $\hat{x} \mapsto \mathbf{U}(\hat{x}) \times \hat{x}$ vanishes, *i.e.* we set

$$ \hat{\mathcal{R}}_i(\mathbf{S}) := \mathcal{R}_i[\hat{\mathbf{S}}](\mathbf{U}) := \int_{\hat{\mathbf{S}}} \mathbf{U}^i(\hat{x}) \hat{x}^{i+1} - \mathbf{U}^{i+1}(\hat{x}) \hat{x}^i \, \mathrm{d}a = \int_{\hat{\mathbf{S}}} (x^i - \hat{x}^i) \hat{x}^{i+1} - (x^{i+1} - \hat{x}^{i+1}) \hat{x}^i \, \mathrm{d}a $$

for $i = 0, 1, 2$ (modulo 3). If we write $\mathbf{S} = (\mathbf{S}^0, \mathbf{S}^1, \mathbf{S}^2)$, with $\mathbf{S}^j \in \mathbb{R}^n$ for $j = 0, 1, 2$, we get

$$ \hat{\mathcal{T}}_i(\mathbf{S}) = \mathcal{T}_i[\hat{\mathbf{S}}](\mathbf{S}) = \hat{\mathbf{M}}(\mathbf{S}^i - \hat{\mathbf{S}}^i) \cdot \mathbf{1} \,, $$

$$ \hat{\mathcal{R}}_i(\mathbf{S}) = \mathcal{R}_i[\hat{\mathbf{S}}](\mathbf{S}) = \hat{\mathbf{M}}(\mathbf{S}^i - \hat{\mathbf{S}}^i) \cdot \hat{\mathbf{S}}^{i+1} - \hat{\mathbf{M}}(\mathbf{S}^{i+1} - \hat{\mathbf{S}}^{i+1}) \cdot \hat{\mathbf{S}}^i \,, $$

where $\mathbf{1} = (1, \dots, 1)^T \in \mathbb{R}^n$ and $\hat{\mathbf{M}} = \mathbf{M}[\hat{\mathbf{S}}] \in \mathbb{R}^{n,n}$ is the mass matrix corresponding to linear FEM basis functions on $\hat{\mathbf{S}}$.

Writing further $F = (F^0, F^1, F^2)$ with $F^j : \mathbf{S} \to \mathbb{R}^n$ and $\partial_i F^j[\mathbf{S}] := \partial_{\mathbf{S}^i} F^j[\mathbf{S}] \in \mathbb{R}^{n,n}$, we finally get

$$
D_{(\mathbf{S},\lambda,\mu)}\mathcal{L}[\mathbf{S}, \lambda, \mu] = \begin{pmatrix}
F^0[\mathbf{S}] + \lambda_0\hat{\mathbf{M}}\mathbf{1} + \mu_0\hat{\mathbf{M}}\hat{\mathbf{S}}^1 - \mu_2\hat{\mathbf{M}}\hat{\mathbf{S}}^2 \\
F^1[\mathbf{S}] + \lambda_1\hat{\mathbf{M}}\mathbf{1} + \mu_1\hat{\mathbf{M}}\hat{\mathbf{S}}^2 - \mu_0\hat{\mathbf{M}}\hat{\mathbf{S}}^0 \\
F^2[\mathbf{S}] + \lambda_2\hat{\mathbf{M}}\mathbf{1} + \mu_2\hat{\mathbf{M}}\hat{\mathbf{S}}^0 - \mu_1\hat{\mathbf{M}}\hat{\mathbf{S}}^1 \\
\hat{\mathbf{M}}(\mathbf{S}^0 - \hat{\mathbf{S}}^0) \cdot \mathbf{1} \\
\hat{\mathbf{M}}(\mathbf{S}^1 - \hat{\mathbf{S}}^1) \cdot \mathbf{1} \\
\hat{\mathbf{M}}(\mathbf{S}^2 - \hat{\mathbf{S}}^2) \cdot \mathbf{1} \\
\hat{\mathbf{M}}(\mathbf{S}^0 - \hat{\mathbf{S}}^0) \cdot \hat{\mathbf{S}}^1 - \hat{\mathbf{M}}(\mathbf{S}^1 - \hat{\mathbf{S}}^1) \cdot \hat{\mathbf{S}}^0 \\
\hat{\mathbf{M}}(\mathbf{S}^1 - \hat{\mathbf{S}}^1) \cdot \hat{\mathbf{S}}^2 - \hat{\mathbf{M}}(\mathbf{S}^2 - \hat{\mathbf{S}}^2) \cdot \hat{\mathbf{S}}^1 \\
\hat{\mathbf{M}}(\mathbf{S}^2 - \hat{\mathbf{S}}^2) \cdot \hat{\mathbf{S}}^0 - \hat{\mathbf{M}}(\mathbf{S}^0 - \hat{\mathbf{S}}^0) \cdot \hat{\mathbf{S}}^2
\end{pmatrix},
$$

which represents the left hand side in (6.3.4) with $\alpha = (\lambda, \mu)$. Moreover, $D^2_{(\mathbf{S},\lambda,\mu)}\mathcal{L}[\mathbf{S}, \lambda, \mu]$ is given by

$\partial_0 F^0[\mathbf{S}]$	$\partial_1 F^0[\mathbf{S}]$	$\partial_2 F^0[\mathbf{S}]$	$\hat{\mathbf{M}}\mathbf{1}$	$\mathbf{0}$	$\mathbf{0}$	$\hat{\mathbf{M}}\hat{\mathbf{S}}^1$	$\mathbf{0}$	$-\hat{\mathbf{M}}\hat{\mathbf{S}}^2$
$\partial_0 F^1[\mathbf{S}]$	$\partial_1 F^1[\mathbf{S}]$	$\partial_2 F^1[\mathbf{S}]$	$\mathbf{0}$	$\hat{\mathbf{M}}\mathbf{1}$	$\mathbf{0}$	$-\hat{\mathbf{M}}\hat{\mathbf{S}}^0$	$\hat{\mathbf{M}}\hat{\mathbf{S}}^2$	$\mathbf{0}$
$\partial_0 F^2[\mathbf{S}]$	$\partial_1 F^2[\mathbf{S}]$	$\partial_2 F^2[\mathbf{S}]$	$\mathbf{0}$	$\mathbf{0}$	$\hat{\mathbf{M}}\mathbf{1}$	$\mathbf{0}$	$-\hat{\mathbf{M}}\hat{\mathbf{S}}^1$	$\hat{\mathbf{M}}\hat{\mathbf{S}}^0$
$(\hat{\mathbf{M}}\cdot\mathbf{1})^T$ $\mathbf{0}^T$ $\mathbf{0}^T$			0	0	0	0	0	0
$\mathbf{0}^T$ $(\hat{\mathbf{M}}\cdot\mathbf{1})^T$ $\mathbf{0}^T$			0	0	0	0	0	0
$\mathbf{0}^T$ $\mathbf{0}^T$ $(\hat{\mathbf{M}}\cdot\mathbf{1})^T$			0	0	0	0	0	0
$(\hat{\mathbf{M}}\hat{\mathbf{S}}^1)^T$ $-(\hat{\mathbf{M}}\hat{\mathbf{S}}^0)^T$ $\mathbf{0}^T$			0	0	0	0	0	0
$\mathbf{0}^T$ $(\hat{\mathbf{M}}\hat{\mathbf{S}}^2)^T$ $-(\hat{\mathbf{M}}\hat{\mathbf{S}}^1)^T$			0	0	0	0	0	0
$-(\hat{\mathbf{M}}\hat{\mathbf{S}}^2)^T$ $\mathbf{0}^T$ $(\hat{\mathbf{M}}\hat{\mathbf{S}}^0)^T$			0	0	0	0	0	0

,

which is required to solve (6.3.4) via Newton's method. To this end, we replace (6.3.2) by

$$
D^2_{(\mathbf{S},\lambda,\mu)}\mathcal{L}[\mathbf{S}, \lambda, \mu] (\Delta\mathbf{S}, \Delta\lambda, \Delta\mu) = -D_{(\mathbf{S},\lambda,\mu)}\mathcal{L}[\mathbf{S}, \lambda, \mu],
$$

which has a unique solution $(\Delta\mathbf{S}, \Delta\lambda, \Delta\mu) \in \mathbb{R}^{3n} \times \mathbb{R}^3 \times \mathbb{R}^3$ since $D^2_{(\mathbf{S},\lambda,\mu)}\mathcal{L}$ is invertible. Note, that the solution depends on the chosen reference shell $\hat{\mathbf{S}}$ that prescribes the zeroth and first momentum. However, this dependence is not crucial and can be removed easily in a post-processing step by applying some kind of rigid registration to translate and rotate the solution to the desired place in space.

6.3.3 Multiresolution schemes

The efficiency of the nonlinear optimization can be increased by a *multiresolution scheme*, *cf*. *e.g.* [KCVS98, KVS99, GSS99, KBS00]. As Kilian *et al*. [KMP07], we decimate all input meshes simultaneously where we use the sum of per-mesh quadric error metrics proposed by Garland and Heckbert [GH97] to prioritize halfedge collapses. In particular, the coarse meshes still have the same connectivity since each halfedge collapse is applied to all input meshes. The nonlinear optimization, *e.g.* the minimization of the discrete path energy, is then performed on the coarse meshes, having less degrees of freedom. Afterwards, the solution of the coarse level is prolongated to the original resolution. This prolongated coarse solution turns out to be an excellent initial value to launch the optimization on the high resolution level, thus Newton's method typically converges within a few iterations (*cf*. Fig. 6.19). In principle, this two-step procedure can be extended to more levels, building a genuine hierarchy as in the context of *progressive meshes* [HDD+93, Hop96, Hop98]. Then the optimization is performed on each level, initialized with the prolongated solution of the previous level. In the remainder of this section we comment on the two main building blocks of an efficient and effective multiresolution scheme, *i.e.* the decimation and the prolongation.

Decimation   The quadric error metric [GH97] has been designed to maintain the overall geometrical shape as well as possible while decreasing the complexity of the mesh. In detail, a cost value is assigned to each edge E_{ij}, connecting vertex X_i and X_j, that reflects the violation of the local geometry if we collapse E_{ij} to a single vertex X_i resp. X_j, *i.e.* remove vertex X_j resp. X_i. Furthermore, a suggestion for the optimal position of the remaining vertex X_i resp. X_j is given along the way. Alternatively, one can position the remaining vertex along the previously removed edge, *i.e.* $X_k = \lambda X_i + (1 - \lambda) X_j$, if $k \in \{i, j\}$ is the global index of the remaining vertex. We refer to the author's diploma thesis [Hee11] for a detailed discussion of the decimation method.

Prolongation   The performance of the prolongation method is crucial for the quality of the initial value on the next level, *i.e.* the prolongated coarse solution, and hence for the overall convergence behaviour. In [KMP07] the prolongation is performed by (i) using so-called relative local coordinates and (ii) by propagating information gathered by the prolongation of the input shapes, see Sec. 4.3.2 in [Hee11] for details. In the fashion of classical progressive meshes, this method depends on several hierachical levels, hence multiple additional optimization parameters have to be adjusted.

To overcome this issue, we make use of an approach based on the separation of low frequency shape information from high frequency detail information (*cf*. [BK03, BK04]), since this method is built on the construction of only *two* levels, *i.e.* the original resolution and one additional coarse level. Usually, the coarse resolution contains at most thousand vertices and Newton's method converges within a few steps on the reduced space, in particular if we choose a smart initialization (*cf*. Sec. 6.3.1). Afterwards, the low frequency shape information—already captured in the coarse meshes—is prolongated to the high resolution by solving a Bi-Laplace equation. Finally, the high frequency information containing all geometrical details is reconstructed from a reference mesh by means of gradient-based deformation transfer [SP04, BSPG06]. This particular scheme has *e.g.* been used in [FB11] in the context of optimizing deformation energies of (discrete) shells. We refer to the appendix A.3 for a detailed description of the multiresolution scheme used in our implementation.
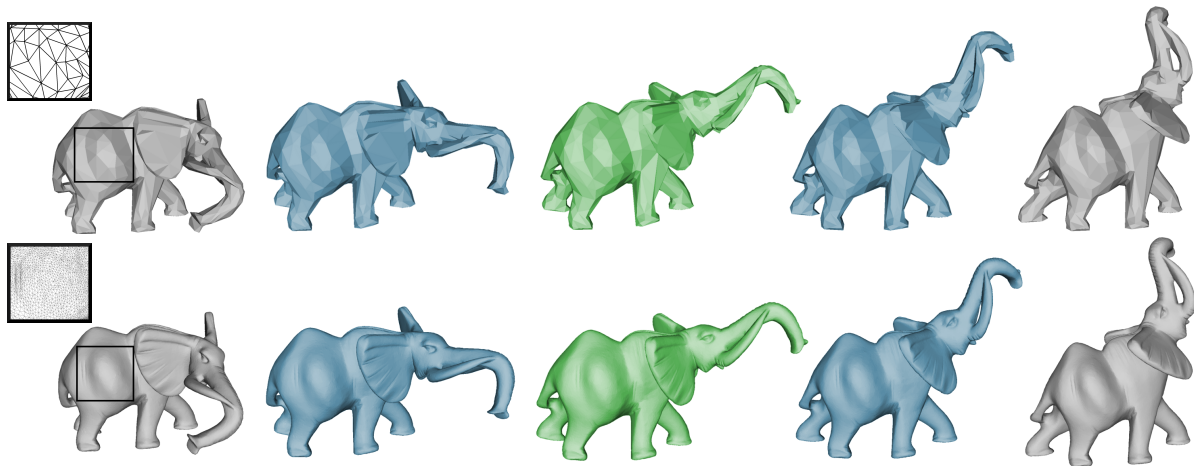
Figure 6.19: *A sketch of the multilevel computation of a time-discrete geodesic.*

Remark 6.3.1.   Note that we sometimes observe a lack of proper termination of the solver for large η values ($\eta > 1$) representing a strong bending energy. Another numerical difficulty is caused by the fact that the mesh decimation algorithm in its current implementation does not take into account the local deformation strength, which varies across the shell. Thus, regions of strong deformation might get coarsened although they should better stay finely resolved. To overcome this issue one could replace the quadric error metric by a metric sensitive to local dissipation rates.

6.4 Discussion and outlook

We have presented a comprehensive time-discrete geodesic calculus on the space of discrete shells which offers several useful tools in typical applications in computer graphics, such as interpolation, extrapolation and detail transfer. Those tools inherit beneficial properties from the underlying geometric structure of the shape space, *e.g.* the interpolation and extrapolation are consistent by definition as they are realized by geodesic connection and geodesic shooting, respectively. Furthermore, the variational time-discretization has proved to be a robust scheme that generates appealing results already for coarse time steps and is intrinsically suitable for a cascadic approach. From a physical point of view, the (discrete) deformation energy induces a physically sound metric on the space of (discrete) shells. The physical parameters can be used to control the visual appearance of the geodesic path in an intuitive and plausible manner. In particular, no additional and artificial regularizer has to be incorporated.

So far we have only considered a smooth (*i.e.* geodesic) interpolation between *two* shapes. In Sec. 7.1 we will modify our model in order to solve the *multiple interpolation* problem, *i.e.* find a smooth curve that interpolates between a couple of prescribed shapes. This method is in particular useful for keyframe animation, an important tool in typical computer graphics applications. From a computational point of view, there is still room for improvements, especially in terms of increasing the efficiency of the algorithm. Let us metion that there are several works using an efficient construction of subspaces which leads to a notable real-time performance in shape interpolation and deformation-based modeling [vTSSH15, BvTH16, vRESH16]. A different approach to accelerate computations is to combine our shell model with a skeleton based animation scheme (*cf*. *e.g.* [LCF00, WSLG07, JBK+12]). Moreover, it would be desirable to get rid of the fixed connectivity constraint in order to be able to compute geodesic paths between meshes with different connectivities. This could either be realized by adding a corresponding matching term at the beginning and end of the sequence or by using ideas from the *functional maps* representation introduced by Ovsjanikov *et al*. [OBCS+12].

Finally, it would be interesting to further exploit local curvature properties of the shell space. So far, little is known about the local and global curvature of shape spaces. Even though such knowledge may not have direct applications in shape animation or exploration, it will help to understand what can be expected from different geometric modeling approaches. For instance, shape spaces of an elliptic character (with positive curvature) may exhibit multiple different shortest geodesics between two given shapes. The example of non-unique shortest geodesics (*cf*. Fig. 6.8) thus reveals a (locally) positive curvature of shell space. Furthermore, initially parallel geodesics converge in a shape space with positive curvature, implying less freedom for shape deformation and modeling. On the other hand, geodesic paths in shape spaces of hyperbolic nature (with negative curvature) are expected to be unique. However, initially close geodesics diverge exponentially, implying instability with respect to small velocity perturbations. Finally, if a shape space turns out to be almost flat, then after a reparameterization of the shape space geodesics become straight lines and all Riemannian operations become linear, which might be exploited for efficient algorithms. Nevertheless, the computation of sectional curvatures by transporting vectors parallely along a closed loop (*cf*. Fig. 6.16) by means of Schild's ladder is numerically very unstable. In fact, Effland [Eff17] shows that the scaling has to be chosen very carefully, otherwise consistency cannot be expected. Moreover, he proposes a different local approximation of the curvature tensor which is shown to be consistent. Instead of using holonomy properties of the manifold one could also make use of a different curvature notion to exploit the local curvature properties in shell space. For example, the definition proposed by Wald [Wal35] approximates the Gauss curvature of an embedded surface locally by means of quadruples which can possibly be transferred to general manifolds.

7 Splines and statistics in shape spaces

In this chapter we present further applications of the fundamental concepts of the discrete geodesic calculus, *i.e.* the time-discrete geodesic and time-discrete exponential map. In Sec. 7.1 we apply the notion of Riemannian splines—developed in a general setup in Sec. 4.3—to the space of discrete shells. In particular, we propose an approximation that allows one to compute spline curves efficiently. In Sec. 7.2 we introduce a generalization of simple linear regression to a generic Riemannian manifold. We demonstrate and evaluate our discrete regression model on the space of viscous volumetric objects by means of real data applications both in 2D and 3D. Finally, we apply the elastic PCA model developed by Rumpf and Wirth [RW09a, RW09b, RW11a] to the space of discrete shells in Sec. 7.3. The results presented in the three sections of this chapter have been published in [HRS$^+$16], [BFH$^+$13] and [ZHRS15], respectively.

7.1 Time-discrete splines in the space of shells

In Sec. 4.3 we have introduced a notion of Riemannian splines as a tool for multiple interpolation in a general Riemannian manifold. Furthermore, we have proposed a consistent time-discretization that fits perfectly into the variational framework of the time-discrete geodesic calculus presented in Sec. 4.2. In this section we apply the notion of time-discrete splines to the space of discrete shells introduced in Sec. 5.2. Interpolating curves in the space of triangular meshes are useful for many applications in computer graphics such as keyframe based animation (*cf*. Fig. 7.2). In particular, globally smooth curves are more desirable than piecewise smooth curves, *cf*. Fig. 7.1. Using splines for smoothly interpolating keyframe poses of animated characters in Euclidean space goes back at least to the pioneering works of Kochanek and Bartels [KB84] and Lasseter [Lak87] in the 1980s. However, realizing shape interpolation through curves in the space of shells—which is considered as a Riemannian manifold—is relatively recent.

Using splines for solving the multiple interpolation problem in (discrete) shell space comes at a price, though. As seen in the previous chapter, the Riemannian metric on shell space is closely related to elastically deforming shells and encapsulates both bending and stretching contributions. For triangle meshes the bending contributions depend on dihedral angles, which are nonlinear functions of vertex positions (*cf*. Def. 6.0.2). Consequently, splines in shell space lead to highly nonlinear optimization problems, whose computational complexity must be reduced to yield practical algorithms.

To address this challenge we switch from vertex positions as primary variables to the so-called $L\Theta A$-*representation* in the spirit of [WDAH10] and [FB11]. In this formulation, the primary variables are the edge lengths of triangles (L), dihedral angles between adjacent triangles (Θ), and triangle areas (A). Splines in $L\Theta A$-space can be evaluated through solving a simple linear system. However, the
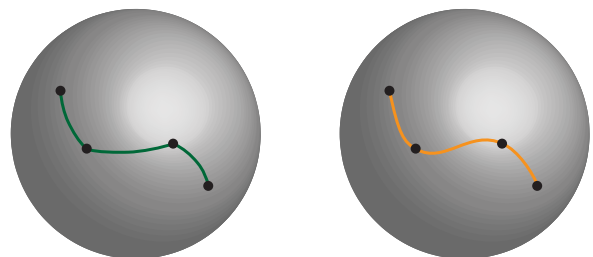
Figure 7.1: *Piecewise geodesic (left) vs. spline (right) interpolation on Riemannian manifolds (sphere for illustration). Notice C^1-discontinuities for piecewise geodesic interpolation.*

resulting curve in $L\Theta A$-space will in general not be realizable as a sequence of triangle meshes in 3D Euclidean space. Instead, we project to the closest curve of realizable triangle meshes in a least squares sense. Overall, this formulation greatly outperforms nonlinear optimization for computing splines based on vertex positions.
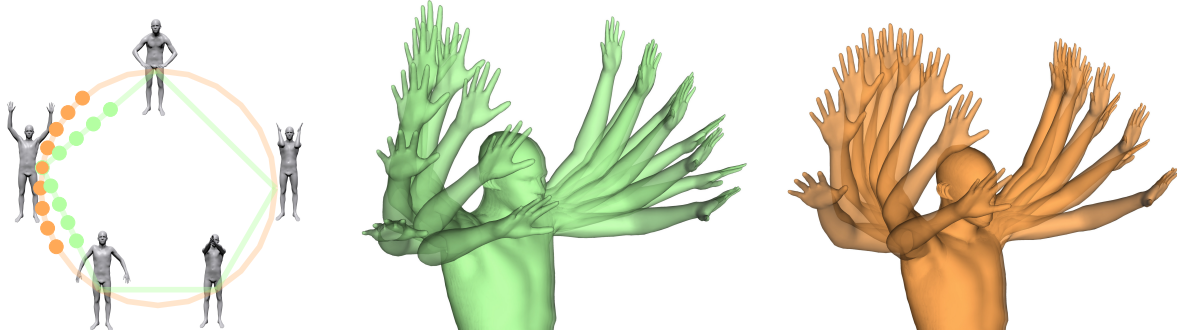
Figure 7.2: *A (periodic) spline in shell space (orange) allows for a temporally smooth interpolation of a given set of shell keyframe poses (gray, left), in contrast to a piecewise geodesic interpolation (green). In particular, the trajectories of the right hand of the character illustrate the smoothness of the spline when compared to the piecewise geodesic curve.*

In order to keep this section self-contained, we recall the notion of time-discrete splines in Sec. 7.1.1 before applying them to discrete shell space. To improve the performance and efficiency of our algorithm we introduce the $L\Theta A$-representation as a suitable approximation in Sec. 7.1.2. In Sec. 7.1.3 we give details on the implementation and finally we discuss and compare our models in Sec. 7.1.4.

Remark 7.1.1. All results presented in this section are joint work with Martin Rumpf, Peter Schröder, Max Wardetzky and Benedikt Wirth, and have been published in [HRS$^+$16].

7.1.1 Nonlinear approach

Splines on Riemannian manifolds   Given a sequence of $J \geq 2$ different time points $t_j \in [0, 1]$ and associated data points as keyframe poses $y^j \in \mathcal{M}$, $j = 1, \ldots, J$, we seek a smooth curve $y : [0, 1] \to \mathcal{M}$ that satisfies the *interpolation constraints*

$$y(t_j) = y^j, \quad j = 1, \ldots, J. \tag{7.1.1}$$

For $J > 2$ there is in general no interpolating geodesic, *i.e.* a curve y satisfying (7.1.1) as well as $\frac{D}{dt}\dot{y}(t) = 0$ for all $t \in [0, 1]$. Moreover, piecewise geodesic interpolation paths are not smooth at the times t_j. As motivated already in Sec. 4.3, we tackle this problem by relaxing the condition $\frac{D}{dt}\dot{y} = 0$. Instead of requiring the interpolating curve to satisfy $\frac{D}{dt}\dot{y} = 0$ exactly, we can penalize a deviation from this constraint by introducing the *spline energy* (*cf*. (4.3.1))

$$\mathcal{F}[y] = \int_0^1 g_{y(t)}\left(\frac{D}{dt}\dot{y}(t), \frac{D}{dt}\dot{y}(t)\right) \mathrm{d}t.$$

In addition to the interpolation constraints, we may optionally impose one of the two boundary conditions

$$\dot{y}(0) = v_0, \quad \dot{y}(1) = v_1 \quad \text{for given } v_0, v_1 \in T\mathcal{M}, \qquad \text{(Hermite b. c.)}$$
$$y(0) = y(1), \quad \dot{y}(0) = \dot{y}(1), \qquad \text{(periodic b. c.)}$$

where $T\mathcal{M}$ denotes the tangent bundle on $\mathcal{M}$. The case without additional conditions is referred to as natural boundary condition. In Sec. 4.3 we have seen that for $\mathcal{M} = \mathbb{R}^d$ equipped with the Euclidean

metric minimizers of $\mathcal{F}$ are given by cubic splines [dB63]. Accordingly, we denoted a minimizer y of $\mathcal{F}[y]$ under the interpolation constraint (7.1.1) as a *Riemannian spline*. In Def. 4.3.3 we have defined the time-discrete spline energy based on a generic dissimilarity measure $\mathcal{W}$ by

$$F^K[y_0, \ldots, y_K] = 4K^3 \sum_{k=1}^{K-1} \mathcal{W}[y_k, \tilde{y}_k], \tag{7.1.2}$$

for a discrete path $(y_0, \ldots, y_K)$. Here, $\tilde{y}_k$ is defined by requiring that $(y_{k-1}, \tilde{y}_k, y_{k+1})$ is a time-discrete geodesic connecting y_{k-1} and y_{k+1} for $k = 1, \ldots, K - 1$, *i.e.*,

$$\tilde{y}_k = \underset{y \in \mathcal{M}}{\arg\min} \left(\mathcal{W}[y_{k-1}, y] + \mathcal{W}[y, y_{k+1}] \right). \tag{7.1.3}$$

We have proved in Thm. 4.3.11 that F^K is a consistent first-order approximation of $\mathcal{F}$ (under suitable assumptions on the manifold $\mathcal{M}$ and on $\mathcal{W}$). However, as mentioned in Rem. 4.3.2 resp. Rem. 4.3.4, existence of minimizers is not guaranteed. This issue can be resolved by augmenting the (discrete) spline energy by the (discrete) path energy [HRW16]. Nevertheless, we stick to the spline energy (without adding the path energy) since we never observed instabilities or blow-ups in our applications.

Splines in shell space   Now we apply the notion of (time-discrete) interpolating splines to the discrete shell space introduced in Sec. 5.2. As before we assume the fixed-connectivity constraint (*cf*. Def. 5.2.2). Hence we can identify a discrete shell with its vector of nodal positions $\mathbf{S} \in \mathbb{R}^{3n}$, where n is the number of vertices of one triangle mesh. As in Def. 6.0.2, we make use of a discrete deformation energy $\mathbf{W}$ to obtain a suitable *discrete* dissimilarity measure on discrete shell space, which is then used to replace the *continuous* dissimilarity measure $\mathcal{W}$ in (7.1.2) and (7.1.3), respectively. Yet different from Def. 6.0.2, we will define $\mathbf{W}$ to be the full *Discrete Shells* energy as proposed in [GHDS03]. This choice will allow us to directly derive a corresponding energy in the simplified $L\Theta A$-space, which will be considered in Sec. 7.1.2.

For a discrete shell $\mathbf{S} \in \mathbb{R}^{3n}$, let $L[\mathbf{S}] = (l_E[\mathbf{S}])_E \in \mathbb{R}^{|\mathcal{E}|}$, $\Theta[\mathbf{S}] = (\theta_E[\mathbf{S}])_E \in \mathbb{R}^{|\mathcal{E}|}$ and $A[\mathbf{S}] = (a_T[\mathbf{S}])_T \in \mathbb{R}^{|\mathcal{T}|}$ be the vector of edge lengths, dihedral angles and triangle areas, respectively. Furthermore, we associate to an edge E the area measure $d_E = \frac{1}{3}(a_{T_1} + a_{T_2})$, if $E = T_1 \cap T_2$. Having these definitions at hand, our discrete deformation energy for deforming $\mathbf{S}$ into $\tilde{\mathbf{S}}$ is

$$\mathbf{W}[\mathbf{S}, \tilde{\mathbf{S}}] = \mu \, \mathbf{W}_L[\mathbf{S}, \tilde{\mathbf{S}}] + \lambda \, \mathbf{W}_A[\mathbf{S}, \tilde{\mathbf{S}}] + \eta \, \mathbf{W}_\Theta[\mathbf{S}, \tilde{\mathbf{S}}], \tag{7.1.4}$$

with physical parameters $\mu, \lambda, \eta \geq 0$ and

$$\mathbf{W}_L[\mathbf{S}, \tilde{\mathbf{S}}] = \sum_{E \in \mathcal{E}} d_E[\mathbf{S}] \Big(\frac{l_E[\mathbf{S}] - l_E[\tilde{\mathbf{S}}]}{l_E[\mathbf{S}]} \Big)^2,$$

$$\mathbf{W}_A[\mathbf{S}, \tilde{\mathbf{S}}] = \sum_{T \in \mathcal{T}} a_T[\mathbf{S}] \Big(\frac{a_T[\mathbf{S}] - a_T[\tilde{\mathbf{S}}]}{a_T[\mathbf{S}]} \Big)^2,$$

$$\mathbf{W}_\Theta[\mathbf{S}, \tilde{\mathbf{S}}] = \sum_{E \in \mathcal{E}} l_E[\mathbf{S}]^2 \frac{(\theta_E[\mathbf{S}] - \theta_E[\tilde{\mathbf{S}}])^2}{d_E[\mathbf{S}]}.$$

Note that $\mu \, \mathbf{W}_L + \lambda \, \mathbf{W}_A$ can be considered as a quadratic approximation of $\mathbf{W}_{\mathrm{mem}}$ in Def. 6.0.2, whereas $\mathbf{W}_\Theta$ coincides exactly with $\mathbf{W}_{\mathrm{bend}}^{\mathrm{DS}}$ defined in (5.3.12) and used in Def. 6.0.2. The colored font is for later reference when we introduce our $L\Theta A$-approximation for efficiently computing splines.
In all numerical experiments we use $\mu = \lambda = 1$, since local change of length (controlled by μ) and local change of area (controlled by λ), respectively, should be penalized equally. However, the optimal
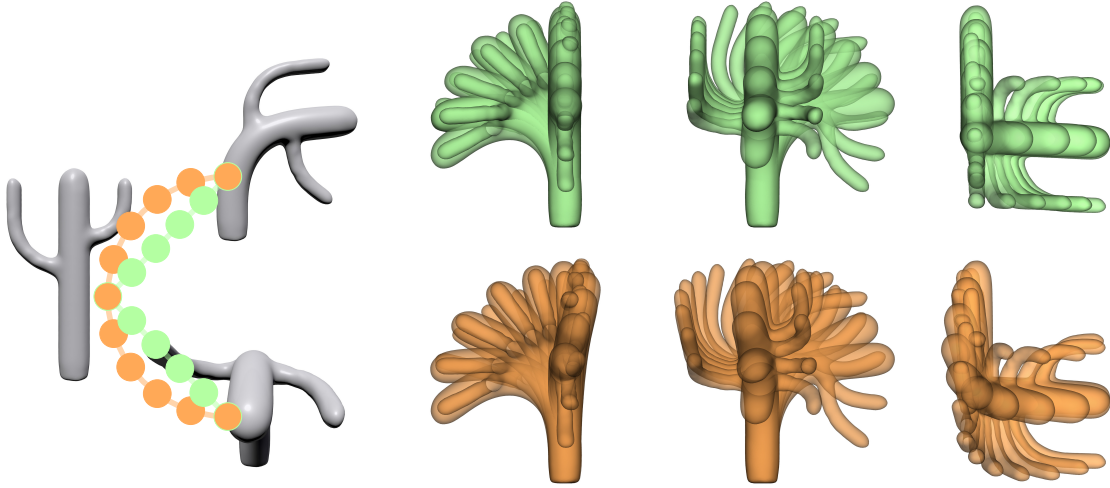
Figure 7.3: *Left: $J = 3$ fixed keyframe poses (gray). Right: Different views of piecewise geodesic (green) and spline interpolation (orange), respectively, using $K = 10$, $\eta = 10^{-3}$.*

bending parameter $\eta = \delta^2$ depends on the application since δ represents the physical thickness of the shell (see Fig. 7.7).

We aim at computing a spline curve in discrete shell space that interpolates a given set of discrete shells $\mathbf{S}^j \in \mathbb{R}^{3n}$ at times $t_j = k_j \tau$ with $j = 1, \ldots, J$, where we assume $k_j \in \{0, \ldots, K\}$ without loss of generality[1]. To this end, one has to minimize the discrete spline energy

$$\mathbf{F}^K[\mathbf{S}_0, \ldots, \mathbf{S}_K] = 4K^3 \sum_{k=1}^{K-1} \mathbf{W}[\mathbf{S}_k, \tilde{\mathbf{S}}_k]\,, \tag{7.1.5}$$

among all discrete curves $(\mathbf{S}_0, \ldots, \mathbf{S}_K)$ subject to the interpolation conditions $\mathbf{S}_{k_j} = \mathbf{S}^j$ for $t_j = k_j \tau$ and $j = 1, \ldots, J$ and the additional built-in constraints

$$\tilde{\mathbf{S}}_k = \underset{\mathbf{S} \in \mathbb{R}^{3n}}{\arg\min} \left(\mathbf{W}[\mathbf{S}_{k-1}, \mathbf{S}] + \mathbf{W}[\mathbf{S}, \mathbf{S}_{k+1}] \right), \quad 0 < k < K\,. \tag{7.1.6}$$

Fig. 7.3 depicts a discrete spline curve for three different keyframe poses of a cactus-type discrete shell and compares it to the piecewise geodesic interpolation ($K = 10$). The boundary keyframe poses $\mathbf{S}_0$ and $\mathbf{S}_{10}$ are given as deformations of the cactus rest pose $\mathbf{S}_5$ in two orthogonal directions, which leads to a sharp corner at $\mathbf{S}_5$ when performing piecewise geodesic interpolation.

Boundary conditions   Our exposition has so far focussed on natural boundary conditions. Periodic boundary conditions are incorporated by identifying $\mathbf{S}_k = \mathbf{S}_{(k+K) \bmod K}$ for $k = 0, \ldots, K$. Hermite boundary conditions, which prescribe endpoint velocities and are useful for blending purposes, are incorporated in the time-discrete setup by fixing $\mathbf{S}_0$ and $\mathbf{S}_1$ as well as $\mathbf{S}_{K-1}$ and $\mathbf{S}_K$, respectively. A comparison of Hermite and natural boundary conditions is shown in Fig. 7.4.

Limitations   Although the interpolating spline curves in discrete shell space look very nice, a big limitation is computational time. Indeed, since the mappings $\mathbf{S} \mapsto \{l_E[\mathbf{S}], d_E[\mathbf{S}], \theta_E[\mathbf{S}], a_T[\mathbf{S}]\}$ are nonlinear functions, the minimization of $\mathbf{F}^K$ is a nonlinear problem in $\mathbb{R}^{3n(K+1-J)}$ with $K - 1$ nonlinear constraints given by (7.1.6). In our numerical experiments this leads to slow convergence even for relatively small n and K. For example, the computation of the short cactus sequence ($n = 5261$, $K = 10$)

---

[1] This restriction can easily be removed using varying time step sizes and suitable adaptations of the energy.
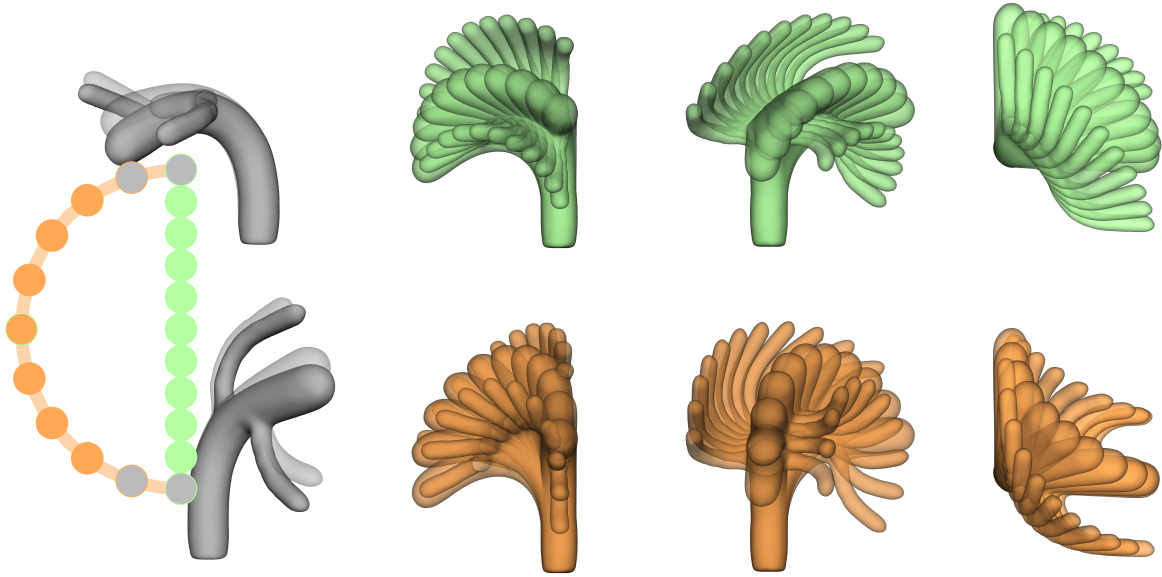
Figure 7.4: *Interpolation of two keyframe poses (gray) via a spline curve with natural boundary conditions (green; equivalent to a geodesic curve) and with Hermite boundary conditions (orange) for $K = 10$, $\eta = 10^{-3}$. The Hermite boundary conditions are emulated by fixing two additional keyframe poses $\mathbf{S}_1$ and $\mathbf{S}_9$ (light gray, taken from the piecewise geodesic curve in Fig. 7.3).*

shown in Fig. 7.3 can take several hours. In order to overcome this limitation, we will introduce an effective change of variables in the next section.

7.1.2 L⊖A approximation

To remedy the problem of high computational cost, we introduce a change of variables in order to turn the nonlinear optimization problem for computing splines in shell space into a linear one. For this change of coordinates we heavily build on the two-step approximation scheme proposed by Fröhlich and Botsch [FB11]. In detail, for a discrete shell $\mathbf{S} \in \mathbb{R}^{3n}$ we consider the vectors of edge lengths $L = L[\mathbf{S}]$, dihedral angles $\Theta = \Theta[\mathbf{S}]$, and triangle areas $A = A[\mathbf{S}]$ as primary degrees of freedom. The key observation is that with these degrees of freedom, the discrete deformation energy $\mathcal{W}$ becomes *quadratic*, provided that the terms in (7.1.4) which depend on purple colored shells are *not* part of the optimization. To achieve this, we work with what we call *reference meshes*, *i.e.*, we replace the purple colored terms in (7.1.4) by a priori given meshes $(\hat{\mathbf{S}}_0, \ldots, \hat{\mathbf{S}}_K)$. In the simplest case, this a priori information is given by using a constant reference mesh $\hat{\mathbf{S}}_k = \mathbf{S}$, $k = 0, \ldots, K$, for one particular keyframe pose $\mathbf{S} \in \mathbb{R}^{3n}$.

Collecting all new primary variables in one variable $\mathbf{Z} = (L, \Theta, A)$ living in the $L\Theta A$-configuration space $\mathcal{Z} := \mathbb{R}^{|\mathcal{E}|} \times \mathbb{R}^{|\mathcal{E}|} \times \mathbb{R}^{|\mathcal{T}|}$, we get an approximation of (7.1.4) via

$$\widehat{\mathbf{W}}_{L\Theta A}[\mathbf{Z}, \tilde{\mathbf{Z}}] = \mu \widehat{\mathbf{W}}_L[L, \tilde{L}] + \lambda \widehat{\mathbf{W}}_A[A, \tilde{A}] + \eta \widehat{\mathbf{W}}_\Theta[\Theta, \tilde{\Theta}], \tag{7.1.7}$$

where the $\widehat{}$ indicates that the functional is now quadratic but dependent on the reference meshes. We refer to this as the $L\Theta A$-energy. Note that the parameters $\mu, \lambda, \eta \geq 0$ have the same physical interpretation as in (7.1.4). As in the nonlinear setup we set $\mu = \lambda = 1$ and chose $\eta = \delta^2$ depending on the application. The discrete interpolation problem can now be re-formulated as follows. We construct a spline curve in the $L\Theta A$-space defined as a minimizer of

$$\hat{\mathbf{F}}_{L\Theta A}^K[\mathbf{Z}_0, \ldots, \mathbf{Z}_K] = 4K^3 \sum_{k=1}^K \widehat{\mathbf{W}}_{L\Theta A}(\mathbf{Z}_k, \tilde{\mathbf{Z}}_k), \tag{7.1.8}$$

where $(\mathbf{Z}_{k-1}, \tilde{\mathbf{Z}}_k, \mathbf{Z}_{k+1})$ is a geodesic in the $L\Theta A$-space, *i.e.*,

$$\tilde{\mathbf{Z}}_k = \underset{\mathbf{Z} \in \mathcal{Z}}{\arg\min} \left(\widehat{\mathbf{W}}_{L\Theta A}[\mathbf{Z}_{k-1}, \mathbf{Z}] + \widehat{\mathbf{W}}_{L\Theta A}[\mathbf{Z}, \mathbf{Z}_{k+1}] \right) .$$

Since $\widehat{\mathbf{W}}_{L\Theta A}$ is *quadratic*, one obtains the explicit solution $\tilde{\mathbf{Z}}_k$ as a linear combination of $\mathbf{Z}_{k-1}$ and $\mathbf{Z}_{k+1}$ with coefficients depending on $\hat{\mathbf{S}}_{k-1}$ and $\hat{\mathbf{S}}_k$ only. In particular, if we make use of a constant reference mesh, then $\tilde{\mathbf{Z}}_k = \frac{1}{2}(\mathbf{Z}_{k-1} + \mathbf{Z}_{k+1})$. This can be inserted into (7.1.8) so that we end up with an *unconstrained* optimization problem. Hence a minimizer of (7.1.8) is a (weighted) cubic spline in the linear space $\mathcal{Z} = \mathbb{R}^{|\mathcal{E}|} \times \mathbb{R}^{|\mathcal{E}|} \times \mathbb{R}^{|\mathcal{T}|}$.

Note that there is no interaction between edge lengths, triangle areas and dihedral angles in a minimizer $(\mathbf{Z}_0, \dots, \mathbf{Z}_K)$ of (7.1.8). Moreover, there is no *spatial* coupling between any two different edge lengths, *i.e.*, an edge length l_E^k of the kth pose interacts only with lengths l_E^j of the same edge E and poses $j \neq k$. The same applies for dihedral angles and triangle areas. As a consequence, the Euler-Lagrange equation for (7.1.8) splits into numerous independent $(K+1)$-dimensional linear systems, *i.e.*, one for each edge length, dihedral angle, and triangle area, which can be solved efficiently and in parallel. Moreover, if one chooses a constant reference mesh, then the matrices representing these linear systems are all given by

$$\begin{pmatrix} 1 & -2 & 1 & & & \\ -2 & 3 & -4 & 1 & & \\ 1 & -4 & 6 & -4 & 1 & \\ & 1 & -4 & 6 & -4 & 1 \\ & & & & \ddots \end{pmatrix} \in \mathbb{R}^{K+1,K+1},$$

which coincides (for interior quantities) to the 2nd order finite difference approximation of 4th derivatives.

However, intermediate values for edge lengths, dihedral angles, and triangle areas, provided by a minimizer $(\mathbf{Z}_0, \dots, \mathbf{Z}_K)$ of (7.1.8), are generally not realizable as an embedded triangle mesh. Hence we consider a reconstruction in a least squares sense, similar to [FB11]. For given optimal values $\mathbf{Z}_k = (L_k, \Theta_k, A_k)$ we define $\mathbf{S}_k$ as the minimizer of the nonlinear mapping

$$\mathbf{S} \mapsto \widehat{\mathbf{W}}_{L\Theta A}(\mathbf{Z}[\mathbf{S}], \mathbf{Z}_k) , \tag{7.1.9}$$

where $\widehat{\mathbf{W}}_{L\Theta A}$ is defined as in (7.1.7). We find the minimizer via the Gauss–Newton method (see Section 6 in [FB11] for details, the "target" values are given by $\mathbf{Z}_k$). Furthermore we use exactly the same physical parameters $\mu, \lambda, \eta \geq 0$ as in the optimization of (7.1.8). The reconstruction can be seen as a projection of the point $\mathbf{Z} \in \mathcal{Z}$ onto the submanifold which is given by all sets of edge lengths, dihedral angles and triangle areas that are actually realizable as an embedded triangle mesh. Necessary conditions for points to lie in this submanifold are given by the Gauss-Codazzi equations, see, *e.g.*, [WLT12] for a discrete version. Computationally, the reconstruction is the hardest part in the $L\Theta A$-space approximation method. Fortunately, it can be parallelized.

Remark 7.1.2. Optimal $\mathbf{Z}$-variables obtained as solutions of linear systems may have negative lengths or areas. This happens rarely in practice and is most easily addressed by setting corresponding edge or area weights to zero (in the reconstruction).

Remark 7.1.3. Different from [FB11], we use an additional area term, *i.e.*, $\lambda > 0$ in (7.1.4) and (7.1.7). While we empirically found that this term is not required for meshes with a reasonable aspect ratio, there are examples (*e.g.*, the running horse application) where we observe artifacts in the reconstruction if $\lambda = 0$. Moreover, when optimizing (7.1.5), the stability of the optimization is increased and the convergence time is decreased if $\lambda > 0$.

7.1.3 Implementation

The nonlinear minimization of (7.1.5) under constraint (7.1.6) is solved via a gradient descent with step-size control in all primal variables $\mathbf{S}_k$; in the appendix of [HRS$^+$16] we provide the requisite partial derivatives. Again, the optimization is performed within the multiresolution scheme presented in Sec. 6.3.3, which is built on the gradient-based *deformation transfer* introduced in [SP04, BSPG06] and summarized in the appendix A.3. This multiresolution scheme is used for the optimization of (7.1.5) as well as for minimizing (7.1.9). The issue of the inheret rigid body motion invariance is again resolved as described in Sec. 6.3.2.

Our $L\Theta A$-space approximation consists of four steps:
1. simultaneous mesh decimation for all keyframe poses,
2. $L\Theta A$-space optimization based on solution of multiple but small linear systems (on coarse level),
3. mesh reconstruction by means of Gauss–Newton (on coarse level),
4. prolongation to fine level.

For the reconstruction—the computationally dominant part—we reproduce the computation times stated in [FB11], as listed in Table 7.1.

	#nodes	G.-N.	decim.	reconstr.
cactus	5.2k	500	140	80
horse	8.5k	700	190	130
armadillo	166k	/	7800	3800

Table 7.1: *Performance statistics for mesh reconstruction (times in ms) measured on Dell Intel(R) Core(TM) i7-2600 3.40GHz. From left to right: number of vertices of high resolution mesh, time for one Gauss–Newton iteration on the original resolution, for the multiresolution preprocessing,* i.e., *the generation of coarse meshes from fine meshes (decimation), and for the reconstruction (see [FB11, Tab. 1]). On the coarse mesh, one Gauss–Newton step takes about 50ms. On the original Armadillo model, the Gauss–Newton step failed due to memory restrictions.*

model (K, γ)	decim.	coarse opt./recon.	prol.	fine opt./recon.
cactus (20, .05)	0.1	1.7	1.7	83
cactus (170, .05)	0.3	22	14	762
horse (40, .10)	0.2	22	5	238
armad. (50, .006)	5.2	80	200	/

Table 7.2: *Total runtime (in s, without parallelization) of $L\Theta A$-space scheme for computing spline curves of length $K + 1$: mesh decimation with γ indicating the fraction of remaining nodes, optimization and reconstruction on coarse level, prolongation using detail transfer, and optimization and reconstruction on fine level using the previous result as initialization for the reconstruction step.*

To enable real-time computations one can take the prolongation of the coarse solution as the final solution, which is visually sufficient. In some examples, we observe local mesh degenerations in single shapes after reconstruction and prolongation, *e.g.*, at the fingers in Fig. 7.2 and the tail in Fig. 7.6, which are removed in a post-processing step. One may also perform the $L\Theta A$-optimization for the high resolution keyframe poses. However, in our experiments, the resulting shells may differ quantitatively but not qualitatively from the computationally more efficient prolongation of coarse grid discrete spline curves. Total runtimes (without parallelization) of the $L\Theta A$-space approximation are shown in Table 7.2. In addition, the reconstruction and the prolongation (which amounts to more than 90% of the cost) can easily be parallelized, thereby reducing runtime proportionally to the number of available threads.

7.1.4 Discussion and outlook

If we compare the spline interpolation to piecewise geodesic interpolation, there are two striking differences: (i) The trajectory of the spline curve exhibits a time-continuous acceleration ($\nabla_{\dot{y}}\dot{y}$) and thus is visually smooth, whereas a piecewise geodesic curve suffers from corners at the keyframe poses (see Fig. 7.2, 7.3, 7.10). The continuous acceleration can in particular be seen in the energy plots in Fig. 7.11 and 7.12. (ii) The spline curve balances acceleration along the path leading to a continuous variation in speed (see Fig. 7.5), whereas the piecewise geodesic approximately has (piecewise) constant speed. Furthermore, splines can incorporate different kinds of boundary conditions, which leads to flexibility in animation, compare, *e.g.*, Fig. 7.3 and 7.4.
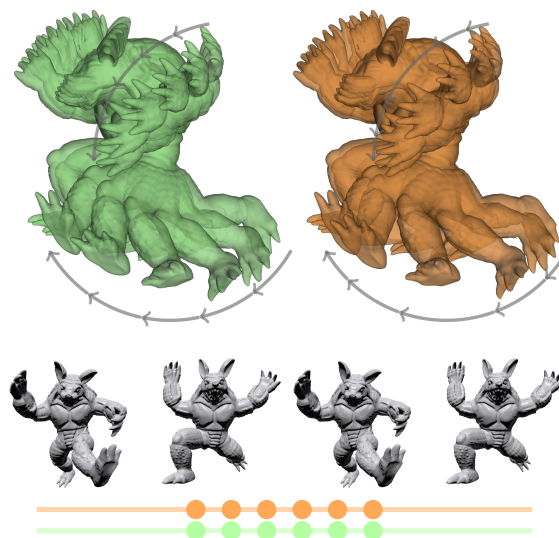

Figure 7.5: Piecewise geodesic (green) and spline curve interpolation (orange) induce similar trajectories but differences in speed.

Overshooting As in the Euclidean case, a particular feature of spline interpolation is the so-called overshooting—a consequence of the smoothness requirement. Fig. 7.6 shows an example of this effect for the case of (discrete) Riemannian splines in shell space (orange shapes). For certain applications this feature might be undesired, though.
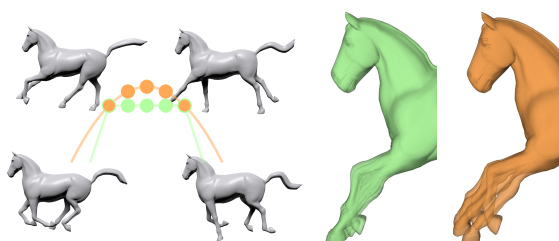

Figure 7.6: Overshooting in spline interpolation.

Dependence on physical parameters Given a set of input shells the resulting spline depends on the physical parameters λ, μ, and η of the model (see Fig. 6.4 for the dependence of discrete geodesics on λ and μ). Let us focus here on the dependence of splines on the thickness parameter η. In the limit $\eta \to 0$ the energy $\mathbf{W}$ measures the deviation from isometric deformations so that a spline stays near the submanifold of isometrically deformed shells. For larger values of η splines may leave this submanifold—also for input shells which are all isometric to each other. Such an example is depicted in Fig. 7.7, where we computed a periodic spline $D \to E \to F \to D$ with different bending weights. Note that all input shells D, E, F are isometric deformations of a regular and flat hexagon H. For $\delta = 10^{-4}$ the spline (almost) stays in the subspace of isometric deformations of H, whereas this is no longer the case for $\delta = 10$, as can be seen by the bending of the middle shape in the bottom row.
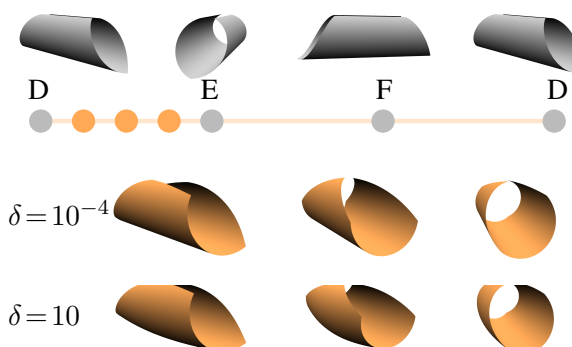
Figure 7.7: Periodic spline $D \to E \to F \to D$ with $K = 12$ and different bending weights $\eta = \delta^2$. The discrete segments $E \to F$ and $F \to D$ are not shown due to the symmetry of the problem.

Physical soundness The nonlinear model is consistent with the notion of Riemannian splines and follows rigorously from the underlying physical model. The simplified $L\Theta A$-model shows the same qualitative behavior as the nonlinear model and is significantly more efficient. Indeed, the simplified energy is quadratic, and geometric compatibility conditions between the triangle lengths, angles, and areas are ignored during the energy minimization, resulting in many but small easily solvable decoupled problems. Yet, using reference meshes in order to obtain a quadratic energy might seem unsatisfactory from a physical point of view since strains are measured with respect to these (artificial) reference meshes.

A more physical approach could be recovered by a fixpoint iteration that alternates between computing an interpolation path via minimizing (7.1.8) and updating the reference meshes. As exemplified in Fig. 7.8 such a fixpoint iteration is expected to converge but typically only leads to very minor interpolation corrections. The decoupling between edge lengths, dihedral angles, and triangle areas represents a more severe deviation from the original model, which may result in different interpolation paths already for simple cases (*cf*. Fig. 7.10).
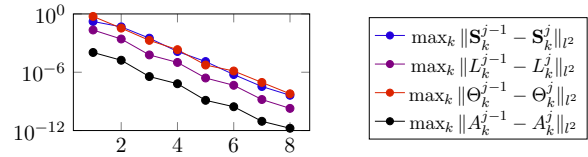

Figure 7.8: Maximum difference in cactus sequence from Fig. 7.3 for $j = 1, \dots, 8$ fixpoint iterations, measured in different norms.

Robustness While the $L\Theta A$-model enables fast computations and works for large K and n, the Gauss–Newton iteration inside the $L\Theta A$-scheme is quite sensitive to mesh quality and physical parameters. For example, it sometimes requires a fine parameter tuning in order to enforce convergence to non-degenerate meshes in all reconstructions. In contrast, the constrained optimization of the nonlinear model is very robust and prevents any mesh degenerations.

Mathematical well-posedness Since the $L\Theta A$-model mainly acts in the Euclidean $L\Theta A$-configuration space, it enjoys all nice mathematical properties of standard Euclidean spline interpolation. In contrast, the existence and convergence analysis for the nonlinear model (*i.e.*, the minimization of $\mathcal{F}$ in the continuous and F in the discrete case) is considerably more involved. Nevertheless it can be performed exploiting similar variational tools as have been used in [RW15]. For details we refer to [HRW16].

Outlook We currently work on a reformulation of the fully nonlinear model that does not depend on nonlinear constraints anymore. A generalization of the parallelogram law leads to the time-discrete functional $\tilde{\mathbf{F}}^K$ as defined in (4.3.14). However, this does not offer a consistent approximation of the spline functional as shown in Sec. 4.3.3. In practice, nevertheless, minimizers of $\tilde{\mathbf{F}}^K$ are often very good approximations of minimizers of the time-discrete spline functional $\mathbf{F}^K$ (as defined in (7.1.5)). The results shown in Fig. 7.9 are based on the input data
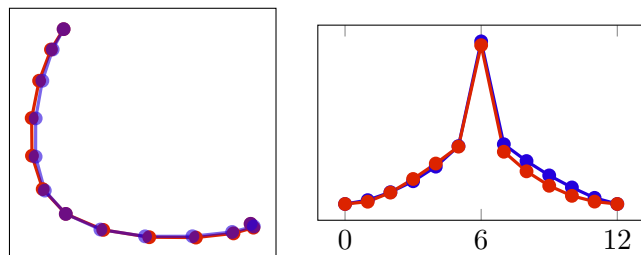

Figure 7.9: Minimizer of $\tilde{\mathbf{F}}^K$ (blue) and of $\mathbf{F}^K$ (red). Left: trajectory of top node of cactus, right: energy density plots.

from Fig. 7.3 with $K = 12$, fixing $\mathbf{S}_k$ for $k \in \{0, 6, 12\}$. Since the minimizer of $\tilde{\mathbf{F}}^K$ and $\tilde{\mathbf{F}}^K$, respectively, are visually indistinguishable, we plot the trajectory of the top node of the cactus in the (x, y)-plane (Fig. 7.9, left). A quantitative comparison in terms of the mapping $k \mapsto \mathbf{W}[\mathbf{S}_k, \tilde{\mathbf{S}}_k]$, with $(\mathbf{S}_{k-1}, \tilde{\mathbf{S}}, \mathbf{S}_{k+1})$ being a discrete geodesic, is shown in Fig. 7.9 (right).
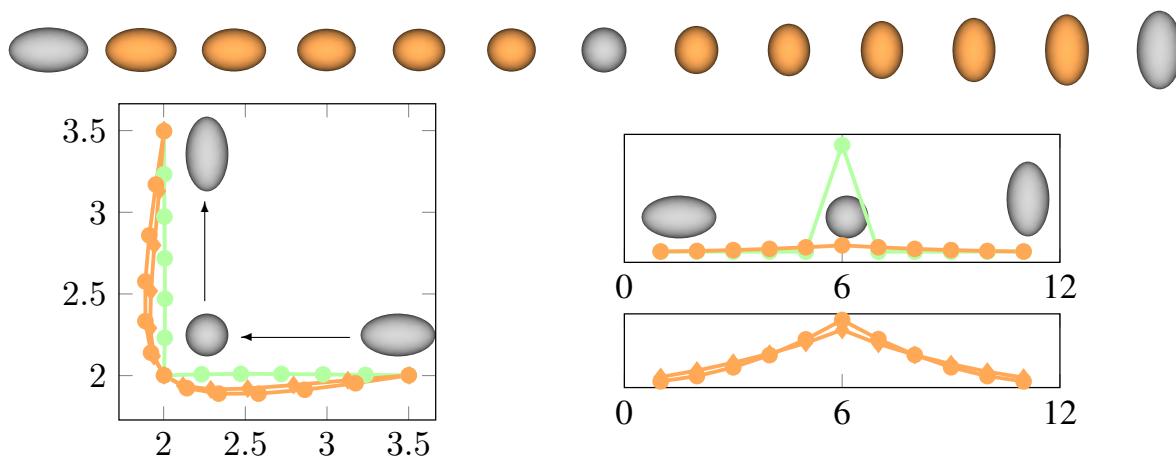
Figure 7.10: *Top row: Spline curve interpolation between $J = 3$ fixed ellipsoids ($K = 12$, $\eta = 10^{-1}$). Bottom, left: Representation of ellipsoids in $\mathbb{R}^2$ by their half axes in x- and y-directions. Plotting the evolution of eccentricity along the deformation one can see the difference between the piecewise geodesic (green), the nonlinear spline (orange circles), and the $L\Theta A$-space approximation (orange diamonds). Bottom, right: Comparison in terms of the energy density $k \mapsto W[\mathbf{S}_k, \tilde{\mathbf{S}}_k]$ of piecewise geodesic (green) vs. nonlinear spline (orange, top) and analogous comparison of the nonlinear spline vs. the $L\Theta A$-space curve (bottom, ordinate rescaled by 10).*
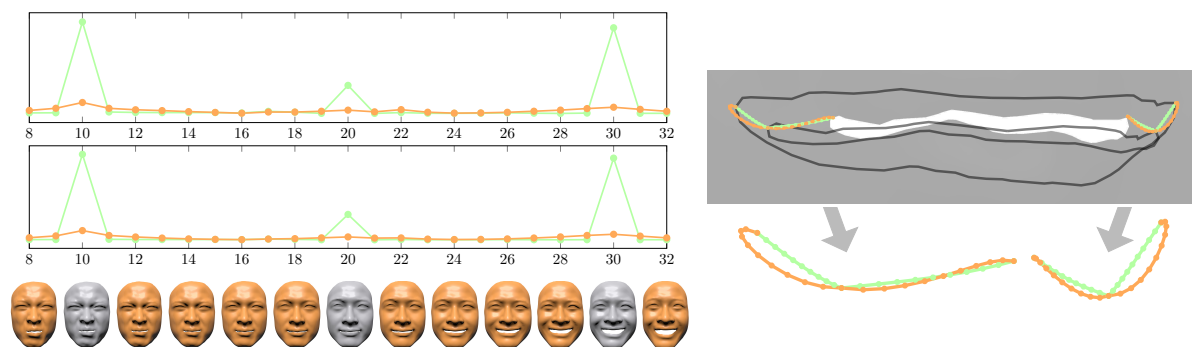

Figure 7.11: *Left: Extract from a spline curve through five fixed keyframe poses (at $k = 0, 10, 20, 30, 40$, three of which are shown in gray) computed via the $L\Theta A$-scheme ($\eta = 1$, $K = 40$). The energy plots show the $L\Theta A$-space energy $k \mapsto \widehat{W}_{L\Theta A}[\mathbf{Z}_k, \tilde{\mathbf{Z}}_k]$ (top row) and the nonlinear energy $k \mapsto W[\mathbf{S}_k, \tilde{\mathbf{S}}_k]$ (second row) for the piecewise geodesic (green) and the spline (orange) interpolation. Right: Zoomed contours of the mouth in keyframe pose $\mathbf{S}_{10}$, $\mathbf{S}_{20}$, and $\mathbf{S}_{30}$ with trajectories of the corners of the mouth.*
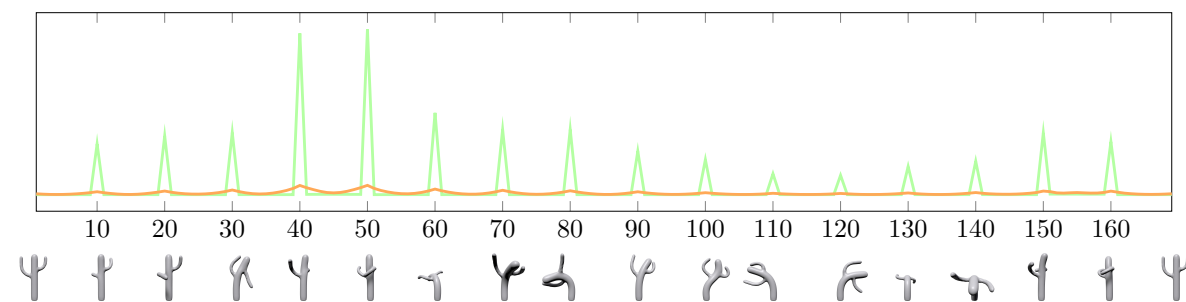
Figure 7.12: *Energy plot of the $L\Theta A$-space energy $k \mapsto \widehat{W}_{L\Theta A}[\mathbf{Z}_k, \tilde{\mathbf{Z}}_k]$ for a spline (orange) and piecewise geodesic (green) interpolation between 17 fixed keyframe poses (gray), computed by $L\Theta A$-space approximation with $\eta = 10^{-3}$, $K = 170$, and natural boundary conditions.*

7.2 Time-discrete regression

This section is concerned with the derivation of a simple regression model on manifolds that represents a generalization of linear regression in the Euclidean space. In detail, for a given set of manifold-valued data points we aim at finding a geodesic curve that fits the data points best. The approach is based on the fact that geodesic curves are the generalization of linear curves in manifolds. Linear curves as well as geodesic curves have two characteristic properties: they are the *shortest* connecting curves between two given points and they have *vanishing (geodesic) curvature*. Similar to the previous section on splines we shall use the latter one to characterize geodesic regression curves, since the former one leads to degenerated curves (if the corresponding end points are not fixed). To this end we control the vanishing curvature property by means of a penalty approach which is realized by augmenting the objective functional, *i.e.* the data term, with the *spline energy*. In applications, this penalty approach enables the control of the realization of the regression curve, as shown in Fig. 7.13.
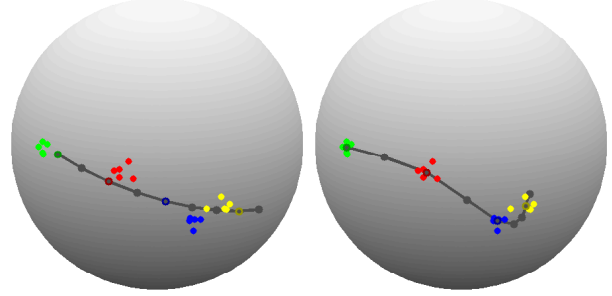
Figure 7.13: *Regression curve (black) for* 20 *input points on the unit sphere for a strong penalty weight (left) and just a mild curve smoothing (right).*

In Sec. 7.2.1, we first present the continuous regression model and then introduce our time-discretization. In Sec. 7.2.2, this fairly general, time-discrete regression model is applied to a concrete shape space, namely the space of viscous fluidic objects (*cf*. Sec. 3.2). In this particular manifold, the method is used to analyze root growth in botany and morphological changes of brain structures due to aging. In terms of implementation, fluidic objects are represented as deformations of suitable reference shapes, which renders the computation of the discrete regression curve as a PDE constrained optimization for a family of deformations. We present these rather technical details as well as a sequence of minor simplifications of the overall model in Sec. 7.2.3. Finally, we comment on future work in Sec. 7.2.4.

Remark 7.2.1. All results presented in this section are joint work with Benjamin Berkels, Tom Fletcher, Martin Rumpf and Benedikt Wirth, and have been published in [BFH$^+$13].

7.2.1 Derivation of the discrete regression model

Let us consider sets of input shapes $\{y_k^i\}_{i=1,\ldots,i_k}$ for $k = 0,\ldots,K$, which represent sets of statistical measurements at times $t_k \in [0,1]$ on the shape manifold $\mathcal{M}$. As a notational simplification let us suppose already here that all times t_k at which input shapes are given are multiples of the time step size $\tau = \frac{1}{K}$ of the discrete model to be introduced later. Indeed, this is no severe restriction because a generalization to discrete geodesics with non-constant time step sizes is straightforward. As a motivation, let us first consider the Euclidean setup, *i.e.* $\mathcal{M} = \mathbb{R}^d$ equipped with the standard Euclidean metric. Then the simple linear regression problem is to find a linear function $y : [0,1] \to \mathbb{R}^d$, usually parametrized as $y(t) = mt + b$ with $m, b \in \mathbb{R}^d$, such that

$$\sum_{k=0}^{K} \sum_{i=1}^{i_k} \|y(t_k) - y_k^i\|^2$$

is minimal. Considering general manifolds $\mathcal{M}$, one now replaces the linear function $y(t) = mt + b$ by a geodesic curve $y : [0,1] \to \mathcal{M}$ and the Euclidean distance by some functional $\mathcal{W} : \mathcal{M} \times \mathcal{M} \to \mathbb{R}$ that measures the *dissimilarity* between the input shapes y_k^i and the associated shapes $y(t_k)$ on the

geodesic curve. In analogy to the standard linear regression model in $\mathbb{R}^d$, where $\mathcal{W}[x, y] = \|x - y\|^2$, the dissimilarity measure $\mathcal{W}[\cdot, \cdot]$ might be (an approximation of) the squared (geodesic) distance on $\mathcal{M}$ (*cf*. [Fle11]) or another in general nonlinear measure of shape dissimilarity. Given such a dissimilarity measure, the simple regression problem on general manifolds is to minimize the *data term*

$$\mathcal{R}[y] = \sum_{k=0}^{K} \sum_{i=1}^{i_k} \mathcal{W}[y(t_k), y_k^i] \,, \tag{7.2.1}$$

under the constraint that y is actually a geodesic, namely that it fulfills the *geodesic equation* $\frac{D}{dt}\dot{y} = 0$. Similar to the previous section, where we considered splines in the space of shells, we will relax this hard constraint by considering a *penalty approach* instead. As before, the penalty functional is given by the spline energy $\mathcal{F}$ (as defined in (4.3.1)) that penalizes violations from the geodesic equation. Then the generalized regression model on manifolds formulated as a penalty approach is to minimize

$$\mathcal{R}^\epsilon[y] = \mathcal{R}[y] + \epsilon^{-1}\mathcal{F}[y] = \mathcal{R}[y] + \epsilon^{-1} \int_0^1 g_{y(t)}\left(\frac{D}{dt}\dot{y}(t), \frac{D}{dt}\dot{y}(t)\right) \, dt \tag{7.2.2}$$

for a small penalty parameter ϵ.

Analogously to the previous section we now derive a discrete analog of the above continuous variational problem and specifically ask for a discrete geodesic regression curve. Again, we consider discrete curves $(y_0, \ldots, y_K)$ in shape space and assume (potentially after reindexing) that $\{y_k^i\}_{i=1,\ldots,i_k}$ is the set of input shapes attached to the time $t_k = k\tau$. If $i_k = 0$ then the corresponding set is empty, and in what follows the associated sums over i are defined to be zero. With this notation at hand, the discrete geodesic regression problem is to find a discrete path $Y^K = (y_0, \ldots, y_K)$ such that the *data term*

$$R[Y^K] = \sum_{k=0}^{K} \sum_{i=1}^{i_k} \mathcal{W}[y_k, y_k^i] \tag{7.2.3}$$

is minimal under the constraint that Y^K is a discrete geodesic, *i.e.* Y^K minimizes $E^K[(y_0, \ldots, y_K)]$ among all discrete paths with same end shapes y_0 and y_K. As in the time-continuous setting, we relax this hard constraint in the following. Replacing the continuous spline functional $\mathcal{F}$ by the time-discrete spline functional F^K as defined in Def. 4.3.3, the *time-discrete regression problem* is to minimize

$$R^{\epsilon, K}[Y^K] = R[Y^K] + \epsilon^{-1}F^K[Y^K] = R[Y^K] + \epsilon^{-1} 4K^3 \sum_{k=1}^{K-1} \mathcal{W}[y_k, \tilde{y}_k] \,, \tag{7.2.4}$$

subject to the constraints

$$\tilde{y}_k = \arg\min_{y \in \mathcal{M}} \left(\mathcal{W}[y_{k-1}, y] + \mathcal{W}[y, y_{k+1}]\right) \,. \tag{7.2.5}$$

Instead of the (discrete) spline functional, one can also consider the (discrete) path energy (*cf*. Def. 4.2.2) as a penalty term (*cf*. [BvTH16]). However, for decreasing ϵ this leads to degenerated curves, as the (discrete) path energy penalizes the total length of the curve whereas the (discrete) spline energy penalizes the geodesic curvature of the curve. Fig. 7.14 shows results of the discrete geodesic regression approach for different penalty parameters ϵ. For decreasing ϵ one observes an increased rounding effect towards the right of the curve, which reflects the global impact of the round input shapes on the resulting approximate discrete geodesic. These results are compared to regression curves obtained when replacing the proposed penalty by the simpler penalty $\epsilon^{-1}E^K[.]$. The latter leads to a collapse of the regression curve to a global *shape average* (as defined in Sec. 7.3, *cf*. [RW09b]).

The discrete regression model developed in this section is fairly general. In the next section, it will be applied to a concrete shape space, namely the space of viscous fluidic objects (*cf*. Sec. 3.2).
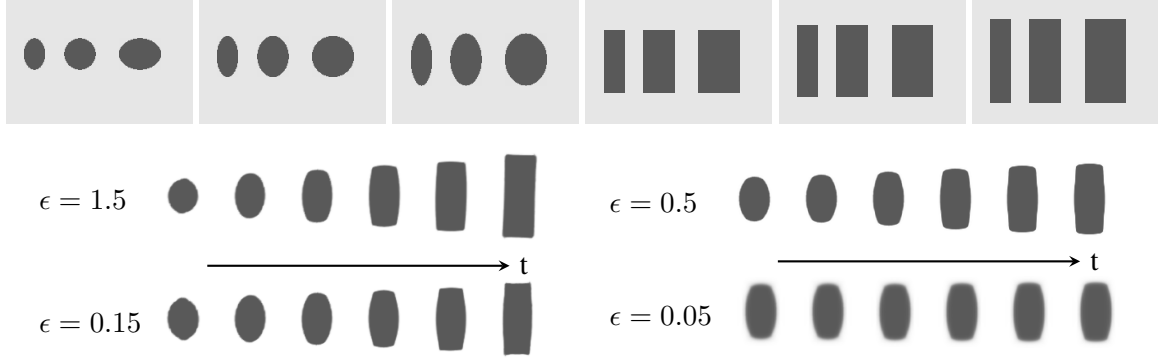
Figure 7.14: *Results of the discrete geodesic regression for given input objects at 6 timesteps (top row) are shown for different penalty functionals and different ϵ, respectively. The penalty is either given by the discrete spline energy $\epsilon^{-1}F^K[Y^K]$ (left) or by the discrete path energy $\epsilon^{-1}E^K[Y^K]$ (right).*

7.2.2 Shape regression in the space of viscous fluidic objects

Now we apply the general approach of discrete geodesic regression to a physically motivated shape space of viscous fluidic objects (denoted by $\mathcal{M}$) with a metric induced by the notion of viscous dissipation (*cf.* Sec. 3.2). Given a shape $\mathcal{S}$, a family $(\phi(t))_{t\in[0,1]}$ of deformations of $\mathcal{S}$ is associated with an Eulerian velocity field $v(t) = \dot{\phi}(t) \circ \phi^{-1}(t)$, and shape variations are equivalence classes of such motion fields with $\tilde{v} \sim v$ if $\tilde{v}\cdot n = v\cdot n$ on $\partial\mathcal{S}$, where n is the outer normal on $\partial\mathcal{S}$. As described in Sec. 3.2, a physically motivated metric on shape variations is given by the minimal rate of dissipation in a Newtonian fluid occupying $\mathcal{S}$ when its free boundary moves according to the shape variation, *i.e.*

$$g_{\mathcal{S}}(v,v) = \min_{\{\tilde{v}\,|\,\tilde{v}\cdot n=v\cdot n\,\text{on}\,\partial\mathcal{S}\}} \int_{\mathcal{S}} \operatorname{diss}[v]\,\mathrm{d}x\,, \quad \operatorname{diss}[v] = \tfrac{\lambda}{2}(\operatorname{tr}\epsilon[\tilde{v}])^2 + \mu\operatorname{tr}(\epsilon[\tilde{v}]^2)\,,$$

where $\operatorname{diss}[v]$ denotes the local rate of viscous dissipation as in (3.2.6). In this context, a matching functional $\mathcal{W}$ to approximate the resulting squared Riemannian distance $\operatorname{dist}^2(\mathcal{S},\mathcal{S}')$ locally can be defined via the minimization of a deformation energy $\hat{\mathcal{W}}[\mathcal{S},\phi] = \int_{\mathcal{S}} W(D\phi)\,\mathrm{d}x$ over all matching deformations ϕ with $\phi(\mathcal{S}) = \mathcal{S}'$ for some particular elastic energy density W. There are primarily two options to choose a W which both ensure the requested consistency of the functional $\mathcal{W}$ and the metric g, *i.e.* $\frac{1}{2}D_\phi^2\hat{\mathcal{W}}[\mathcal{S},\mathrm{id}] = g_{\mathcal{S}}$, *cf.* Thm. 4.2.6. One could consider a simple linearized model with the density defined in (3.2.4), *i.e.*

$$W^l(D\phi) = \tfrac{\lambda}{2}(\operatorname{tr}\epsilon[\phi-\mathrm{id}])^2 + \mu\operatorname{tr}(\epsilon[\phi-\mathrm{id}]^2)\,.$$

The advantage of W^l is that it is quadratic in ϕ so that the Euler–Lagrange equations for a functional composed of such energy densities will be linear. However, this is at the expense of the resulting energy being rigid body motion invariant only in an infinitesimal sense so that a relatively large number K of time steps is required when optimizing the time-discrete path energy to obtain an approximate frame indifference of discrete geodesic paths (*cf.* also Rem. 3.2.1). Full rigid body motion invariance for large deformations can be guaranteed only for certain classes of nonlinear models $W = W^{nl}$. A specifically useful example is the energy density defined in (3.2.5), *i.e.*

$$W^{nl}(D\phi) = \frac{\mu}{2}\operatorname{tr}(D\phi^T D\phi) + \frac{\lambda}{4}\det(D\phi)^2 - \left(\mu + \frac{\lambda}{2}\right)\log\det D\phi - \frac{d\mu}{2} - \frac{\lambda}{4}\,.$$

In our application of discrete geodesic regression the computationally most demanding task is the continual computation of the shapes $\tilde{\mathcal{S}}_k$ via (7.2.5). Therefore, it turns out to be favorable to use the linear deformation energy $\mathcal{W}^l$, *i.e.*

$$\mathcal{W}^l[\mathcal{S},\tilde{\mathcal{S}}] := \min_{\phi(\mathcal{S})=\tilde{\mathcal{S}}} \hat{\mathcal{W}}^l[\mathcal{S},\phi] \quad \text{with} \quad \hat{\mathcal{W}}^l[\mathcal{S},\phi] = \int_{\mathcal{S}} W^l(D\phi)\,\mathrm{d}x\,, \tag{7.2.6}$$

in the definition of the $\tilde{\mathcal{S}}_k$ as well as in the definition of the discrete spline energy F^K, along with a large number of time steps K leading to a sufficiently small time step size $\tau = \frac{1}{K}$. Thus the condition on $\tilde{\mathcal{S}}_k$ in (7.2.5) turns into

$$\tilde{\mathcal{S}}_k = \underset{\mathcal{S} \in \mathcal{M}}{\arg\min} \left(\mathcal{W}^l[\mathcal{S}_{k-1}, \mathcal{S}] + \mathcal{W}^l[\mathcal{S}, \mathcal{S}_{k+1}] \right) . \tag{7.2.7}$$

The treatment of the data term in (7.2.3) is computationally less critical. Since we would like to consider large scale variations between shapes of the discrete geodesic $\mathcal{S}_k$ and corresponding input shapes $\mathcal{S}_k^i$, we make use of the nonlinear deformation model (by using $W = W^{nl}$) here. Hence the terms in (7.2.3) read

$$\mathcal{W}^{nl}[\mathcal{S}_k, \mathcal{S}_k^i] := \min_{\phi(\mathcal{S}_k) = \mathcal{S}_k^i} \hat{\mathcal{W}}^{nl}[\mathcal{S}_k, \phi] \text{ with } \hat{\mathcal{W}}^{nl}[\mathcal{S}_k, \phi] = \int_{\mathcal{S}_k} W^{nl}(D\phi) \, \mathrm{d}x . \tag{7.2.8}$$

To render the method computationally feasible, we assume all deformations to be defined on a computational domain D containing all shapes under consideration (we use $D = [0,1]^d$ in the applications). Furthermore, we suppose that the material properties outside any of the shapes are by a factor δ softer than inside the shapes ($\delta = 0.01$ in the examples). Thus, we replace $\hat{\mathcal{W}}^{nl/l}[\mathcal{S}, \phi]$ by

$$\hat{\mathcal{W}}_\delta^{nl/l}[\mathcal{S}, \phi] := \int_D ((1-\delta)\chi_{\mathcal{S}} + \delta) W^{nl/l}(D\phi) \, \mathrm{d}x ,$$

where the superscript l or nl identifies the linear and the nonlinear model, respectively.

To emphasize the qualitative behavior of geodesic regression we have computed the regression curve for a very basic test case. Fig. 7.15 displays a discrete geodesic and shows the differences with respect to the corresponding group averages (obtained by minimizing (7.2.3) without constraint) and Fig. 7.16 underlines that the resulting regression curves are actually very close to discrete geodesics.
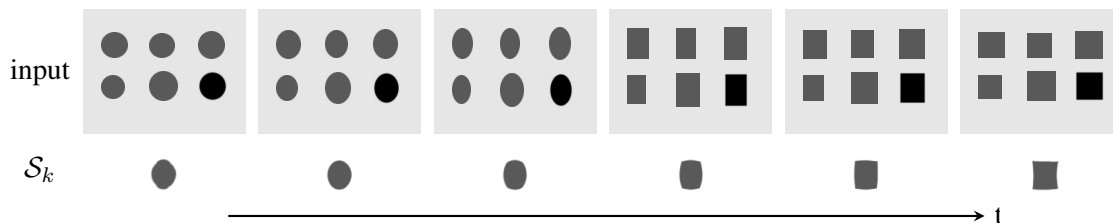

Figure 7.15: *Top: regression input shapes $(\mathcal{S}_k^i)_{k=0,\dots,5}^{i=1,\dots,5}$ (gray) and group averages (black), bottom: discrete regression curve $(\mathcal{S}_k)_{k=0}^5$.*
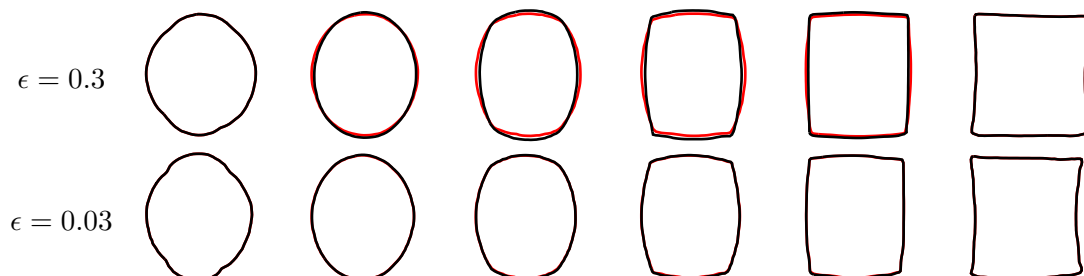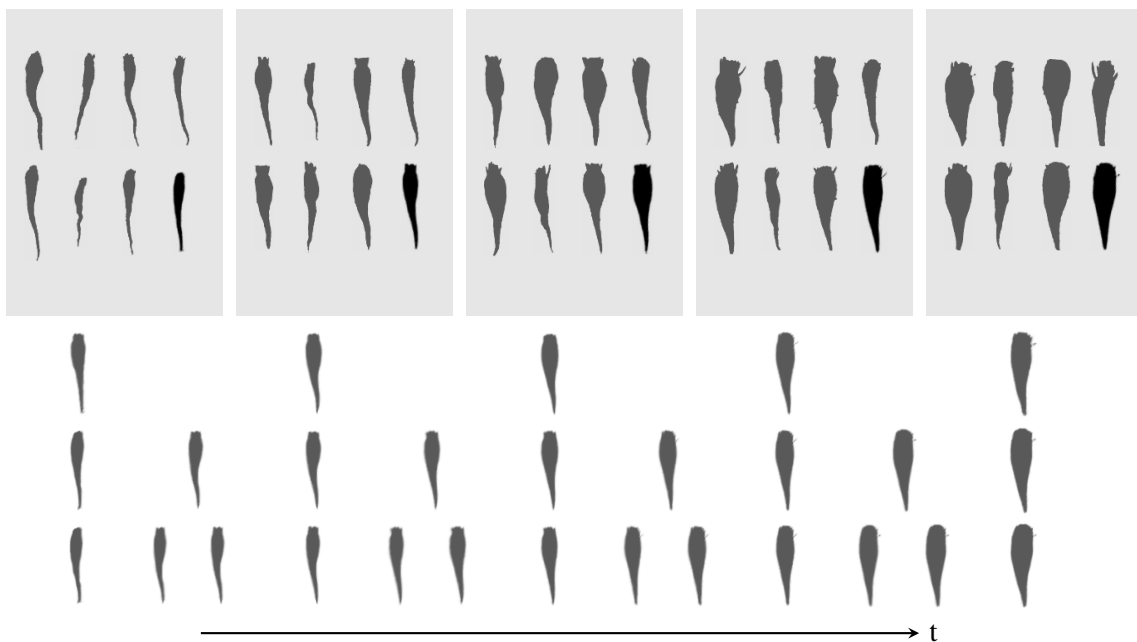

Figure 7.16: *Difference between the discrete regression curve (black) and the true discrete geodesic (red) connecting its end shapes for different ϵ.*

Furthermore, we applied the geodesic regression approach to the statistical analysis of the aging of the human corpus callosum and to the growth of sugar beet roots over a vegetation period. Fig. 7.17 shows the discrete regression curve for the corpus callosum input shapes, which clearly reflects a substantial thinning of the structure with increasing age (*cf*. the results in [Fle11] on a similar data set).
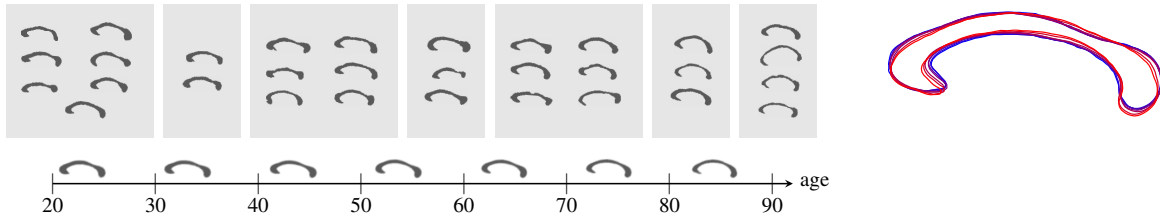
Figure 7.17: *Discrete geodesic regression curve for 31 shapes representing slices of the corpus callosum of humans at different age (2nd to 8th decade). On the right the 7 contours are overlayed showing a thinning process with increasing age (blue to red).*

Fig. 7.18 presents results obtained for 2D slices of sugar beet roots. Here, we also show the effect of an increasing number of intermediate shapes along the regression curve. Fig. 7.19 once more demonstrates that already for moderately small penalty parameter ϵ the resulting curves are very close to a geodesic.

Figure 7.18: *From top to bottom: 2D input slices of sugar beets at five time points (gray) and shape averages for each time (black), regression curves for $\epsilon = 0.08$ and $K = 4, 8, 12$.*

$\epsilon = 8$ $\qquad\qquad\qquad\qquad$ $\epsilon = 0.8$ $\qquad\qquad\qquad\qquad$ $\epsilon = 0.08$
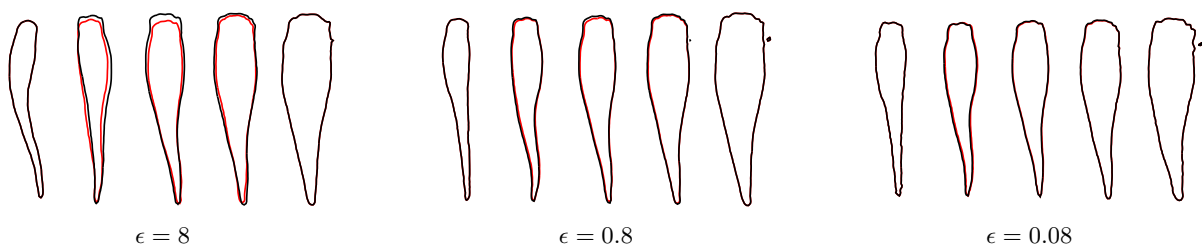
Figure 7.19: *Difference between the discrete regression curve (black) and the true discrete geodesic (red) connecting the end shapes for three different values of ϵ.*

Finally, Fig. 7.20 shows some quantitative analysis of the regression curve for sugar beets in 3D.

day 54   day 69   day 83   day 96   day 109
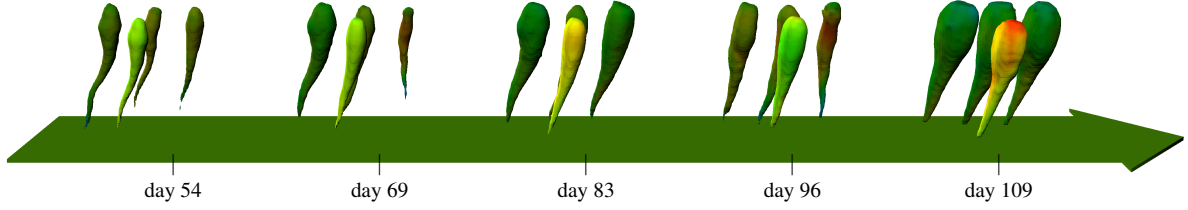
Figure 7.20: *For the discrete sugar beet regression curve the shapes $\mathcal{S}_k$ in the front are color coded according to the signed distance from the shape average at each time point and the input shapes in the back according to the distance from the regression shape in front (colorcode: -0.127* ▬▬ *0.061, maximal root height ≈ 0.75).*

Remark 7.2.2. The examples above are based on MRI scans. The raw data has been obtained by thresholding the MRI signal to obtain characteristic functions on $D = [0,1]^3$. Afterwards, we restricted each data set to the largest connected component and applied some hole-filling and smoothing tool. The 2D data sets are obtained by considering particular slices of the pre-processed 3D data sets.

7.2.3 The optimization algorithm

In this section we briefly describe the main algorithmic ingredients to minimize (7.2.4) in the context of the space of viscous fluidic objects. The main difference to the space of discrete shells considered before is the fact that we do not have a one-to-one-correspondence between different shapes here. This means, shapes as well as deformations bet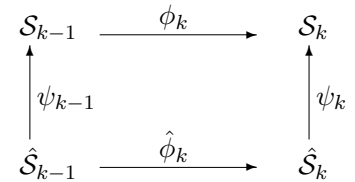ween shapes have to be considered as degrees of freedom. To this end, the presented variational approach for shape regression is based on functionals which depend on shapes and deformations defined on these shapes. To render the method computationally feasible, we first parametrize shapes via deformations acting on reference shapes and work solely with deformations as unknowns. Then, we consider a gradient descent algorithm for the PDE constrained variational approach.

Parametrizing shapes via deformations For the actual computation of discrete regregression curves in the space of viscous objects, we parametrize shapes via deformations as in [RW13]. As an example, let us consider the computation of time-discrete geodesics as minimizers of the discrete path energy

$$E^K[\mathcal{S}_1,\ldots,\mathcal{S}_{K-1};\phi_1,\ldots,\phi_K] = K\sum_{k=1}^{K}\mathcal{W}[\mathcal{S}_k,\phi_k], \quad \text{s.t.} \quad \phi_k(\mathcal{S}_{k-1}) = \mathcal{S}_k\,,$$

where—in the fashion of [WBRS11]—the degrees of freedom are $K-1$ shapes ($\mathcal{S}_0$ and $\mathcal{S}_K$ are given) and K optimal matching deformations. In contrast, the approach described in [RW13] replaces the shapes $\mathcal{S}_0,\ldots,\mathcal{S}_K$ as arguments of the energy E^K by associated *parametrizing deformations* ψ_k. These parametrizing deformations are defined over a set of reference domains $\hat{\mathcal{S}}_k$ such that $\mathcal{S}_k$ is implicitly determined via $\mathcal{S}_k = \psi_k(\hat{\mathcal{S}}_k)$. Following [RW13] further, one can assume that *reference matching deformations* $\hat{\phi}_1,\ldots,\hat{\phi}_K$ are given with $\hat{\mathcal{S}}_k = \hat{\phi}_k(\hat{\mathcal{S}}_{k-1})$. As depicted in Fig. 7.21, the matching deformations ϕ_k as original dependant variables can then be replaced by concatinating *parametrizing deformations* and *reference matching deformations*, *i.e.* $\phi_k = \psi_k \circ \hat{\phi}_k \circ \psi_{k-1}^{-1}$. Using the transformation rule one can now rephrase all energy terms as integrals over the reference domain $\hat{\mathcal{S}}_k$. By this technique, instead of K deformations and $K-1$ domain descriptions (as in [WBRS11]) one only considers $K+1$ parametrizing deformations.

$$\begin{array}{ccc}
\mathcal{S}_{k-1} & \xrightarrow{\phi_k} & \mathcal{S}_k \\
\downarrow{\scriptstyle\psi_{k-1}} & & \downarrow{\scriptstyle\psi_k} \\
\hat{\mathcal{S}}_{k-1} & \xrightarrow{\hat{\phi}_k} & \hat{\mathcal{S}}_k
\end{array}$$

Figure 7.21: *Expressing shapes and deformation via parametrizing and reference matching deformations as in [RW13].*

We now apply this concept to our situation, which can be thought of as a generalization of the approach considered in [RW13]. The shapes $\mathcal{S}_k$ of the discrete regression curve as well as the constraint shapes $\tilde{\mathcal{S}}_k$ are hence represented via parametrizing deformations ψ_k and $\tilde{\psi}_k$ of fixed reference shapes $\hat{\mathcal{S}}_k$, *i.e.* $\mathcal{S}_k = \psi_k(\hat{\mathcal{S}}_k)$ and $\tilde{\mathcal{S}}_k = \tilde{\psi}_k(\hat{\mathcal{S}}_k)$ (*cf.* Fig. 7.22). Likewise, we consider parametrizing deformations ψ_k^i on $\hat{\mathcal{S}}_k$ describing the input shapes, *i.e.* $\mathcal{S}_k^i = \psi_k^i(\hat{\mathcal{S}}_k)$ for $i = 1, \ldots, i_k$. Using these parametrizing deformations we can now rephrase:

i) the deformations $\tilde{\phi}_k$ from $\mathcal{S}_k$ onto $\tilde{\mathcal{S}}_k$, which occur in (7.2.4) via (7.2.7), by

$$\tilde{\phi}_k = \tilde{\psi}_k \circ \psi_k^{-1} \,,$$

ii) the deformations ϕ_k^i from $\mathcal{S}_k$ onto the input shapes $\mathcal{S}_k^i$, which are used in (7.2.1) via (7.2.8), by

$$\phi_k^i = \psi_k^i \circ \psi_k^{-1} \,.$$
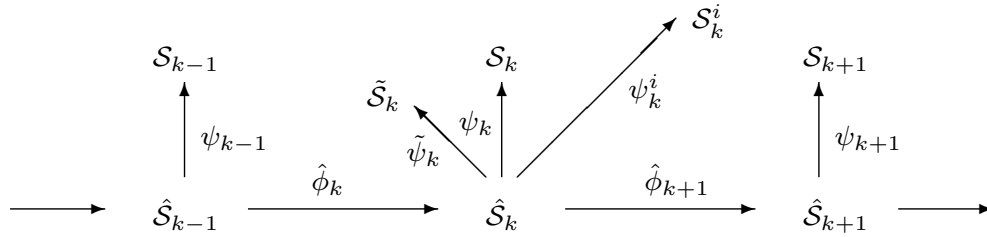
Figure 7.22: *A diagram illustrating the parametrization of the shapes $\mathcal{S}_k$ via deformations over reference shapes $\hat{\mathcal{S}}_k$. Here, $\hat{\phi}_k$ are given deformations such that $\hat{\mathcal{S}}_k = \hat{\phi}_k(\hat{\mathcal{S}}_{k-1})$.*

Realization of the objective functional To ensure that ϕ_k^i matches (at least approximately) $\hat{\mathcal{S}}_k$ onto the input shape $\mathcal{S}_k^i$ we employ a penalty functional

$$\mathcal{P}[\hat{\mathcal{S}}_k, \mathcal{S}_k^i, \psi_k^i] := \int_D |\chi_{\hat{\mathcal{S}}_k} - \chi_{\mathcal{S}_k^i} \circ \psi_k^i|^2 \, \mathrm{d}\hat{x} \tag{7.2.9}$$

which is added to the data term (7.2.3) for all $k = 0, \ldots, K$ and $i = 1, \ldots, i_k$.
To simplify notation, we denote by $\Psi^K := (\psi_k, (\psi_k^i)_{i=1,\ldots,i_k})_{k=0,\ldots,K}$ the vector of all deformations which are considered as our actual degrees of freedom and by $\tilde{\Psi}^K := (\tilde{\psi}_1, \ldots, \tilde{\psi}_{K-1})$ the vector of all constraint deformations. The energy $R^{\epsilon,K}[\mathcal{S}^K]$ over which we minimize in (7.2.4) is rewritten as an energy $R_{\delta\eta}^{\epsilon,K}[\Psi^K] = R_{\delta\eta}^{\epsilon,K}[\Psi^K, \tilde{\Psi}^K]$ of Ψ and $\tilde{\Psi}$, *i.e.*

$$R_{\delta\eta}^{\epsilon,K}[\Psi^K] = \sum_{k=0}^{K} \left(\sum_{i=1}^{i_k} \left(\hat{\mathcal{W}}_{\delta}^{nl}[\psi_k(\hat{\mathcal{S}}_k), \psi_k^i \circ \psi_k^{-1}] + \tfrac{1}{\eta} \mathcal{P}[\hat{\mathcal{S}}_k, \mathcal{S}_k^i, \psi_k^i] \right) \right)$$
$$+ \frac{4K^3}{\epsilon} \sum_{k=1}^{K-1} \hat{\mathcal{W}}_{\delta}^{l}[\psi_k(\hat{\mathcal{S}}_k), \tilde{\psi}_k \circ \psi_k^{-1}] \,, \tag{7.2.10}$$

where we use $\eta = 0.1$ in all examples. By the transformation rule we obtain a computationally more efficient reformulation of the involved deformation energies, *i.e.*

$$\hat{\mathcal{W}}_{\delta}^{nl/l}[\psi_k(\hat{\mathcal{S}}_k), \psi \circ \psi_k^{-1}] = \int_D ((1-\delta)\chi_{\hat{\mathcal{S}}_k} + \delta) W^{nl/l}\big(D\psi (D\psi_k)^{-1} \big) \det D\psi_k \, \mathrm{d}\hat{x} \,,$$

for $\psi = \psi_k^i$ or $\psi = \tilde{\psi}_k$, respectively.

Realization of the constraint   We aim at minimizing (7.2.10) subject to the constraint (7.2.7). Recall that for $k = 1, \ldots, K - 1$ the components $\tilde{\psi}_k$ of the vector of deformations $\tilde{\Psi}^K$ describe the middle shape $\tilde{\mathcal{S}}_k = \tilde{\psi}_k(\hat{\mathcal{S}}_k)$ of a discrete 3-shape geodesic with end shapes $\mathcal{S}_{k-1} = \psi_{k-1}(\hat{\mathcal{S}}_{k-1})$ and $\mathcal{S}_{k+1} = \psi_{k+1}(\hat{\mathcal{S}}_{k+1})$. If we insert the parametrization over reference deformations into (7.2.6) and (7.2.7), the parametrization $\tilde{\psi}_k$ of $\tilde{\mathcal{S}}_k$ is precisely given by the minimizer of the mapping

$$\psi \mapsto \left(\min_{\phi^-:(\phi^- \circ \psi_{k-1})(\hat{\mathcal{S}}_{k-1}) = \psi(\hat{\mathcal{S}}_k)} \hat{\mathcal{W}}^l_\delta[\psi_{k-1}(\hat{\mathcal{S}}_{k-1}), \phi^-] + \min_{\phi^+:(\phi^+ \circ \psi)(\hat{\mathcal{S}}_k) = \psi_{k+1}(\hat{\mathcal{S}}_{k+1})} \hat{\mathcal{W}}^l_\delta[\psi(\hat{\mathcal{S}}_k), \phi^+] \right) .$$

Making use of the reference matching deformations $\hat{\phi}_k$ resp. $\hat{\phi}_{k+1}$ as depicted in Fig. 7.22, *i.e.* we have $\hat{\mathcal{S}}_k = \hat{\phi}_k(\hat{\mathcal{S}}_{k-1})$ and $\hat{\mathcal{S}}_{k+1} = \hat{\phi}_{k+1}(\hat{\mathcal{S}}_k)$, we can re-write the (violet) matching constraints as

$$\phi^-(\mathcal{S}_{k-1}) = (\phi^- \circ \psi_{k-1})(\hat{\mathcal{S}}_{k-1}) = \psi(\hat{\mathcal{S}}_k) = (\psi \circ \hat{\phi}_k)(\hat{\mathcal{S}}_{k-1}) = (\psi \circ \hat{\phi}_k \circ \psi_{k-1}^{-1})(\mathcal{S}_{k-1}) ,$$

$$\phi^+(\tilde{\mathcal{S}}_k) = (\phi^+ \circ \psi)(\hat{\mathcal{S}}_k) = \psi_{k+1}(\hat{\mathcal{S}}_{k+1}) = (\psi_{k+1} \circ \hat{\phi}_{k+1})(\hat{\mathcal{S}}_k) = (\psi_{k+1} \circ \hat{\phi}_{k+1} \circ \psi^{-1})(\tilde{\mathcal{S}}_k) .$$

We now modify (7.2.7) by eliminating the minimization over $\phi^{-/+}$ and set $\phi^- = \psi \circ \hat{\phi}_k \circ \psi_{k-1}^{-1}$ and $\phi^+ = \psi_{k+1} \circ \hat{\phi}_{k+1} \circ \psi^{-1}$, respectively. This leads to the simplified constraint formulation

$$\tilde{\psi}_k = \arg\min_\psi \left(\hat{\mathcal{W}}^l_\delta[\psi_{k-1}(\hat{\mathcal{S}}_{k-1}), \psi \circ \hat{\phi}_k \circ \psi_{k-1}^{-1}] + \hat{\mathcal{W}}^l_\delta[\psi(\hat{\mathcal{S}}_k), \psi_{k+1} \circ \hat{\phi}_{k+1} \circ \psi^{-1}] \right) .$$

Note that we have artificially introduced a point-to-point correspondence $\psi_{k+1} \circ \hat{\phi}_{k+1} \circ \hat{\phi}_k \circ \psi_{k-1}^{-1}$ between $\mathcal{S}_{k-1}$ and $\mathcal{S}_{k+1}$, which was not the case originally. Nevertheless, in the limit for $K \to \infty$ and $\epsilon \to 0$ the discrete path experimentally converges to a continuous geodesic (*cf*. Fig. 7.16 and 7.19).

To fully exploit the quadratic deformation energy in the context of the above-mentioned constraint it is advantageous to further replace $\hat{\mathcal{W}}^l_\delta[\psi(\hat{\mathcal{S}}_k), \psi_{k+1} \circ \hat{\phi}_{k+1} \circ \psi^{-1}]$ by $\hat{\mathcal{W}}^l_\delta[\psi_{k+1}(\hat{\mathcal{S}}_{k+1}), \psi \circ \hat{\phi}_{k+1}^{-1} \circ \psi_{k+1}^{-1}]$, which is quadratic in ψ and replaces the relaxation of the energy $\min_{\phi(\mathcal{S})=\mathcal{S}_{k+1}} \hat{\mathcal{W}}^l[\mathcal{S}, \phi]$ in (7.2.7) by the relaxation of a similar energy based on the inverse deformation $\min_{\phi(\mathcal{S})=\mathcal{S}_{k+1}} \hat{\mathcal{W}}^l[\mathcal{S}_{k+1}, \phi^{-1}]$. For our applications (*e.g.* Fig. 7.16) we experimentally validated that for this computationally motivated modification the resulting discrete curves converge towards discrete geodesics. Altogether we obtain the following variational definition,

$$\tilde{\psi}_k := \arg\min_\psi \mathcal{C}_k[\psi_{k-1}, \psi, \psi_{k+1}] \tag{7.2.11}$$

for all $k = 1, \ldots, K - 1$, where

$$\begin{aligned} \mathcal{C}_k[\psi_{k-1}, \psi, \psi_{k+1}] :=& \hat{\mathcal{W}}^l_\delta[\psi_{k-1}(\hat{\mathcal{S}}_{k-1}), \psi \circ \hat{\phi}_k \circ \psi_{k-1}^{-1}] \\ &+ \hat{\mathcal{W}}^l_\delta[\psi_{k+1}(\hat{\mathcal{S}}_{k+1}), \psi \circ \hat{\phi}_{k+1}^{-1} \circ \psi_{k+1}^{-1}] + \nu \hat{\mathcal{W}}^l[D, \psi] . \end{aligned}$$

Here, we added $\nu \hat{\mathcal{W}}^l[D, \psi]$ as regularizer with $\nu \sim 10^{-2} h$ to ensure that not only the compositions of deformations are regular but also the deformation ψ (here h denotes the grid size).

Dealing with rigid body motions   Different from the nonlinear energy $\hat{\mathcal{W}}^{nl}$, which is strictly rigid body motion invariant, the quadratic energy $\hat{\mathcal{W}}^l$ is rigid body motion invariant solely in an infinitesimal sense (*cf*. Rem. 3.2.1). Thus, in the case of large shape variability in the input data it turned out to be appropriate to enforce the preservation of the center of mass, $\int_D ((1 - \delta)\chi_{\hat{\mathcal{S}}} + \delta)\psi \, d\hat{x} = 0$, and the preservation of the angular momentum, $\int_D ((1 - \delta)\chi_{\hat{\mathcal{S}}} + \delta) (D\psi - D\psi^T) \, d\hat{x} = 0$, assuming the input shapes are co-aligned with respect to the zero moment and the direction of the first moment. This is implemented as an additional set of linear constraints in the minimization in (7.2.11) and in the outer minimization with respect to the energy term $\mathcal{W}^{nl}_\delta[\hat{\mathcal{S}}_k, \psi_k]$. The latter is realized by a projective gradient descent scheme (*cf*. also [Ber10, 3.2.4]), the former by a Lagrange multiplier approach.

Reference shapes and matching deformations We assume the reference shapes $\hat{\mathcal{S}}_k$ and sufficiently smooth reference matching deformations $\hat{\phi}_k : \hat{\mathcal{S}}_{k-1} \to \mathbb{R}^d$ with $\hat{\phi}(\hat{\mathcal{S}}_{k-1}) = \hat{\mathcal{S}}_k$ to be given. Otherwise, we pre-compute $\hat{\mathcal{S}}_k$ as the shape mean of the input shapes at time t_k in the sense of [RW09b], *i.e.*

$$\hat{\mathcal{S}}_k = \arg\min_{\mathcal{S} \in \mathcal{M}} \sum_{i=1}^{i_k} \mathcal{W}^{nl}[\mathcal{S}, \mathcal{S}_k^i].$$

Afterwards, we pre-compute reference matching deformations $\hat{\phi}_k$ by solving the registration problem

$$\hat{\phi}_k = \arg\min_{\phi} \left(\mathcal{P}[\hat{\mathcal{S}}_{k-1}, \hat{\mathcal{S}}_k, \phi] + \lambda \mathcal{H}[\hat{\mathcal{S}}_{k-1}, \phi] \right),$$

where $\mathcal{P}$ has been defined in (7.2.9), $\mathcal{H}$ is a regularization functional and $\lambda > 0$ represents the regularization parameter. Typically, we choose either $\mathcal{H}[\mathcal{S}, \phi] = \hat{\mathcal{W}}_\delta^{nl}[\mathcal{S}, \phi]$ or the *Dirichlet energy*

$$\mathcal{H}[\mathcal{S}, \phi] = \frac{1}{2} \int_D ((1-\delta)\chi_{\mathcal{S}} + \delta) \, \|D\phi\|^2 \, \mathrm{d}x.$$

Inverse reference matching deformations $\hat{\phi}_k^{-1}$ (needed to evaluate the constraint (7.2.11)) and reference parametrizations ψ_k^i of the input data are pre-computed analogously.

Spatial discretization and optimization For the spatial discretization we employ multilinear finite elements on the computational domain $D = [0,1]^d$, which is overlaid with a regular square grid of $2^n + 1$, $n \in \mathbb{N}$, nodes in each direction. Energies are computed via Simpson quadrature on each element. Furthermore, we apply a cascadic approach, first computing the regression curve with a coarse spatial resolution for all involved deformations and then proceeding iteratively from coarse to fine. In this cascadic approach one can also adopt the reference shapes $\hat{\mathcal{S}}_k$ and the associated reference deformations $\hat{\phi}_k$ starting on the coarsest level with a single reference shape chosen as one of the coarsely resolved end shapes.

We apply a standard Fletcher–Reeves nonlinear conjugate gradient descent to the above minimization problem, which at each step requires evaluation of the functional $R_{\delta\eta}^{\epsilon,K}[\Psi] := R_{\delta\eta}^{\epsilon,K}[\Psi, \tilde{\Psi}[\Psi]]$ and its gradient. For the functional evaluation, the quadratic optimization problem (7.2.11) is solved for each $k = 1, \dots, K-1$ by a preconditioned linear conjugate gradient iteration. Using the standard adjoint method in constrained optimization [Fle87] we obtain the Gâteaux derivative of $R_{\delta\eta}^{\epsilon,K}[\Psi]$. For details we refer to the appendix A.4.

7.2.4 Conclusion and outlook

We have described a time-discrete geodesic regression approach on manifolds and applied it to the shape space of viscous fluidic objects. The method requires the solution of a PDE constrained optimization problem for deformations defined on a family of reference shapes. Applications in the context of plant growth and anatomical brain structures demonstrate the method's potential in time-dependent shape statistics. The current implementation based on a gradient descent approach requires several hours to compute a regression geodesic for 2D shapes and several days for 3D shapes. There is a great potential for faster energy relaxation using Newton type methods and more efficient parallel implementations.

In the future, it would be interesting to investigate the generalization to more general classes of regression curves, *e.g.* in the spirit of Hinkle *et al.* [HMFJ12]. Furthermore, the application to other shape spaces, *e.g.* the space of discrete shells, is immediate. However, due to the fixed connectivity constraint imposed on the discrete shell space it is difficult to obtain suitable data sets. One possibility to solve this problem is to create consistent triangulations via remeshing in a pre-processing step. A more promising solution, however, is to only represent the discrete regression curve by triangular meshes (which are in dense correspondence) while the input data is given implicitly, *e.g.* as level set functions. The data term (7.2.1) then consists of matching functionals between implicit surfaces and triangular meshes (*cf.* [IRS15]).

7.3 PCA in the space of shells

Statistical models, such as a principal component analysis (PCA), are supposed to extract low-dimensional but essential information from a possibly high-dimensional data set, that represents the variability (or variance) within the data set as well as possible. Typically, variability is measured with respect to an inner product, or more generally, with respect to a Riemannian metric. The performance and usefulness of a statistical model therefore depends substantially on the choice of such a metric. For example, a PCA performed in standard Euclidean space assumes that the input data lies on (or can be well approximated by) a hyper-planar manifold, the axes of which are those that capture maximal variance. This makes it optimal with respect to linear variations but a poor choice when the data contains highly nonlinear variations.

Important applications in computer vision and graphics include the statistical modeling of human faces [YWS+11, SHK11, SK15] and bodies [ASK+05, FB12, PMRMB15], which are often represented as triangular meshes, *i.e. discrete shells*. In this case, shape variability is usually induced by changes in identity or dynamic deformations, which typically include highly nonlinear variations. A widespread approach in computer vision is to perform statistical modeling of triangle meshes by means of the so-called *Procrustes analysis* [Sib78, Ken84, BV99, PS09]. In this setup, all shapes are registered by rigid body motions and afterwards a linear analysis based on the Euclidean metric is applied to the vector of nodal positions. However, this approach fails to capture nonlinear variations properly. In contrast, the results presentend in the previous chapter suggest that the time-discrete geodesic calculus on discrete shells, which is built on a physically-motivated, nonlinear model of surfaces, potentially provides a useful tool in modeling the nonlinear variability in a sparsely sampled set of triangular meshes. This motivates the idea to perform statistical shape analysis in (discrete) shell space.

In Sec. 7.3.1, we define a (nonlinear) distance measure by means of the (discrete) elastic shell deformation energy derived in Sec. 5.3 and introduce a notion of covariance based on the Hessian of such an elastic energy which has been proven to be suitable metric on shell space (*cf.* Sec. 6.1.2). In analogy to a standard PCA in linear Euclidean space, we extract principal components based on an eigendecomposition of the resulting covariance matrix. The resulting principal components are able to capture nonlinear articulations and complex deformations. In Sec. 7.3.2, we finally provide results on human face and body data and discuss our PCA model.

Remark 7.3.1. The nonlinear elastic PCA model has been proposed originally by Rumpf and Wirth in the space of volumetric objects [RW09a, RW09b, RW11a]. We report here on applying this elastic PCA to the space of discrete shells. The results presented in this section are joint work with Martin Rumpf, William Smith and Chao Zhang and have been published in [ZHRS15].

7.3.1 Fréchet mean and covariance operator

A principal component analysis (PCA) relies on notions of averaging and covariance and uses an eigendecomposition of the covariance matrix in order to extract linear principal components. Following [RW09a, RW09b, RW11a] we now introduce for a given set of input data (i) a general notion of an average (depending on a distance measure dist) and (ii) a covariance operator as a generalization of a covariance matrix (depending on an inner product g). We introduce two particular choices for dist and g, respectively, namely the standard Euclidean distance/metric, which represents Procrustes analysis, and a physically-based distance/metric induced by an elastic shell deformation energy. The corresponding PCA is refered to as Euclidean PCA in the former and as elastic resp. shell PCA in the latter setup.

Consider a given set of input data $\mathcal{S}_1, \ldots, \mathcal{S}_m$ which we now consider as triangular meshes that are in dense correspondence. Hence we can represent each mesh $\mathcal{S}_i$ by its vector of nodal positions $\mathbf{S}_i \in \mathbb{R}^{3n}$.

For a given (squared) distance measure $\mathbf{W} : \mathbb{R}^{3n} \times \mathbb{R}^{3n} \to \mathbb{R}$ the group average $\hat{\mathbf{S}} \in \mathbb{R}^{3n}$ is given by the Fréchet mean [Fré48] (*cf*. also [Kar77])

$$\hat{\mathbf{S}} := \underset{\mathbf{S} \in \mathbb{R}^{3n}}{\arg\min} \sum_{i=1}^{m} \mathbf{W}[\mathbf{S}_i, \mathbf{S}] \,. \tag{7.3.1}$$

In the Euclidean setup we have $\mathbf{W}[\mathbf{S}, \tilde{\mathbf{S}}] = \|\mathbf{S} - \tilde{\mathbf{S}}\|^2$ and hence $\hat{\mathbf{S}}_{\mathrm{euc}} = \frac{1}{m} \sum_{i=1}^{m} \mathbf{S}_i$. However, in the elastic PCA setup we define $\mathbf{W}$ to be the discrete shell deformation energy as defined in Def. 6.0.2, *i.e.*

$$\mathbf{W}[\mathbf{S}, \tilde{\mathbf{S}}] = \mathbf{W}_{\mathrm{mem}}[\mathbf{S}, \tilde{\mathbf{S}}] + \eta \, \mathbf{W}_{\mathrm{bend}}^{\mathrm{DS}}[\mathbf{S}, \tilde{\mathbf{S}}] \,, \tag{7.3.2}$$

and (7.3.1) becomes a nonlinear optimization problem. In particular, the elastic average $\hat{\mathbf{S}}_{\mathrm{elast}}$ has to fulfill the necessary condition $\sum_{i=1}^{m} \partial_2 \mathbf{W}[\mathbf{S}_i, \hat{\mathbf{S}}_{\mathrm{elast}}] = 0$.

Inherently a PCA is defined on a linear space. Hence we will consider the linear space of nodal displacements $\mathbf{U}_i = \mathbf{S}_i - \hat{\mathbf{S}} \in \mathbb{R}^{3n}$, $i = 1, \dots, m$, from the average $\hat{\mathbf{S}}$. Given an inner product g on $\mathbb{R}^{3n}$, we define the covariance operator

$$\mathbf{Cov}\,\mathbf{V} = \frac{1}{m} \sum_{i=1}^{m} g(\mathbf{V}, \mathbf{U}_i) \mathbf{U}_i \tag{7.3.3}$$

and the *Gram matrix* $C = (C_{ij})_{ij} \in \mathbb{R}^{m,m}$ via

$$C_{ij} := g(\mathbf{U}_i, \mathbf{U}_j) \,. \tag{7.3.4}$$

Obviously, C is symmetric and positive semi-definite, that means there is a spectral decomposition $C = O \Lambda O^T$, $\Lambda = \mathrm{diag}(\lambda_1, \dots, \lambda_m)$, where $\lambda_1 \geq \dots \geq \lambda_m \geq 0$ are eigenvalues of C and O is an orthogonal matrix, *i.e.* $OO^T = O^T O = \mathbb{1}_m$. We define $\mathbf{W}_1, \dots, \mathbf{W}_m$ via

$$\mathbf{W}_k := \frac{1}{\sqrt{\lambda_k}} \sum_{i=1}^{m} O_{ik} \mathbf{U}_i \tag{7.3.5}$$

if $\lambda_k > 0$ and $\mathbf{W}_k = 0$ else. A straightforward calculation reveals that

$$\mathbf{Cov}\,\mathbf{W}_k = \frac{\lambda_k}{m} \mathbf{W}_k$$

and $g(\mathbf{W}_k, \mathbf{W}_l) = \delta_{kl}$, *i.e.* $\mathbf{W}_1, \dots, \mathbf{W}_m$ are in fact eigenvectors of $\mathbf{Cov}$. Formally, we can extend $\mathbf{W}_1, \dots, \mathbf{W}_m$ to an orthonormal basis of $\mathbb{R}^{3n}$ with $\mathbf{Cov}\,\mathbf{W}_k = 0$ for $k > m$.

Note that eigenvectors of $\mathbf{Cov}$ are usually found by a spectral decomposition of the $(3n)$-by-$(3n)$ covariance matrix. However, as in most applications $m \ll 3n$ it is more efficient to decompose $C \in \mathbb{R}^{m,m}$ as defined in (7.3.4) and obtain eigenvectors via (7.3.5).

Remark 7.3.2. Due to the rigid body motion invariance the representation of a discrete shell $\mathbf{S} \in \mathbb{R}^{3n}$ is not unique. In fact, $\mathbf{S}$ is represented by an equivalence class induced by rigid body motions. This issue becomes crucial when defining nodal displacements $\mathbf{U} = \mathbf{S} - \hat{\mathbf{S}}$, as we can construct an arbitrary large displacement by a simple translation. However, this obstacle is overcome by taking $\mathbf{S}$ such that $\|\mathbf{S} - \hat{\mathbf{S}}\|^2 \leq \|\tilde{\mathbf{S}} - \hat{\mathbf{S}}\|^2$ for all $\tilde{\mathbf{S}}$ in the equivalence class.

For a data set $\mathbf{U}_1, \ldots, \mathbf{U}_m$ the first component $\mathbf{V}_{(1)}$ of a PCA is defined as

$$\mathbf{V}_{(1)} = \arg\max_{\|\mathbf{V}\|=1} \sum_{i=1}^{m} g(\mathbf{V}, \mathbf{U}_i)^2 = \arg\max_{\|\mathbf{V}\|=1} g(\mathbf{Cov}\,\mathbf{V}, \mathbf{V}), \qquad (7.3.6)$$

where we used the definition (7.3.3) of $\mathbf{Cov}$ in the second equality. If we now write $\mathbf{V} = \sum_k \alpha_k \mathbf{W}_k$, *i.e.* represent $\mathbf{V}$ in the orthonormal basis as defined in (7.3.5), we get $g(\mathbf{Cov}\,\mathbf{V}, \mathbf{V}) = \sum_k \alpha_k^2 \lambda_k$. Hence (7.3.6) is equivalent to solving

$$\bar{\alpha} = \arg\max_{\|\alpha\|=1} \sum_{k=1}^{m} \alpha_k^2 \lambda_k \,.$$

As λ_1 is the largest eigenvalue we have $\bar{\alpha} = (1, 0, 0, \ldots)$ and hence $\mathbf{V}_{(1)} = \mathbf{W}_1$. Similarly we obtain further components $\mathbf{V}_{(k)}$ as $\mathbf{V}_{(k)} = \mathbf{W}_k$ for $k = 2, \ldots, m$. Hence the principal components are given by the eigendisplacements of $\mathbf{Cov}$ as defined in (7.3.5).

Choice of metric   We have not specified an inner product g on the space of discrete shells yet. For the Euclidean setup, which corresponds to a Procrustes analysis, we can define g as the standard scalar product on $\mathbb{R}^{3n}$, *i.e.* $g_{\mathrm{euc}}(\mathbf{U}, \mathbf{V}) = \mathbf{U}^T \mathbf{V}$. We have seen in Sec. 6.1.2 that for an elastic deformation energy as defined in (7.3.2) the bilinear form

$$g_{\mathrm{elast}}(\mathbf{U}, \mathbf{V}) = \frac{1}{2} \mathbf{U}^T (\mathrm{Hess}\mathbf{W})[\hat{\mathbf{S}}_{\mathrm{elast}}, \hat{\mathbf{S}}_{\mathrm{elast}}] \mathbf{V} \qquad (7.3.7)$$

in fact defines a metric on the space of discrete shells modulo rigid body motions. Here $\mathrm{Hess}\mathbf{W} = \partial_2^2 \mathbf{W} \in \mathbb{R}^{3n,3n}$ denotes the Hessian matrix w.r.t. the second argument of $\mathbf{W}$ which is a positive semi-definite symmetric matrix whose nullspace corresponds to displacements induced by rigid body motions.

Representation of principal modes   Our PCA model amounts to an average shape $\hat{\mathbf{S}} \in \mathbb{R}^{3n}$ and eigendisplacements $(\mathbf{W}_k)_k$ obtained by the PCA. A simple linear representation of these dominant modes is to compute meshes via $\hat{\mathbf{S}} + t\,\mathbf{W}_k$, where $t \in [-T, T]$. However, a more reasonable way to express pure nonlinear variations is to use the nonlinear shooting method via the time-discrete exponential map (*cf*. Sec. 6.2.3). Here, we use the exponential map on shell space as a natural extrapolation of shell variations given by the (nonlinear) principal modes of variation. Hence we consider the elastic average $\hat{\mathbf{S}}$ as start point and a (possibly scaled) mode $t\,\mathbf{W}_k, t \in [-T, T]$, as the initial velocity.

Projection and reconstruction   In an analogous fashion to Euclidean PCA, the elastic PCA can also be used for reconstructing shapes from a set of PCA coefficients. Given the elastic average $\hat{\mathbf{S}}$, the eigenvectors $(\mathbf{W}_k)_k$ and some (possibly unseen) shape $\mathbf{S} \in \mathbb{R}^{3n}$, we first compute the nodal displacement $\mathbf{U} = \mathbf{S} - \hat{\mathbf{S}}$. We then project $\mathbf{U}$ onto the elastic PCA space $\mathcal{W}_m$, where $\mathcal{W}_m$ is the linear subspace spanned by the principal modes $\mathbf{W}_k, k = 1, \ldots, m$. The projection is given by

$$P_{\mathcal{W}_m} : \mathbf{U} \mapsto P_{\mathcal{W}_m}\mathbf{U} := \sum_{k=1}^{m} g_{\mathrm{elast}}(\mathbf{W}_k, \mathbf{U})\,\mathbf{W}_k \,.$$

Finally, we are able to get the reconstruction via nonlinear shooting, *i.e.* we compute $\mathrm{EXP}_{\hat{\mathbf{S}}}(P_{\mathcal{W}_m}\mathbf{U})$.

7.3.2 Qualitative results and discussion

Here, we provide a qualitative evaluation of the elastic PCA model[1]. We visualize the dominant principal modes and compare reconstructions using Euclidean and elastic PCA. We use two datasets in our experiments. The first dataset contains scans of human bodies drawn from the FAUST dataset [BRLB14]. The 5 training shapes are shown in Fig. 7.23. The meshes are watertight, genus zero and we apply groupwise simplification to reduce their resolution to 6,000 vertices. For thi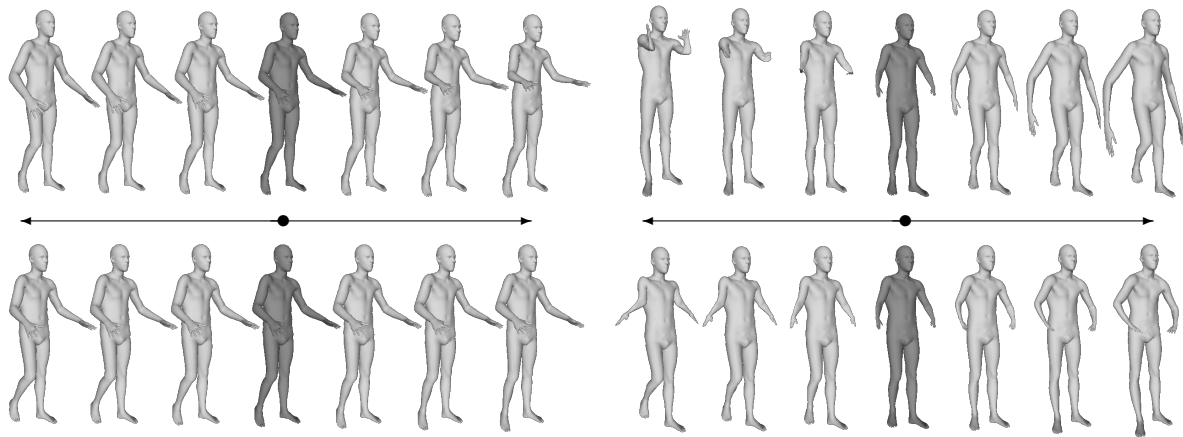s dataset, Euclidean PCA fails to obtain a meaningful average, let alone principal components due to the articulated motion (*cf*. Fig. 7.24). The second dataset is the B3D(AC)^2 [FGR$^+$10]

Figure 7.23: Human bodies data with large non-linear, articulated deformations (FAUST dataset [BRLB14]).

dataset containing facial motion sequences in dense correspondence. From this dataset, we extract a subset containing 40 expressions of a single subject. The meshes are genus three (holes for the mouth and eyes) with a boundary. Once again, we apply groupwise simplification to reduce the mesh resolution to 3,000 vertices. Note that in both cases, the training data is extremely sparse and that there are large, nonlinear deformations between shapes.

Figure 7.24: First two principal modes of variation for elastic model (left) and Euclidean model (right).

In Fig. 7.24 we show the first two principal components for the body data. The elastic average for elastic PCA and the linear average for Euclidean PCA are depicted in the middle column (shapes in dark gray), respectively. In each row, we show a geodesic path traversing from the average in each direction along the principal component. The elastic PCA modes successfully capture the nonlinear, articulated motion. The first mode appears to represent the raising and lowering of the arms and the second the bending of the leg. Euclidean PCA fails to capture meaningful deformations and leads to degenerated surfaces. To emphasize the nonlinear nature of the elastic PCA modes, we show vertex trajectories for the first principal component in Fig. 7.25. This is done by generating a sequence of shapes by nonlinear shooting and plotting the resulting trajectories in red. For comparison, the Euclidean PCA trajectories are shown in blue. Obviuosly, our elastic shell PCA leads to nonlinear trajectories.
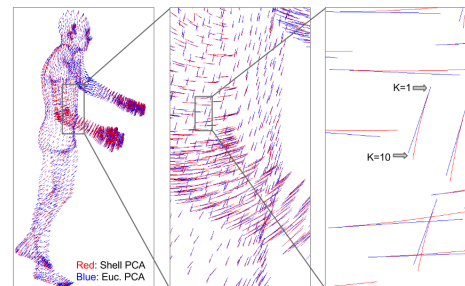
Figure 7.25: Vertex trajectories of first mode of elastic PCA vs. Euclidean PCA.

---

[1]The corresponding quantitative evaluation has been done by Chao Zhang and is not shown here, *cf*. [ZHRS15].

In Fig. 7.26 (left), we present the first three principal components for the facial expression data. We show Euclidean PCA in the first row and elastic PCA with nonlinear shooting in the second row. Note that, while both Euclidean and elastic PCA capture similar characteristics in their principal three modes, elastic PCA with nonlinear shooting prevents the surface from folding over itself and retains a more plausible face shape. For example, mode 1 of Euclidean PCA appears to correspond approximately to mode 3 of elastic PCA but elastic PCA preserves a more plausible chin shape in the positive direction.

first mode   second mode   third mode $d=5$ $d=10$ $d=39$
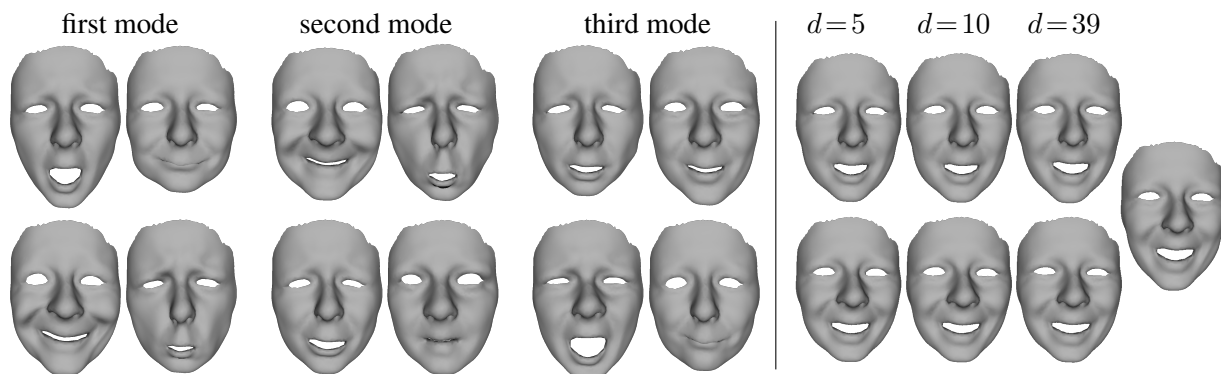
Figure 7.26: *Left: First three principal modes for Euclidean (top) and elastic PCA (bottom). Right: reconstruction of unseen shape (rightmost shape) using d principal modes taken from Euclidean (top) and elastic PCA (bottom).*

In Fig. 7.26 (right) we show the result of reconstructing an unseen face using an increasing number d of model dimensions. The results in the top row are for Euclidean PCA and in the bottom row for elastic PCA. Obviously, there is a perceptual improvement in the reconstruction results using elastic PCA. Using only $d = 5$ dimensions, elastic PCA has successfully reconstructed the strong elastic deformation of the smile while the Euclidean PCA reconstruction does not successfully convey the smiling expression.

Remark 7.3.3. Fig. 7.24, Fig. 7.25 and Fig. 7.26 have been prepared by Chao Zhang (*cf*. [ZHRS15]).

Discussion and outlook We have presented a principal component analysis (PCA) on discrete shell space, providing a hybrid between physical and statistical modeling of shape variation. Principal components are obtained via an eigendecomposition of a covariance matrix arising from an inner product based on the Hessian of an elastic energy. In contrast to a PCA in the ambient Euclidean space, *i.e.* the widespread Procrustes analysis, our model is better able to capture the nonlinear variations present in articulated body pose data and face expression data with complex deformations.

However, we here consider the linear space of (possibly large) nodal displacements and *not* the tangent space in a Riemannian setup of infinitesimal displacements[1]. This is computationally more efficient (no higher resolution of geodesic paths from the average to each input shapes is required) and surprisingly sufficient also for large displacements, probably due to the involved nonlinear elastic deformation energy and its invariance with respect to rigid body motions. Nevertheless, the ultimate goal is to present a fully Riemannian PCA on the space of shells in the spirit of Fletcher *et al*. [FLJ03, FLPJ04]. In this setup, the PCA is performed on the logarithms of the input shapes with respect to the average. The logarithm enables the linear representation of possibly highly nonlinear deformed input shapes in the tangent space at the average. Additionally, the average itself is a proper Riemannian average, *i.e.* the functional (7.3.1) sums over all (squared) Riemannian distances to the input data. Here it is in particular crucial to exploit efficient optimization schemes to compute the Riemannian average, as each evaluation of the functional (7.3.1) requires the computation of m time-discrete geodesics of a certain length. Finally, it is also desirable to derive a formulation that does not require the computation of nodal displacements at all, *cf*.

---

[1]Nevertheless, the input displacements as well as the resulting principal modes can be considered as approximate tangent vectors in the Riemannian tangent space at the average shape, whereas this approximation is only valid locally.

Rem. 7.3.2. This applies to the assembling of Gram's matrix (7.3.4) via (7.3.7), as well as to several operations during projection and reconstruction of unseen data.

8 Optimal branching patterns

Martensitic phase transitions lead to mixtures of distinct phases or phase variants with characteristic fine-scale structures. An almost universal phenomenon is that of *twinning*, whereby distinct variants of the martensite phase occur in long, thin lamellae. This twinning is typically due to the presence of an interface to the more stable austenite phase—which is determined by higher crystallographic symmetry. The formation of microstructures along these so-called *austenite-twinned-martensite interfaces* can be explained on the basis of elastic energy minimization, *cf.* [Kha67, Kha69, Kha83, BJ87, BJ92]. From a mathematical point of view, the fine-scale structure arises because the elastic functional is not lower semi-continuous. Hence minimizing sequences develop spatial oscillations which correspond physically to the observed microstructure. In particular, elastic energy minimization is able to reproduce some general features of the microgeometry, such as the orientation and direction of interfaces. On the other hand, this method does not allow for a prediction of characteristic length scales. To account for these fine-scale structures one has to include a *surface energy*, which offers a selection criterion [Mül90, Mül93]. The minimization of an elastic energy plus a surface term has been considered by many authors, *cf. e.g.* [Kha83, Roi69, BJ87]. A typical choice is the strain-gradient type functional

$$E_\kappa[u] = \int_{\Omega_L} \tfrac{1}{2}\, \kappa^2\, u_{yy}^2 + \sigma\,(u_y^2 - 1)^2 + u_x^2 \,\mathrm{d}x\,\mathrm{d}y\,, \tag{8.0.1}$$

for $\Omega_L = (0, L) \times (0, 1) \subset \mathbb{R}^2$ and a macroscopic deformation[1] $u : \Omega_L \to \mathbb{R}$. The boundary $x = 0$ corresponds to the austenite-martensite interface. For simplicity, we assume the austenite phase $\{x < 0\}$ to be completely rigid, *i.e.* we impose the Dirichlet boundary condition

$$u = 0 \quad \text{at} \quad x = 0\,, \tag{8.0.2}$$

which accounts for the elastic compatability at the interface. More generally and actually more realistically, one can relax this hard boundary condition and augment (8.0.1) by a term describing the elastic energy in the austenite, *e.g.* the Dirichlet energy $\int_{x<0} |\nabla u|^2 \,\mathrm{d}x\,\mathrm{d}y$ or the $H^{1/2}$-norm of the boundary function $y \mapsto u(0, y)$ [KM92, Con06]. The double-well potential $\sigma(u_y^2 - 1)^2 + u_x^2$ represents the elastic energy of the martensite, where the preferred values $\nabla u = (0, \pm 1)$ are the stress-free states of two distinct variants of martensite. Note that this particular choice of potential accounts for the assumption that we are dealing with two variants of martensite with equal volume fractions; we refer to the work by Zwicknagl [Zwi14] and Diermeier [Die16] for the treatment of general and low-volume fractions, respectively. The strain-gradient term $\tfrac{1}{2}\kappa^2 u_{yy}^2$ represents surface or interfacial energy. Several models have been suggested for this interfacial energy, however, most of them are based on second derivatives of the deformation [Bha04]. Due to the structure of the double-well potential and the boundary condition (8.0.2), oscillations are expected primarily in u_y, such that the essential variation is mainly in y-direction. Hence the u_{yy}-term is believed to be sufficient to regularize the problem [KM94]. As motivated above, there is no minimizer of $E_\kappa[u]$ for $\kappa = 0$, although it is easy to construct a minimizing sequence $(u_k)_k$ with $E_\kappa[u_k] \to 0$ as $k \to \infty$. However, as soon as $\kappa > 0$, the minimum is attained (*cf.* Thm. 2.1 in [KM94]) since the higher-order term $\tfrac{1}{2}\kappa^2 u_{yy}^2$ limits the oscillations of u_y and establishes a length scale for the microstructure [KM94, Con00b].

---

[1] Actually, the objective material is three-dimensional, *i.e.* $\tilde{\Omega} \subset \mathbb{R}^3$, deformed by a macroscopic deformation $\tilde{u} : \tilde{\Omega} \to \mathbb{R}^3$. However, in this thesis we confine ourselves to the reduced, *i.e.* two-dimensional and scalar-valued, problem. For the treatment of the more general vector-valued problem as well as the derivation of the reduction we refer *e.g.* to [Bha04, Zwi14].

Prior to the seminal work by Kohn and Müller [KM92, KM94], most of the approaches to minimize (8.0.1) subject to (8.0.2) assume a *one-dimensional* configuration for the martensitic twinning. This means, all interfaces separating different variants of martensite are parallel for $x > \delta$ and there is a small boundary layer $(0, \delta) \times (0, 1)$ where linear interpolation is used to account for the Dirichlet boundary condition (*cf*. Fig. 8.1, left). To this end, the optimal elastic energy is supposed to scale as $\kappa^{1/2} L^{1/2}$. However, for fixed $\kappa > 0$ and $L \to \infty$ (or equivalently for fixed $L > 0$ and $\kappa \to 0$), the optimal scaling law is actually $\kappa^{2/3} L^{1/3}$ [KM92, KM94]. In particular, the twins are not essentially one-dimensional—they branch as they approach the austenite (*cf*. Fig. 8.1, middle). Intuitively, this behaviour can be explained as follows. The elastic energy prefers fine twins at the austenite-martensite interface, however, far from this interface, the fine-scale structure is no longer energetically advantageous but costs surface energy—hence the twins coarsen.
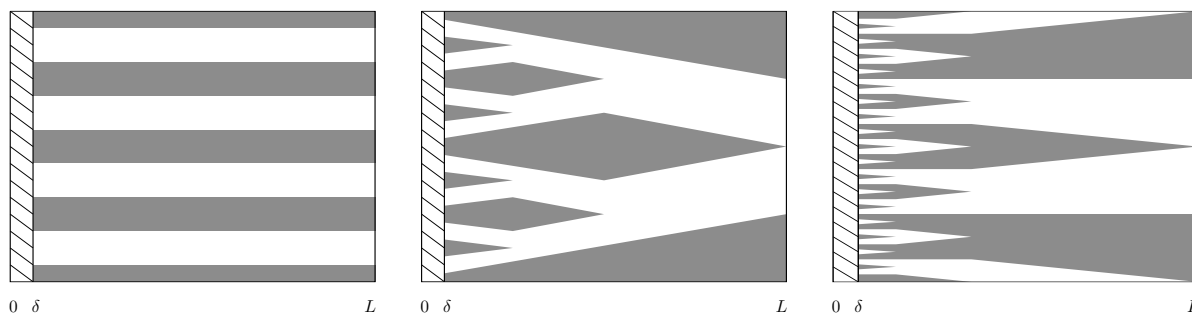
Figure 8.1: *One-dimensional construction of parallel martensite interfaces (left) and branching constructions considered by Kohn and Müller [KM92, KM94] (middle) as well as by Li [Li03] (right). Different colors represent regions with $u_y = \pm 1$. Linear interpolation is considered only in the boundary layer $(0, \delta) \times (0, 1)$.*

Nevertheless, the analysis of Kohn and Müller [KM92, KM94] as well as many further investigations [Con00b, Con06] are based on a slightly different functional which is supposed to approximate (8.0.1) or at least characteristic properties of the functional or its minimizers. In detail, one studies the minimization of the energy functional

$$F_\epsilon[u] = \int_{\Omega_L} \epsilon \, |u_{yy}| + u_x^2 \, \mathrm{d}x \, \mathrm{d}y \tag{8.0.3}$$

for $\Omega_L = (0, L) \times (0, 1) \subset \mathbb{R}^2$ and a suitable $u \in \mathcal{A}$ with

$$\mathcal{A} = \{ u \in H^1(\Omega_L) \; : \; u_y = \pm 1 \, a.e. \, ,$$

$$u_{yy} \text{ is Radon measure on } \Omega_L \text{ with finite mass, } u = 0 \text{ at } x = 0 \} \, .$$

From an analytical point of view, the minimization of (8.0.1) involves lots of technical details such as smoothing sawtooth functions, whereas the optimization of (8.0.3) is basically a geometric problem. Indeed, the essential unknown is the set $\{(x, y) \in \Omega_L : u_y(x, y) = 1\}$ which determines u via integration in y-direction (if one imposes *e.g.* $u(x, 0) = u(x, 1) = 0$). The elastic energy of the martensite is now represented solely by u_x^2 and the surface energy density $\epsilon |u_{yy}|$ effectively counts the number of interfaces. As in the original model (8.0.1), one can relax the hard boundary condition incorporated in $\mathcal{A}$ and augment F_ϵ by a term describing the elastic energy in the austenite, *cf*. [KM92, Con06].

The rigorous connection between the *diffuse interface model* (8.0.1) and the *sharp interface model* (8.0.3) has not been investigated in detail so far, however, there are a couple of remarks in this direction [KM94, Con00a]. We refer to [MM77, Mod87] for a rigorous analysis of a related first-order problem and to [Mül90, Mül93] for results on a corresponding one-dimensional problem. However, we provide a quantitative relation between the constants κ in (8.0.1) and ϵ in (8.0.3), respectively, which also offers a

link between (8.0.1) and (8.0.3). Let us consider a small neighborhood of an interface where u_y changes sign from approximately -1 to approximately $+1$. We have the elementary inequality

$$\tfrac{1}{2}\kappa^2\, u_{yy}^2 + \sigma\,(u_y^2 - 1)^2 \geq \sqrt{2\sigma}\,\kappa\,|1 - u_y^2|\,|u_{yy}|\,,$$

which becomes sharp if $\kappa u_{yy} = \pm\sqrt{2\sigma}(u_y^2 - 1)$, *i.e.*, if we choose the right profile locally. Defining $W(s) = (1 - s^2)^2$, the corresponding (optimal) interfacial energy of (8.0.1) can be computed as (*cf.* [KM92, eq. (12)]):

$$\int \tfrac{1}{2}\kappa^2\, u_{yy}^2 + \sigma\, W(u_y)\, \mathrm{d}y = \sqrt{2\sigma}\,\kappa \int W^{1/2}(u_y)\, u_{yy}\, \mathrm{d}y = \sqrt{2\sigma}\,\kappa \int_{-1}^{1} W^{1/2}(z)\, \mathrm{d}z = \frac{4\sqrt{2\sigma}}{3}\kappa\,.$$

On the other hand, the sharp interface model (8.0.3) assigns 2ϵ to such an interface, *i.e.* we have

$$2\epsilon = \frac{4\sqrt{2\sigma}}{3}\kappa \quad \Rightarrow \quad \epsilon = \frac{2\sqrt{2\sigma}}{3}\kappa\,. \tag{8.0.4}$$

Kohn and Müller [KM94] prove the existence of a minimizer of (8.0.3) and show that there are constants $c, C > 0$ such that

$$c\,\epsilon^{2/3}L^{1/3} \leq \min_{u\in\mathcal{A}} F_\epsilon[u] \leq C\,\epsilon^{2/3}L^{1/3}\,, \tag{8.0.5}$$

subject to the condition that $\epsilon > 0$ is sufficiently small, which is assumed to be the case throughout this thesis. In order to recover the upper bound they use an explicitly constructed branching pattern (*cf.* Fig. 8.1, middle) which – after some optimization – yields a constant $C \approx 6.86$ [KM92, eq. (45)]; the corresponding constant in the lower bound is $c \approx 2.08$ [KM94, Lemma 2.8]. However, an explicit construction of the minimizer is still an open problem, although characteristic properties of such a minimizer have already been proved. For example, Conti [Con00b] provided a *local* upper bound on the energy and on the minimizer itself and proved self-similarity of the minimizer near the austenite-martensite interface in the sense that the sequence $u_j(x,y) = \theta^{-2j/3}u(\theta^j x, \theta^{2j/3}y)$ admits a $W^{1,2}$-strongly converging subsequence ($0 < \theta < 1$).

What is the contribution of this thesis?   The objective of this work is to present a new type of branching pattern and to show numerically and analytically that it leads to a significantly lower constant C in the upper bound in (8.0.5). Since the explicit formulation of the minimizer is still unknown our new pattern provides a hint in this direction that might be useful in further analytical investigations.

The remainder of this chapter is organized as follows. In Sec. 8.1, the diffuse interface model (8.0.1) is optimized numerically by means of a conforming finite element method. Based on the insight from this numerical simulation, we (numerically) investigate a novel, low dimensional family of branching microstructures for the sharp interface model (8.0.3) in Sec. 8.2. In Sec. 8.3, we construct explicit branching patterns for different models that allow for a closed-form computation of an upper bound. We finally discuss our findings and their implications in Sec. 8.4.

Remark 8.0.1. The results presented in Sec.8.1 and Sec. 8.2 are joint work with Martin Rumpf and Patrick Dondl, and have been published in [DHR16].

8.1 Simulations based on subdivision finite elements

The new branching pattern investigated in this thesis is derived from the results of a finite element simulation of the diffuse interface model (8.0.1). As motivated above, this functional approximates the sharp interface model (8.0.3) without imposing the nonlinear condition $|u_y| = 1$, which is hard to realize numerically. To minimize the energy (8.0.1) via a conforming finite element method, H^2-regular ansatz functions have to be taken into account. We construct an appropiate ansatz space by using (Loop) subdivision surface basis functions which results in a H^2-conforming method [Loo87]. There are many papers investigating the theory of subdivision surfaces, describing the corresponding implementation and performing numerical simulations. Most relevant, Reif [Rei95] developed a unified framework to prove C^1-regularity using the so-called characteristic map embedding. Later, Reif and Schröder [RS01] showed H^2-regularity and Arden [Ard01] investigated further approximation properties of subdivision surfaces. The H^2-regularity is in particular essential for higher order finite element simulations, as performed *e.g.* in [COS00, DSB07, CL11]. In terms of the implementation of an efficient subdivision code we refer to [Sta99, SZ00, BLZ00, GKS02].

To compute a minimizer $u \in H^2(\Omega)$ of (8.0.1) we set $L = 1$, *i.e.* we have $\Omega = (0,1)^2$, and consider zero Dirichlet boundary conditions on $\partial \Omega$. For a given function $u^0 : \Omega \to \mathbb{R}$ and for some $T > 0$, we define a L^2-gradient flow $u(t,x,y) : [0,T] \times \Omega \to \mathbb{R}$ with $u(0,x,y) = u^0(x,y)$ by

$$(u_t, \phi)_{L^2} = -\partial_u E_\kappa[u](\phi) \,, \tag{8.1.1}$$

where $\partial_u E_\kappa[u](\phi) := \frac{d}{ds} E_\kappa[u + s\phi]|_{s=0}$ denotes the Gâteaux-derivative of E_κ in some test direction $\phi \in H^2(\Omega) \cap H_0^1(\Omega)$. However, E_κ is not convex, hence the Hessian of E_κ is not positive definite. That means, multiple equilibria of (8.0.1) may exist and the gradient flow can expand in u. In order to treat the gradient flow in a numerically efficient manner, we use a convex-concave splitting algorithm proposed by Eyre [Eyr98]. To this end, one decomposes the energy functional into a convex energy plus a concave energy, *i.e.* $E_\kappa = G_{\kappa,\lambda}^+ + G_{\kappa,\lambda}^-$. In this decomposition, $G_{\kappa,\lambda}^+$ is convex for all $\lambda > 0$ and $G_{\kappa,\lambda}^-$ is (essentially) concave for all $\lambda > c$ for a finite constant $c > 0$. Then one evolves (8.1.1) using a semi-implicit timestepping scheme in which $G_{\kappa,\lambda}^+$ is treated implicitly and $G_{\kappa,\lambda}^-$ explicitly. This splitting method has become popular especially for treating diffuse interface equations such as the Cahn-Hilliard equation which is related to (8.0.1), *e.g.* in [BEG07]. Motivated by [BEG07] we define

$$G_{\kappa,\lambda}^+[u] := \int_\Omega \frac{1}{2}\kappa^2 u_{yy}^2 + \lambda u_y^2 + u_x^2 \,\mathrm{d}x\,\mathrm{d}y \,, \qquad G_{\kappa,\lambda}^-[u] := (E_\kappa - G_{\kappa,\lambda}^+)[u] \,. \tag{8.1.2}$$

Note that $G_{\kappa,\lambda}^+$ is designed such that $u \mapsto \partial_u G_{\kappa,\lambda}^+[u]$ is linear. As we assume $|u_y| \approx 1$ we can choose a (finite) $\lambda > 0$, such that

$$G_{\kappa,\lambda}^-[u] = \sigma \int_\Omega 1 - \left(2 + \frac{\lambda}{\sigma}\right) u_y^2 + u_y^4 \,\mathrm{d}x\,\mathrm{d}y$$

is concave. We write $u^k(x,y) = u(k\tau, x, y)$ for some time stepsize $\tau > 0$ and apply (8.1.1) to (8.1.2):

$$(u^{k+1} - u^k, \phi)_{L^2} = -\tau \left(\partial_u G_{\kappa,\lambda}^+[u^{k+1}](\phi) + \partial_u G_{\kappa,\lambda}^-[u^k](\phi) \right) \,. \tag{8.1.3}$$

Note that $G_{\kappa,\lambda}^+$ is treated implicitly, whereas $G_{\kappa,\lambda}^-$ is treated explicitly.

For the spatial discretization we introduce a regular triangulation[1] Ω_h of Ω with n nodes $(x_i, y_i) \in \mathbb{R}^2$, $i = 1, \ldots, n$. We approximate u^k by $U^k(x,y) := \sum_i \bar{U}_i^k \varphi_i(x,y)$, where $(\varphi_i)_{1 \le i \le n}$ is the basis function

---

[1] In the context of subdivision surfaces, one is interested in dealing with regular control meshes, *i.e.* meshes with as many *regular* vertices as possible—a regular vertex is a vertex with valence 6. In particular, the domain $\Omega = [0,1]^2$ can be described by a mesh having nothing but regular vertices in the interior. However, the treatment of (irregular) boundary vertices is more involed, see *e.g.* [BLZ00].

set consisting of subdivision functions. In a nutshell, the graph of φ_i is defined as the subdivision surface with reference net Ω_h and control vertices (x_j, y_j, δ_{ij}). The effective unknowns are collected in the coefficient vector $\bar{U}^k = (\bar{U}_i^k)_i \in \mathbb{R}^n$. Hence we can rewrite (8.1.3) in matrix-vector-notation as a linear system

$$\left(\mathbf{M} + \tau\kappa^2\mathbf{L_{yy}} + 2\tau\lambda\mathbf{L_y} + 2\tau\mathbf{L_x}\right)\bar{U}^{k+1} = \left(\mathbf{M} + 2\tau\left(2\sigma + \lambda\right)\mathbf{L_y} - 4\tau\sigma\mathbf{Q}[U^k]\right)\bar{U}^k, \qquad (8.1.4)$$

which is solved for $\bar{U}^{k+1} \in \mathbb{R}^n$ in every iteration step for given $\bar{U}^k \in \mathbb{R}^n$ and $n \times n$ - matrix quantities

$$\mathbf{M}_{ij} = \int_\Omega \varphi_i\varphi_j \; \mathrm{d}x \, \mathrm{d}y\,, \quad (\mathbf{L_z})_{ij} = \int_\Omega \partial_z\varphi_i \; \partial_z\varphi_j \; \mathrm{d}x \, \mathrm{d}y\,, \quad \mathbf{Q}[\omega]_{ij} = \int_\Omega \omega^2(x,y)\,\partial_y\varphi_i\;\partial_y\varphi_j\;\mathrm{d}x\,\mathrm{d}y\,.$$

In our numerical scheme we approximate these integrals by a three-point Gauss integration. With all the relevant matrices pre-assembled, this time stepping system is fairly easy to implement and can be shown to be unconditionally stable (as long as the convexity and concavity conditions are observed). Each iteration step then consists of updating the right hand side and solving (8.1.4). Since the system matrix on the left-hand-side in (8.1.4) does not depend on k, it can be factorized once at the beginning, *e.g.* by a Cholesky-factorization. The Dirichlet boundary condition is fulfilled by setting corresponding entries in $\bar{U}^k$ to zero.
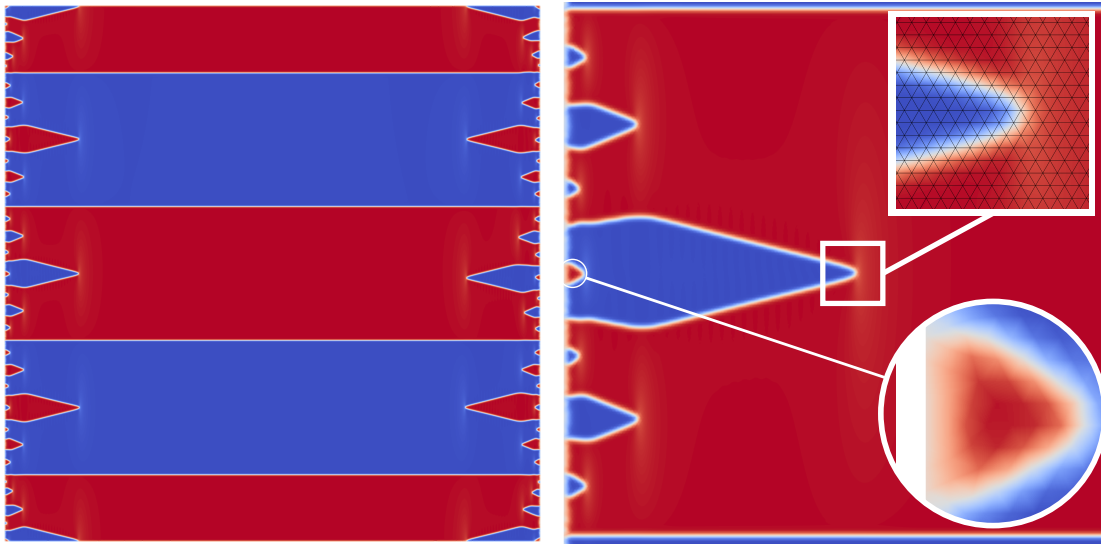
Figure 8.2: *Different zooms for a minimizer of E_κ in (8.0.1) with 10^6 elements on $\Omega = [0,1]^2$ with $\kappa = 2\sqrt{5}\cdot 10^{-3}$ and $\sigma = 10$, where blue resp. red encodes $u_y \approx \pm 1$. The spatial resolution is shown in the square zoom (top, right); the circle zoom (bottom, right) highlights an inner needle.*

By this method the (numerical) minimizer u of (8.0.1) can be computed robustly and independently of the choosen initial data u^0. Fig. 8.2 depicts corresponding u_y-values which induce a characteristic branching pattern. Due to the double-well potential in (8.0.1), we observe $|u_y| \approx 1$ everywhere outside of small transition layers (where u_y changes sign) and boundary layers close to $x = 0$ and $x = 1$, respectively. Obviously, the pattern is topologically different from the branching pattern investigated by Kohn and Müller [KM92], where the inner needles (Fig. 8.2, circle zoom) are not taken into account (*cf*. Fig. 8.1, middle). Furthermore, the pattern in our simulations differs geometrically from the pattern proposed by Li [Li03], where inner needles are generated on every level (*cf*. Fig. 8.1, right) whereas in our pattern they arise *every other* level. Let us mention that a topologically equivalent, however geometrically some-what distorted pattern has been found in less accurate simulations by Muite [Mui09].

8.2 Optimal branching patterns for a reduced sharp interface model

In this section, we will use the findings for the diffuse interface model from the previous section to derive a geometrically simple, reduced model for the sharp interface problem (8.0.3). Then we optimize over its degrees of freedom and compare it in terms of the stored energy with correspondingly optimized version of the patterns proposed by Kohn and Müller (*cf.* Fig. 8.1, middle) and by Li (*cf.* Fig. 8.1, right).

8.2.1 A reduced sharp interface model

Topology In the reduced model we consider functions $u : \Omega \to \mathbb{R}$ with $|u_y| = 1$ a.e. by construction. In fact, we divide Ω into regions bounded by piecewise polygonal lines. Connected components separated by these lines then describe regions with $u_y = \pm 1$ and the polygonal lines represent interfaces where the gradient of u jumps. Using the boundary condition along $y = 0$, one can explicitly reconstruct u on Ω by integrating in y-direction, *i.e.* u is completely determined by these interfaces[1]. In the following, we describe how the piecewise polygonal interfaces are constructed *topologically*. The positions of the vertices of the polygonal lines represent the geometric degrees of freedom (to be optimized later). As the construction is refined subsequently for $x \searrow 0$, the interfaces actually form a branching pattern.

The branching pattern is constructed by defining *needles* of different size, which are bounded by polygonal lines—as mentioned above. We assume that one needle consists of a trunk (t) and a spike (s) on top of it, material outside a needle is refered to as facet (f), *cf.* Fig. 8.3. The generation of a particular branching pattern is described best by the action of an *automaton* $\mathcal{A}$. We consider the alphabet $\{f, s, t, |\}$, where $|$ denotes an interface. The initial word is given by $\omega_0 = f$. A branching pattern after K iterations is defined by

$$\mathcal{B}_K = \omega_0; \ \mathcal{A}(\omega_0); \ \ldots; \ \mathcal{A}^K(\omega_0),$$

Figure 8.3: Trunk is green, facets yellow and spikes red.

where ; represents the generation of a new level. The action of $\mathcal{A}$ on a word is realized letter by letter where $\mathcal{A}(|) = |$ for all patterns. Different branching patterns are characterized by the action of $\mathcal{A}$ on the three letters $\{f, s, t\}$. The new branching pattern (NEW) described in Sec. 8.1 (*cf.* Fig. 8.2) is characterized by

$$\mathcal{A}(s) = t, \qquad \mathcal{A}(t) = \mathcal{A}(f) = f \,|\, s \,|\, f,$$

as depicted in Fig. 8.4. The pattern (KM) proposed by Kohn and Müller [KM92] (*cf.* Fig. 8.1, middle) is generated by the rules

$$\mathcal{A}(s) = t, \qquad \mathcal{A}(t) = t, \qquad \mathcal{A}(f) = f \,|\, s \,|\, f,$$

and the pattern (L) investigated by Li [Li03] (*cf.* Fig. 8.1, right) is given by the rules

$$\mathcal{A}(s) = \mathcal{A}(f) = f \,|\, s \,|\, f.$$

Note that there are no trunks t in the Li model.

A periodic cell $\mathcal{P}_K$ with K levels is now defined by computing $\mathcal{B}_K$ (as described above) and then reflecting half of the pattern to either side along two straight additional interfaces (as shown in Fig. 8.4, right). The constructed pattern consists of connected components (bounded by polygonal lines) which will later represent different phases of martensite, *i.e.* regions with $u_y = \pm 1$ (cf. Fig. 8.4 vs. 8.5). This construction enables a periodic extension in y-direction. In particular, the (periodic) boundary conditions $u(x, 1) = u(x, 0)$ are fulfilled by construction.

---

[1] In particular, we will ensure $u(x, 1) = u(x, 0)$ by suitable reflections and periodic extensions to be described later.

Figure 8.4: *Constructing a periodic cell $\mathcal{P}_3$ with $K = 3$ levels. Starting from the intial word $\mathcal{B}_0 = \omega_0 = f$, the automaton is applied three times to construct $\mathcal{B}_1, \mathcal{B}_2, \mathcal{B}_3$ (using the (NEW) scheme). Afterwards, a y-periodic cell $\mathcal{P}_3$ is constructed by reflecting half of the pattern $\mathcal{B}_3$ to either side along two straight additional interfaces (right). Color code: facet (■), spike (■) and trunk (■), black lines denote interfaces separating regions with $|u_y| = \pm 1$. All patterns $\mathcal{B}_k$ and $\mathcal{P}_3$ have been rotated by 90° for better visualization. Note that the color coding does* not *represent different phases of martensite (as in Fig. 8.5).*

Geometry Now we describe the geometric arrangement of $\Omega = [0, L] \times [0, 1]$ as well as the degrees of freedom of the reduced model. There is a region without branching between $x = l$ and $x = L$ (*cf.* Fig. 8.5). Here we allow for a lamellar pattern which is advantageous far away from the austenite-martensite interface at $x = 0$. Branching starts at $x = l$, where we shall consider $l \in (0, L)$ as a degree of freedom. The kth branching level (whose topology is described by the automaton) is located between $x_k = \theta^k l$ and $x_{k-1} = \theta^{k-1} l$, for $k > 0$. By construction, the pattern is symmetric along $y = \frac{1}{2}$, ensuring periodic boundary conditions as mentioned above. We choose constant zero boundary condidions $u(x, 0) = u(x, 1) = 0$ which directly implies $u(x, \frac{1}{2}) = 0$, *i.e.* $u_x(x, \frac{1}{2}) = 0$. We assume that the tip of an (initial) needle and the tip of all needles being generated *within* this initial needle lie on a horizontal line. Note that this only applies to (NEW) and (L) as (KM) never produces new needles *within* one existing needle.
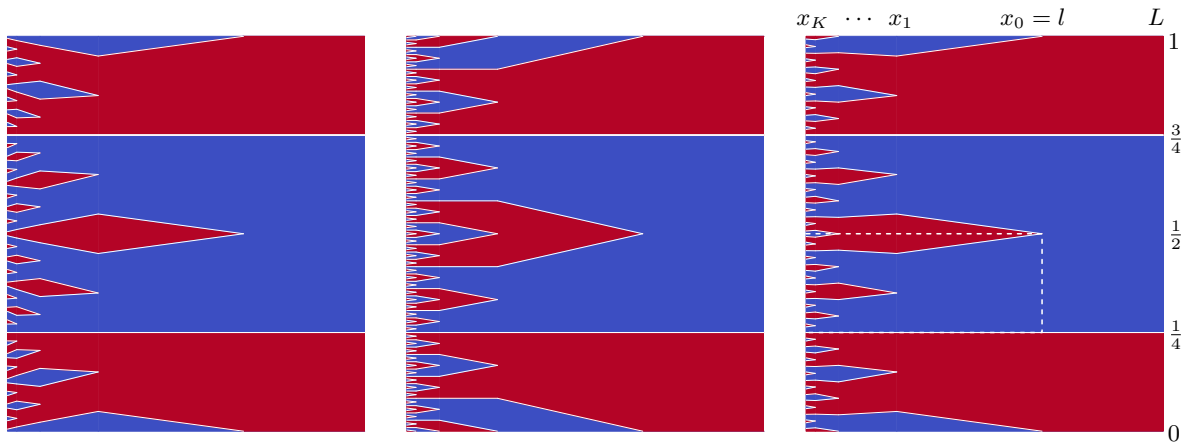
Figure 8.5: *Periodic cell $\mathcal{P}_4$ for (KM), (L) and (NEW) from left to right, with $x_k = \theta^k l$ for $k \geq 0$ and $l < L$. Here the color encodes the sign of u_y. The computational domain $\mathcal{C}_K = [x_K, x_0] \times [\frac{1}{4}, \frac{1}{2}]$ is surrounded by the dotted line in the (NEW) scheme. By construction, the pattern is symmetric along $y = \frac{1}{2}$, ensuring periodic boundary conditions, i.e. $u(x, 0) = u(x, 1)$. Later, $\mathcal{P}_K$ is rescaled in y-direction by N^{-1} to allow N repetitions in y-direction within Ω.*

Derivation of surface energy   The surface energy counts the number of interfaces, *i.e.* the number of jumps of $|u_y|$ in $y-$direction. In particular, as $|u_y| = 1$, there is a jump height of 2. Let I_k denote the number of interfaces in $\mathcal{S}_k = \{(x, y) : x_k < x < x_{k-1}\} \subset \mathcal{P}_K$. Then we have

$$\int_{\mathcal{S}_k} \epsilon |u_{yy}| \, \mathrm{d}x \, \mathrm{d}y = 2\epsilon \, (x_{k-1} - x_k) \, I_k = 2\epsilon \, (1 - \theta) \theta^{k-1} l \, I_k$$

for the interface energy. Obviously

$$I_k = 2 \cdot \left(1 + 2 \sum_{i=1}^{k} s_i\right), \tag{8.2.1}$$

where s_i denotes the number of spikes in $\mathcal{S}_i$ between two parallel interfaces shown as vertical black lines in Fig. 8.4 (right). Note that each spike consists of two interfaces and that there are also interfaces parallel to the x-axis which have to be accounted for. If we consider N repetitions of a rescaled cell $\mathcal{P}_K$ we get

$$F_{\mathrm{surf}}^{K,\epsilon}[\theta, N, l] = \int_{x_K < x < l} \epsilon |u_{yy}| \, \mathrm{d}x \, \mathrm{d}y = 2\epsilon N(1 - \theta) l \sum_{k=1}^{K} \theta^{k-1} I_k \,, \tag{8.2.2}$$

and the surface energy of the laminates in $\{(x, y) \in \Omega : l < x < L\}$ reads

$$B_{\mathrm{surf}}^{\epsilon,L}[N, l] = \int_{l < x < L} \epsilon |u_{yy}| \, \mathrm{d}x \, \mathrm{d}y = 4\epsilon N(L - l) \,. \tag{8.2.3}$$

Finally, the remaining surface energy in $\Omega_\partial := [0, x_K] \times [0, 1]$ is given by

$$R_{\mathrm{surf}}^{K,\epsilon}[\theta, N, l] = \int_{\Omega_\partial} \epsilon |u_{yy}| \, \mathrm{d}x \, \mathrm{d}y = 2\epsilon N(1 - \theta) l \sum_{k > K} \theta^{k-1} I_k \,. \tag{8.2.4}$$

Note that we observe the well-known scaling behaviour

$$F_{\mathrm{surf}}^{K,\epsilon}[\theta, N, l] + R_{\mathrm{surf}}^{K,\epsilon}[\theta, N, l] = \int_{0 < x < l} \epsilon |u_{yy}| \, \mathrm{d}x \, \mathrm{d}y \quad = \quad c_{\mathrm{surf}}(\theta) \, 2\epsilon \, l \, N \,, \tag{8.2.5}$$

where $c_{\mathrm{surf}}(\theta)$ will be specified later. Subsequently, we deduce different recursive definitions for the sequences $(s_i)_i$, depending on the model (NEW), (KM) and (L), respectively. In particular, this enables to write (8.2.1) as a closed formula which allows the evaluation of the infinite sum in (8.2.4).

(NEW) According to the automaton (*cf*. Fig. 8.4), each spike at some level k becomes a trunk on level $k + 1$, which is enclosed by two finer spikes. Additionally, each spike at some level k creates one spike in its trunk at level $k + 2$. Hence we have the recursive formula $s_1 = 1$, $s_2 = 2$ and

$$s_i = 2s_{i-1} + s_{i-2} \,, \quad i > 2 \,.$$

This is a generalized Fibonacci sequence, *i.e.* we have the explicit representation

$$s_i = \frac{\alpha^i - \beta^i}{2\sqrt{2}} \,, \quad \alpha = 1 + \sqrt{2} \,, \quad \beta = 1 - \sqrt{2} \,.$$

Hence

$$2 \sum_{i=1}^{k} s_i = \frac{\alpha}{\sqrt{2}} \sum_{i=0}^{k-1} \alpha^i - \frac{\beta}{\sqrt{2}} \sum_{i=0}^{k-1} \beta^i = \frac{\alpha}{\sqrt{2}} \frac{\alpha^k - 1}{\alpha - 1} - \frac{\beta}{\sqrt{2}} \frac{\beta^k - 1}{\beta - 1} = \frac{1}{2} \alpha^{k+1} + \frac{1}{2} \beta^{k+1} - 1 \,,$$

and finally

$$I_k = \alpha^{k+1} + \beta^{k+1}.$$

Proof of Fibonacci representation: For a recursive sequence $a_k = p a_{k-1} + q a_{n-2}$ for $k > 1$ and a_0 and a_1 given, we have $a_n = \frac{r\alpha^n - s\beta^n}{\alpha - \beta}$, where α and β are the roots of $x^2 - px - q = 0$ and r, s are determined by a_0 and a_1. For $p = 2$, $q = 1$, $a_0 = 1$ and $a_1 = 2$ we get $a_n = \frac{r\alpha^n - s\beta^n}{2\sqrt{2}}$ with $\alpha = 1 + \sqrt{2}$ and $\beta = 1 - \sqrt{2}$. We further solve

$$1 = a_0 = \frac{r - s}{2\sqrt{2}}, \quad 2 = a_1 = \frac{r\alpha - s\beta}{2\sqrt{2}}$$

for r and s, *i.e.* $r = s + 2\sqrt{2}$ and $4\sqrt{2} = s(\alpha - \beta) + 2\sqrt{2}\alpha$, *i.e.* $s = 2 - \alpha = \beta$ and $r = \alpha$.

(KM) As prescribed by the automaton, each spike at some level k becomes a trunk on level $k+1$, which is enclosed by two finer spikes. Hence we have $s_i = 2^{i-1}$ for $i > 0$ and obtain

$$I_k = 2\left(1 + 2 \cdot \sum_{i=1}^{k} s_i\right) = 2\left(1 + 2 \cdot \sum_{i=0}^{k-1} 2^i\right) = 2\left(1 + 2\frac{2^k - 1}{2 - 1}\right) = 2^{k+2} - 2.$$

(L) Each spike at some level k generates one interior spike and two outer spikes on level $k+1$. Hence we have $s_i = 3^{i-1}$ for $i > 0$ and obtain

$$I_k = 2\left(1 + 2 \cdot \sum_{i=1}^{k} s_i\right) = 2\left(1 + 2 \cdot \sum_{i=0}^{k-1} 3^i\right) = 2\left(1 + 2\frac{3^k - 1}{3 - 1}\right) = 2 \cdot 3^k.$$

Derivation of elastic energy For the computation of the elastic energy it is convenient to introduce a computational domain $\mathcal{C}_K \subset \mathcal{P}_K$ which is limited to $\mathcal{C}_K = [\theta^K l, l] \times [\frac{1}{4}, \frac{1}{2}]$, as indicated by the dotted lines in Fig. 8.5 (right). The geometry of $\mathcal{C}_K$ is described by θ and the y coordinates of the interior vertices of the polygonal interfaces. As indicated in Fig. 8.6, we denote the vertices on the line with $x_k = \theta^k l$ by $y_{k,n}$ for $n = 1, \dots n_k$ and the open sets of constant slope u_y between the lines $x_{k-1} = \theta^{k-1} l$ and $x_k = \theta^k l$ by $\mathcal{R}_{k,i}$ for $i = 1, \dots i_k$. That means we have

$$u_y|_{\mathcal{R}_{k,i}} = -u_y|_{\mathcal{R}_{k,i+1}}$$

for all $k > 0$ and for all $i > 0$. In the following we show that u_x is constant on $\mathcal{R}_{k,i}$ for all i, k.

Proposition 8.2.1. *For $[y_{k-1,\overline{n}(k,i)}, y_{k,\underline{n}(k,i)}]$ being the upper edge of $\mathcal{R}_{k,i}$, the piecewise constant quantity u_x on the stripe $\mathcal{C}_K \cap \{x_k \le x \le x_{k-1}\}$ is described iteratively by*

$$u_x|_{\mathcal{R}_{k,0}} = 0,$$
$$u_x|_{\mathcal{R}_{k,i+1}} = u_x|_{\mathcal{R}_{k,i}} + 2\,sign\left(u_y|_{\mathcal{R}_{k,i}}\right) \frac{y_{k-1,\overline{n}(k,i)} - y_{k,\underline{n}(k,i)}}{\theta^{k-1}l - \theta^k l}, \quad i \ge 0. \tag{8.2.6}$$

Proof: See Lemma A.1.7 in the appendix.

Using Prop. 8.2.1 the elastic energy in $\mathcal{C}_K$ is given by

$$F_{\text{elast}}[\mathcal{C}_K] = \int_{\mathcal{C}_K} u_x^2 \, \mathrm{d}x \, \mathrm{d}y = \sum_{k=1}^{K} \sum_{i>0} (u_x|_{\mathcal{R}_{k,i}})^2 \cdot |\mathcal{R}_{k,i}|.$$
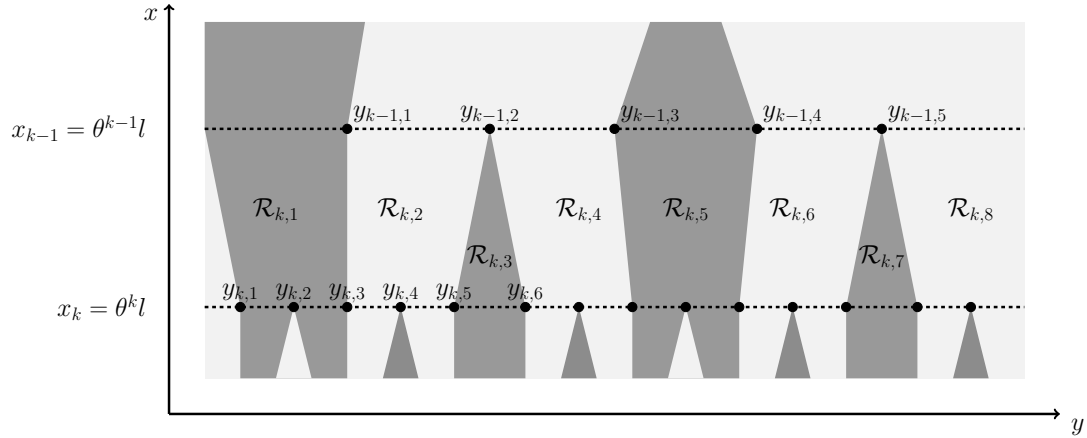
Figure 8.6: *Degrees of freedom in y-direction (black dots),* i.e. $y_{k,n}$ *for* $n = 1, \ldots, n_k$ *for each level* k. *Areas* $\mathcal{R}_{k,i}$ *separated in y-directions by interfaces and in x-direction by dotted, artificial lines along* $x = x_{k-1}$ *and* $x = x_k$, *respectively, represent regions with constant slope* u_x.

Due to the symmetry of $\mathcal{P}_K$ we have $F_{\text{elast}}[\mathcal{P}_K] = 4\, F_{\text{elast}}[\mathcal{C}_K]$. If we now rescale $\mathcal{P}_K$ in y-direction by N^{-1} (to allow N repetitions of $\mathcal{P}_K$) we have $u_x \sim N^{-1}$ and $|\mathcal{R}_{k,i}| \sim N^{-1}$. The total elastic energy F_{elast}^K in $\{(x,y) \in \Omega : x_K < x < l\}$ is then given by summing over all N repetitions of $\mathcal{P}_K$, *i.e.* if we collect all $y_{k,i}$ in a vector $\mathbf{Y}$ we have

$$F_{\text{elast}}^K[\theta, N, l, \mathbf{Y}] = \int_{x_K < x < l} u_x^2 \, \mathrm{d}x \, \mathrm{d}y = 4N^{-2} \sum_{k=1}^{K} \sum_{i>0} \left(u_x|_{\mathcal{R}_{k,i}}\right)^2 \cdot |\mathcal{R}_{k,i}| \,. \tag{8.2.7}$$

Note that there is no contribution to the elastic energy in the stripe $\{(x,y) \in \Omega : l < x < L\}$, *i.e.*

$$\int_{l < x < L} u_x^2 \, \mathrm{d}x \, \mathrm{d}y = 0 \,.$$

Finally, the remaining elastic energy in $\Omega_\partial = [0, x_K] \times [0,1]$ is given by

$$\int_{\Omega_\partial} u_x^2 \, \mathrm{d}x \, \mathrm{d}y = 4N^{-2} \sum_{k>K} \sum_{i>0} \left(u_x|_{\mathcal{R}_{k,i}}\right)^2 \cdot |\mathcal{R}_{k,i}| \,. \tag{8.2.8}$$

Since $u_x|_{\mathcal{R}_{k,i}} \sim l^{-1}$ and $|\mathcal{R}_{k,i}| \sim l$, we observe the well-known scaling behaviour

$$F_{\text{elast}}^K[\theta, N, l, \mathbf{Y}] \quad = \quad c_{\text{elast}}(\theta, \mathbf{Y})\, l^{-1} N^{-2} \,.$$

Remark 8.2.2. In contrast to the surface energy, we neither have a closed formula for the finite sum in (8.2.7) nor for the infinite sum in (8.2.8), which causes two problems. First, we are only able to perform computations for a *finite* number of levels K, the remaining term in (8.2.8) has to be estimated from above. We present a suitable upper bound subsequently. Second, I_k and hence the number of regions $\mathcal{R}_{k,i}$ grows exponentially in k, which results in a rapidly growing number of terms in the sum in (8.2.7) which have to be evaluated. Accordingly, the computation time as well as memory requirements increase dramatically, which renders numerical simulations unfeasible for large K. Although the choice $K \approx 15$ already touches the computational limit, the resulting rest term in (8.2.8) is vanishing in comparison to (8.2.7).

Boundary conditions and rest terms   So far, the degrees of freedoms (*dof*s) are given by the division ratio $\theta \in (0,1)$ in x-direction, a number $N \in \mathbb{N}$ that represents the repetitions of periodic cells in y-direction, a parameter $l \in (0, L)$ which defines the beginning of the branching and a vector $\mathbf{Y}$ collecting all degrees of freedom in y-direction within the computational domain (*cf.* Fig. 8.6). More precisely, we have $\mathbf{Y} = \bigcup_{k \geq 0} (y_{k,i})_i$. In the following, we will make use of the notation

$$\mathbf{Y} = \mathbf{Y}^K \cup \mathbf{Y}^\infty, \quad \text{with} \quad \mathbf{Y}^K = \bigcup_{k=0}^{K} (y_{k,i})_i, \quad \mathbf{Y}^\infty = \bigcup_{k>K} (y_{k,i})_i.$$
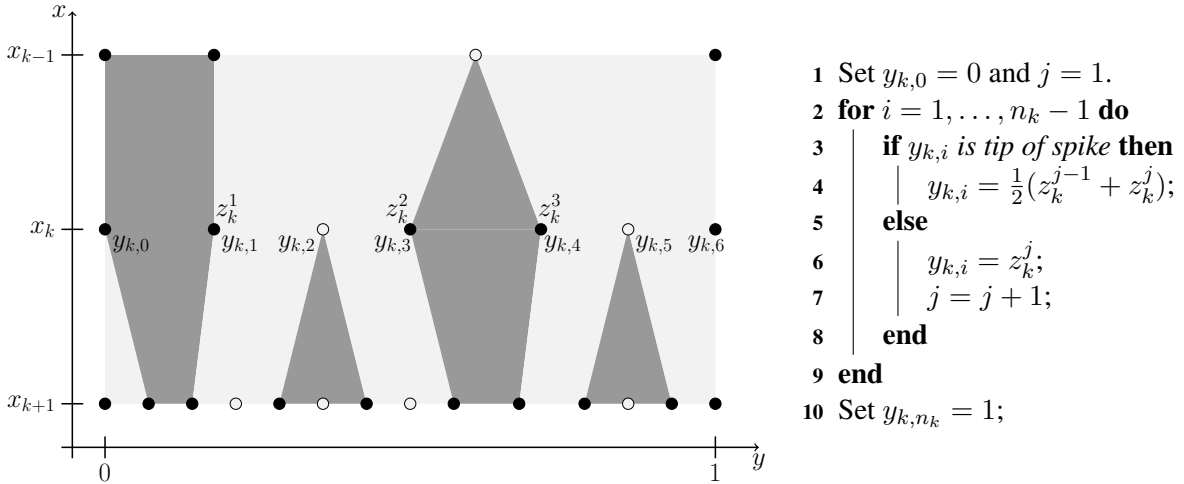
In particular, $\mathbf{Y}^K$ contains a finite number of *dof*s, whereas $\mathbf{Y}^\infty$ is infinite. Note that a function $u : \Omega \to \mathbb{R}$ is uniquely determined by θ, l, N and $\mathbf{Y}$, since for each $x \in (0, L)$ we can compute $u(x, y)$ by integration in y-direction using the boundary condition along $y = 0$, *i.e.* $u(x, y) = u(x, 0) + \int_0^x u_y(x, z)\,\mathrm{d}z$. According to Rem. 8.2.2, we restrict ourselves to the optimization of the first K levels, hence the *dof*s in y-direction are actually given by $\mathbf{Y}^K$. In the following, we describe how to set $\mathbf{Y}^\infty$ in order to (i) account for the boundary conditions $u(0, y) = 0$ and (ii) enable a suitable upper bound on (8.2.8).

We assume $N = 1$, *i.e.* we are dealing with only one periodic cell (the general case for arbitrary N will be considered later). First, we enlarge the set $\mathbf{Y}^\infty$. As illustrated in Fig. 8.6 the sequence $(y_{k,i})_i$ lives in the computational domain, *i.e.* $y_{k,i} \in (\frac{1}{4}, \frac{1}{2})$ for $i = 1, \dots, n_k$ and $k \leq K$. For $k > K$, however, we will extend the sequence of *dof*s (as illustrated in Fig. 8.7) by considering

$$y_{k,0} = 0 < y_{k,1} < \dots < y_{k,n_k} = 1, \quad k > K.$$

Our construction of u in $\Omega_\partial = [0, x_K] \times [0, 1]$, *i.e.* the definition of $\mathbf{Y}^\infty$ for given θ, l and N, is based on the construction in Lemma 2.2 resp. Lemma 2.3 by Conti [Con00b]. The main idea of our construction is that the particular branching pattern, *i.e.* (NEW), (L) or (KM), is extended infinitely in terms of the *topological* structure prescribed by the automaton. To this end, the surface energy in Ω_∂ of our constructed function u is precisely given by (8.2.4) and we have to provide only an upper bound for (8.2.8).


```
1  Set y_{k,0} = 0 and j = 1.
2  for i = 1, …, n_k − 1 do
3      if y_{k,i} is tip of spike then
4          y_{k,i} = ½(z_k^{j−1} + z_k^j);
5      else
6          y_{k,i} = z_k^j;
7          j = j + 1;
8      end
9  end
10 Set y_{k,n_k} = 1;
```

Figure 8.7: *Algorithm to define the geometric degrees of freedom $y_{k,i}$ for $k > K$ in the boundary layer $\Omega_\partial = [0, x_K] \times [0,1]$ by means of the discontinuities of $(v_k)_y$ denoted by z_k^i.*

Let $u_\partial(y) = u(x_K, y)$ be the function along $x = x_K$ and $u_0(y) = 0$ for all $y \in [0, 1]$. We define the linear interpolation $u_l : \Omega_\partial \to \mathbb{R}$ between u_∂ and u_0 by

$$u_l(x, y) = \frac{x}{x_K} u_\partial(y).$$

Since $|(u_\partial)_y| = 1$ we have $|(u_l)_y| \leq 1$. As introduced above, I_k denotes the number of interfaces in $\{(x, y) : x_k < x < x_{k-1}\}$. For $k > K$ we define a function $v_k : [0, 1] \to \mathbb{R}$ such that

$$v_k(iI_k^{-1}) = u_l(x_k, iI_k^{-1}), \quad i = 0, \ldots, I_k,$$

and $|(v_k)_y| = 1$ a.e. In particular, we have $v_k(0) = v_k(1) = 0$. By construction, $(v_k)_y$ changes sign (at most) I_k times, whereas we might assume that it changes sign *exactly* I_k times, since $|(u_l(x, y))_y| < 1$ for $x < x_K$. Let $0 < z_k^1 < z_k^2 < \ldots < z_k^{I_k} < 1$ be the (ordered) discontinuities of $(v_k)_y$, as depicted in Fig. 8.7 (left). We define the positions of the $y_{k,i}$ by the algorithm shown in Fig. 8.7 (right). Note that this procedure is well-defined if we set

$$n_k := I_k + \#\{\text{spikes on level } k + 1\} + 1, \quad k > K.$$

Furthermore, if $y_{k,i}$ corresponds to the tip of a spike on level $k + 1$, then neither $y_{k,i-1}$ nor $y_{k,i+1}$ correspond to the tip of another spike (at least for the three types of automatons considered here). As mentioned above, u is completely determined in Ω_∂ by θ, l and $\mathbf{Y}^\infty$. Analogously to the proof of Lemma 2.3 in [Con00b], we arrive at (2.17) and get for $\mathcal{S}_k = \{(x, y) : x_k < x < x_{k-1}\}$ and $h_k = I_k^{-1}$ with $k > K$:

$$\int_{\mathcal{S}_k} (u - u_l)_x^2 \, \mathrm{d}x \, \mathrm{d}y \leq \frac{16}{3} \frac{I_k^{-2}}{x_{k-1} - x_k}.$$

Using Lemma A.1.8 in the appendix (with $l_y = 1$ and $l_x = x_{k-1} - x_k$) we have

$$\int_{\mathcal{S}_k} u_x^2 \, \mathrm{d}x \, \mathrm{d}y = \int_{\mathcal{S}_k} (u - u_l)_x^2 \, \mathrm{d}x \, \mathrm{d}y + \int_{\mathcal{S}_k} (u_l)_x^2 \, \mathrm{d}x \, \mathrm{d}y$$

$$\leq \frac{16}{3} \frac{I_k^{-2}}{(1 - \theta) \theta^{k-1} l} + \int_0^1 \frac{(u_l(x_{k-1}, y) - u_l(x_k, y))^2}{x_{k-1} - x_k} \, \mathrm{d}y.$$

Due to the linearity of $x \mapsto u_l(x, y)$ we get for $k > K$:

$$\int_0^1 \frac{(u_l(x_{k-1}, y) - u_l(x_k, y))^2}{x_{k-1} - x_k} \, \mathrm{d}y = (x_{k-1} - x_k) \cdot \int_0^1 \left(\frac{u_l(x_{k-1}, y) - u_l(x_k, y)}{x_{k-1} - x_k} \right)^2 \, \mathrm{d}y$$

$$= (x_{k-1} - x_k) \cdot \int_0^1 \left(\frac{u_l(x_K, y) - u_l(0, y)}{x_K - 0} \right)^2 \, \mathrm{d}y$$

$$= \frac{x_{k-1} - x_k}{x_K^2} \cdot \int_0^1 u_\partial^2(y) \, \mathrm{d}y.$$

Finally, we sum over all $k > K$ and obtain

$$\int_{\Omega_\partial} u_x^2 \, \mathrm{d}x \, \mathrm{d}y \leq \frac{8}{3} \frac{\theta}{(1 - \theta) l} \sum_{k > K} I_k^{-2} \theta^{-k} + x_K^{-2} \cdot \int_0^1 u_\partial^2(y) \, \mathrm{d}y \cdot \sum_{k > K} (x_{k-1} - x_k)$$

$$= \frac{8}{3} \frac{\theta}{(1 - \theta) l} \sum_{k > K} I_k^{-2} \theta^{-k} + \frac{\|u(x_K, \cdot)\|_{L^2(0,1)}^2}{\theta^K l}.$$

Next, we give an upper bound on the term $\sum_{k > K} I_k^{-2} \theta^{-k}$, which depends on the model. For $k > 0$ the following estimates hold for the number of interfaces (with $\alpha = 1 + \sqrt{2}$ and $\beta = 1 - \sqrt{2}$ as above):

$$I_k = \begin{cases} \alpha^{k+1} + \beta^{k+1} > \alpha^{k+1} - 1 > \alpha^k, & \text{for (NEW)}, \\ 2 \cdot 3^k, & \text{for (L)}, \\ 2^{k+2} - 2 > 2 \cdot 2^k, & \text{for (KM)}. \end{cases} \quad (8.2.9)$$

Hence the geometric series $\sum_{k>K} I_k^{-2} \theta^{-k}$ converges if $\alpha^2 \theta > 1$ for (NEW), $4\theta > 1$ for (KM) and $9\theta > 1$ for (L) and an upper bound on the limit is given by $\theta^{-K} c_{\text{rem}}^K(\theta)$ with:

$$
c_{\text{rem}}^K(\theta) = \begin{cases} (\alpha^2)^{-K} \frac{\alpha^2 \theta}{\alpha^2 \theta - 1}, & \text{for (NEW)}, \\[2ex] 9^{-K} \frac{9\theta}{9(9\theta - 1)}, & \text{for (L)}, \\[2ex] 4^{-K} \frac{4\theta}{4(4\theta - 1)}, & \text{for (KM)}. \end{cases}
$$

Finally, we account for the case that $N \in \mathbb{N}$ has been chosen arbitrarily, *i.e.* we obtain for $N \in \mathbb{N}$:

$$
\int_{\Omega_\partial} u_x^2 \, \mathrm{d}x \, \mathrm{d}y \leq \frac{8}{3} \frac{\theta \, c_{\text{rem}}^K(\theta)}{(1-\theta)\theta^K l N^2} + \frac{\|u(x_K, .)\|_{L^2(0,1)}^2}{\theta^K l} =: R_{\text{elast}}^K[\theta, N, l, \mathbf{Y}]. \tag{8.2.10}
$$

Here $\|u(x_K, .)\|^2$ depends on $(y_{K,i})_i$ and scales like N^{-2}, *i.e.* $R_{\text{elast}}^K[\theta, N, l, \mathbf{Y}] \sim l^{-1} N^{-2}$ as expected.

Remark 8.2.3. Due to the estimates in (8.2.9), the upper bound on $\sum_{k>K} I_k^{-2} \theta^{-k}$ is sharp for (L), but not for (NEW) and (KM). For instance, already for moderate k we actually have $|\beta^k| \ll 1$, *i.e.* $I_k \approx \alpha^{k+1}$ for (NEW), hence $c_{\text{rem}}^K(\theta)$ could actually be scaled by a factor α^{-2}.

Due to Rem. 8.2.2 we are only able to perform simulations for a finite number $K \in \mathbb{N}$. Nevertheless, we have constructed the extension of u in the boundary layer Ω_∂, such that the surface energy of u in Ω_∂ is *exactly* given by (8.2.4). In the following, we give a closed formula for the surface energy, *i.e.* the sum of (8.2.2) and (8.2.4), depending on the model.

(NEW) Using $I_k = \alpha^{k+1} + \beta^{k+1}$ we get for $\alpha\theta < 1$:

$$
\begin{aligned}
c_{\text{surf}}(\theta) &= (1-\theta) \sum_{k=1}^\infty \theta^{k-1} I_k = (1-\theta)\Big(\alpha^2 \sum_{k=0}^\infty (\alpha\theta)^k + \beta^2 \sum_{k=0}^\infty (\beta\theta)^k\Big) \\
&= \frac{\alpha^2(1-\theta)}{1-\alpha\theta} + \frac{\beta^2(1-\theta)}{1-\beta\theta}.
\end{aligned} \tag{8.2.11}
$$

(L) Using $I_k = 2 \cdot 3^k$ we get for $3\theta < 1$:

$$
c_{\text{surf}}(\theta) = (1-\theta) \sum_{k=1}^\infty \theta^{k-1} I_k = 6(1-\theta) \sum_{k=0}^\infty (3\theta)^k = \frac{6(1-\theta)}{1-3\theta}.
$$

(KM) Using $I_k = 2^{k+2} - 2$ we get for $2\theta < 1$:

$$
c_{\text{surf}}(\theta) = (1-\theta) \sum_{k=1}^\infty \theta^{k-1} I_k = 8(1-\theta) \sum_{k=0}^\infty (2\theta)^k - 2(1-\theta) \sum_{k=0}^\infty \theta^k = \frac{8(1-\theta)}{1-2\theta} - 2.
$$

Using $c_{\text{surf}}(\theta)$, the surface energy (8.2.5) can be computed explicitly.

8.2.2 Numerical optimization and results

Summing the surface energies (8.2.2), (8.2.3) and (8.2.4), as well as the elastic energies (8.2.7) and (8.2.10) we obtain the objective functional for $\epsilon > 0$ and $K \in \mathbb{N}$, namely

$$F^{K,\epsilon}[\theta, N, l, \mathbf{Y}^K] = F_{\text{surf}}^{K,\epsilon}[\theta, N, l] + R_{\text{surf}}^{K,\epsilon}[\theta, N, l] + B_{\text{surf}}^{\epsilon,L}[N, l]$$
$$+ F_{\text{elast}}^{K}[\theta, N, l, \mathbf{Y}^K] + R_{\text{elast}}^{K}[\theta, N, l, \mathbf{Y}^K]. \quad (8.2.12)$$

Optimizing $F^{K,\epsilon}$ for N yields $N \sim \epsilon^{-1/3} l^{-2/3}$, *i.e.* we get the expected scaling $F^{K,\epsilon} \sim \epsilon^{2/3} l^{1/3}$. Note that we allow for a lamellar *and* a branching pattern, controlled by the variable $0 < l \leq L$. In constrast, in the construction presented in [KM92, KM94], branching starts already at the very right boundary of Ω which corresponds to fixing $l = L$.

We now optimize $F^{K,\epsilon}$ in (8.2.12) with respect to $\theta \in (0, 1)$, $l \in (0, L]$ and $\mathbf{Y}^K$ for fixed $\epsilon > 0$, $L = 0.5$, $N = 2$ and $K \in \mathbb{N}$ for the three different reduced models (L), (KM) and (NEW). One may also consider $N \in \mathbb{N}$ as an additional degree of freedom which is realized by assuming $N \in \mathbb{R}$ in the simulations. In order to compare the results to the finite element simulation of the diffuse interface model shown in Fig. 8.2, where $\kappa = 2\sqrt{5} \cdot 10^{-3}$ and $\sigma = 10$ we set $\epsilon = \frac{2\sqrt{2}\sigma}{3}\kappa \approx 0.013$ in the reduced model—according to (8.0.4). The simulation is initialized on level $K = 4$ with the patterns shown in Fig. 8.5. After optimizing all degrees of freedom on this level, K is increased by one by extrapolating the solution of the last level and the whole pattern is optimized again[1]. This procedure is repeated iteratively.
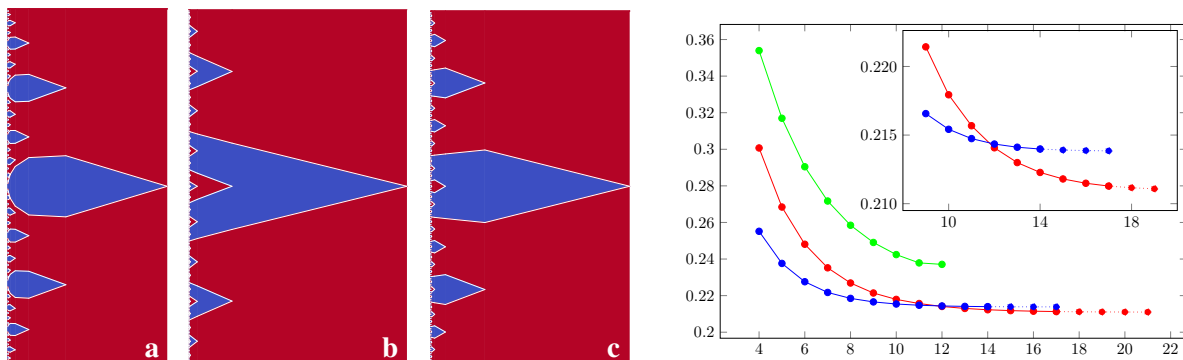
Figure 8.8: *From left to right: optimal patterns of the reduced model (with $\epsilon = 0.013$ and fixed $N = 2$) for (KM) with $K = 12$, (L) with $K = 14$ and (NEW) with $K = 17$, restricted to the domain $[\theta^K l, l] \times [3/8, 5/8]$. Right: Optimal energy for (NEW) in red, (L) in blue and (KM) in green, with enlargements of crucial details. Dotted lines are extrapolations without optimization, nevertheless, energies are monotonically decreasing. Numerical optimization breaks down for (KM) if $K > 12$ due to degeneration of geometry on high levels.*

The optimal patterns of the reduced models (for fixed $N = 2$) are compared to each other in Fig. 8.8. First, the reduced (KM) pattern degenerates already at level $K = 13$, *i.e.* monotonicity of the sequence $(y_{k,i})_i$ for $k \approx K$ is violated. In particular, it is energetically not competitive (cf. Fig. 8.9 and 8.8, right). Qualitatively, the optimal pattern of (NEW) in Fig. 8.8c, is very similar to the optimal pattern of the diffuse interface model in Fig. 8.2. Striking is the fact that all needles of (NEW) are actually diamond-shaped, *i.e.* bounded by a polygon consisting of *four straight* lines. Up to some numerical perturbations (probably due to boundary effects) this can also be observed in the pattern in Fig. 8.2. However, these straight lines are not mandatory in the reduced model due to the freedom to move $y_{k,i}$. For instance, this

---

[1] We comment on the definition of this extrapolation at the end of this section.

is not the case for the optimal pattern of (L) and (KM), cf. Fig. 8.8a and 8.8b.

The similarity between the optimal (NEW) pattern and the optimal pattern of the diffuse interface model also holds quantitatively. First, for (NEW) the optimal value $\theta = 0.273$ reflects very well the corresponding measured ratio $\theta \approx 0.26$ in Fig. 8.2. Second, the ratio "width-to-height" of the largest needle is approximately 2.6 in Fig. 8.2 and 2.7 for the optimal pattern of (NEW) in Fig. 8.8c. Furthermore, this ratio decreases in both patterns almost equally when going to the second largest needle.

Among the reduced models the (NEW) pattern performs best energetically, with a relative difference of $> 1\%$ with respect to the optimal energy of (L), see Fig. 8.9. Although the difference is not particularly large, it is stable with respect to a variation of the model parameters ϵ, L and N (not shown here).

	$F^{K,\epsilon}$	R^K_{elast}	l	θ
NEW	0.2113	$5.1 \cdot 10^{-4}$	0.146	0.273
L	0.2140	$2.9 \cdot 10^{-4}$	0.158	0.198
KM	0.2371	$1.3 \cdot 10^{-2}$	0.119	0.366

Figure 8.9: *Optimal values for NEW ($K = 17$), L ($K = 14$) and KM ($K = 12$) for fixed $N = 2$.*

In particular, this remains true when optimizing over all degrees of freedom, *i.e.* considering $N \in \mathbb{R}$ as additional degree of freedom (*cf*. Fig. 8.10). Fig. 8.10 further reveals that the difference $\Delta F^{K,\epsilon}$ of the optimal energies is of order 10^{-3} whereas the error (due to the estimate (8.2.10) in the boundary layer Ω_∂) is of order 10^{-4}. Furthermore, the estimate (8.2.10) is not sharp and hence R^K_{elast} is dominant for small K which leads to a substantial over-prediction of the energy in this regime. This effect is in particular striking in the energy decay of our model (NEW) for $K < 13$ (*cf*. Fig. 8.8, right), as explained in Rem. 8.2.3.

	$F^{K,\epsilon}$	R^K_{elast}	N	l	θ
NEW	0.2073	$4.4 \cdot 10^{-4}$	2.661	0.095	0.273
L	0.2096	$2.5 \cdot 10^{-4}$	2.689	0.101	0.198

Figure 8.10: *Optimal values for NEW ($K = 17$) and L ($K = 14$) with free $N \in \mathbb{R}$. Note that $\Delta F^{K,\epsilon} \sim 10^{-3}$ whereas $R^K_{elast} \sim 10^{-4}$.*

We compute $C = \min(F^{K,\epsilon})L^{-1/3}\epsilon^{-2/3}$ to compare our results to the upper constant $C \approx 6.86$ given in [KM92] and get $C \approx 4.81$ ($N = 2$ fixed) or even $C \approx 4.72$ (free $N \in \mathbb{R}$) for (NEW) and $C \approx 4.87$ or $C \approx 4.78$ for (L), respectively.

On the extrapolation For arbitrary $0 < k < K$, the geometric degrees of freedom $(y_{k,i})_i$ are distributed along $x = x_k$. Let $(\tilde{y}_{k,i})_i \subset (y_{k,i})_i$ denote the set of points that do *not* represent the tip of a spike on level $k + 1$, *cf*. Fig. 8.7. Due to the well-defined action of the automaton, one can determine for each pair $(\tilde{y}_{k,i}, \tilde{y}_{k,i+1})$, if the segment $[\tilde{y}_{k,i}, \tilde{y}_{k,i+1}]$ represents a spike, a trunk or a facet on level k. If, for instance, $[\tilde{y}_{k,i}, \tilde{y}_{k,i+1}]$ represents a spike, we denote the value $|\tilde{y}_{k,i+1} - \tilde{y}_{k,i}|$ as the *width* of that particular spike. Furthermore, let $\bar{s}_k \in \mathbb{R}$ denote the arithmetic mean value of all spike widths on level k. Likewise, we define the width of a trunk and the width of a facet and corresponding mean values $\bar{t}_k, \bar{f}_k \in \mathbb{R}$. Let $S_k, T_k, F_k \in \mathbb{N}$ denote the number of spikes, trunks and facets, respectively, on level k. Then we have for some $c > 0$:

$$\bar{s}_k S_k + \bar{t}_k T_k + \bar{f}_k F_k = c \quad \forall k. \tag{8.2.13}$$

As $S_k, T_k, F_k \to \infty$ we have $s_k, t_k, f_k \to 0$ for $k \to \infty$. Nevertheless, in an optimized branching structure with K levels, we observed two interesting features numerically (for $0 \ll k \ll K$):

1. The variance about the mean values $\bar{s}_k$, $\bar{t}_k$ and $\bar{f}_k$, respectively, is very small.

2. The ratios $\bar{t}_k/\bar{s}_k$ and $\bar{f}_k/\bar{s}_k$ (and hence all other ratios of $\bar{s}_k$, $\bar{t}_k$ and $\bar{f}_k$) are (approximately) independent of k, *i.e.* constant.

Moreover, we made that observation for all three models, whereas the numerical values of the respective ratios differ between the models. Nevertheless, having optimized a pattern with K levels, we are able to extrapolate the branching pattern *geometrically* to some level k for $k > K$, by using (8.2.13) and the constant ratios. Note that S_k, T_k and F_k are prescribed by the automaton. One can refer from Fig. 8.8 (right) that this extrapolation is indeed very reasonable, as the energy further decays. However, we were only able to extrapolate to a moderate number of additional levels due to memory restrictions.

8.3 Non-optimized self-similar branching patterns

In the last section, we derived elastic energies for reduced branching models. However, as mentioned in Rem. 8.2.2, we were not able to find a closed formula depending on all degrees of freedom, *i.e.* $\theta \in (0, 1)$, $N > 0$, $l \in (0, L)$ and the y-positions of the nodes $\mathbf{Y} = (y_{k,i})_{k,i}$ (as depicted in Fig. 8.6). In this section, we derive a closed formula for the elastic energy of Li's model as well as for our branching model by prescribing $\mathbf{Y}$ in an appropiate way and setting $l = L$ (for simplicity). This ansatz produces a self-similar branching pattern and allows us to evaluate the total energy for infinitely many refinement levels, *i.e.* to compute a *non-optimized* limit functional[1]. Analogously to the construction of the test function for the upper bound in [KM92, KM94], we shall optimize the limit functionals for the remaining degrees of freedom and obtain a better constant in the upper bound.

A limit for the non-optimized Li model

First, we compute the limit energy for a non-optimized Li pattern as shown in Fig. 8.1 (right). We assume that there are $2N3^{k-1}$ periodic cells (as depicted in Fig. 8.11) on the kth level with width $w_k = (2N3^{k-1})^{-1}$ and height $h_k = (\theta^{k-1} - \theta^k)L$ for $k > 0$. The only degrees of freedom are $N > 0$ and $0 < \theta < 1$, analogously to the computation of the constant for the upper bound in [KM92]. Note that $u = 0$ on the left and right boundary of the periodic cell (and hence $u_x = 0$ along the boundary) which is essential to ensure periodicity.
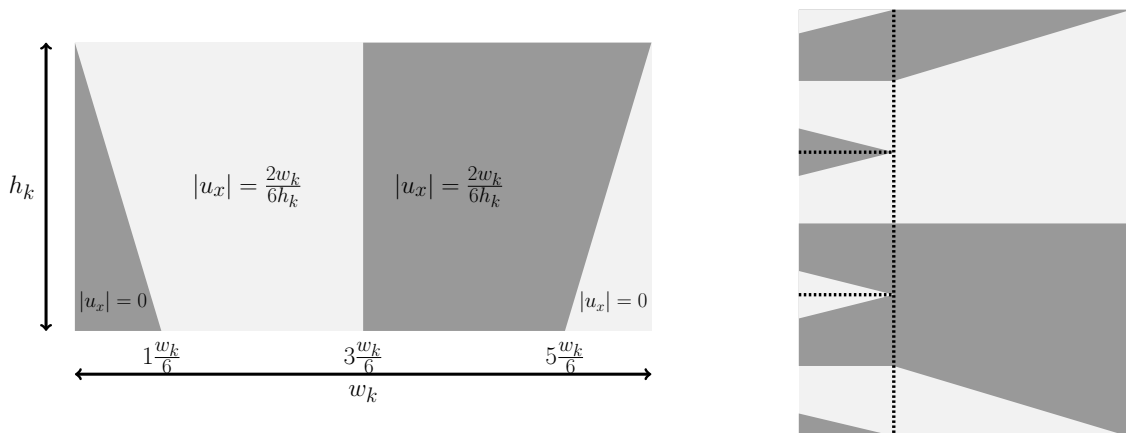
Figure 8.11: *Left: Periodic cell $\mathcal{P}_k = [0, w_k] \times [0, h_k]$ rotated by $90°$, right: one refinement step.*

---

[1] Here the term *non-optimized* refers to the fact that certain degrees of freedom are prescribed.

For $\theta < 3^{-1}$ the surface energy in $\Omega = [0, L] \times [0, 1]$ is given by (*cf.* (8.2.9))

$$F_{\text{surf}}[N, \theta, L, \epsilon] = 2N\epsilon L(1-\theta) \sum_{k=0}^{\infty} \left(2 \cdot 3^{k+1} \theta^k \right) = \frac{12N\epsilon L(1-\theta)}{1-3\theta} \,.$$

The elastic energy of a single periodic cell $\mathcal{P}_k = [0, w_k] \times [0, h_k]$ (*cf.* Fig. 8.11) is given by

$$F_{\text{elast}}[\mathcal{P}_k] = \int_{\mathcal{P}_k} u_x^2 \, \mathrm{d}x \, \mathrm{d}y = \left(2\frac{w_k}{6h_k} \right)^2 \cdot \frac{5}{6} w_k h_k = \frac{5w_k^3}{54h_k} \,.$$

Hence the total elastic energy in $\Omega = [0, L] \times [0, 1]$ is given by

$$F_{\text{elast}}[N, \theta, L] = \sum_{k=0}^{\infty} 2N3^k \, F_{\text{elast}}[\mathcal{P}_k] = 2N \sum_{k=0}^{\infty} 3^k \frac{5((2N)^{-1}3^{-k})^3}{54\,(1-\theta)L\theta^k}$$

$$= \frac{10}{54 \cdot 8N^2(1-\theta)L} \sum_{k=0}^{\infty} (3^2\theta)^{-k} = \frac{5}{24} N^{-2} L^{-1} \cdot \frac{\theta}{(9\theta-1)(1-\theta)}$$

for $\theta > 3^{-2}$. Altogether we have for $3^{-2} < \theta < 3^{-1}$:

$$F[N, \theta, L, \epsilon] = 12NL\epsilon \frac{1-\theta}{1-3\theta} + \frac{5}{24} N^{-2} L^{-1} \frac{\theta}{(9\theta-1)(1-\theta)} \,.$$

As in [KM92], we first optimize for $N > 0$. Solving $\partial_N F[N, \theta, L, \epsilon] = 0$ yields

$$\bar{N} = \sqrt[3]{\frac{5}{144}} L^{-2/3} \epsilon^{-1/3} \left(\frac{\theta(1-3\theta)}{(9\theta-1)(1-\theta)^2} \right)^{1/3} \,.$$

Plugging this back into $F[N, \theta, L, \epsilon]$ yields

$$F[\theta, L, \epsilon] := \min_{N>0} F[N, \theta, L, \epsilon] = \frac{3}{2} \sqrt[3]{60} \cdot L^{\frac{1}{3}} \epsilon^{\frac{2}{3}} \cdot \left(\frac{\theta\,(1-\theta)}{(1-3\theta)^2(9\theta-1)} \right)^{\frac{1}{3}} \,.$$

Now we optimize for $3^{-2} < \theta < 3^{-1}$. We get $\bar{\theta} \approx 0.17018$ as unique solution of $\partial_\theta F[\theta, L, \epsilon] = 0$ in the interval $(3^{-2}, 3^{-1})$. Plugging $\bar{\theta}$ back into $F[\theta, L, \epsilon]$ yields

$$F[L, \epsilon] := \min_{3^{-2} < \theta < 3^{-1}} \min_{N>0} F[N, \theta, L, \epsilon] = \frac{3}{2} \sqrt[3]{60} \cdot \left(\frac{\bar{\theta}\,(1-\bar{\theta})}{(1-3\bar{\theta})^2(9\bar{\theta}-1)} \right)^{\frac{1}{3}} \cdot L^{\frac{1}{3}} \epsilon^{\frac{2}{3}} = C \cdot L^{\frac{1}{3}} \epsilon^{\frac{2}{3}} \,,$$

with $C \approx 6.08$, whereas the upper constant in the construction in [KM92, KM94] is $C \approx 6.86$.

A limit for our non-optimized model

Next, we compute the limit energy for a non-optimized version of our branching pattern. As in [KM92, KM94] and for Li's model above, the key ingredient is the construction of a so-called periodic cell which induces the self-similarity. A fundamental property of such a periodic cell $\mathcal{P}_k = [0, w_k] \times [0, h_k]$ is that the corresponding elastic energy only depends on the width $w_k > 0$ and the height $h_k > 0$, *i.e.*

$$F_{\text{elast}}[\mathcal{P}_k] = F_{\text{elast}}[w_k, h_k] = \int_{\mathcal{P}_k} u_x^2 \, \mathrm{d}x \, \mathrm{d}y \,,$$

and possibly on further geometric properties that can be represented relatively within a single cell, such as *e.g.* certain angles of interfaces. Moreover, to evaluate the integral on the right hand side it is a necessary condition that $u_x = c_k$ at the "left" boundary of $\mathcal{P}_k$, where $c_k = 0$ is the only admissible

choice due to boundary conditions. In contrast to the model of Kohn-Müller (*cf*. Fig. 8.1, middle) or the model of Li (*cf*. Fig. 8.11), whose self-similar patterns are each based on *one* fundamental periodic cell, we shall make use of *three* different periodic cells, namely $\mathcal{A}$, $\mathcal{B}$ and $\mathcal{C}$, respectively, for our model. However, we will ensure $F_{\text{elast}}[\mathcal{C}] = 0$ by construction, hence we are dealing effectively with two non-trivial periodic cells. The topological construction of our branching pattern is depicted in Fig. 8.12 (top), where light and dark gray regions correspond to $u_y = \pm 1$, respectively. The two non-trivial periodic cells $\mathcal{A}$ resp. $\mathcal{B}$ of our construction are shown in Fig. 8.12 (bottom) on the left resp. right hand side. The trivial cell $\mathcal{C}$ is given by a rectangle indicated by diagonal red lines in Fig. 8.12 (top). We denote the layer $\{(x,y) : \theta^{k+1} < x < \theta^k\}$ by the kth level of the construction for $k \geq 0$. Cells on the kth level are denoted by $\mathcal{A}_k$, $\mathcal{B}_k$ and $\mathcal{C}_k$, respectively. We have the topological refinement rules:

$$\mathcal{A}_k \mapsto \{\mathcal{C}_{k+1}, \mathcal{B}_{k+1}, \mathcal{A}_{k+1}\}, \quad \mathcal{B}_k \mapsto \{\mathcal{A}'_{k+1}, \mathcal{B}'_{k+1}, \mathcal{C}'_{k+1}\}, \quad \mathcal{C}_k \mapsto \{\mathcal{A}_{k+1}\}. \tag{8.3.1}$$

Here $\mathcal{P}'$ corresponds to a reflected cell $\mathcal{P}$, with $(\mathcal{P}')' = \mathcal{P}$ and $F_{\text{elast}}[\mathcal{P}'] = F_{\text{elast}}[\mathcal{P}]$. In Fig. 8.12 (top) our pattern is depicted with four refinement levels (in x-direction). According to (8.3.1), the zeroth level is given by $\{\mathcal{A}_0\}$, the first level by $\{\mathcal{C}_1, \mathcal{B}_1, \mathcal{A}_1\}$ and the second level by $\{\mathcal{A}_2, \mathcal{A}'_2, \mathcal{B}'_2, \mathcal{C}'_2, \mathcal{C}_2, \mathcal{B}_2, \mathcal{A}_2\}$. Note that these rules induce the same branching pattern as the automaton described in Sec. 8.2.1, *cf*. also Fig. 8.4, *i.e.* the cell shown in Fig. 8.12 (top) corresponds topologically to $\mathcal{B}_4$ in Fig. 8.4 up to one global duplication-reflection operation. However, we here make use of periodic cells as atomic modules instead of spikes, trunks and facets used by the automaton.
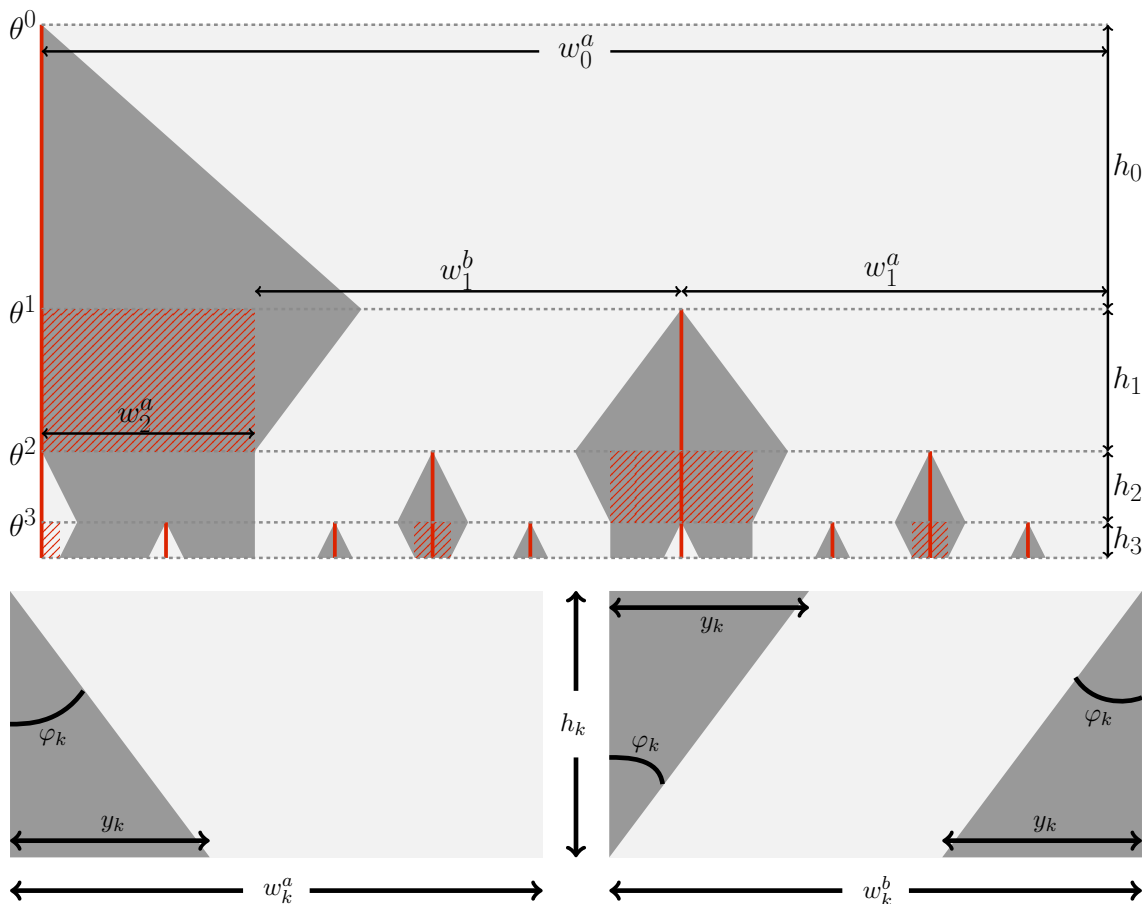
Figure 8.12: *One quarter (in y-direction, here horizontal axis) and four refinement levels (in x-direction, here vertical axis) of our self-similar branching pattern (top) consisting of three fundamental periodic cells, namely $\mathcal{A}$ (bottom, left), $\mathcal{B}$ (bottom, right) and $\mathcal{C}$ (top, diagonal red lines).*

Now we consider the geometric structure of the periodic cells. Let $w_k^a, w_k^b, w_k^c > 0$ be the width of $\mathcal{A}_k$, $\mathcal{B}_k$ and $\mathcal{C}_k$, respectively, and let $h_k = \theta^k L - \theta^{k+1} L = (1 - \theta) L \theta^k$ be the height of a cell on the kth level (*cf*. Fig. 8.12, top). Then we have $\mathcal{A}_k = [0, w_k^a] \times [0, h_k]$, $\mathcal{B}_k = [0, w_k^b] \times [0, h_k]$ and $\mathcal{C}_k = [0, w_k^c] \times [0, h_k]$. To satisfy the fundamental property of periodic cells mentioned above, *i.e.* $u_x = 0$ along the red lines in Fig. 8.12 (top), we have to ensure by construction that $w_k^a = w_k^b$ as well as that all interfaces on the kth level have the same angle $\varphi_k > 0$, *cf*. Fig. 8.12 (bottom). The latter one is equivalent to the condition that $y_k = \tan \varphi_k \cdot h_k$ is constant on each level. If $a_k, b_k \in \mathbb{N}$ denote the number of corresponding cells $\mathcal{A}_k$ resp. $\mathcal{B}_k$ on the kth level, we can then compute the total elastic energy by

$$F_{\text{elast}}[\Omega] = F_{\text{elast}}[L, N, \theta] = 4N \cdot \sum_{k \geq 0} \left(a_k F_{\text{elast}}[\mathcal{A}_k] + b_k F_{\text{elast}}[\mathcal{B}_k] \right), \tag{8.3.2}$$

since $F_{\text{elast}}[\mathcal{C}_k] = 0$ by construction. Here N denotes the number of repetitions of the branching pattern in y-direction.

To evaluate $F_{\text{elast}}[\mathcal{A}_k] = F_{\text{elast}}[w_k^a, h_k, y_k]$ and $F_{\text{elast}}[\mathcal{B}_k] = F_{\text{elast}}[w_k^b, h_k, y_k]$, we have to find a closed form of $(w_k^a)_k$ and $(y_k)_k$, where $w_k^b = w_k^a$ for all k. We observe from the refinement rules (8.3.1) as well as from Fig. 8.12 (top) the recursive relation

$$w_k^a = w_{k-2}^a - 2 w_{k-1}^a, \quad k \geq 2,$$

where we set $w_0^a = 1$ (for the time being) and $w_1^a < 1$ is a degree of freedom. As in Sec. 8.2.1 this is again a generalized Fibonacci sequence with a closed form representation given by

$$w_k^a = c_1(w_1^a) \cdot (\sqrt{2} - 1)^k - c_2(w_1^a) \cdot (-\sqrt{2} - 1)^k,$$

with constants $c_i(w_1^a) \in \mathbb{R}$. Obviously, $w_k^a > 0$ for all $k \in \mathbb{N}$ iff. $c_2(w_1^a) = 0$. A simple calculation reveals that this is the case iff. $w_1^a = \sqrt{2} - 1$, *i.e.* we have $c_1(w_1^a) = 1$. Taking into account that we actually have $w_0^a = (4N)^{-1}$ and setting $\gamma = \sqrt{2} - 1$, we arrive at the formula

$$w_k^a = \frac{\gamma^k}{4N}, \quad k \geq 0.$$

One can infer from the figure on the right the relation

$$y_k = y_{k-1} - w_{k+1}^a, \quad k > 0,$$

where $y_0 = c\, w_2^a$ with $c > 1$ to be chosen later. An evaluation of a finite geometric series yields

$$y_k = \frac{\gamma^2}{4N} \cdot \left(c - \frac{1 - \gamma^k}{1 - \gamma} \right) = \frac{\gamma^2}{4\delta N} \cdot \left((\delta c - 1) + \gamma^k \right), \quad k \geq 0,$$

where we set $\delta = 1 - \gamma = 2 - \sqrt{2} < 1$. Note that $\gamma^k \to 0$ as $k \to \infty$. Since $y_k \to 0$ as $k \to \infty$ we must have $\delta c = 1$, *i.e.* $c = \delta^{-1} > 1$. We obtain

$$y_k = \frac{\gamma^2}{4\delta N} \gamma^k, \quad k \geq 0,$$

Next, we compute the terms $F_{\text{elast}}[\mathcal{A}_k]$ and $F_{\text{elast}}[\mathcal{B}_k]$. Note that $u_x = 0$ in the dark gray regions of the cells $\mathcal{A}_k$ resp. $\mathcal{B}_k$ in Fig. 8.12 (bottom).

139
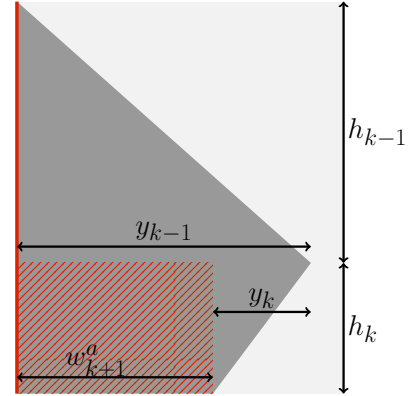
According to Prop. 8.2.1, we have $|u_x| = 2\,y_k/h_k$ in the light gray regions. Hence the elastic energies are given by u_x^2 multiplied by the area of the light gray regions, *i.e.*

$$F_{\text{elast}}[\mathcal{A}_k] = 4\left(\frac{y_k}{h_k}\right)^2 \cdot \left(h_k w_k^a - \tfrac{1}{2}h_k y_k\right) = \frac{4\,y_k^2(w_k^a - \tfrac{1}{2}y_k)}{h_k}\,, \tag{8.3.3}$$

$$F_{\text{elast}}[\mathcal{B}_k] = 4\left(\frac{y_k}{h_k}\right)^2 \cdot \left(h_k w_k^a - 2\tfrac{1}{2}h_k y_k\right) = \frac{4\,y_k^2(w_k^a - y_k)}{h_k}\,. \tag{8.3.4}$$

To evaluate the infinite sum in (8.3.2) we need to have a closed form for $(a_k)_k$ and $(b_k)_k$. Both sequences fulfill the recursive relation $a_k = 2a_{k-1} + a_{k-2}$ for $k > 1$, where we have $a_0 = a_1 = 1$ and $b_0 = 0$, $b_1 = 1$. Hence we obtain

$$a_k = \frac{\alpha^k + \beta^k}{2}\,, \quad b_k = \frac{\alpha^k - \beta^k}{2\sqrt{2}}\,, \quad k \geq 0\,, \tag{8.3.5}$$

with $\alpha = 1 + \sqrt{2}$ and $\beta = 1 - \sqrt{2}$, as above. Finally, we can plug (8.3.3), (8.3.4) and (8.3.5) into (8.3.2):

Proposition 8.3.1. *The elastic energy of N repetitions of our infinite branching pattern is given by*

$$F_{elast}[N, \theta, L] = \frac{\theta}{64N^2(1-\theta)L} \cdot \left(\frac{4+\sqrt{2}}{\alpha^2\theta - 1} + \frac{4+3\sqrt{2}}{\alpha^4\theta + 1}\right). \tag{8.3.6}$$

The energy is finite iff. the geometric series converge iff. $\theta > \alpha^{-2}$ for $\alpha = 1 + \sqrt{2}$.

Proof: See Prop. A.1.9 in the appendix.

Using (8.2.5) and (8.2.11), the corresponding surface energy is given by

$$F_{\text{surf}}[N, \theta, L, \epsilon] = 2\epsilon\,L\,N\left(\frac{\alpha^2\,(1-\theta)}{1-\alpha\theta} + \frac{\beta^2\,(1-\theta)}{1-\beta\theta}\right),$$

which is finite iff. $\theta < \alpha^{-1}$. Hence the total energy reads

$$F[N, \theta, L, \epsilon] = \frac{\theta}{64N^2(1-\theta)L} \cdot f_1(\theta) + 2\epsilon\,L\,N(1-\theta)f_2(\theta)\,,$$

with $N > 0$, $\theta \in (\alpha^{-2}, \alpha^{-1})$ and

$$f_1(\theta) = \frac{4+\sqrt{2}}{\alpha^2\theta - 1} + \frac{4+3\sqrt{2}}{\alpha^4\theta + 1}\,, \quad f_2(\theta) = \frac{\alpha^2}{1-\alpha\theta} + \frac{\beta^2}{1-\beta\theta}\,.$$

Again, we first optimize for $N > 0$, *i.e.* $\partial_N F[N, \theta, L, \epsilon] = 0$ yields

$$\bar{N} = \frac{1}{4}\theta^{1/3}(1-\theta)^{-2/3}L^{-2/3}\epsilon^{-1/3}f_1(\theta)^{1/3}f_2(\theta)^{-1/3}\,.$$

Hence

$$F[\theta, L, \epsilon] = \min_{N>0} F[N, \theta, L, \epsilon] = \tfrac{3}{4}\,\epsilon^{2/3}\,\theta^{1/3}\,(1-\theta)^{1/3}\,L^{1/3}\,f_1(\theta)^{1/3}\,f_2(\theta)^{2/3}\,.$$

Finally, we optimize for $\theta \in (\alpha^{-2}, \alpha^{-1})$. An optimization by means of a computer algebra program yields an optimal theta $\bar{\theta} \approx 0.23900$ and hence

$$F[L, \epsilon] = \min_{\theta \in (\alpha^{-2}, \alpha^{-1})} \min_{N > 0} F[N, \theta, L, \epsilon] = C\,L^{1/3}\,\epsilon^{2/3}\,,$$

with $C \approx 6.02$, which is better than the constant $C \approx 6.86$ in the upper bound in [KM92, KM94] and also slightly better than the constant $C \approx 6.08$ induced by the non-optimized Li model.

The gap between the optimal upper constants computed in this section and the ones obtained in the numerical simulations in the previous section is probably due to the fact, that we have prescribed certain degrees of freedom to generate a periodic cell in the former approach. For example, the fixation of **Y** prevents our branching pattern to produce diamond-shaped needles as seen in *cf*. Fig. 8.8c, and the fixation of $l = L$ forces the model to start branching directly at the right boundary $x = L$ of $\Omega = [0, L] \times [0, 1]$, instead of allowing a (probably cheaper) lamellar pattern far away from the left boundary $x = 0$.

8.4 Conclusion

In this thesis, we have investigated an improvement of the upper bound for a minimizer of the sharp interface model (8.0.3), *i.e.* a better constant C in (8.0.5). To this end, we have computed a (numerical) minimizer of the related diffuse interface model (8.0.1) by means of a conforming finite element method (FEM) based on subdivision surface basis functions. The microstructure induced by (the y-derivative of) the minimizer reveals a particular branching pattern, that differs topologically resp. geometrically from the construction studied by Kohn and Müller [KM92, KM94] resp. by Li [Li03].

Based on the insights from the numerical experiment we have constructed a novel, low dimensional family of branching microstructures for the sharp interface model (8.0.3). Optimized over all geometric degrees of freedom, our reduced model generates a branching pattern that shows a striking geometric resemblance of the FEM results and yields a significantly better constant C in (8.0.5). Although being inferior to our new branching pattern, the pattern proposed by Li [Li03] also improves the upper constant C induced by the Kohn-Müller pattern [KM92]. These findings suggest that the incorporation of inner needles within the branching pattern is obviously energetically advantageous. Furthermore, the possibility to merge a laminated structure into a branching structure when approaching the austenite-martensite interface is probably favorable. In contrast, the original model proposed by Kohn and Müller solely considers a pure branching pattern.

Unfortunately, we have not been able to derive a closed-form expression for the elastic energy induced by the reduced model which depends on *all* geometric degrees of freedom (*dof*s). Nevertheless, we have shown that prescribing a certain subset of *dof*s leads to a periodic and self-similar microstructure whose energy can be described in a closed form. Optimizing this energy analytically and with respect to all remaining *dof*s again reveals significantly better constants for the upper bound in (8.0.5)—although being inferior to the ones obtained by the numerical optimization of all *dof*s. For example, the prescribtion of certain *dof*s prohibits the incorporation of a laminated structure which was admissible in the numerical optimization. Nevertheless, it is probably feasible but laboriuos to derive a closed-form expression that allows for laminates as well.

Future work From a computational point of view it is certainly worthwhile to perform further FEM simulations with an substantially increased spatial resolution. This might reveal additional branching layers that have not been visible so far. An ultimate goal in this direction is definitely the implementation of an adaptive scheme (as *e.g.* in [GKS02]), since the high resolution is actually only required locally, *i.e.* at branching interfaces close to the boundary. Concerning the investigation of the reduced models for the sharp interface problem, it might be interesting to relax the condition of a totally rigid austenite phase.

To this end, one would study a more general model that accounts for the elastic energy in the austenite by means of an additional boundary term, as *e.g.* in [KM92, Con06]. Finally, it remains an open problem to examine whether the function u that represents our new branching pattern is a minimizer of (8.0.3).

Bibliography

[ACOL00]   Marc Alexa, Daniel Cohen-Or, and David Levin. As-rigid-as-possible shape interpolation. In *Proc. of SIGGRAPH 00*, Annual Conference Series, pages 157–164, 2000.

[Ale02]   Marc Alexa. Recent advances in mesh morphing. *Comput. Graph. Forum*, 21(2):173–198, 2002.

[Ard01]   Greg Arden. *Approximation Properties of Subdivision Surfaces*. PhD thesis, University of Washington, 2001.

[ASK+05]   Dragomir Anguelov, Praveen Srinivasan, Davne Koller, Sebastian Thrun, Jim Rodgers, and James Davis. SCAPE: Shape Completion and Animation of PEople. *ACM Trans. Graph.*, 24(3):408–416, 2005.

[Bal77]   John M. Ball. Convexity conditions and existence theorems in nonlinear elasiticity. *Arch. Ration. Mech. Anal.*, 63:337–403, 1977.

[Bär00]   Christian Bär. *Elementare Differentialgeometrie*. Walter de Gruyter, 2000.

[Bar13]   Sören Bartels. Approximation of large bending isometries with discrete Kirchhoff triangles. *SIAM J. Numer. Anal.*, 51(1):516–525, 2013.

[BB00]   Jean-David Benamou and Yann Brenier. A computational fluid mechanics solution to the Monge-Kantorovich mass transfer problem. *Numer. Math.*, 84(3):375–393, 2000.

[BB11]   Martin Bauer and Martins Bruveris. A new Riemannian setting for surface registration. In *Proc. of MICCAI Workshop on Mathematical Foundations of Computational Anatomy*, pages 182–194, 2011. arXiv:1106.0620.

[BBH80]   Jean-Louis Batoz, Klaus-Jürgen Bathe, and Lee-Wing Ho. A study of three-node triangular plate bending elements. *Internat. J. Numer. Methods Engrg.*, 15(12):1771–1812, 1980.

[BBK08]   Alexander M. Bronstein, Michael M. Bronstein, and Ron Kimmel. *Numerical Geometry of Non-Rigid Shapes*. Monographs in Computer Science. Springer, 2008.

[BBK09]   Alexander M. Bronstein, Michael M. Bronstein, and Ron Kimmel. Topology-invariant similarity of nonrigid shapes. *Inter. J. Comput. Vision*, 81(3):281–301, 2009.

[BBM16]   Martin Bauer, Martins Bruveris, and Peter W. Michor. Why use Sobolev metrics on the space of curves. In P. Turaga and A. Srivastava, editors, *Riemannian computing in computer vision*, pages 223–255. Springer, 2016.

[BBMM14]   Martin Bauer, Martins Bruveris, Stephen Marsland, and Peter W. Michor. Constructing reparametrization invariant metrics on spaces of plane curves. *Differential Geom. Appl.*, 34:139–165, 2014.

[BEG07]   Andrea L. Bertozzi, Selim Esedoglu, and Alan Gillette. Inpainting of binary images using the Cahn-Hilliard equation. *IEEE Trans. Image Proc.*, 16(1):285–291, 2007.

[Ber10]   Benjamin Berkels. *Joint methods in imaging based on diffuse image representations.* Dissertation, University of Bonn, 2010.

[BER15]   Benjamin Berkels, Alexander Effland, and Martin Rumpf. Time discrete geodesic paths in the space of images. *SIAM J. Imaging Sci.*, 8 (3):1457–1488, 2015.

[BFH$^+$13] Benjamin Berkels, P. Thomas Fletcher, Behrend Heeren, Martin Rumpf, and Benedikt Wirth. Discrete geodesic regression in shape space. In *Proc. of International Conference on Energy Minimization Methods in Computer Vision and Pattern Recognition*, volume 8081 of *Lecture Notes in Computer Science*, pages 108–122. Springer, 2013.

[BGN07]   John W. Barrett, Harald Garcke, and Robert Nürnberg. A parametric finite element method for fourth order geometric evolution equations. *J. Comp. Phys.*, 222:441–467, 2007.

[BGN08]   John W. Barrett, Harald Garcke, and Robert Nürnberg. Parametric approximation of Willmore flow and related geometric evolution equations. *SIAM J. Sci. Comput.*, 31:225–253, 2008.

[Bha04]   Kaushik Bhattacharya. *Microstructure of Martensite.* Oxford Series on Materials Modelling. Oxford University Press, 2004.

[BHM11]   Martin Bauer, Philipp Harms, and Peter W. Michor. Sobolev metrics on shape space of surfaces. *J. Geom. Mech.*, 3(4):389–438, 2011.

[BHM12a]   Martin Bauer, Philipp Harms, and Peter W. Michor. Almost local metrics on shape space of hypersurfaces in n-space. *SIAM J. Imaging Sci.*, 5:244–310, 2012.

[BHM12b]   Martin Bauer, Philipp Harms, and Peter W. Michor. Curvature weighted metrics on shape space of hypersurfaces in n-space. *Differential Geom. Appl.*, 30(1):33–41, 2012.

[BHM12c]   Martin Bauer, Philipp Harms, and Peter W. Michor. Sobolev metrics on shape space, II: Weighted Sobolev metrics and almost local metrics. *J. Geom. Mech.*, 4(4):365–383, 2012.

[BJ87]   John M. Ball and Richard D. James. Fine phase mixtures as minimizers of energy. *Arch. Ration. Mech. Anal.*, 100:13–52, 1987.

[BJ92]   John M. Ball and Richard D. James. Proposed experimental tests of a theory of fine microstructure and the two-well problem. *Philos. Trans. Roy. Soc. London Ser. A*, 338:389–450, 1992.

[BK03]   Mario Botsch and Leif Kobbelt. Multiresolution surface representation based on displacement volumes. *Comput. Graph. Forum*, 22(3):483–491, 2003.

[BK04]   Mario Botsch and Leif Kobbelt. An intuitive framework for real-time freeform modeling. *ACM Trans. Graph.*, 23(3):630–634, 2004.

[BK08]   Blaise Bourdin and Robert V. Kohn. Optimization of structural topology in the high-porosity regime. *J. Mech. Phys. Solids*, 56(3):1043–1064, 2008.

[BLZ00]   Henning Biermann, Adi Levin, and Denis Zorin. Piecewise smooth subdivision surfaces with normal control. In *Proc. of SIGGRAPH 00*, Annual Conference Series, pages 113–120, 2000.

[BMF03]   Robert Bridson, Sebastian Marino, and Ronald Fedkiw. Simulation of clothing with folds and wrinkles. In *Proc. of ACM SIGGRAPH/Eurographics Symposium on Computer Animation*, 2003.

[BMM14]   Martins Bruveris, Peter W. Michor, and David Mumford. Geodesic completeness for Sobolev metrics on the space of immersed plane curves. *Forum Math. Sigma*, 2, 2014.

[BMTY05]   M. Faisal Beg, Michael I. Miller, Alain Trouvé, and Laurent Younes. Computing large deformation metric mappings via geodesic flows of diffeomorphisms. *Inter. J. Comput. Vision*, 61(2):139–157, 2005.

[BPGK06]   Mario Botsch, Mark Pauly, Markus Gross, and Leif Kobbelt. PriMo: Coupled prisms for intuitive surface modeling. In *Proc. of Eurographics Symposium on Geometry Processing*, pages 11–20, 2006.

[BR12]   Nadine Balzani and Martin Rumpf. A nested variational time discretization for parametric Willmore flow. *Interfaces Free Bound.*, 14(4):431–454, 2012.

[Bra02]   Andrea Braides. Γ-*convergence for beginners*, volume 22 of *Oxford Lecture Series in Mathematics and its Applications*. Oxford University Press, Oxford, 2002.

[Bra07]   Dietrich Braess. *Finite elements*. Cambridge University Press, Cambridge, third edition, 2007. Theory, fast solvers, and applications in elasticity theory, Translated from the German by Larry L. Schumaker.

[BRLB14]   Federica Bogo, Javier Romero, Matthew Loper, and Michael J. Black. FAUST: Dataset and evaluation for 3D mesh registration. In *Proc. of IEEE Conference on Computer Vision and Pattern Recognition*, pages 3794–3801, 2014.

[Bru15]   Martins Bruveris. Completeness properties of Sobolev metrics on the space of curves. *J. Geom. Mech.*, 7(2):125–150, 2015.

[BS08]   Mario Botsch and Olga Sorkine. On linear variational surface deformation methods. *IEEE Trans. Vis. Comput. Graph.*, 14(1):213–230, 2008.

[BSBK02]   Mario Botsch, Stephan Steinberg, Stephan Bischoff, and Leif Kobbelt. Openmesh - a generic and efficient polygon mesh data structure. OpenSG Symposium, 2002.

[BSBW14]   Alan Brunton, Augusto Salazar, Timo Bolkart, and Stefanie Wuhrer. Review of statistical shape spaces for 3D data with comparative analysis for human faces. *Computer Vision and Image Understanding*, 128:1–17, 2014.

[BSPG06]   Mario Botsch, Robert Sumner, Mark Pauly, and Markus Gross. Deformation transfer for detail-preserving surface editing. In *Proc. of Vision, Modeling & Visualization*, pages 357–364, 2006.

[BV99]   Volker Blanz and Thomas Vetter. A morphable model for the synthesis of 3D faces. In *Proc. of SIGGRAPH 99*, Annual Conference Series, pages 187–194, 1999.

[BvTH16]   Christopher Brandt, Christoph von Tycowicz, and Klaus Hildebrandt. Geometric flows of curves in shape space for processing motion of deformable objects. *Comput. Graph. Forum*, 35(2):295–305, 2016.

[BWH+06]   Miklos Bergou, Max Wardetzky, David Harmon, Denis Zorin, and Eitan Grinspun. A quadratic bending model for inextensible surfaces. In *Proc. of Eurographics Symposium on Geometry Processing*, 2006.

[BWR+08]   Miklos Bergou, Max Wardetzky, Stephen Robinson, Basile Audoly, and Eitan Grinspun. Discrete elastic rods. *ACM Trans. Graph.*, 27(3):63:1–63:12, 2008.

[CB98]   Dominique Chapelle and Klaus-Jürgen Bathe. Fundamental considerations for the finite element analysis of shell structures. *Comput. & Structures*, 66:19–36, 1998.

[CCW16]   Edward Chien, Renjie Chen, and Ofir Weber. Bounded distortion harmonic shape interpolation. *ACM Trans. Graph.*, 35(4), 2016.

[CET01]   Timothy F. Cootes, Gareth J. Edwards, and Christopher J. Taylor. Active appearance models. *IEEE Trans. Pattern Anal. Mach. Intell.*, 23(6):681–685, 2001.

[CFKM06]   Guillaume Charpiat, Olivier Faugeras, Renaud Keriven, and Pierre Maurel. Distance-based shape statistics. In *Proc. of IEEE International Conference on Acoustics Speech and Signal Processing*, volume 5, 2006.

[Cia78]   Philippe G. Ciarlet. *The finite element method for elliptic problems*. North-Holland Publishing Co., Amsterdam-New York-Oxford, 1978. Studies in Mathematics and its Applications, Vol. 4.

[Cia88]   Philippe G. Ciarlet. *Mathematical elasticity. Vol. I*, volume 20 of *Studies in Mathematics and its Applications*. North-Holland Publishing Co., Amsterdam, 1988. Three-dimensional elasticity.

[Cia00]   Philippe G. Ciarlet. *Mathematical elasticity. Vol. III*, volume 29 of *Studies in Mathematics and its Applications*. North-Holland Publishing Co., Amsterdam, 2000. Theory of shells.

[Cia05]   Philippe G. Ciarlet. *An Introduction to Differential Geometry with Applications to Elasticity*. Springer, Dordrecht, 2005.

[CL11]   Fehmi Cirak and Quan Long. Subdivision shells with exact boundary control and non–manifold geometry. *Internat. J. Numer. Methods Engrg.*, 88(9):897–923, 2011.

[CLR04]   Ulrich Clarenz, Nathan Litke, and Martin Rumpf. Axioms and variational problems in surface parameterization. *Comput. Aided Geom. Design*, 21(8):727–749, 2004.

[CM90]   Alexandre J. Chorin and Jerrold E. Marsden. *A Mathematical Introduction to Fluid Mechanics*, volume 4 of *Texts in Applied Mathematics*. Springer, 1990.

[CM08]   Philippe G. Ciarlet and Christinel Mardare. An introduction to shell theory. In *Differential geometry: theory and applications*, volume 9 of *Ser. Contemp. Appl. Math. CAM*, pages 94–184. Higher Ed. Press, Beijing, 2008.

[CO01]   Fehmi Cirak and Michael Ortiz. Fully C1–conforming subdivision elements for finite deformation thin–shell analysis. *Internat. J. Numer. Methods Engrg.*, 51(7):813–833, 2001.

[Con00a]   Sergio Conti. Asymptotic self similarity in a model of branching in microstructured materials. In *Proc. of International Conference on Differential Equations, Vol. 1, 2 (Berlin, 1999)*, pages 442–447. World Sci. Publ., River Edge, NJ, 2000.

[Con00b]   Sergio Conti. Branched microstructures: scaling and asymptotic self-similarity. *Comm. Pure Appl. Math.*, 53(11):1448–1474, 2000.

[Con06]   Sergio Conti. A lower bound for a variational model for pattern formation in shape-memory alloys. *Contin. Mech. Thermodyn.*, 17(6):469–476, 2006.

[COS00]   Fehmi Cirak, Michael Ortiz, and Peter Schröder. Subdivision surfaces: a new paradigm for thin-shell finite–element analysis. *Internat. J. Numer. Methods Engrg.*, 47(12):2039–72, 2000.

[CPSS10]   Isaac Chao, Ulrich Pinkall, Patrick Sanan, and Peter Schröder. A simple geometric model for elastic deformations. *ACM Trans. Graph.*, 29(4), 2010.

[CSA⁺02]   Fehmi Cirak, Michael J. Scott, Erik K. Antonsson, Michael Ortiz, and Peter Schröder. Integrated modeling, finite–element analysis and engineering design for thin–shell structures using subdivision. *Comput.-Aided Des.*, 34(2):137–148, 2002.

[CSL95]   Peter Crouch and Fatima Silva Leite. The dynamic interpolation problem: On Riemannian manifold, Lie groups and symmetric spaces. *J. Dynam. Control Systems*, 1(2):177–202, 1995.

[CSM03]   David Cohen-Steiner and Jean-Marie Morvan. Restricted Delaunay triangulations and normal cycle. In *Proc. of Symposium on Computational Geometry*, pages 312–321, 2003.

[CTCG95]   Tim F. Cootes, Christopher J. Taylor, David H. Cooper, and Jim Graham. Active shape models—their training and application. *Computer Vision and Image Understanding*, 61(1):38–59, 1995.

[CWKBC13]   Renjie Chen, Ofir Weber, Daniel Keren, and Mirela Ben-Chen. Planar shape interpolation with bounded distortion. *ACM Trans. Graph.*, 32(4), 2013.

[dB63]   Carl de Boor. Best approximation properties of spline functions of odd degree. *J. Math. Mech.*, 12:747–749, 1963.

[dC76]   Manfredo P. do Carmo. *Differential geometry of curves and surfaces.* Prentice Hall, 1976. Translated from the Portuguese.

[dC92]   Manfredo P. do Carmo. *Riemannian geometry.* Birkhäuser Boston Inc., 1992. Translated from the second Portuguese edition.

[DFBJ07]   Brad Davis, P. Thomas Fletcher, Elizabeth Bullitt, and Sarang Joshi. Population shape regression from random design data. In *Proc. of IEEE International Conference on Computer Vision*, 2007.

[DGDM83]   Ennio De Giorgi and Gianni Dal Maso. Γ-convergence and calculus of variations. In *Mathematical theories of optimization (Genova, 1981)*, volume 979 of *Lecture Notes in Math.*, pages 121–143. Springer, Berlin, 1983.

[DGM98]   Paul Dupuis, Ulf Grenander, and Michael I. Miller. Variational problems on flows of diffeomorphisms for image matching. *Quart. Appl. Math.*, 56:587–600, 1998.

[DH02]   Peter Deuflhard and Andreas Hohmann. *Numerische Mathematik. I.* de Gruyter Lehrbuch. [de Gruyter Textbook]. Walter de Gruyter & Co., Berlin, third edition, 2002. Eine algorithmisch orientierte Einführung. [An algorithmically oriented introduction].

[DHLM05]   Mathieu Desbrun, Anil N. Hirani, Melvin Leok, and Jerrold E. Marsden. Discrete exterior calculus, 2005. arXiv:math.DG/0508341 on arxiv.org.

[DHR16]   Patrick W. Dondl, Behrend Heeren, and Martin Rumpf. Optimization of the branching pattern in coherent phase transitions. *C. R. Math. Acad. Sci. Paris*, 354(6):639–644, 2016.

[Die16]   Johannes Diermeier. *Analysis of martensitic microstructures in shape-memory-alloys: a low volume-fraction limit.* PhD thesis, University of Bonn, 2016.

[DKT08]   Mathieu Desbrun, Eva Kanso, and Yiying Tong. Discrete differential forms for computational modeling. In *Discrete Differential Geometry*, volume 38 of *Oberwolfach Semin.*, pages 287–324. Birkhäuser, Basel, 2008.

[DMA02]   Mathieu Desbrun, Mark Meyer, and Pierre Alliez. Intrinsic parameterization of surface meshes. *Comput. Graph. Forum*, 21(3):209–218, 2002.

[DMSB99]   Mathieu Desbrun, Mark Meyer, Peter Schröder, and Alan Barr. Implicit fairing of irregular meshes using diffusion and curvature flow. In *Proc. of SIGGRAPH 99*, Annual Conference Series, pages 317–324, 1999.

[DRT06]   Samuel Dambreville, Yogesh Rathi, and Allen Tannenbaum. A shape-based approach to robust image segmentation. In *Proc. of Conference on Image Analysis and Recognition*, volume 4141 of *Lecture Notes in Computer Science*, pages 173–183, 2006.

[DSB07]   Patrick W. Dondl, Ching-Ping Shen, and Kaushik Bhattacharya. Computational analysis of martensitic thin films using subdivision surfaces. *Internat. J. Numer. Methods Engrg.*, 72(1):72–94, 2007.

[Dyn92]   Nira Dyn. Subdivision schemes in computer-aided geometric design. In *Advances in numerical analysis, Vol. II*, volume 2, pages 36–104. Oxford Univ. Press, New York, 1992.

[Dyn02]   Nira Dyn. Interpolatory subdivision schemes. In Armin Iske, Ewald Quak, and Michael S. Floater, editors, *Tutorials on Multiresolution in Geometric Modelling*, pages 25–50. Springer, Berlin, 2002.

[Dzi88]   Gerhard Dziuk. Finite elements for the Beltrami operator on arbitrary surfaces. In S. Hildebrandt and R. Leis, editors, *Partial Differential Equations and Calculus of Variations*, volume 1357 of *Lecture Notes in Math.*, pages 142–155. Springer, Berlin, 1988.

[Dzi91]   Gerhard Dziuk. An algorithm for evolutionary surfaces. *Numer. Math.*, 58(6):603–611, 1991.

[Eff17]   Alexander Effland. *Discrete Riemannian Calculus on Shape Space*. Dissertation, University of Bonn, 2017.

[EPS72]   Jürgen Ehlers, Felix A. E. Pirani, and Alfred Schild. The geometry of free fall and light propagation. In *General relativity (papers in honour of J. L. Synge)*, pages 63–84. Clarendon Press, Oxford, 1972.

[ERS+15]   Alexander Effland, Martin Rumpf, Stefan Simon, Kirsten Stahn, and Benedikt Wirth. Bézier curves in the space of images. In *Proc. of International Conference on Scale Space and Variational Methods in Computer Vision*, volume 9087 of *Lecture Notes in Computer Science*, pages 372–384. Springer, Cham, 2015.

[ES10]   Charles M. Elliott and Björn Stinner. Modeling and computation of two phase geometric biomembranes using surface finite elements. *J. Comput. Phys.*, 229(18):6585 – 6612, 2010.

[Eyr98]   David J. Eyre. Unconditionally gradient stable time marching the Cahn-Hilliard equation. In *Computational and mathematical models of microstructural evolution (San Francisco, CA, 1998)*, volume 529 of *Mater. Res. Soc. Sympos. Proc.*, pages 39–46. MRS, Warrendale, PA, 1998.

[FB11]   Stefan Fröhlich and Mario Botsch. Example-driven deformations based on discrete shells. *Comput. Graph. Forum*, 30(8):2246–2257, 2011.

[FB12]   Oren Freifeld and Michael J. Black. Lie bodies: A manifold representation of 3D human shape. In *Proc. of European Conference on Computer Vision*, pages 1–14. Springer, 2012.

[FGR$^+$10] Gabriele Fanelli, Jürgen Gall, Harald Romsdorfer, Thibaut Weise, and Luc Van Gool. A 3-d audio-visual corpus of affective communication. *IEEE Trans. Multimedia*, 12(6):591–598, 2010.

[FJM02a]   Gero Friesecke, Richard D. James, and Stefan Müller. Rigorous derivation of nonlinear plate theory and geometric rigidity. *C. R. Math. Acad. Sci. Paris*, 334(2):173–178, 2002.

[FJM02b]   Gero Friesecke, Richard D. James, and Stefan Müller. A theorem on geometric rigidity and the derivation of nonlinear plate theory from three-dimensional elasticity. *Comm. Pure Appl. Math.*, 55(11):1461–1506, 2002.

[FJMM03]   Gero Friesecke, Richard D. James, Maria Giovanna Mora, and Stefan Müller. Derivation of nonlinear bending theory for shells from three-dimensional nonlinear elasticity by Gamma-convergence. *C. R. Math. Acad. Sci. Paris*, 336(8):697–702, 2003.

[FJSY09]   Matthias Fuchs, Bert Jüttler, Otmar Scherzer, and Huaiping Yang. Shape metrics based on elastic deformations. *J. Math. Imaging Vision*, 35(1):86–102, 2009.

[Fle87]   Roger Fletcher. *Practical Methods of Optimization*. A Wiley-Interscience Publication. John Wiley & Sons, Ltd., Chicheste, second edition, 1987.

[Fle11]   P. Thomas Fletcher. Geodesic regression on Riemannian manifolds. In *Proc. of MICCAI Workshop on Mathematical Foundations of Computational Anatomy*, pages 75–86, 2011.

[FLJ03]   P. Thomas Fletcher, Conglin Lu, and Sarang Joshi. Statistics of shape via principal geodesic analysis on Lie groups. In *Proc. of IEEE Conference on Computer Vision and Pattern Recognition*, volume 1, pages 95–101, 2003.

[FLPJ04]   P. Thomas Fletcher, Conglin Lu, Stephen M. Pizer, and Sarang Joshi. Principal geodesic analysis for the study of nonlinear statistics of shape. *IEEE Trans. Med. Imaging*, 23(8):995–1005, 2004.

[Fré48]   Maurice Fréchet. Les éléments aléatoires de nature quelconque dans un espace distancié. *Ann. Inst. H. Poincaré*, 10:215–310, 1948.

[FW06]   P. Thomas Fletcher and Ross T. Whitaker. Riemannian metrics on the space of solid shapes. In *MICCAI Workshop on Mathematical Foundations of Computational Anatomy*, pages 47–57, 2006.

[GGRZ06]   Eitan Grinspun, Yotam Gingold, Jason Reisman, and Denis Zorin. Computing discrete shape operators on general meshes. *Comput. Graph. Forum*, 25(3):547–556, 2006.

[GGWZ07]   Akash Garg, Eitan Grinspun, Max Wardetzky, and Denis Zorin. Cubic shells. In *Proc. of ACM SIGGRAPH/Eurographics Symposium on Computer animation*, pages 91–98, 2007.

[GH97]   Michael Garland and Paul Heckbert. Surface simplification using quadric error metrics. In *Proc. of SIGGRAPH 97*, Annual Conference Series, pages 209–216, 1997.

[GHDS03]   Eitan Grinspun, Anil N. Hirani, Mathieu Desbrun, and Peter Schröder. Discrete shells. In *Proc. of ACM SIGGRAPH/Eurographics Symposium on Computer animation*, pages 62–67, 2003.

[GKS02]   Eitan Grinspun, Petr Krysl, and Peter Schröder. CHARMS: A simple framework for adaptive simulation. *ACM Trans. Graph.*, 21(3):281–290, 2002.

[GSS99]   Igor Guskov, Wim Sweldens, and Peter Schröder. Multiresolution signal processing for meshes. In *Proc. of SIGGRAPH 99*, Annual Conference Series, 1999.

[HDD$^+$93]   Hugues Hoppe, Tony DeRose, Tom Duchamp, John McDonald, and Werner Stuetzle. Mesh optimization. In *Proc. of SIGGRAPH 93*, Annual Conference Series, 1993.

[Hee11]   Behrend Heeren. Geodätische im Raum von Schalenformen. diploma thesis, 2011.

[Hir03]   Anil N. Hirani. *Discrete Exterior Calculus*. PhD thesis, California Institute of Technology, 2003.

[HJS$^+$12]   Yi Hong, Sarang Joshi, Mar Sanchez, Martin Styner, and Marc Niethammer. Metamorphic geodesic regression. In *Proc. of International Conference on Medical Image Computing and Computer-Assisted Intervention*, volume 7512 of *Lecture Notes in Computer Science*, pages 197–205, 2012.

[HMFJ12]   Jacob Hinkle, Prasanna Muralidharan, P. Thomas Fletcher, and Sarang Joshi. Polynomial regression on Riemannian manifolds. In *Proc. of European Conference on Computer Vision*, volume 7574 of *Lecture Notes in Computer Science*, pages 1–14, 2012.

[Hop96]   Hugues Hoppe. Progressive meshes. In *Proc. of SIGGRAPH 96*, Annual Conference Series, 1996.

[Hop98]   Hugues Hoppe. Efficient implementation of progressive meshes. *Computers & Graphics*, 22(1):27–36, 1998.

[HP04a]   Klaus Hildebrandt and Konrad Polthier. Anisotropic filtering of non-linear surface features. *Comput. Graph. Forum*, 23(3):391–400, 2004.

[HP04b]   Michael Hofer and Helmut Pottmann. Energy-minimizing splines in manifolds. *ACM Trans. Graph.*, 23(3):284–293, 2004.

[HP11]   Klaus Hildebrandt and Konrad Polthier. Generalized shape operators on polyhedral surfaces. *Comput. Aided Geom. Design*, 28(5):321–343, 2011.

[HPW06]   Klaus Hildebrandt, Konrad Polthier, and Max Wardetzky. On the convergence of metric and geometric properties of polyhedral surfaces. *Geom. Dedicata*, 123:89–112, 2006.

[HRS$^+$14]   Behrend Heeren, Martin Rumpf, Peter Schröder, Max Wardetzky, and Benedikt Wirth. Exploring the geometry of the space of shells. *Comput. Graph. Forum*, 33(5):247–256, 2014.

[HRS$^+$16]   Behrend Heeren, Martin Rumpf, Peter Schröder, Max Wardetzky, and Benedikt Wirth. Splines in the space of shells. *Comput. Graph. Forum*, 35(5):111–120, 2016.

[HRW16]   Behrend Heeren, Martin Rumpf, and Benedikt Wirth. Variational time discretization of Riemannian splines. 2016. in preparation.

[HRWW12]   Behrend Heeren, Martin Rumpf, Max Wardetzky, and Benedikt Wirth. Time-discrete geodesics in the space of shells. *Comput. Graph. Forum*, 31(5):1755–1764, 2012.

[HSTP11]   Klaus Hildebrandt, Christian Schulz, Christoph von Tycowicz, and Konrad Polthier. Interactive surface modeling using modal analysis. *ACM Trans. Graph.*, 30(5):119:1–11, 2011.

[HTY09]   Darryl Holm, Alain Trouvé, and Laurent Younes. The Euler-Poincaré theory of metamorphosis. *Quart. Appl. Math.*, 67:661–685, 2009.

[Hug87]   Thomas J. R. Hughes. *Finite Element Method - Linear Static and Dynamic Finite Element Analysis*. Prentice-Hall, Englewood Cliffs, 1987.

[IRS15]   José A. Iglesias, Martin Rumpf, and Otmar Scherzer. Shape aware matching of implicit surfaces based on thin shell energies. 2015. submitted.

[JBK$^+$12]   Alec Jacobson, Ilya Baran, Ladislav Kavan, Jovan Popović, and Olga Sorkine. Fast automatic skinning transformations. *ACM Trans. Graph.*, 31(4), 2012.

[Joh65]   Fritz John. Estimates for the derivatives of the stresses in a thin shell and interior shell equations. *Comm. Pure Appl. Math.*, 18:235–267, 1965.

[Kan42]   Leonid Vitalévich Kantorovitch. On the translocation of masses. *C. R. (Doklady) Acad. Sci. URSS (N.S.)*, 37:199–201, 1942.

[Kan48]   Leonid Vitalévich Kantorovitch. On a problem of Monge. *Uspekhi Mat. Nauk*, 3:225–226, 1948.

[Kar77]   Hermann Karcher. Riemannian center of mass and mollifier smoothing. *Comm. Pure Appl. Math.*, 30(5):509–541, 1977.

[KB84]   Doris H. U. Kochanek and Richard H. Bartels. Interpolating splines with local tension, continuity, and bias control. *Computer Graphics*, 18(3):33–41, 1984.

[KBS00]   Leif P. Kobbelt, Thilo Bareuther, and Hans-Peter Seidel. Multiresolution shape deformations for meshes with dynamic vertex connectivity. *Comput. Graph. Forum*, 19(3):C249–C260, 2000.

[KCVS98]   Leif Kobbelt, S. Campagna, J. Vorsatz, and H.-P. Seidel. Interactive multi-resolution modeling on arbitrary meshes. *ACM SIGGRAPH 98 proceedings*, pages 105–114, 1998.

[Ken84]   David G. Kendall. Shape manifolds, Procrustean metrics, and complex projective spaces. *Bull. London Math. Soc.*, 16(2):81–121, 1984.

[KG08]   Scott Kircher and Michael Garland. Free-form motion processing. *ACM Trans. Graph.*, 27(2), 2008.

[Kha67]   Armen G. Khachaturyan. Some questions concerning the theory of phase transformations in solids. *Soviet Physics Solid State*, 8:2163–2168, 1967.

[Kha69]   Armen G. Khachaturyan. Theory of macroscopic periodicity for a phase transition in the solid state. *Soviet Physics JETP*, 29:557–561, 1969.

[Kha83]   Armen G. Khachaturyan. *Theory of structural transformations in solids*. Wiley, New York, 1983.

[Kir50]   Gustav Kirchhoff. Über das Gleichgewicht und die Bewegung einer elastischen Scheibe. *J. Reine Angew. Math.*, 40:51–88, 1850. Journal für die Reine und Angewandte Mathematik. [Crelle's Journal].

[KKDS10]   Sebastian Kurtek, Eric Klassen, Zhaohua Ding, and Anuj Srivastava. A novel Riemannian framework for shape analysis of 3D objects. In *Proc. of IEEE Conference on Computer Vision and Pattern Recognition*, pages 1625–1632, 2010.

[Kli95]   Wilhelm P. A. Klingenberg. *Riemannian geometry*, volume 1 of *de Gruyter Studies in Mathematics*. Walter de Gruyter & Co., Berlin, second edition, 1995.

[KM92]   Robert V. Kohn and Stefan Müller. Branching of twins near an austenite–twinned-martensite interface. *Philosophical Mag. A*, 66(5):697–715, 1992.

[KM94]   Robert V. Kohn and Stefan Müller. Surface energy and microstructure in coherent phase transitions. *Comm. Pure Appl. Math.*, 47(4):405–435, 1994.

[KMBG09]   Peter Kaufmann, Sebastian Martin, Mario Botsch, and Markus Gross. Flexible simulation of deformable models using discontinuous Galerkin FEM. *Graphical Models*, 71(4):153–167, 2009.

[KMN00]   Arkady Kheyfets, Warner A. Miller, and Gregory A. Newton. Schild's ladder parallel transport procedure for an arbitrary connection. *Internat. J. Theoret. Phys.*, 39(12):2891–2898, 2000.

[KMP07]   Martin Kilian, Niloy J. Mitra, and Helmut Pottmann. Geometric modeling in shape space. *ACM Trans. Graph.*, 26:1–8, 2007.

[Koi66]   Warner Tjardus Koiter. On the nonlinear theory of thin elastic shells. *Nederl. Akad. Wetensch. Proc. Ser. B*, 69:1–54, 1966.

[KSMJ04]   Eric Klassen, Anuj Srivastava, Washington Mio, and Shantanu H. Joshi. Analysis of planar shapes using geodesic paths on shape spaces. *IEEE Trans. Pattern Anal. Mach. Intell.*, 26(3):372–383, 2004.

[KVS99]   Leif Kobbelt, Jens Vorsatz, and Hans-Peter Seidel. Multiresolution hierarchies on unstructured triangle meshes. *Computational Geometry: Theory and Applications*, 14(1-3):5–24, 1999.

[Lak87]   Roderic Lakes. Foam structures with a negative Poisson's ratio. *Science*, 235(4792):1038–1040, 1987.

[Lan95]   Serge Lang. *Differential and Riemannian Manifolds*, volume 160 of *Graduate Texts in Mathematics*. Springer-Verlag, New York, third edition, 1995.

[LAP11]   Marco Lorenzi, Nicholas Ayache, and Xavier Pennec. Schild's ladder for the parallel transport of deformations in time series of images. In *Proc. of International Conference on Information Processing in Medical Imaging*, volume 6801 of *Lecture Notes in Computer Science*, pages 463–474, 2011.

[LCF00]   John P. Lewis, Matt Cordner, and Nickson Fong. Pose space deformation: a unified approach to shape interpolation and skeleton-driven deformation. In *Proc. of SIGGRAPH 00*, Annual Conference Series, pages 165–172, 2000.

[LDR95]   Hervé Le Dret and Annie Raoult. The nonlinear membrane model as variational limit of nonlinear three-dimensional elasticity. *J. Math. Pures Appl. (9)*, 74(6):549–578, 1995.

[LDR96]   Hervé Le Dret and Annie Raoult. The membrane shell model in nonlinear elasticity: a variational asymptotic derivation. *J. Nonlinear Sci.*, 6(1):59–84, 1996.

[LDRS05]   Nathan Litke, Mark Droske, Martin Rumpf, and Peter Schröder. An image processing approach to surface matching. In *Proc. of Eurographics Symposium on Geometry Processing*, pages 207–216, 2005.

[LGF00]   Michael E. Leventon, W. Eric L. Grimson, and Olivier Faugeras. Statistical shape influence in geodesic active contours. In *Proc. of IEEE Conference on Computer Vision and Pattern Recognition*, 2000.

[Li03]   Zhiping Li. Numerical justification of branched laminated microstructure with surface energy. *SIAM J. Sci. Comput.*, 24(3):1054–1075, 2003.

[Loo87]   Charles Loop. Smooth subdivision surfaces based on triangles. Master's thesis, 1987.

[Lov88]   Augustus Edward Hough Love. The small free vibrations and deformation of a thin elastic shell. *Philos. Trans. R. Soc. Lond. Ser. A Math. Phys. Eng. Sci.*, 179:491–546, 1888.

[LR12]   Nicole Lehmann and Ulrich Reif. Notes on the curvature tensor. *Graphical Models*, 74(6):321–325, 2012.

[LSDM10]   Xiuwen Liu, Yonggang Shi, Ivo Dinov, and Washington Mio. A computational model of multidimensional shape. *Int. J. Comput. Vis.*, 89(1):69–83, 2010.

[LSLCO05] Yaron Lipman, Olga Sorkine, David Levin, and Daniel Cohen-Or. Linear rotation-invariant coordinates for meshes. *ACM Trans. Graph.*, 24:479–487, 2005.

[MDSB02]   Mark Meyer, Mathieu Desbrun, Peter Schröder, and Alan H. Barr. Discrete differential-geometry operators for triangulated 2-manifolds. In *Visualization and Mathematics III*, pages 35–57. Springer Berlin Heidelberg, 2002.

[MH94]   Jerrold E. Marsden and Thomas J. R. Hughes. *Mathematical foundations of elasticity*. Dover Publications, Inc., New York, 1994. Corrected reprint of the 1983 original.

[Mil63]   John Milnor. *Morse Theory*. Based on lecture notes by M. Spivak and R. Wells. Annals of Mathematics Studies, No. 51. Princeton University Press, Princeton, N.J., 1963.

[MM77]   Luciano Modica and Stefano Mortola. Un esempio di Γ^--convergenza. *Boll. Un. Mat. Ital. B (5)*, 14(1):285–299, 1977.

[MM05]   Peter W. Michor and David Mumford. Vanishing geodesic distance on spaces of submanifolds and diffeomorphisms. *Doc. Math.*, 10:217–245, 2005.

[MM06]   Peter W. Michor and David Mumford. Riemannian geometries on spaces of plane curves. *J. Eur. Math. Soc.*, 8(1):1–48, 2006.

[MM07]   Peter W. Michor and David Mumford. An overview of the Riemannian metrics on spaces of curves using the Hamiltonian approach. *Appl. Comput. Harmon. Anal.*, 23(1):74–113, 2007.

[Mod87]   Luciano Modica. The gradient theory of phase transitions and the minimal interface criterion. *Arch. Rational Mech. Anal.*, 98(2):123–142, 1987.

[Mon81]   Gaspard Monge. *Mémoire sur la théorie des déblais et des remblais*. De l'Imprimerie Royale, 1781.

[MRSS15]   Jan Maas, Martin Rumpf, Carola Schönlieb, and Stefan Simon. A generalized model for optimal transport of images including dissipation and density modulation. *ESAIM Math. Model. Numer. Anal.*, 49(6):1745–1769, 2015.

[MS05]   Facundo Mémoli and Guillermo Sapiro. A theoretical and computational framework for isometry invariant recognition of point cloud data. *Foundations of Computational Mathematics*, 5(3):313–347, 2005.

[MTY02]   Michael I. Miller, Alain Trouvé, and Laurent Younes. On the metrics and Euler-Lagrange equations of computational anatomy. *Annu. Rev. Biomed. Eng.*, 4(1):375–405, 2002.

[Mui09]   Benson K. Muite. *Analysis, Modelling and Simulation of Shape Memory Alloys*. PhD thesis, The Queen's College, University of Oxford, 2009.

[Mül90]   Stefan Müller. Minimizing sequences for nonconvex functionals, phase transitions and singular perturbations. In *Problems involving change of type (Stuttgart, 1988)*, volume 359 of *Lecture Notes in Phys.*, pages 31–44. Springer, Berlin, 1990.

[Mül93]   Stefan Müller. Singular perturbations as a selection criterion for periodic minimizing sequences. *Calc. Var. Partial Differential Equations*, 1(2):169–204, 1993.

[MY01]   Michael I. Miller and Laurent Younes. Group actions, homeomorphisms, and matching: a general framework. *Int. J. Comput. Vis.*, 41(1–2):61–84, 2001.

[MYS08]   Andrea Mennucci, Anthony Yezzi, and Ganesh Sundaramoorthi. Properties of Sobolev-type metrics in the space of curves. *Interfaces Free Bound.*, 10(4):423–445, 2008.

[NHP89]   Lyle Noakes, Greg Heinzinger, and Brad Paden. Cubic splines on curved spaces. *IMA J. Math. Control Inform.*, 6(4):465–473, 1989.

[NHV11]   Marc Niethammer, Yang Huang, and François-Xavier Vialard. Geodesic regression for image time-series. In *Proc. of International Conference on Medical Image Computing and Computer-Assisted Intervention*, volume 6892 of *Lecture Notes in Computer Science*, pages 655–662, 2011.

[NŠ91]   Jindrich Nečas and Miroslav Šilhavý. Multipolar viscous fluids. *Quart. Appl. Math.*, 49(2):247–265, 1991.

[NW99]   Jorge Nocedal and Stephen J. Wright. *Numerical Optimization*. Springer Series in Operations Research. Springer-Verlag, New York, 1999.

[OBCS$^+$12] Maks Ovsjanikov, Mirela Ben-Chen, Justin Solomon, Adrian Butcher, and Leonidas Guibas. Functional maps: a flexible representation of maps between shapes. *ACM Trans. Graph.*, 31(4), 2012.

[Pen06]   Xavier Pennec. Intrinsic statistics on Riemannian manifolds: Basic tools for geometric measurements. *J. Math. Imaging Vision*, 25(1):127–154, 2006.

[Per15]   Ricardo Perl. *Isogeometric Approximation of Variational Problems for Shells*. PhD thesis, University of Bonn, 2015.

[PFR12]   Gabriel Peyré, Jalal Fadili, and Julien Rabin. Wasserstein active contours. In *Proc. of IEEE International Conference on Image Processing*, pages 2541–2544, 2012.

[PH05]   Helmut Pottmann and Michael Hofer. A variational approach to spline curves on surface. *Comput. Aided Geom. Design*, 22(7):693–709, 2005.

[PL11]   Xavier Pennec and Marco Lorenzi. Which parallel transport for the statistical analysis of longitudinal deformations? In *Proc. of Colloque GRETSI*, September 2011.

[PMR05]   Dimitrios Perperidis, Raad Mohiaddin, and Daniel Rueckert. Construction of a 4d statistical atlas of the cardiac anatomy and its use in classification. In J. Duncan and G. Gerig, editors, *Medical Image Computing and Computer Assisted Intervention*, volume 3750 of *Lecture Notes in Computer Science*, pages 402–410, 2005.

[PMRMB15] Gerard Pons-Moll, Javier Romero, Naureen Mahmood, and Michael J. Black. Dyna: A model of dynamic human shape in motion. *ACM Trans. Graph.*, 34(4), 2015.

[PN07]   Tomasz Popiel and Lyle Noakes. Bézier curves and C^2 interpolation in Riemannian manifolds. *J. Approx. Theory*, 148(2):111–127, 2007.

[PP93]   Ulrich Pinkall and Konrad Polthier. Computing discrete minimal surfaces and their conjugates. *Experimental Mathematics*, 2 (1):15–35, 1993.

[PPKC10]   Gabriel Peyré, Mickael Péchaud, Renaud Keriven, and Laurent D Cohen. Geodesic methods in computer vision and graphics. *Foundations and Trends in Computer Graphics and Vision*, 5(3–4):197–397, 2010.

[PPR14]   Ricardo Perl, Paola Pozzi, and Martin Rumpf. A nested variational time discretization for parametric anisotropic willmore flow. In Michael Griebel, editor, *Singular Phenomena and Scaling in Mathematical Models*, pages 221–241. Springer, Cham, 2014.

[PS09]   Ankur Patel and William A. P. Smith. 3D morphable face models revisited. In *Proc. of IEEE Conference on Computer Vision and Pattern Recognition*, pages 1327–1334, 2009.

[Ray96]   John William Strutt Baron Rayleigh. *The theory of sound*, volume 2. Macmillan, 1896.

[RDS$^+$05] Inam Ur Rahman, Iddo Drori, Victoria C. Stodden, David L. Donoho, and Peter Schröder. Multiscale representations for manifold-valued data. *Multiscale Model. Sim.*, 4(4):1201–1232, 2005.

[RE55]   Ronald Samuel Rivlin and Jerald Laverne Ericksen. Stress-deformation relations for isotropic materials. *J. Rational Mech. Anal.*, 4:323–425, 1955.

[Rei67]   Christian H. Reinsch. Smoothing by spline functions. *Numer. Math.*, 10:177–183, 1967.

[Rei95]   Ulrich Reif. A unified approach to subdivision algorithms near extraordinary vertices. *Comput. Aided Geom. Design*, 12(2):153–174, 1995.

[Roi69]   Alexander L. Roitburd. The domain structure of crystals formed in the solid phase. *Soviet Physics Solid State*, 10(12):2870–2876, 1969.

[RS01]   Ulrich Reif and Peter Schröder. Curvature integrability of subdivision surfaces. *Adv. Comput. Math.*, 14(2):157–174, 2001.

[RS10]   Sergey Repin and Stefan A. Sauter. Estimates of the modeling error for the Kirchhoff-Love plate model. *C. R. Math. Acad. Sci. Paris*, 348(17-18):1039–1043, 2010.

[Rum15]   Martin Rumpf. Variational discretization of geometric calculus on shape spaces, July 2015. Lecture Notes for the Advanced Courses in Mathematics CRM Barcelona.

[Rus05]   Raluca E. Rusu. An algorithm for the elastic flow of surfaces. *Interfaces Free Bound.*, 7(3):229–239, 2005.

[RW09a]   Martin Rumpf and Benedikt Wirth. An elasticity approach to principal modes of shape variation. In *Proc. of International Conference on Scale Space Methods and Variational Methods in Computer Vision*, volume 5567 of *Lecture Notes in Computer Science*, pages 709–720, 2009.

[RW09b]   Martin Rumpf and Benedikt Wirth. A nonlinear elastic shape averaging approach. *SIAM J. Imaging Sci.*, 2(3):800–833, 2009.

[RW11a]   Martin Rumpf and Benedikt Wirth. An elasticity-based covariance analysis of shapes. *Int. J. Comput. Vis.*, 92(3):281–295, 2011.

[RW11b]   Martin Rumpf and Benedikt Wirth. Variational methods in shape analysis. In Otmar Scherzer, editor, *Handbook of Mathematical Methods in Imaging*, pages 1363–1401. Springer, 2011.

[RW13]   Martin Rumpf and Benedikt Wirth. Discrete geodesic calculus in shape space and applications in the space of viscous fluidic objects. *SIAM J. Imaging Sci.*, 6(4):2581–2602, 2013.

[RW14]   Martin Rumpf and Max Wardetzky. Geometry processing from an elastic perspective. *GAMM-Mitt.*, 37(2):184–216, 2014.

[RW15]   Martin Rumpf and Benedikt Wirth. Variational time discretization of geodesic calculus. *IMA J. Numer. Anal.*, 35(3):1011–1046, 2015.

[SBYA05]   Matthias Söhn, Mattias Birkner, Di Yan, and Markus Alber. Modelling individual geometric variation based on dominant eigenmodes of organ deformation: implementation and evaluation. *Phys. Med. Biol.*, 50(24):5893–5908, 2005.

[SCC06]   Frank R. Schmidt, Michael Clausen, and Daniel Cremers. Shape matching by variational computation of geodesics on a manifold. In *Proc. of Conference on Pattern Recognition*, volume 4174 of *Lecture Notes in Computer Science*, pages 142–151. Springer, 2006.

[Sch64a]   Isaac Jacob Schoenberg. On interpolation by spline functions and its minimal properties. In *On Approximation Theory (Proceedings of Conference in Oberwolfach, 1963)*, pages 109–129. Birkhäuser, Basel, 1964.

[Sch64b]   Isaac Jacob Schoenberg. Spline interpolation and best quadrature formulae. *Bull. Amer. Math. Soc.*, 70:143–148, 1964.

[Sch66]   Daniel G. Schweikert. An interpolation curve using a spline in tension. *J. Math. and Phys.*, 45:312–317, 1966.

[Sch73]   Isaac Jacob Schoenberg. *Cardinal spline interpolation*. Society for Industrial and Applied Mathematics, Philadelphia, Pa., 1973. Conference Board of the Mathematical Sciences Regional Conference Series in Applied Mathematics, No. 12.

[SHK11]   Dominik Sibbing, Martin Habbecke, and Leif Kobbelt. Markerless reconstruction and synthesis of dynamic facial expressions. *Computer Vision and Image Understanding*, 115(5):668–680, 2011.

[Sib78]   Robin Sibson. Studies in the robustness of multidimensional scaling: Procrustes statistics. *J. Roy. Statist. Soc. Ser. B*, 40(2):234–238, 1978.

[SJJK06]   Anuj Srivastava, Aastha Jain, Shantanu H. Joshi, and David Kaziska. Statistical shape models using elastic-string representations. In *Proc. of Asian Conference on Computer Vision*, volume 3851 of *Lecture Notes in Computer Science*, pages 612–621, 2006.

[SK15]   Dominik Sibbing and Leif Kobbelt. Data driven 3D face tracking based on a facial deformation model. In *Proc. of Conference on Vision, Modeling and Visualization*, 2015.

[SKJJ11]   Anuj Srivastava, Eric Klassen, Shantanu H. Joshi, and Ian H. Jermyn. Shape analysis of elastic curves in euclidean spaces. *IEEE Trans. Pattern Anal. Mach. Intell.*, 33(7):1415–1428, 2011.

[SMSY11]   Ganesh Sundaramoorthi, Andrea Mennucci, Stefano Soatto, and Anthony Yezzi. A new geometric metric in the space of curves, and applications to tracking deforming objects by prediction and filtering. *SIAM J. Imaging Sci.*, 4(1):109–145, 2011.

[Sor06]   Olga Sorkine. Differential representations for mesh processing. *Comput. Graph. Forum*, 25(4):789–807, 2006.

[SP04]   Robert W. Sumner and Jovan Popović. Deformation transfer for triangle meshes. *ACM Trans. Graph.*, 23(3):399–405, 2004.

[SS13]   Bernhard Schmitzer and Christoph Schnörr. A hierarchical approach to optimal transport. In *Proc. of International Conference on Scale Space and Variational Methods in Computer Vision*, volume 7893 of *Lecture Notes in Computer Science*, pages 452–464, 2013.

[Sta99]   Jos Stam. Evaluation of Loop subdivision surfaces. SIGGRAPH 99 Course Notes, 1999.

[SYM07]   Ganesh Sundaramoorthi, Anthony Yezzi, and Andrea Mennucci. Sobolev active contours. *Int. J. Comput. Vis.*, 73(3):345–366, 2007.

[SZ00]   Peter Schröder and Denis Zorin. Subdivision for modeling and animation. SIGGRAPH 00 Course Notes, 2000.

[SZGP05]   Robert W. Sumner, Matthias Zwicker, Craig Gotsman, and Jovan Popović. Mesh-based inverse kinematics. *ACM Trans. Graph.*, 24(3):488–495, 2005.

[Tau95]   Gabriel Taubin. Estimating the tensor of curvature of a surface from a polyhedral approximation. In *Proc. of International Conference on Computer Vision*, pages 902–907, 1995.

[TPBF87]   Demetri Terzopoulos, John Platt, Alan Barr, and Kurt Fleischer. Elastically deformable models. *Computer Graphics*, 21(4):205–214, 1987.

[TV12]   Alain Trouvé and François-Xavier Vialard. Shape splines and stochastic shape evolutions : A second order point of view. *Quart. Appl. Math.*, 70(2):219–251, 2012.

[TW06]   Bernhard Thomaszewsk and Markus Wacker. Bending models for thin flexible objects. In *Proc. of International Conference on Computer Graphics, Visualization and Computer Vision*, 2006.

[TWS06]   Bernhard Thomaszewski, Markus Wacker, and Wolfgang Straßer. A consistent bending model for cloth simulation with corotational subdivision finite elements. In *Proc. of ACM SIGGRAPH/Eurographics Symposium on Computer Animation*, pages 107–116, 2006.

[TY05a]   Alain Trouvé and Laurent Younes. Local geometry of deformable templates. *SIAM J. Math. Anal.*, 37(1):17–59, 2005.

[TY05b]   Alain Trouvé and Laurent Younes. Metamorphoses through Lie group action. *Found. Comput. Math.*, 5(2):173–198, 2005.

[TYW+03]   Andy Tsai, Anthony Yezzi, William Wells, Clare Tempany, Dewey Tucker, Ayres Fan, W. Eric Grimson, and Alan Willsky. A shape-based approach to the segmentation of medical imagery using level sets. *IEEE Trans. Med. Imaging*, 22(2):137–154, 2003.

[vRESH16]   Phillip von Radziewsky, Elmar Eisemann, Hans-Peter Seidel, and Klaus Hildebrandt. Optimized subspaces for deformation-based modeling and shape interpolation. *Computers & Graphics*, 58(C):128–138, 2016.

[vTSSH13]   Christoph von Tycowicz, Christian Schulz, Hans-Peter Seidel, and Klaus Hildebrandt. An efficient construction of reduced deformable objects. *ACM Trans. Graph.*, 32(6):213:1–213:10, 2013.

[vTSSH15]   Christoph von Tycowicz, Christian Schulz, Hans-Peter Seidel, and Klaus Hildebrandt. Real-time nonlinear shape interpolation. *ACM Trans. Graph.*, 34(3):34:1–34:10, 2015.

[VVP+16]   Libor Vása, Petr Vanecek, Martin Prantl, Vera Skorkovská, Petr Martínek, and Ivana Kolingerová. Mesh statistics for robust curvature estimation. *Comput. Graph. Forum*, 35(5), 2016.

[Wal35]   Abraham Wald. Begründung einer koordinatenlosen Differentialgeometrie der Flächen. Ergebn. math. Kolloqu. Wien 7, 1935. pages 24–46.

[Wal04]   Johannes Wallner. Existence of set-interpolating and energy-minimizing curves. *Comput. Aided Geom. Design*, 21(9):883–892, 2004.

[Wal06]   Johannes Wallner. Smoothness analysis of subdivision schemes by proximity. *Constr. Approx.*, 24(3):289–318, 2006.

[War06]   Max Wardetzky. *Discrete Differential Operators on Polyhedral Surfaces - Convergence and Approximation*. PhD thesis, Freie Universität Berlin, 2006.

[War08]   Max Wardetzky. Convergence of the cotangent formula: an overview. In *Discrete differential geometry*, volume 38 of *Oberwolfach Semin.*, pages 275–286. Birkhäuser, Basel, 2008.

[War11]   Max Wardetzky. Discrete cosserat shells. unpublished, 2011.

[WBH+07]   Max Wardetzky, Miklós Bergou, David Harmon, Denis Zorin, and Eitan Grinspun. Discrete quadratic curvature energies. *Comput. Aided Geom. Design*, 24(8-9):499–518, 2007.

[WBRS09]   Benedikt Wirth, Leah Bar, Martin Rumpf, and Guillermo Sapiro. Geodesics in shape space via variational time discretization. In *Proc. of International Conference on Energy Minimization Methods in Computer Vision and Pattern Recognition*, volume 5681 of *Lecture Notes in Computer Science*, pages 288–302, 2009.

[WBRS11]   Benedikt Wirth, Leah Bar, Martin Rumpf, and Guillermo Sapiro. A continuum mechanical approach to geodesics in shape space. *Int. J. Comput. Vis.*, 93(3):293–318, 2011.

[WD05]   Johannes Wallner and Nira Dyn. Convergence and C^1 analysis of subdivision schemes on manifolds by proximity. *Comput. Aided Geom. Design*, 22(7):593–622, 2005.

[WDAH10]   Tim Winkler, Jens Drieseberg, Marc Alexa, and Kai Hormann. Multi-scale geometry interpolation. *Comput. Graph. Forum*, 29(2):309 – 318, 2010. Proceedings of Eurographics.

[Wir09]   Benedikt Wirth. *Variational methods in shape space*. Dissertation, University Bonn, 2009.

[WLT12]   Yuanzhen Wang, Beibei Liu, and Yiying Tong. Linear surface reconstruction from discrete fundamental forms on triangle meshes. *Comput. Graph. Forum*, 31(8):2277–2287, 2012.

[WSLG07]   Ofir Weber, Olga Sorkine, Yaron Lipman, and Craig Gotsman. Context-aware skeletal shape deformation. *Comput. Graph. Forum*, 26(3):265–274, 2007.

[YLSL11]   I-Cheng Yeh, Chao-Hung Lin, Olga Sorkine, and Tong-Yee Lee. Template-based 3D model fitting using dual-domain relaxation. *IEEE Trans. Vis. Comput. Graph.*, 17(8):1178–1190, 2011.

[YMSM08]   Laurent Younes, Peter W. Michor, Jayant Shah, and David Mumford. A metric on shape space with explicit geodesics. *Atti Accad. Naz. Lincei Cl. Sci. Fis. Mat. Natur. Rend. Lincei (9) Mat. Appl.(9) Mat. Appl.*, 19(1):25–57, 2008.

[YWS+11]   Fei Yang, Jue Wang, Eli Shechtman, Lubomir Bourdev, and Dimitri Metaxas. Expression flow for 3D-aware face component transfer. *ACM Trans. Graph.*, 30(4), 2011.

[ZHRS15]   Chao Zhang, Behrend Heeren, Martin Rumpf, and William Smith. Shell PCA: statistical shape modelling in shell space. In *Proc. of IEEE International Conference on Computer Vision*, 2015.

[ZT00]   Olgierd C. Zienkiewicz and Robert L. Taylor. *The finite element method. Vol. 1*, volume 1. Butterworth-Heinemann, Oxford, fifth edition, 2000. The basis.

[Zwi14]   Barbara Zwicknagl. Microstructures in low-hysteresis shape memory alloys: scaling regimes and optimal needle shapes. *Arch. Ration. Mech. Anal.*, 213(2):355–421, 2014.

A Appendix

A.1 Proofs of technical lemmas

Local estimates on the approximate squared distance function

Lemma A.1.1. *For $y_0, y_1 \in \mathcal{M}$ with $\|y_0 - y_1\|_{\mathbf{V}}$ sufficiently small s.t. $|\mathcal{W}[y_0, y_1] - \mathrm{dist}^2(y_0, y_1)| = O(\mathrm{dist}^3(y_0, y_1))$ we get*

$$
\begin{array}{rll}
(i) & \mathcal{W}[y_0, y_1] = & \mathcal{W}[y_1, y_0] + O(\|y_0 - y_1\|_{\mathbf{V}}^3)\,, \\
(ii) & \mathcal{W}[y_0, y_1] = & g_{y_1}(y_0 - y_1, y_0 - y_1) + O(\|y_0 - y_1\|_{\mathbf{V}}^3) \\
& = & g_{y_0}(y_0 - y_1, y_0 - y_1) + O(\|y_0 - y_1\|_{\mathbf{V}}^3)\,.
\end{array}
$$

Proof: Part (i) is induced by the symmetry of dist. The smoothness of $\mathcal{W}$ (*i.e.* continuity in the first argument of $\mathcal{W}_{,11}$) implies for arbirary $v, w \in \mathbf{V}$:

$$
\|\mathcal{W}_{,11}[y_1 + t(y_0 - y_1), y_1](v, w) - \mathcal{W}_{,11}[y_1, y_1](v, w)\| \le t \, \|y_0 - y_1\|_{\mathbf{V}} \, \|v\|_{\mathbf{V}} \, \|w\|_{\mathbf{V}}\,. \tag{A.1.1}
$$

We use (a) a second order Taylor expansion of $\mathcal{W}[y_0, y_1]$ around (y_0, y_0) with $\mathcal{W}[y, y] = 0$, $\mathcal{W}_{,1}[y, y] = 0$ and $\mathcal{W}_{,2}[y, y] = 0$, (b) the smoothness of $\mathcal{W}$ as in (A.1.1) and (c) the consistency with the metric in Thm. 4.2.6, *i.e.* $\mathcal{W}_{,11}[y, y] = 2\, g_y$:

$$
\begin{aligned}
\mathcal{W}[y_0, y_1] &= \int_0^1 (1 - t)\mathcal{W}_{,11}[y_1 + t(y_0 - y_1), y_1](y_0 - y_1, y_0 - y_1)\, \mathrm{d}t \\
&= \int_0^1 (1 - t)\mathcal{W}_{,11}[y_1, y_1](y_0 - y_1, y_0 - y_1) + (1 - t)\, t\, \|y_1 + t(y_0 - y_1) - y_1\|_{\mathbf{V}} \, \|y_0 - y_1\|_{\mathbf{V}}^2\, \mathrm{d}t \\
&= 2\, g_{y_1}(y_0 - y_1, y_0 - y_1) \cdot \int_0^1 (1 - t)\, \mathrm{d}t + \|y_0 - y_1\|_{\mathbf{V}}^3 \int_0^1 (1 - t)\, t\, \mathrm{d}t \\
&= g_{y_1}(y_0 - y_1, y_0 - y_1) + O(\|y_0 - y_1\|_{\mathbf{V}}^3)
\end{aligned}
$$

The second part of (ii) follows analogously (or by using the continuity of the metric). $\square$

Lemma A.1.2. *Let (y_0, y_1, y_2) be a discrete geodesic. Then*

$$
\begin{array}{rll}
(i) & \mathcal{W}[y_0, y_2] = 4\mathcal{W}[y_0, y_1] + O(\max\{\|y_0 - y_1\|_{\mathbf{V}}, \|y_1 - y_2\|_{\mathbf{V}}\}^3)\,, \\
(ii) & \mathcal{W}[y_0, y_1] = \mathcal{W}[y_1, y_2] + O(\max\{\|y_0 - y_1\|_{\mathbf{V}}, \|y_1 - y_2\|_{\mathbf{V}}\}^3)\,.
\end{array}
$$

Proof: The Euler–Lagrange equation for the discrete geodesic (y_0, y_1, y_2) reads

$$
\mathcal{W}_{,2}[y_0, y_1] + \mathcal{W}_{,1}[y_1, y_2](\psi) = 0 \quad \forall \psi \in \mathbf{V}\,. \tag{A.1.2}
$$

Using a first order expansion and $\mathcal{W}[y, y] = 0$ we can rewrite

$$
\begin{aligned}
\mathcal{W}[y_0, y_1] &= \int_0^1 \mathcal{W}_{,1}[y_1 + t(y_0 - y_1), y_1](y_0 - y_1)\, \mathrm{d}t\,, \\
\mathcal{W}[y_1, y_2] &= \int_0^1 \mathcal{W}_{,2}[y_1, y_1 + t(y_2 - y_1)](y_2 - y_1)\, \mathrm{d}t\,.
\end{aligned}
$$

Defining $y_{ij}^{\text{lin}}(t) = y_i + t\,(y_j - y_i)$ we obtain for a test direction $\psi \in \mathbf{V}$

$$\mathcal{W}_{,2}[y_0, y_1](\psi) = \partial_{y_1}\Big(\int_0^1 \mathcal{W}_{,1}[y_1 + t(y_0 - y_1), y_1](y_0 - y_1)\,\mathrm{d}t\Big)(\psi)\,,$$

$$= \int_0^1 \mathcal{W}_{,11}[y_{10}^{\text{lin}}(t), y_1](y_0 - y_1, \psi)\cdot(1-t) + \mathcal{W}_{,12}[y_{10}^{\text{lin}}(t), y_1](y_0 - y_1, \psi) - \mathcal{W}_{,1}[y_{10}^{\text{lin}}(t), y_1](\psi)\,\mathrm{d}t\,,$$

and analogously

$$\mathcal{W}_{,1}[y_1, y_2](\psi) = \partial_{y_1}\Big(\int_0^1 \mathcal{W}_{,2}[y_1, y_1 + t(y_2 - y_1)](y_2 - y_1)\,\mathrm{d}t\Big)(\psi)\,,$$

$$= \int_0^1 \mathcal{W}_{,21}[y_1, y_{12}^{\text{lin}}(t)](y_2 - y_1, \psi) + \mathcal{W}_{,22}[y_1, y_{12}^{\text{lin}}(t)](y_2 - y_1, \psi)\cdot(1-t) - \mathcal{W}_{,2}[y_1, y_{12}^{\text{lin}}(t)](\psi)\,\mathrm{d}t\,.$$

Inserting $\mathcal{W}_{,2}[y_0, y_1]$ and $\mathcal{W}_{,1}[y_1, y_2]$ into the Euler–Lagrange equation (A.1.2) we obtain

$$\begin{aligned}
0 \;=\; & \int_0^1 (1-t)\big(\mathcal{W}_{,11}[y_1 + t(y_0 - y_1), y_1](y_0 - y_1, \psi) + \mathcal{W}_{,22}[y_1, y_1 + t(y_2 - y_1)](y_2 - y_1, \psi)\big) \\
& + \mathcal{W}_{,12}[y_1 + t(y_0 - y_1), y_1](y_0 - y_1, \psi) + \mathcal{W}_{,21}[y_1, y_1 + t(y_2 - y_1)](y_2 - y_1, \psi) \\
& - \mathcal{W}_{,1}[y_1 + t(y_0 - y_1), y_1](\psi)\,\mathrm{d}t - \mathcal{W}_{,2}[y_1, y_1 + t(y_2 - y_1)](\psi)
\end{aligned} \tag{A.1.3}$$

for all $\psi \in \mathbf{V}$.

Next, using $\mathcal{W}_{,1}[y, y] = \mathcal{W}_{,2}[y, y] = 0$ and expanding the last two terms of (A.1.3)

$$\mathcal{W}_{,1}[y_1 + t(y_0 - y_1), y_1](\psi) \;=\; \int_0^1 t\,\mathcal{W}_{,11}[y_1 + tr(y_0 - y_1), y_1](y_0 - y_1, \psi)\,\mathrm{d}r\,,$$

$$\mathcal{W}_{,2}[y_1, y_1 + t(y_2 - y_1)](\psi) \;=\; \int_0^1 t\,\mathcal{W}_{,22}[y_1, y_1 + tr(y_2 - y_1)](y_2 - y_1, \psi)\,\mathrm{d}r$$

we obtain

$$\begin{aligned}
0 = & \int_0^1 (1-t)\big(\mathcal{W}_{,11}[y_1 + t(y_0 - y_1), y_1](y_0 - y_1, \psi) + \mathcal{W}_{,22}[y_1, y_1 + t(y_2 - y_1)](y_2 - y_1, \psi)\big) \\
& + \mathcal{W}_{,12}[y_1 + t(y_0 - y_1), y_1](y_0 - y_1, \psi) + \mathcal{W}_{,21}[y_1, y_1 + t(y_2 - y_1)](y_2 - y_1, \psi) \\
& - t\Big(\int_0^1 \mathcal{W}_{,11}[y_{10}^{\text{lin}}(tr), y_1](y_0 - y_1, \psi)\,\mathrm{d}r + \mathcal{W}_{,22}[y_1, y_{12}^{\text{lin}}(tr)](y_2 - y_1, \psi)\,\mathrm{d}r\Big)\,\mathrm{d}t\,.
\end{aligned}$$

Using the smoothness property (A.1.1)—where analogous estimates hold for $\mathcal{W}_{,22}$ and the mixed second derivatives—and the consistency with the metric in Thm. 4.2.6, *i.e.*

$$\mathcal{W}_{,11}[y, y] = \mathcal{W}_{,22}[y, y] = -\mathcal{W}_{,12}[y, y] = -\mathcal{W}_{,21}[y, y] = 2g_y\,, \tag{A.1.4}$$

we achieve

$$\begin{aligned}
0 \;=\; & g_{y_1}(y_0 - y_1, \psi) + g_{y_1}(y_2 - y_1, \psi) + \Big(c_1\|y_0 - y_1\|_{\mathbf{V}}^2 + c_2\|y_1 - y_2\|_{\mathbf{V}}^2\Big)\cdot\|\psi\|_{\mathbf{V}} \\
\;=\; & g_{y_1}(y_0 - y_1, \psi) + g_{y_1}(y_2 - y_1, \psi) + O(\max\{\|y_0 - y_1\|_{\mathbf{V}}, \|y_1 - y_2\|_{\mathbf{V}}\}^2)\|\psi\|_{\mathbf{V}}\,.
\end{aligned}$$

Testing this equation first with $\psi = y_2 - y_1$ and then with $\psi = y_1 - y_0$ yields

$$g_{y_1}(y_0 - y_1, y_0 - y_1) \;=\; -g_{y_1}(y_0 - y_1, y_2 - y_1) + O(\max\{\|y_0 - y_1\|_{\mathbf{V}}, \|y_1 - y_2\|_{\mathbf{V}}\}^3) \tag{A.1.5}$$

$$\;=\; g_{y_1}(y_2 - y_1, y_2 - y_1) + O(\max\{\|y_0 - y_1\|_{\mathbf{V}}, \|y_1 - y_2\|_{\mathbf{V}}\}^3) \tag{A.1.6}$$

Using (a) a second order Taylor expansion of $\mathcal{W}[y_0, y_2]$ around (y_1, y_1), (b) the smoothness of $\mathcal{W}$ and (c) the consistency with the metric (A.1.4) we get:

$$\mathcal{W}[y_0, y_2] = \int_0^1 (1-t) \frac{\mathrm{d}2}{\mathrm{d}t^2} \mathcal{W}[y_1 + t(y_0 - y_1), y_1 + t(y_2 - y_1)] \, \mathrm{d}t$$

$$= \int_0^1 (1-t) \Big(\mathcal{W}_{,11}[y_1 + t(y_0 - y_1), y_1 + t(y_2 - y_1)](y_0 - y_1, y_0 - y_1)$$
$$+ \mathcal{W}_{,12}[y_1 + t(y_0 - y_1), y_1 + t(y_2 - y_1)](y_0 - y_1, y_2 - y_1)$$
$$+ \mathcal{W}_{,21}[y_1 + t(y_0 - y_1), y_1 + t(y_2 - y_1)](y_2 - y_1, y_0 - y_1)$$
$$+ \mathcal{W}_{,22}[y_1 + t(y_0 - y_1), y_1 + t(y_2 - y_1)](y_2 - y_1, y_2 - y_1) \Big) \, \mathrm{d}t$$

$$= g_{y_1}(y_0 - y_1, y_0 - y_1) - g_{y_1}(y_0 - y_1, y_2 - y_1) - g_{y_1}(y_2 - y_1, y_0 - y_1) + g_{y_1}(y_2 - y_1, y_2 - y_1)$$

$$+ \int_0^1 (1-t) \, t \, \mathrm{d}t \cdot \Big(\|y_0 - y_1\|_{\mathbf{V}} + \|y_2 - y_1\|_{\mathbf{V}} \Big) \cdot \Big(\|y_0 - y_1\|_{\mathbf{V}} + \|y_2 - y_1\|_{\mathbf{V}} \Big)^2$$

$$= g_{y_1}(y_0 - y_1, y_0 - y_1) - 2 \, g_{y_1}(y_0 - y_1, y_2 - y_1) + g_{y_1}(y_2 - y_1, y_2 - y_1)$$

$$+ O(\max\{\|y_0 - y_1\|_{\mathbf{V}}, \|y_1 - y_2\|_{\mathbf{V}}\}^3) \, .$$

Finally, we get from (A.1.6), (A.1.5) and Lemma A.1.1(ii)

$$
\begin{aligned}
4\mathcal{W}[y_0, y_1] - \mathcal{W}[y_0, y_2] &= 4 g_{y_1}(y_0 - y_1, y_0 - y_1) \\
&\quad - g_{y_1}(y_0 - y_1, y_0 - y_1) + 2 g_{y_1}(y_0 - y_1, y_2 - y_1) - g_{y_1}(y_2 - y_1, y_2 - y_1) \\
&\quad + O(\max\{\|y_0 - y_1\|_{\mathbf{V}}, \|y_1 - y_2\|_{\mathbf{V}}\}^3) \\
&= O(\max\{\|y_0 - y_1\|_{\mathbf{V}}, \|y_1 - y_2\|_{\mathbf{V}}\}^3)
\end{aligned}
$$

which proves (i).

Hence we get from (A.1.6), (A.1.5) and Lemma A.1.1(ii)

$$
\begin{aligned}
\mathcal{W}[y_0, y_1] - \mathcal{W}[y_1, y_2] &= g_{y_1}(y_0 - y_1, y_0 - y_1) - g_{y_1}(y_2 - y_1, y_2 - y_1) \\
&\quad + O(\max\{\|y_0 - y_1\|_{\mathbf{V}}, \|y_2 - y_1\|_{\mathbf{V}}\}^3) \\
&= O(\max\{\|y_0 - y_1\|_{\mathbf{V}}, \|y_2 - y_1\|_{\mathbf{V}}\}^3)
\end{aligned}
$$

which proves (ii). $\square$

Lemma A.1.3. *Let (y_0, y_1, y_2) a discrete geodesic. Then*

$$\left\| y_1 - \frac{y_0 + y_2}{2} \right\|_{\mathbf{V}} = \max\{\|y_1 - y_0\|_{\mathbf{V}}, \|y_2 - y_1\|_{\mathbf{V}}\}^2 \, .$$

Proof: The optimality condition for (y_0, y_1, y_2) being a discrete geodesic is given by

$$\mathcal{W}_{,2}[y_0, y_1](\psi) + \mathcal{W}_{,1}[y_1, y_2](\psi) = 0 \, . \tag{A.1.7}$$

A Taylor expansion around (y_1, y_1) and the consistency of the metric (A.1.4) yields

$$\mathcal{W}_{,2}[y_0, y_1](\psi) = \mathcal{W}_{,2}[y_1, y_1](\psi) + \int_0^1 \mathcal{W}_{,21}[y_1 + t(y_0 - y_1), y_1](\psi, y_0 - y_1) \, \mathrm{d}t$$

$$= 0 + \int_0^1 \mathcal{W}_{,21}[y_1, y_1](\psi, y_0 - y_1) + t \, O(\|y_0 - y_1\|_{\mathbf{V}}^2 \|\psi\|_{\mathbf{V}}) \, \mathrm{d}t$$

$$= \mathcal{W}_{,21}[y_1, y_1](\psi, y_0 - y_1) + O(\|y_0 - y_1\|_{\mathbf{V}}^2 \|\psi\|_{\mathbf{V}})$$

$$= 2 \, g_{y_1}(\psi, y_1 - y_0) + O(\|y_0 - y_1\|_{\mathbf{V}}^2 \|\psi\|_{\mathbf{V}})$$

and

$$\mathcal{W}_{,1}[y_1, y_2](\psi) = 2\, g_{y_1}(\psi, y_1 - y_2) + O(\|y_2 - y_1\|_\mathbf{V}^2 \|\psi\|_\mathbf{V})\,.$$

Plugging this into the optimality condition (A.1.7) we get

$$0 = 4\, g_{y_1}\left(\psi, y_1 - \frac{y_0 + y_2}{2}\right) + O(\|y_2 - y_1\|_\mathbf{V}^2 \|\psi\|_\mathbf{V}) + O(\|y_0 - y_1\|_\mathbf{V}^2 \|\psi\|_\mathbf{V})\,,$$

and using the coercivity of g_{y_1} finishes the proof. $\square$

Upper bound on the squared Riemannian distance

Lemma A.1.4. *Let $(y_0, \ldots, y_K) \subset \mathcal{M}$ be a discrete K-path. Then we have*

$$\mathrm{dist}^2(y_0, y_K) \leq K \sum_{k=1}^K \mathrm{dist}^2(y_{k-1}, y_k)\,.$$

Proof: As $\mathrm{dist}(y_0, y_K) \leq \sum_{k=1}^K \mathrm{dist}(y_{k-1}, y_k)$ is trivial, we have to show $\left(\sum_{k=1}^K a_k\right)^2 \leq K \sum_{k=1}^K a_k^2$ for $a_k = \mathrm{dist}(y_{k-1}, y_k) \geq 0$. Obviously $(a_1 + a_2)^2 \leq 2\,(a_1^2 + a_2^2)$. We show the statement of the lemma by induction in K, whereas the basis for $K = 2$ has been given. Inductive step $K \rightsquigarrow K + 1$:

$$\left(\sum_{k=1}^{K+1} a_k\right)^2 = \underbrace{\left(\sum_{k=1}^K a_k\right)^2}_{\leq K\sum_{k=1}^K a_k^2} + \underbrace{2\, a_{K+1} \sum_{k=1}^K a_k}_{\leq K a_{K+1}^2 + \sum_{k=1}^K a_k^2} + a_{K+1}^2 \leq (K+1) \sum_{k=1}^K a_k^2 + (K+1) a_{K+1}^2\,. \quad \square$$

Lemma A.1.5. *Let $(y_0, \ldots, y_K) \subset \mathcal{M}$ be a discrete K-path. Then we have*

$$\mathrm{dist}^2(y_0, y_K) = K \sum_{k=1}^K \mathrm{dist}^2(y_{k-1}, y_k)$$

iff. there is a geodesic $y : [0, 1] \to \mathcal{M}$ such that $y(k\tau) = y_k$ for $k = 0, \ldots, K$ and $\tau = K^{-1}$.

Proof: Let $y : [0, 1] \to \mathcal{M}$ be a geodesic between $y(0)$ and $y(1)$ and $y_k = y(t_k)$ for $t_k = k\tau$ and $k = 0, \ldots, K$. We define $f_k(s) = t_{k-1} + \tau s$ for $s \in [0, 1]$, *i.e.* $f'(s) = \tau$ and $(y \circ f_k)'(s) = \dot{y}(f(s))\tau$.

$$
\begin{aligned}
\mathrm{dist}^2(y_0, y_K) \;\underset{[y\,\mathrm{geod.}]}{=}\; & \int_0^1 g_{y(t)}\left(\dot{y}(t), \dot{y}(t)\right)\,\mathrm{dt} = \sum_{k=1}^K \int_{t_{k-1}}^{t_k} g_{y(t)}\left(\dot{y}(t), \dot{y}(t)\right)\,\mathrm{dt} \\
= \; & \sum_{k=1}^K \tau \int_0^1 g_{y(f_k(s))}\left(\dot{y}(f_k(s)), \dot{y}(f_k(s))\right)\,\mathrm{ds} \\
= \; & \sum_{k=1}^K \tau^{-1} \int_0^1 g_{(y \circ f_k)(s)}\left((y \stackrel{\cdot}{\circ} f_k)(s), (y \stackrel{\cdot}{\circ} f_k)(s)\right)\,\mathrm{ds} \\
\underset{[y \circ f_k\,\mathrm{geod.}]}{=}\; & K \sum_{k=1}^K \mathrm{dist}^2\left((y \circ f_k)(0), (y \circ f_k)(1)\right) = K \sum_{k=1}^K \mathrm{dist}^2(y_{k-1}, y_k)\,,
\end{aligned}
$$

where we have used that $y \circ f_k = y|_{[t_{k-1}, t_k]}$ is a geodesic as y is a geodesic.

For the other implication we use the proof of Lemma A.1.4 and get

$$\text{dist}^2(y_0, y_K) = K \sum_{k=1}^{K} \text{dist}^2(y_{k-1}, y_k) \geq \left(\sum_{k=1}^{K} \text{dist}(y_{k-1}, y_k) \right)^2 \geq \left(\text{dist}(y_0, y_K) \right)^2 ,$$

whereas the last inequality becomes an equality iff. all y_k lie on a geodesic y and the first inequality becomes an equality iff. $\text{dist}(y_{k-1}, y_k) = \text{dist}(y_k, y_{k+1})$ for all k (*cf.* proof of Lemma A.1.4). That means there are $0 = t_0 < \ldots < t_K = 1$, such that $y_k = y(t_k)$, and $y = \arg\min_{\tilde{y}} \mathcal{E}[\tilde{y}]$ is a geodesic. The constant speed property of geodesic curves implies $t_k = k/K$. $\square$

Representation of the relative shape operator in the reference domain

Lemma A.1.6. *Let $\mathcal{S} \subset \mathbb{R}^3$ be a regular surface patch and $\phi : \mathcal{S} \to \mathbb{R}^3$ an isometric deformation thereof. For $p \in \mathcal{S}$ let $x : \omega \to \mathbb{R}^3$ a (local) chart with $x(\xi) = p$ for some $\xi \in \omega$. Let $S(p) : T_p\mathcal{S} \to T_p\mathcal{S}$ be the shape operator of the undeformed surface $\mathcal{S}$ and $S_\phi^*(p) : T_p\mathcal{S} \to T_p\mathcal{S}$ be the pulled-back shape operator of the deformed surface $\phi(\mathcal{S})$, i.e.*

$$g_p\left(S(p)v, w\right) = h_p\left(v, w\right) , \quad g_p\left(S_\phi^*(p)v, w\right) = h_{\phi(p)}\left(D\phi v, D\phi w\right) . \tag{A.1.8}$$

for all $v, w \in T_p\mathcal{S}$. We define for the relative shape operator $S_\phi^{rel}(p) = S(p) - S_\phi^*(p)$ a matrix representation $s_\phi^{rel}(\xi) \in \mathbb{R}^{2,2}$ in the parameter domain by

$$s_\phi^{rel}(\xi) = g^{-1}(\xi) \left(h(\xi) - h^\phi(\xi) \right) ,$$

where $g, h \in \mathbb{R}^{2,2}$ are the first and second fundamental form of $\mathcal{S}$, respectively, and $h^\phi \in \mathbb{R}^{2,2}$ the second fundamental form of $\phi(\mathcal{S})$, represented in the parameter domain. Then we have

$$\|S_\phi^{rel}(p)\|_F^2 = \text{tr}\,(s_\phi^{rel}(\xi))^2 \quad \text{and} \quad \text{tr}\,(S_\phi^{rel}(p)) = \text{tr}\,(s_\phi^{rel}(\xi)) .$$

Proof: In the following we drop the specification of the point $p \in \mathcal{S}$ resp. $\xi \in \omega$ in the notation. We have

$$\|S_\phi^{\text{rel}}\|_F^2 = \|S - S_\phi^*\|_F^2 = \sum_{i,j=1}^{2} \left[\langle e_i, Se_j \rangle_{\mathbb{R}^3} - \langle e_i, S_\phi^* e_j \rangle_{\mathbb{R}^3} \right]^2 ,$$

$$\text{tr}\, S_\phi^{\text{rel}} = \text{tr}\,(S - S_\phi^*) = \sum_{i=1}^{2} \left[\langle e_i, Se_i \rangle_{\mathbb{R}^3} - \langle e_i, S_\phi^* e_i \rangle_{\mathbb{R}^3} \right] ,$$

where (e_1, e_2, e_3) is the canonical basis of $\mathbb{R}^3$. Let us assume that a neighboorhud of $p \in \mathcal{S}$ is parametrized by some chart $x : \omega \subset \mathbb{R}^2 \to \mathbb{R}^3$. For $\xi \in \omega$ such that $p = x(\xi)$ we have another basis (v_1, v_2, n) with $[v_1|v_2] = Dx(\xi)$ and $n = n(p)$ with

$$e_i = a_{1i}v_1 + a_{2i}v_2 + a_{3i}n , \quad a_i := \begin{pmatrix} a_{1i} \\ a_{2i} \\ a_{3i} \end{pmatrix} = [v_1|v_2|n]^{-1} e_i$$

Hence using the linearity of S we can write

$$\langle e_i, Se_j \rangle = \langle a_{1i}v_1 + a_{2i}v_2 + a_{3i} \underbrace{n}_{\in T_p\mathcal{S}^\perp} , \; a_{1j} \underbrace{Sv_1}_{\in T_p\mathcal{S}} + a_{2j} \underbrace{Sv_2}_{\in T_p\mathcal{S}} + a_{3j} \underbrace{Sn}_{=0} \rangle = \sum_{k,l=1}^{2} a_{ki}a_{lj} \underbrace{g(v_k, Sv_l)}_{=h_{kl}}$$

Since $g_p(v_k, S_{vl}^*) = h_{\phi(p)}(D\phi v_k, D\phi v_l) = h_{kl}^\phi$ w.r.t. the chart $x_\phi = \phi \circ x$, we analogously get

$$\langle e_i, S_\phi^* e_j \rangle = \sum_{k,l=1}^{2} a_{ki} a_{lj} h_{kl}^\phi \,.$$

If we set $A := [a_1|a_2|a_3] = [v_1|v_2|n]^{-1}$, we have with $g = [v_1|v_2]^T [v_1|v_2]$ and $v_i \perp n$:

$$AA^T = \left(\begin{array}{c|c} g^{-1} & \begin{array}{c} 0 \\ 0 \end{array} \\ \hline 0 \quad 0 & 1 \end{array} \right) \,.$$

Let $\tilde{h} \in \mathbb{R}^{3,3}$ with $\tilde{h}_{i,j} = h_{ij}$ if $i,j < 3$ and $\tilde{h}_{ij} = 0$ else. Then using the representations above we have

$$\|S_\phi^{\text{rel}}\|_F^2 = \sum_{i,j=1}^{2} \left[\langle e_i, Se_j \rangle_{\mathbb{R}^3} - \langle e_i, S_\phi^* e_j \rangle_{\mathbb{R}^3} \right]^2 = \sum_{i,j=1}^{3} \left[\sum_{k,l} a_{ki} a_{lj} (h_{kl} - h_{kl}^\phi) \right]^2$$

$$= \sum_{i,j=1}^{3} \left(A^T(\tilde{h} - \tilde{h}_\phi) A \right)_{ij}^2 = \|A^T(\tilde{h} - \tilde{h}_\phi)A\|_F^2 = \text{tr}\left(A^T(\tilde{h} - \tilde{h}_\phi) AA^T (\tilde{h} - \tilde{h}_\phi) A \right)$$

$$= \text{tr}\left(\left(\begin{array}{c|c} g^{-1} & \begin{array}{c} 0 \\ 0 \end{array} \\ \hline 0 \quad 0 & 1 \end{array} \right) \left(\begin{array}{c|c} h - h^\phi & \begin{array}{c} 0 \\ 0 \end{array} \\ \hline 0 \quad 0 & 0 \end{array} \right) \left(\begin{array}{c|c} g^{-1} & \begin{array}{c} 0 \\ 0 \end{array} \\ \hline 0 \quad 0 & 1 \end{array} \right) \left(\begin{array}{c|c} h - h^\phi & \begin{array}{c} 0 \\ 0 \end{array} \\ \hline 0 \quad 0 & 0 \end{array} \right) \right)$$

$$= \text{tr}\left(g^{-1}(h - h^\phi) \right)^2$$

and analogously

$$\text{tr}\, S_\phi^{\text{rel}} = \sum_{i=1}^{2} \left[\langle e_i, Se_i \rangle_{\mathbb{R}^3} - \langle e_i, S_\phi^* e_i \rangle_{\mathbb{R}^3} \right] = \text{tr}\left(g^{-1}(h - h^\phi) \right) ,$$

which finishes the proof. $\square$

Lemmas on branching

Proposition A.1.7. *For $[y_{k-1,\overline{n}(k,i)}, y_{k,\underline{n}(k,i)}]$ being the upper edge of $\mathcal{R}_{k,i}$, the piecewise constant quantity u_x on the stripe $\mathcal{C}_K \cap \{x_k \leq y \leq x_{k-1}\}$ is described iteratively by*

$$u_x|_{\mathcal{R}_{k,0}} = 0 \,,$$

$$u_x|_{\mathcal{R}_{k,i+1}} = u_x|_{\mathcal{R}_{k,i}} + 2 \, sign\left(u_y|_{\mathcal{R}_{k,i}} \right) \frac{y_{k-1,\overline{n}(k,i)} - y_{k,\underline{n}(k,i)}}{\theta^{k-1}l - \theta^k l} \,, \quad i \geq 0 \,. \tag{A.1.9}$$

Proof: Since $u_x(x, \frac{1}{2}) = 0$, we have $u_x|_{\mathcal{R}_{k,0}} = 0$. We now investigate the behaviour of u_x when passing an interface separating $\mathcal{R}_{k,i}$ and $\mathcal{R}_{k,i+1}$. Assume, this interface has a slope $\alpha = \frac{\Delta x}{\Delta y}$ with $\Delta x = x_{k-1} - x_k$ and $\Delta y = y_{k-1,\overline{n}(k,i)} - y_{k,\underline{n}(k,i)}$. We denote the adjacent regions by Q_1 and Q_2, respectively, as shown in Fig. A.1, *i.e.* $Q_1 := \{(s,t) : s \leq \Delta x, \, t > \alpha s\}$ and $Q_2 := \{(s,t) : s \leq \Delta x, \, t < \alpha s\}$. Note that we have $u_y = \pm 1$ on Q_1 and $u_y = \mp 1$ on Q_2. The following evaluations of u_x resp. u in $[0, \Delta x] \times [0, \Delta y]$
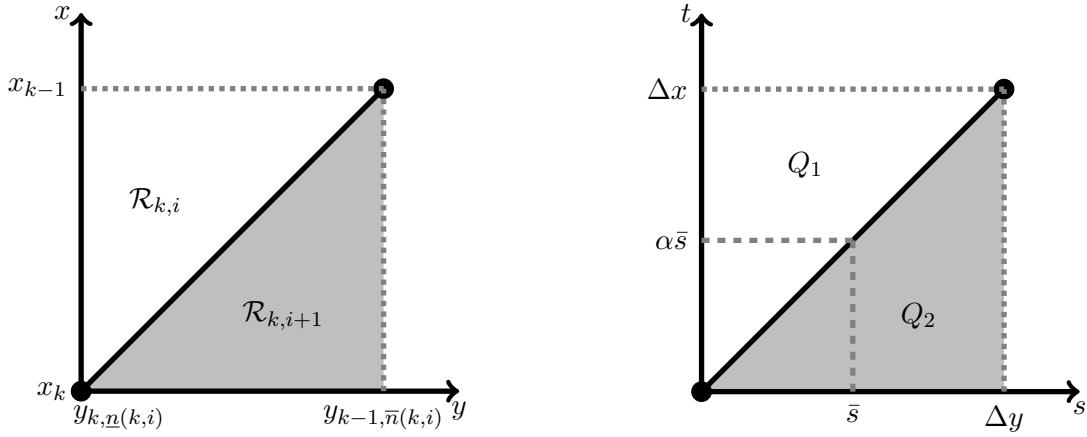
Figure A.1: *Local notation accross a single interface separating regions with $u_y \pm 1$.*

hold:

$$
\begin{aligned}
u_x(t,0) &= \frac{u(\Delta x, 0) - u(0,0)}{\Delta x} =: u_x^0 \,, \\
u(t,0) &= u(0,0) + t\, u_x(t,0) = u(0,0) + t\, u_x^0 \,, \\
u(0,s) &= u(0,0) \mp s \,, \\
u(\Delta x, s) &= u(\Delta x, 0) \pm s \,, \\
u(\alpha s, s) &= u(\alpha s, 0) \pm s = u(0,0) + \alpha s u_x^0 \pm s \,.
\end{aligned}
$$

Hence we have on Q_1

$$
\frac{u(\Delta x, s) - u(\alpha s, s)}{\Delta x - \alpha s} = \frac{u(\Delta x, 0) \pm s - \big(u(0,0) + \alpha s u_x^0 \pm s\big)}{\Delta x - \alpha s} = \frac{\Delta x u_x^0 - \alpha s u_x^0}{\Delta x - \alpha s} = u_x^0 \,,
$$

and on Q_2

$$
\frac{u(\alpha s, s) - u(0,s)}{\alpha s} = \frac{u(0,0) + \alpha s u_x^0 \pm s - \big(u(0,0) \mp s\big)}{\alpha s} = \frac{\alpha s u_x^0 \pm 2s}{\alpha s} = u_x^0 \pm 2\frac{\Delta y}{\Delta x} \,. \quad \square
$$

Lemma A.1.8. *Let $R = (0, l_x) \times (0, l_y)$ and $u_L, u_R : (0, l_y) \to \mathbb{R}$. Consider $u : R \to \mathbb{R}$ with $u(0,y) = u_L(y)$ and $u(l_x, y) = u_R(y)$, and the linear interpolation $u_l(x,y) = (x u_L(y) + (1-x) u_R(y))/l_x$. Then*

$$
\int_R u_x^2 \, \mathrm{d}x \, \mathrm{d}y = \int_R (u - u_l)_x^2 \, \mathrm{d}x \, \mathrm{d}y + \frac{\int_0^{l_y} (u_L - u_R)^2 \, \mathrm{d}y}{l_x} \,.
$$

Proof: We write $u_{lx} = (u_l)_x$. First, we have $u_{lx}(x,y) = (u_L(y) - u_R(y))/l_x$ and hence

$$
\int_R u_{lx}^2 = l_x^{-2} \int_0^{l_y} \int_0^{l_x} (u_L(y) - u_R(y))^2 \, \mathrm{d}x \, \mathrm{d}y = \frac{\int_0^{l_y} (u_L - u_R)^2 \, \mathrm{d}y}{l_x} \,.
$$

Second, we have

$$
\int_R (u - u_l)_x^2 = \int_R u_x^2 + \int_R u_{lx}^2 - 2 \int_R u_x u_{lx} = \int_R u_x^2 - \int_R u_{lx}^2 \,,
$$

since

$$\int_R u_x u_{lx} = \int_0^{l_y} \int_0^{l_x} u_x(x,y) u_{lx}(x,y) \, \mathrm{d}x \, \mathrm{d}y = \int_0^{l_y} \frac{u_L(y) - u_R(y)}{l_x} \left(\int_0^{l_x} u_x(x,y) \, \mathrm{d}x \right) \mathrm{d}y$$

$$= \int_0^{l_y} \frac{u_L(y) - u_R(y)}{l_x} \left(u(l_x, y) - u(0, y) \right) \mathrm{d}y = \int_0^{l_y} \frac{(u_L(y) - u_R(y))^2}{l_x} \, \mathrm{d}y$$

$$= \int_0^{l_x} \int_0^{l_y} \frac{(u_L(y) - u_R(y))^2}{l_x^2} \, \mathrm{d}y \, \mathrm{d}x = \int_R u_{lx}^2 . \quad \square$$

Proposition A.1.9. *The elastic energy of N repetitions of our infinite branching pattern is*

$$F_{elast}[N, L, \theta] = \frac{\theta}{64 N^2 (1 - \theta) L} \cdot \left(\frac{4 + \sqrt{2}}{\alpha^2 \theta - 1} + \frac{4 + 3\sqrt{2}}{\alpha^4 \theta + 1} \right).$$

Proof: We set $\alpha = 1 + \sqrt{2}$, $\beta = 1 - \sqrt{2}$, $\gamma = \sqrt{2} - 1$ and $\delta = 2 - \sqrt{2}$. The elastic energy terms in one *quarter* stripe (as depicted in Fig. 8.12, top), *i.e.* $(4N)^{-1} F_{\mathrm{elast}}[N, L, \theta]$, can be computed by plugging (8.3.3),(8.3.4) and (8.3.5) into (8.3.2):

$$\sum_{k \geq 0} a_k F_{\mathrm{elast}}[\mathcal{A}_k] = \frac{2}{(1 - \theta) L} \sum_{k \geq 0} (\alpha^k + \beta^k) \cdot \frac{y_k^2 (w_k^a - \frac{1}{2} y_k)}{\theta^k}$$

$$= \frac{1}{(1 - \theta) L} \left(2 \sum_{k \geq 0} \alpha^k y_k^2 w_k^a \theta^{-k} + 2 \sum_{k \geq 0} \beta^k y_k^2 w_k^a \theta^{-k} - \sum_{k \geq 0} \alpha^k y_k^3 \theta^{-k} - \sum_{k \geq 0} \beta^k y_k^3 \theta^{-k} \right)$$

and

$$\sum_{k \geq 0} b_k F_{\mathrm{elast}}[\mathcal{B}_k] = \frac{\sqrt{2}}{(1 - \theta) L} \sum_{k \geq 0} (\alpha^k - \beta^k) \cdot \frac{y_k^2 (w_k^a - y_k)}{\theta^k}$$

$$= \frac{\sqrt{2}}{(1 - \theta) L} \left(\sum_{k \geq 0} \alpha^k y_k^2 w_k^a \theta^{-k} - \sum_{k \geq 0} \beta^k y_k^2 w_k^a \theta^{-k} - \sum_{k \geq 0} \alpha^k y_k^3 \theta^{-k} + \sum_{k \geq 0} \beta^k y_k^3 \theta^{-k} \right).$$

Using $w_k^a = (4N)^{-1} \gamma^k$ for $k \geq 0$ and

$$y_k = \frac{\gamma^2}{4 \delta N} \gamma^k , \quad y_k^2 = \frac{\gamma^4}{16 \delta^2 N^2} \gamma^{2k} , \quad y_k^3 = \frac{\gamma^6}{64 \delta^3 N^3} \gamma^{3k} , \quad k \geq 0 ,$$

we can write

$$\sum_{k \geq 0} \alpha^k y_k^2 w_k^a \theta^{-k} = \frac{\gamma^4}{64 \delta^2 N^3} \sum_{k \geq 0} \left(\alpha^2 \theta \right)^{-k} = \frac{\gamma^4}{64 \delta^2 N^3} \frac{\alpha^2 \theta}{\alpha^2 \theta - 1} ,$$

$$\sum_{k \geq 0} \alpha^k y_k^3 \theta^{-k} = \frac{\gamma^6}{64 \delta^3 N^3} \sum_{k \geq 0} \left(\alpha^2 \theta \right)^{k} = \frac{\delta}{2} \cdot \frac{\gamma^4}{64 \delta^2 N^3} \frac{\alpha^2 \theta}{\alpha^2 \theta - 1} ,$$

where we have used $\gamma^2/\delta^2 = 1/2$ and $\gamma \alpha = 1$. Note that the geometric series converge iff. $\theta > \alpha^2$. Analogously, using $\gamma = -\beta$ and $\beta^{-1} = -\alpha$, we get

$$\sum_{k \geq 0} \beta^k y_k^2 w_k^a \theta^{-k} = \frac{\gamma^4}{64 \delta^2 N^3} \sum_{k \geq 0} \left(\frac{-\beta^4}{\theta} \right)^k = \frac{\gamma^4}{64 \delta^2 N^3} \sum_{k \geq 0} \left(-\alpha^4 \theta \right)^{-k} = \frac{\gamma^4}{64 \delta^2 N^3} \frac{\alpha^4 \theta}{\alpha^4 \theta + 1} ,$$

$$\sum_{k \geq 0} \beta^k y_k^3 \theta^{-k} = \frac{\gamma^6}{64 \delta^3 N^3} \sum_{k \geq 0} \left(\frac{-\beta^4}{\theta} \right)^k = \frac{\gamma^6}{64 \delta^3 N^3} \sum_{k \geq 0} \left(-\alpha^4 \theta \right)^{-k} = \frac{\delta}{2} \cdot \frac{\gamma^4}{64 \delta^2 N^3} \frac{\alpha^4 \theta}{\alpha^4 \theta + 1} .$$

Convergence is ensured since $\theta > \alpha^2 > \alpha^4$.

Finally, plugging everything together, we obtain

$$
\begin{aligned}
\sum_{k \geq 0} a_k F_{\text{elast}}[\mathcal{A}_k] + b_k F_{\text{elast}}[\mathcal{B}_k] =& \frac{2+\sqrt{2}}{(1-\theta)L} \sum_{k \geq 0} \alpha^k y_k^2 w_k^a \theta^{-k} + \frac{2-\sqrt{2}}{(1-\theta)L} \sum_{k \geq 0} \beta^k y_k^2 w_k^a \theta^{-k} \\
& - \frac{1+\sqrt{2}}{(1-\theta)L} \sum_{k \geq 0} \alpha^k y_k^3 \theta^{-k} - \frac{1-\sqrt{2}}{(1-\theta)L} \sum_{k \geq 0} \beta^k y_k^3 \theta^{-k} \\
=& \frac{2+\sqrt{2}}{(1-\theta)L} \cdot \frac{\gamma^4}{64\delta^2 N^3} \cdot \frac{\alpha^2 \theta}{\alpha^2 \theta - 1} + \frac{2-\sqrt{2}}{(1-\theta)L} \cdot \frac{\gamma^4}{64\delta^2 N^3} \cdot \frac{\alpha^4 \theta}{\alpha^4 \theta + 1} \\
& - \frac{\delta}{2} \cdot \frac{1+\sqrt{2}}{(1-\theta)L} \cdot \frac{\gamma^4}{64\delta^2 N^3} \cdot \frac{\alpha^2 \theta}{\alpha^2 \theta - 1} - \frac{\delta}{2} \cdot \frac{1-\sqrt{2}}{(1-\theta)L} \cdot \frac{\gamma^4}{64\delta^2 N^3} \cdot \frac{\alpha^4 \theta}{\alpha^4 \theta + 1} \\
=& \frac{\gamma^4}{64\delta^2 N^3 (1-\theta)L} \cdot \Big[(2+\sqrt{2}) \cdot \frac{\alpha^2 \theta}{\alpha^2 \theta - 1} - \frac{\delta}{2} \cdot (1+\sqrt{2}) \cdot \frac{\alpha^2 \theta}{\alpha^2 \theta - 1} \\
& + (2-\sqrt{2}) \cdot \frac{\alpha^4 \theta}{\alpha^4 \theta + 1} - \frac{\delta}{2} \cdot (1-\sqrt{2}) \cdot \frac{\alpha^4 \theta}{\alpha^4 \theta + 1} \Big] \\
=& \frac{\theta}{256 N^3 (1-\theta)L} \cdot \Big(\frac{4+\sqrt{2}}{\alpha^2 \theta - 1} + \frac{4+3\sqrt{2}}{\alpha^4 \theta + 1} \Big).
\end{aligned}
$$

where we used $\gamma^2/\delta^2 = 1/2$ and $\gamma\alpha = 1$ in the last step. Multiplication by $4N$ finishes the proof. $\square$

A.2 On the discrete embedded shape operator

In Sec. 5.3.2 we have introduced a matrix representation $B \in \mathbb{R}^{2,2}$ of a discrete shape operator on the reference domain. However, the definition of the discrete shape operator defined in our corresponding publication [HRWW12] is given on an embedded polyhedral surface. To establish a connection between these two representations, we derive in this section the discrete shape operator on an embedded polyhedral surface $\mathbf{S} \subset \mathbb{R}^3$, *i.e.* a linear operator represented by a matrix in $\mathbb{R}^{3,3}$.

As in Sec. 5.3.2 we start with the assumption that the embedded shape operator is constant on faces. Yet different from Sec. 5.3.2, the derivation of the embeddded representation will be based on the pulled-back defintion (5.1.8) induced by a deformation $\Phi : \mathbf{S} \to \mathbb{R}^3$, *i.e.* we write $B_T^*[\Phi] \in \mathbb{R}^{3,3}$ for a face $T \in \mathbf{S}$. Finally, we will show that the mean curvature induced by $B_T^*[\text{id}] \in \mathbb{R}^{3,3}$ coincides with the mean curvature induced by $B_T \in \mathbb{R}^{2,2}$ as defined in (5.3.7).

We aim at defining a (pulled-back) shape operator $B_T^*[\Phi]$ that is elementwise constant, *i.e.* we have

$$
g_T \left(B_T^*[\Phi]V, W \right) = h_{\Phi(T)} \left(D\Phi V, D\Phi W \right) \tag{A.2.1}
$$

for all $V, W \in \mathbb{R}^3$. Similar to Sec. 5.3.2, $B_T^*[\Phi]$ lives in the three-dimensional subspace $\mathcal{B}_T \subset \mathbb{R}^{3,3}$ defined by

$$
\mathcal{B}_T = \{ M \in \mathbb{R}^{3,3} : M N_T = 0, \ M \text{ symmetric} \}.
$$

If $R_{T,\pi} \in SO(3)$ denotes a rotation in the plane of T by π the subspace $\mathcal{B}_T$ is spanned by

$$
M_i = (R_{T,\pi} E_i) \otimes (R_{T,\pi} E_i), \quad i = 0, 1, 2,
$$

where E_i denotes an edge of T. Now we write $B_T^*[\Phi] = \sum_j b_j^\Phi M_j$ and the three coefficients $b_0^\Phi, b_1^\Phi, b_2^\Phi \in \mathbb{R}$ are uniqely defined by the evaluation of (A.2.1) for three different choices of $V, W \in \mathbb{R}^3$. We make the choice $V = W = E_i$ for $i = 0, 1, 2$, which yields the linear system

$$
g_T \left(B_T^*[\Phi] E_i, E_i \right) = h_{\Phi(T)} \left(D\Phi E_i, D\Phi E_i \right), \quad i = 0, 1, 2. \tag{A.2.2}
$$

Since g simply denotes the standard Euclidean scalar product in $\mathbb{R}^3$ we have due to Lemma A.2.1

$$g_T\left(B_T^*[\Phi]E_i, E_i\right) = \sum_{j=0}^{2} b_j^\Phi\left(\langle E_i, R_{T,\pi}E_j\rangle_{\mathbb{R}^3}\right)^2 = 4|T|^2\sum_{j\neq i} b_j^\Phi\,. \qquad (A.2.3)$$

For the evaluation of the right hand side in (A.2.2), *i.e.* the evalutation of a discrete second fundamental form, we make use of the derivation in Sec. 5.3.2 (*cf*. also [Hee11, HRWW12]), which results in (5.3.5):

$$h_{\Phi(T)}\left(D\Phi E_i, D\Phi E_i\right) = 2\langle N_j^\Phi - N_k^\Phi, E_i^\Phi\rangle_{\mathbb{R}^3} =: H_i^\Phi\,, \qquad (A.2.4)$$

where N^Φ and E^Φ are quantities living on the deformed mesh. In particular, N_i^Φ is the edge normal sitting at the midpoint of E_i^Φ. Plugging (A.2.3) and (A.2.4) into (A.2.2) we can solve for the coefficients b_j^Φ and arrive at

$$b_i^\Phi = \frac{1}{8|T|^2}(H_i^\Phi - H_j^\Phi - H_k^\Phi)\,.$$

Using $E_i^\Phi + E_j^\Phi + E_k^\Phi = 0$ and $\langle N_i^\Phi, E_i^\Phi\rangle = 0$ yields

$$\begin{aligned}
H_i^\Phi - H_j^\Phi - H_k^\Phi &= 2\langle N_j^\Phi - N_k^\Phi, E_i^\Phi\rangle - 2\langle N_k^\Phi - N_i^\Phi, E_j^\Phi\rangle - 2\langle N_i^\Phi - N_j^\Phi, E_k^\Phi\rangle \\
&= 2\left(\langle N_j^\Phi, E_i^\Phi\rangle - \langle N_k^\Phi, E_i^\Phi\rangle - \langle N_k^\Phi, E_j^\Phi\rangle + \langle N_i^\Phi, E_j^\Phi\rangle - \langle N_i^\Phi, E_k^\Phi\rangle + \langle N_j^\Phi, E_k^\Phi\rangle\right) \\
&= 2\left(\langle N_j^\Phi, E_i^\Phi + E_k^\Phi\rangle + \langle N_k^\Phi, -E_i^\Phi - E_j^\Phi\rangle + \langle N_i^\Phi, E_j^\Phi - E_k^\Phi\rangle\right) \\
&= 2\left(\langle N_j^\Phi, -E_j^\Phi\rangle + \langle N_k^\Phi, E_k^\Phi\rangle + \langle N_i^\Phi, -2E_k^\Phi - E_i^\Phi\rangle\right) \\
&= -4\langle N_i^\Phi, E_k^\Phi\rangle = -4\langle N_i^\Phi, E_{i-1}^\Phi\rangle = -8\frac{|T^\Phi|}{|E_i^\Phi|}\cos\frac{\alpha_i^\Phi}{2}\,,
\end{aligned}$$

where the last identity has been derived in Sec. 5.3.2. Hence we get as matrix representation for the embedded, pulled-back discrete shape operator

$$B_T^*[\Phi] = \frac{1}{8|T|^2}\sum_{i=0}^{2}(H_i^\Phi - H_j^\Phi - H_k^\Phi)M_i = -\frac{1}{|T|^2}\sum_{i=0}^{2}|T^\Phi|\frac{\cos\frac{\pi+\theta_i^\Phi}{2}}{|E_i^\Phi|}M_i\,, \qquad (A.2.5)$$

which coincides with eq. (14) in [HRWW12].

For $\Phi = \text{id}$ a linearization of this representation leads to the *triangle-averaged operator* defined in eq. (4) in [GGRZ06]. This can be seen by using the Taylor expansion $-2\cos\frac{\theta+\pi}{2} \approx \theta + O(\theta^2)$ as in Sec. 5.3.2. Furthermore, for the identity mapping $\Phi = \text{id}$ we get for the mean curvature

$$\operatorname{tr} B_T^*[\text{id}] = -\frac{1}{|T|}\sum_{i=0}^{2}\frac{\cos\frac{\pi+\theta_i}{2}}{|E_i|}\operatorname{tr} M_i = -\sum_{i=0}^{2}\frac{\cos\frac{\pi+\theta_i}{2}}{|T|}|E_i|\,,$$

since $\operatorname{tr} M_i = |E_i|^2$ for $i = 0, 1, 2$, which coincides exactly with (5.3.10).

Lemma A.2.1. *Let $T \subset \mathbb{R}^3$ be a triangle with edges $E_0, E_1, E_2 \in \mathbb{R}^3$ and face normal N. Let R_i be a rotation of E_i by π in the plane of T, i.e. one can write $R_i = E_i \times N$. Then we have*

$$\langle E_i, R_j\rangle_{\mathbb{R}^3} = \begin{cases} 2\,|T|, & i \neq j \\ 0, & i = j \end{cases}\,.$$

Proof: Obviously $\langle E_i, R_i\rangle = 0$ as $R_i \perp E_i$. If $i \neq j$ we have $|T| = \frac{1}{2}|E_i \times E_j|$. Hence

$$\begin{aligned}
\langle E_i, R_j\rangle^2 &= \langle E_i, E_j \times N\rangle^2 = (\det[E_i \mid E_j \mid N])^2 = \det\left([E_i \mid E_j \mid N]^T[E_i \mid E_j \mid N]\right) \\
&= |E_i|^2|E_j|^2 - \langle E_i, E_j\rangle^2 = |E_i \times E_j|^2 = 4\,|T|^2\,. \quad \square
\end{aligned}$$

A.3 Multiresolution scheme based on deformation transfer

In this section we describe the multilevel scheme applied to various optimization problems in this thesis. Its core ingredient is the gradient-based deformation transfer that has been proposed in [BSPG06, SP04], for additional information we refer to [KCVS98, KVS99, KBS00, BK03, BK04].

Consider a sequence of high resolution *input meshes* $\mathbf{S}_1, \ldots, \mathbf{S}_N$ with n vertices, *i.e.* $\mathbf{S}_i \in \mathbb{R}^{3n}$. Our objective is to compute a high resolution *optimal shape* $\mathbf{S} = \mathbf{S}[\mathbf{S}_1, \ldots, \mathbf{S}_N]$, *e.g.* an average shape. Analogously, the method can be applied to compute a sequence of optimal shapes, *e.g.* a time-discrete geodesic but for simplicity we assume here to have only one optimal shape. Since solving a (nonlinear) optimization problem in a large dimensional space $\mathbb{R}^{3n}$ is neither easy nor efficient, we make use of a hierarchical scheme, *i.e.* we follow three steps, *cf*. Fig. A.2:

   (i) compute simplifications (by means of mesh decimation) of the input meshes,

   (ii) optimize the low dimensional simplifications and

   (iii) prolongate the optimal shapes to the high resolution space.

Simplification We choose one of the input meshes to be the so-called *reference mesh* $\hat{\mathbf{S}}$, *e.g.* $\hat{\mathbf{S}} = \mathbf{S}_1$. The sequence $\mathbf{S}_1, \ldots, \mathbf{S}_N$ is then simplified simultaneously and we obtain a sequence of coarse meshes $\mathbf{C}_1, \ldots, \mathbf{C}_N$ with $m \ll n$ vertices, *i.e.* we have $\mathbf{C}_i \in \mathbb{R}^{3m}$. In the following we refer to $\hat{\mathbf{C}}$ as the *coarse reference mesh*, *i.e.* $\hat{\mathbf{C}} = \mathbf{C}_1$ in this example. Note that the simplication method have to ensure that all vertices $q_i \in \mathbf{C}_j$, $i = 1, \ldots, m$, in the coarse mesh also exist in the corresponding high resolution mesh (just having a different index). That means there is a mapping $\pi : \mathcal{N}_c \to \mathcal{N}_h$ between the two node index sets $\mathcal{N}_c = \{1, \ldots, m\}$ and $\mathcal{N}_h = \{1, \ldots, n\}$, such that $q_i = p_{\pi(i)}$ for some $p_{\pi(i)} \in \mathbf{S}_j$ and $i = 1, \ldots, m$.

Optimization on the coarse level This depends on the application, *e.g.* we might minimize the discrete path energy or compute an average shape $\mathbf{C} = \mathbf{C}[\mathbf{C}_1, \ldots, \mathbf{C}_N]$.

Prolongation We compute a high resolution solution $\mathbf{S}$ by lifting the coarse solution $\mathbf{C} \in \mathbb{R}^{3m}$ to $\mathbb{R}^{3n}$. Therefor we separate *low frequency shape information* from *high frequency detail information* and treat them differently (*cf*. Fig. A.2). This procedure is based on the work by Botsch *et al.* [BSPG06] and will be desribed in detail in the following.

Recovering low frequency shape information

First, we compute a low frequency *base mesh* $\hat{\mathbf{B}} \in \mathbb{R}^{3n}$ corresponding to the reference mesh $\hat{\mathbf{S}}$. This is done by solving the Bi-Laplace problem (often refered to as thin-plate problem), *i.e.*

$$\begin{aligned}
\Delta_{\mathcal{M}}^2(\hat{b}_i) &= 0 \quad \forall i \in \mathcal{N}_h\,, \\
\hat{b}_{\pi(i)} &= \hat{q}_i \quad \forall i \in \mathcal{N}_c\,.
\end{aligned} \tag{A.3.1}$$

where $\hat{b}_i \in \mathbb{R}^3$ and $\hat{q}_i \in \mathbb{R}^3$ are the nodal positions of $\hat{\mathbf{B}}$ and $\hat{\mathbf{C}}$, respectively. Note that $\hat{b}_{\pi(i)} = \hat{q}_i = \hat{p}_{\pi(i)}$ for all $i \in \mathcal{N}_c$ by definition of π where $\hat{p}_i \in \mathbb{R}^3$ are nodal positions of $\hat{\mathbf{S}}$. Then we compute a low frequency *optimal base mesh* $\mathbf{B} \in \mathbb{R}^{3n}$ with nodal positions $b_i \in \mathbb{R}^3$ corresponding to the (yet unknown) optimal shape $\mathbf{S}$ by solving

$$\begin{aligned}
\Delta_{\mathcal{M}}^2(b_i) &= 0 \quad \forall i \in \mathcal{N}_h \\
b_{\pi(i)} &= q_i \quad \forall i \in \mathcal{N}_c\,.
\end{aligned} \tag{A.3.2}$$

where q_i are the nodal positions of the coarse optimal shell $\mathbf{C}$. To discretize the Laplace-Beltrami operator $\Delta_{\mathcal{M}}$ we make use of the cotan formula [PP93, DMSB99, MDSB02] (*cf*. also Sec. 5.4), *i.e.*

$$\Delta_{\mathcal{M}}(p_i) = \frac{2}{A_i} \sum_{j \sim i} (\cot \alpha_{ij} + \cot \beta_{ij})(p_i - p_j), \qquad (A.3.3)$$

where $j \sim i$ means that p_j is a neighbour of p_i, A_i is an area associated with p_i and α_{ij} and β_{ij} are certain angles within the 1-ring of p_i. If $P = (p_i)_i$ is the vector of nodal positions we can interpret (A.3.3) as linear system, assemble a matrix L and have $\Delta_{\mathcal{M}}(p_i) = (L\,P)_i$. Furthermore, we define $\Delta_{\mathcal{M}}^k(p_i) = (L^k\,P)_i$.

Let us comment on the discrete Bi-Laplace equation $\Delta_{\mathcal{M}}^2(p_i) = 0$ used above. Here $p_i \in \mathbb{R}^3$ represents a node of some discrete shell, which is represented by its vector of nodal positions $P = (p_i)_i$. The most important thing to be aware of is that $\Delta_{\mathcal{M}}$ depends on this shell itself, *i.e.* $\mathcal{M} = P$. In detail, the cotan weights depend on the embedding, *i.e.* the nodal positions, and hence we actually have $L = L[P]$. This means, the equation $\Delta_{\mathcal{M}}^k P = 0$ resp. its discretization $L^k P = 0$ is *not* linear in P. However, due to the required efficiency it is unfeasible to solve the full nonlinear thin-plate problem. To overcome this issue, it is a common practice to assemble the matrix L once by using some particular mesh, *e.g.* the designated reference mesh $\hat{\mathbf{S}}$. Then the problems (A.3.1) resp. (A.3.2) become linear in $\hat{\mathbf{B}}$ resp. $\mathbf{B}$.
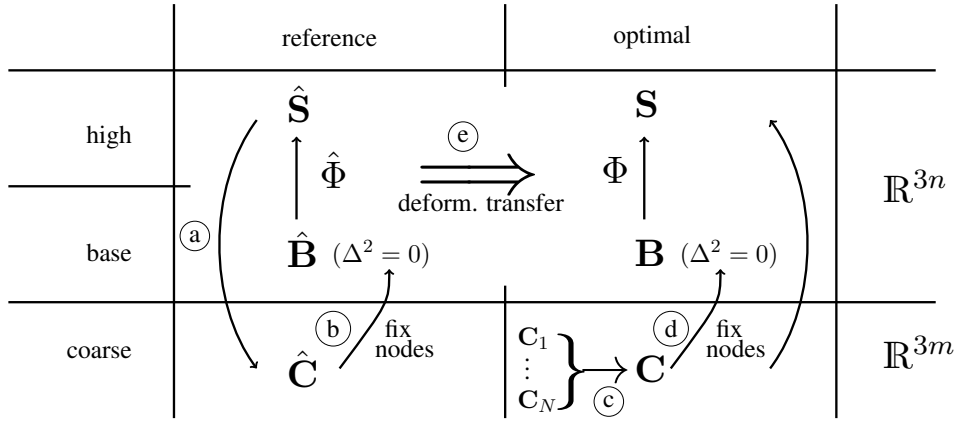
Figure A.2: *Multiresolution scheme based on deformation transfer [BSPG06]. (a) compute coarse reference mesh $\hat{\mathbf{C}}$ by decimation while keeping positions of remaining vertices fixed, i.e. $\hat{\mathbf{C}} \subset \hat{\mathbf{S}}$; (b) compute reference base mesh $\hat{\mathbf{B}}$ by solving Bi-Laplace equation while fixing vertices prescribed by $\hat{\mathbf{C}}$; (c) solve nonlinear optimization problem on coarse level to obtain optimal coarse mesh $\mathbf{C}$; (d) compute optimal base mesh $\mathbf{B}$ by solving Bi-Laplace equation while fixing vertices prescribed by $\mathbf{C}$; (e) apply transformation transfer $\hat{\Phi} \Rightarrow \Phi$ to obtain optimal high resolution mesh $\mathbf{S} = \Phi(\mathbf{B})$.*

Transferring high frequency detail information

We might think of the high resolution reference mesh $\hat{\mathbf{S}} \in \mathbb{R}^{3n}$ as being a deformed version of the high resolution base mesh $\hat{\mathbf{B}} \in \mathbb{R}^{3n}$. This deformation $\hat{\Phi} : \hat{\mathbf{B}} \to \hat{\mathbf{S}}$ can be described by computing the deformation gradient $D\hat{\Phi}|_T$ for each triangle T. Once having these gradients we are able to *reconstruct* $\hat{\mathbf{S}}$ from the information stored in $\hat{\mathbf{B}}$ and $(D\hat{\Phi}_T)_T$ by solving a linear system. That means we can write $\hat{\mathbf{S}} = \mathcal{A}(\hat{\mathbf{B}}, (D\hat{\Phi}_T)_T)$, where $\mathcal{A}$ is a linear operator. Using this property we can now *transfer* the gradient based information by replacing $\hat{\mathbf{B}}$ in the reconstruction step by some different base mesh $\mathbf{B}$, *i.e.* we define $\mathbf{S} := \mathcal{A}(\mathbf{B}, (D\hat{\Phi}_T)_T)$. In the remainder of this section we describe this deformation transfer in detail.

We consider a mesh $\mathbf{S}$ with vertex positions $p_i \in \mathbb{R}^3$, $i = 1, \ldots, n$ and faces T_j, $j = 1, \ldots, m$. Linear FEM basis functions $\Psi_i : \mathbf{S} \to \mathbb{R}$ (also known as hat functions) are located at vertices, *i.e.* $\Psi_i(p_j) = \delta_{ij}$. A deformation $\Phi(\mathbf{S})$ of $\mathbf{S}$ can be described by its vector of nodal positions $(q_i)_i$, $q_i = \Phi(p_i) \in \mathbb{R}^3$, $i = 1, \ldots, n$. Alternatively, the piecewise linear deformation $\Phi : \mathbf{S} \to \mathbb{R}^3$ resp. the deformation gradient is explicitly given by

$$\Phi(x) = \sum_{i=1}^{n} \Psi_i(x) q_i, \quad \nabla \Phi(x) = \sum_{i=1}^{n} \nabla \Psi_i(x) q_i^T.$$

If $x \in T_j$ and $q_{j_0}, q_{j_1}, q_{j_2}$ are the (deformed) nodal positions of $\Phi(T_j)$ we have $q(x) = \sum_k \Psi_{j_k}(x) q_{j_k}$ and

$$\nabla \Phi(x) = \sum_{k=0}^{2} \nabla \Psi_{j_k}(x) q_{j_k}^T = \sum_{k=0}^{2} \nabla \Psi_{j_k}\big|_{T_j} q_{j_k}^T$$

as $\nabla \Psi_i \in \mathbb{R}^3$ is constant on each triangle. Hence we get

$$G_j[\Phi] := \nabla \Phi(x)\big|_{T_j} = \left[\nabla \Psi_{j_0}\big|_{T_j}, \nabla \Psi_{j_1}\big|_{T_j}, \nabla \Psi_{j_2}\big|_{T_j} \right] \cdot \left[q_{j_0}, q_{j_1}, q_{j_2} \right]^T \in \mathbb{R}^{3,3}. \qquad \text{(A.3.4)}$$

The gradients of the basis functions are uniquely defined by the following equations

$$
\begin{array}{lll}
(p_{j_1} - p_{j_0}) \cdot \nabla \Psi_{j_0} = -1 & (p_{j_1} - p_{j_0}) \cdot \nabla \Psi_{j_1} = 1 & (p_{j_1} - p_{j_0}) \cdot \nabla \Psi_{j_2} = 0 \\
(p_{j_2} - p_{j_0}) \cdot \nabla \Psi_{j_0} = -1 & (p_{j_2} - p_{j_0}) \cdot \nabla \Psi_{j_1} = 0 & (p_{j_2} - p_{j_0}) \cdot \nabla \Psi_{j_2} = 1 \\
N_j \cdot \nabla \Psi_{j_0} = 0 & N_j \cdot \nabla \Psi_{j_1} = 0 & N_j \cdot \nabla \Psi_{j_2} = 0
\end{array}
$$

where $N_j = \tilde{N}_j / |\tilde{N}_j|$, $\tilde{N}_j = (p_{j_1} - p_{j_0}) \times (p_{j_2} - p_{j_0})$ is the unit triangle normal of T_j. This system reveals an explicit formula of the matrix $[\nabla \Psi_{j_0}\big|_{T_j}, \nabla \Psi_{j_1}\big|_{T_j}, \nabla \Psi_{j_2}\big|_{T_j}] \in \mathbb{R}^{3,3}$, which can be plugged into (A.3.4), and one obtains

$$G_j[\Phi] = \left[(p_{j_1} - p_{j_0}), (p_{j_2} - p_{j_0}), N_j \right]^{-T} \cdot \begin{pmatrix} -1 & 1 & 0 \\ -1 & 0 & 1 \\ 0 & 0 & 0 \end{pmatrix} \cdot \left[q_{j_0}, q_{j_1}, q_{j_2} \right]^T. \qquad \text{(A.3.5)}$$

Hence we can define a global matrix $A[\mathbf{S}] \in \mathbb{R}^{3m,n}$, that only depends on the undeformed nodal positions, *i.e.*

$$A[\mathbf{S}] \cdot \begin{pmatrix} q_1 \\ \vdots \\ q_n \end{pmatrix} = \begin{pmatrix} G_1[\Phi] \\ \vdots \\ G_m[\Phi] \end{pmatrix}.$$

Now suppose we are given gradients $G_j' \in \mathbb{R}^{3,3}$ for $j = 1, \ldots, m$ that correspond to an (unknown) deformation. Then we can reconstruct the deformed positions $p_i' \in \mathbb{R}^3$, $i = 1, \ldots, n$, by solving the weighted least squares problem

$$A[\mathbf{S}]^T D[\mathbf{S}] A[\mathbf{S}] \cdot \begin{pmatrix} p_1' \\ \vdots \\ p_n' \end{pmatrix} = A[\mathbf{S}]^T D[\mathbf{S}] \begin{pmatrix} G_1' \\ \vdots \\ G_m' \end{pmatrix}$$

where $D[\mathbf{S}] \in \mathbb{R}^{m,m}$ is a diagonal matrix containing area elements of $\mathbf{S}$. As $A[\mathbf{S}]^T D[\mathbf{S}] A[\mathbf{S}]$ turns out to be the matrix representation of the discrete Laplace-Beltrami operator, we essentially have to solve a Poission problem.

The high frequency detail information of $\hat{\mathbf{S}}$ is encoded in a deformation $\hat{\Phi} : \hat{\mathbf{B}} \rightarrow \hat{\mathbf{S}}$ of the reference base mesh $\hat{\mathbf{B}}$. Recall that all base meshes only contain low frequency information as the high frequencies have been smoothed out by the Bi-Laplace filtering. The detail information $\hat{\Phi} : \hat{\mathbf{B}} \rightarrow \hat{\mathbf{S}}$ is now transfered to $\mathbf{B}$, which already contains the low frequency information of the optimal coarse shell $\mathbf{C}$, by the gradient-based deformation transfer, *i.e.* by solving

$$A[\mathbf{B}]^T D[\mathbf{B}] \, A[\mathbf{B}] \cdot \begin{pmatrix} q_1 \\ \vdots \\ q_n \end{pmatrix} = A[\mathbf{B}]^T D[\mathbf{B}] \begin{pmatrix} G_1[\hat{\Phi}] \\ \vdots \\ G_m[\hat{\Phi}] \end{pmatrix}$$

for $(q_1, \ldots, q_n)$ which represents the nodal position vector of the desired shell $\mathbf{S}$. The deformation gradients $G_j[\hat{\Phi}]$ on the right hand side can either be obtained by (A.3.5) or the explicit formula

$$G_j[\hat{\Phi}] = \left[\hat{p}_{j_1} - \hat{p}_{j_0} \,\middle|\, \hat{p}_{j_2} - \hat{p}_{j_0} \,\middle|\, N_j[\hat{\mathbf{S}}] \right] \cdot \left[\hat{b}_{j_1} - \hat{b}_{j_0} \,\middle|\, \hat{b}_{j_2} - \hat{b}_{j_0} \,\middle|\, N_j[\hat{\mathbf{B}}] \right]^{-1}$$

where (j_0, j_1, j_2) are the local node indices of the jth triangle and $\hat{p}_i \in \hat{\mathbf{S}}$ resp. $\hat{b}_i \in \hat{\mathbf{B}}$.

A.4 Partial derivatives of constrained functionals

In this section we compute partial derivatives of the discrete regression functional (7.2.10), which is defined subject to a variational constraint. We focus on the formulation in the continuous, *i.e.* infinite dimensional, setup. For an analogous computation in the finite-dimensional, discrete setup, we refer to the appendix of [HRS$^+$16]. Note that the regression functional consists of a weighted sum of the (constrained) spline energy and a (simple) data term. Hence the following computations are in particular helpful to compute partial derivatives of the spline energy.

We define $\Psi = (\psi_0, \dots, \psi_K)$ and $\tilde{\Psi} = (\tilde{\psi}_1, \dots, \tilde{\psi}_{K-1})$, where $\tilde{\psi}_k = \tilde{\psi}_k[\psi_{k-1}, \psi_{k+1}]$. To keep things simple, we focus here on the original discrete regression functional (7.2.4), which reads

$$\mathcal{R}[\Psi, \tilde{\Psi}] = \sum_{k=0}^{K} \sum_{i=1}^{i_k} \mathcal{W}[\psi_k, \phi_k^i] + c \sum_{k=1}^{K-1} \mathcal{W}[\psi_k, \tilde{\psi}_k] \,,$$

$$\tilde{\psi}_k = \arg\min_{\psi} \mathcal{C}^k[\psi_{k-1}, \psi_{k+1}, \psi] \,, \quad k = 1, \dots, K-1 \,,$$

$$\mathcal{C}^k[\psi_{k-1}, \psi_{k+1}, \psi] = \mathcal{W}[\psi_{k-1}, \psi] + \mathcal{W}[\psi, \psi_{k+1}] \,.$$

The condition on the $\tilde{\psi}_k$ can locally be rewritten in terms of the corresponding optimality condition,

$$0 = \partial_\psi \mathcal{C}^k[\psi_{k-1}, \psi_{k+1}, \tilde{\psi}_k](\vartheta) = \partial_2 \mathcal{W}[\psi_{k-1}, \tilde{\psi}_k](\vartheta) + \partial_1 \mathcal{W}[\tilde{\psi}_k, \psi_{k+1}](\vartheta) \quad \forall \vartheta \,, \quad k = 1, \dots, K-1 \,.$$

Upon differentiation with respect to ψ_j, $j \in \{k-1, k+1\}$,

$$0 = \partial_{\psi_j} \partial_\psi \mathcal{C}^k[\psi_{k-1}, \psi_{k+1}, \tilde{\psi}_k](\vartheta, \theta) + \partial_\psi \partial_\psi \mathcal{C}^k[\psi_{k-1}, \psi_{k+1}, \tilde{\psi}_k](\vartheta, \partial_{\psi_j} \tilde{\psi}_k(\theta)) \quad \forall \vartheta, \theta \,.$$

Now choose p_k to solve

$$0 = c\,(\partial_{\tilde{\psi}_k} \mathcal{R})[\Psi, \tilde{\Psi}](\vartheta) + \partial_\psi \partial_\psi \mathcal{C}^k[\psi_{k-1}, \psi_{k+1}, \tilde{\psi}_k](p_k, \vartheta) \quad \forall \vartheta$$

$$= c\,(\partial_{\tilde{\psi}_k} \mathcal{R})[\Psi, \tilde{\Psi}](\vartheta) + \left(\partial_2^2 \mathcal{W}[\psi_{k-1}, \tilde{\psi}_k] + \partial_1^2 \mathcal{W}[\tilde{\psi}_k, \psi_{k+1}] \right)(p_k, \vartheta) \quad \forall \vartheta \,,$$

then the Gâteaux derivative of $\mathcal{R}$ with respect to ψ_k in some test direction ϑ is given by

$$\partial_{\psi_k} \left(\mathcal{R}[\Psi, \tilde{\Psi}] \right)(\vartheta) = (\partial_{\psi_k} \mathcal{R})[\Psi, \tilde{\Psi}](\vartheta) + c\,(\partial_{\tilde{\psi}_{k-1}} \mathcal{R})[\Psi, \tilde{\Psi}](\partial_{\psi_k} \tilde{\psi}_{k-1}(\vartheta))$$

$$+ c\,(\partial_{\tilde{\psi}_{k+1}} \mathcal{R})[\Psi, \tilde{\Psi}](\partial_{\psi_k} \tilde{\psi}_{k+1}(\vartheta))$$

$$= (\partial_{\psi_k} \mathcal{R})[\Psi, \tilde{\Psi}](\vartheta) - c\,\partial_\psi \partial_\psi \mathcal{C}^{k-1}[\psi_{k-2}, \psi_k, \tilde{\psi}_{k-1}](p_{k-1}, \partial_{\psi_k} \tilde{\psi}_{k-1}(\vartheta))$$

$$- c\,\partial_\psi \partial_\psi \mathcal{C}^{k+1}[\psi_k, \psi_{k+2}, \tilde{\psi}_{k+1}](p_{k+1}, \partial_{\psi_k} \tilde{\psi}_{k+1}(\vartheta))$$

$$= (\partial_{\psi_k} \mathcal{R})[\Psi, \tilde{\Psi}](\vartheta) + c\,\partial_{\psi_k} \partial_\psi \mathcal{C}^{k-1}[\psi_{k-2}, \psi_k, \tilde{\psi}_{k-1}](p_{k-1}, \vartheta)$$

$$+ c\,\partial_{\psi_k} \partial_\psi \mathcal{C}^{k+1}[\psi_k, \psi_{k+2}, \tilde{\psi}_{k+1}](p_{k+1}, \vartheta)$$

$$= (\partial_{\psi_k} \mathcal{R})[\Psi, \tilde{\Psi}](\vartheta) + c\,\partial_2 \partial_1 \mathcal{W}[\tilde{\psi}_{k-1}, \psi_k](p_{k-1}, \vartheta)$$

$$+ c\,\partial_1 \partial_2 \mathcal{W}[\psi_k, \tilde{\psi}_{k+1}](p_{k+1}, \vartheta) \,.$$

where

$$(\partial_{\psi_k} \mathcal{R})[\Psi, \tilde{\Psi}](\vartheta) = \sum_{i=1}^{i_k} \partial_1 \mathcal{W}[\psi_k, \phi_k^i](\vartheta) + c\,\partial_1 \mathcal{W}[\psi_k, \tilde{\psi}_k](\vartheta) \,.$$

A.5 Derivatives of discrete deformation energies

First derivatives for the Discrete Shells bending energy

Let $\mathbf{S} \in \mathbb{R}^{3n}$ be a discrete shell and $\tilde{\mathbf{S}} = \Phi(\mathbf{S})$. The *Discrete Shells* bending energy [GHDS03], as defined in (5.3.12), is given (up to a multiplicative constant) by

$$\tilde{\mathbf{W}}_{\text{bend}}[\mathbf{S}, \tilde{\mathbf{S}}] = \sum_{E \in \mathcal{E}} \frac{(\theta_E - \theta_{\Phi(E)})^2}{A_E} |E|^2$$

where $A_E = |T_1| + |T_2|$ if $E = T_1 \cap T_2$ and $\theta_E, \theta_{\Phi(E)}$ denote the dihedral angle at the undeformed and deformed edge, respectively. Furthermore, $A_{k,l}$ will denote the area of element $T_k = ijk$ and $T_l = jil$, respectively, $p_\iota \in \mathbb{R}^3$ will denote the vertex position for $\iota = i, j, k, l$. Using the notation in the figure on the right we have
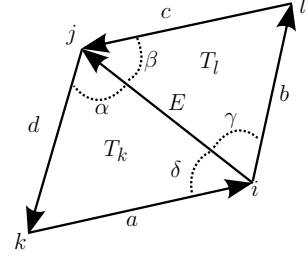
$$|E| = |p_j - p_i|\,,$$

$$A_k = |T_k| = \frac{1}{2}|d \times a|\,, \ A_l = |T_l| = \frac{1}{2}|b \times c|\,,$$

$$N_k = \frac{1}{2A_k} d \times a\,, \ N_l = \frac{1}{2A_l} b \times c\,.$$

When we differentiate $\tilde{\mathbf{W}}_{\text{bend}}$ with respect to nodal positions, we end up with differentiating the quatities above with respect to four vertices (namely i, j, k, l in local coordinates). We denote the variation of a quantity Q w.r.t. some node $p \in \{i, j, k, l\}$ by $\nabla_p Q \in \mathbb{R}^3$. Note that one distinguishes between two cases, namely i, j *vs.* k, l.

$$\nabla_j |E| = \frac{E}{|E|} \ \nabla_i |E| = -\frac{E}{|E|}\,, \ \nabla_k |E| = \nabla_l |E| = 0\,,$$

$$\nabla_k A_k = \frac{1}{2}(d \cot \delta - a \cot \alpha) = \frac{1}{2} N_k \times E\,,$$

$$\nabla_k \theta_E = -\frac{|E|}{2A_k} N_k\,, \ \nabla_l \theta_E = -\frac{|E|}{2A_l} N_l\,.$$

The further derivatives are are little bit more subtle, for derivations we refer to the appendix of [DMA02].

$$\nabla_i \theta_e = \frac{\cot \alpha}{|e|} N_k + \frac{\cot \beta}{|e|} N_l = \frac{|d| \cos \alpha}{2A_k} N_k + \frac{|c| \cos \beta}{2A_l} N_l = \frac{-e * d}{|e|^2}\left(-\nabla_k \theta_E\right) + \frac{e * c}{|e|^2}\left(-\nabla_l \theta_E\right)$$

$$\nabla_j \theta_e = \frac{\cot \delta}{|e|} N_k + \frac{\cot \gamma}{|e|} N_l = \frac{|a| \cos \delta}{2A_k} N_k + \frac{|b| \cos \gamma}{2A_l} N_l = \frac{-e * a}{|e|^2}\left(-\nabla_k \theta_E\right) + \frac{e * b}{|e|^2}\left(-\nabla_l \theta_E\right)$$

We finally write down the full derivatives with respect to the *undeformed* configuration:

$$\nabla_k \frac{(\theta_E - \tilde{\theta}_E)^2 |E|^2}{A_k + A_l} = 2(\theta_E - \tilde{\theta}_E)\frac{|E|^2}{A_l + A_k}\nabla_k \theta_E - \frac{(\theta_E - \tilde{\theta}_E)^2 |E|^2}{(A_k + A_l)^2}\nabla_k A_k$$

$$\nabla_l \frac{(\theta_E - \tilde{\theta}_E)^2 |E|^2}{A_k + A_l} = 2(\theta_E - \tilde{\theta}_E)\frac{|E|^2}{A_l + A_k}\nabla_l \theta_E - \frac{(\theta_E - \tilde{\theta}_E)^2 |E|^2}{(A_k + A_l)^2}\nabla_l A_l$$

$$\nabla_i \frac{(\theta_E - \tilde{\theta}_E)^2 |E|^2}{A_k + A_l} = 2(\theta_E - \tilde{\theta}_E)\frac{|E|^2}{A_l + A_k}\nabla_i \theta_E - \frac{(\theta_E - \tilde{\theta}_E)^2 |E|^2}{(A_k + A_l)^2}(\nabla_i A_k + \nabla_i A_l) - \frac{2(\theta_E - \tilde{\theta}_E)^2}{A_k + A_l}E$$

$$\nabla_j \frac{(\theta_E - \tilde{\theta}_E)^2 |E|^2}{A_k + A_l} = 2(\theta_E - \tilde{\theta}_E)\frac{|E|^2}{A_l + A_k}\nabla_j \theta_E - \frac{(\theta_E - \tilde{\theta}_E)^2 |E|^2}{(A_k + A_l)^2}(\nabla_j A_k + \nabla_j A_l) + \frac{2(\theta_E - \tilde{\theta}_E)^2}{A_k + A_l}E$$

where we have used the notation $\tilde{\theta}_E = \theta_{\Phi(E)}$. The derivatives with respect to the *deformed* configuration are given by the first term of each row multiplied by -1.

Second derivatives for the Discrete Shells bending energy

We will use the same notation as above: nodes related to one hinge (*i.e.* two triangles sharing one edge) are denoted by i, j, k, l. Note that $E = E(i, j)$, $\theta = \theta(i, j, k, l)$, $A_k = A_k(i, j, k)$ and $A_l = A_l(i, j, l)$. Furthermore we will use the following notation:

$$\mathcal{H}_E = \frac{(\Delta\theta)^2 |E|^2}{A}, \quad \Delta\theta := \theta_E - \tilde{\theta}_E, \qquad A := A_k + A_l \, ,$$

as well as $\varepsilon_i = -1$, $\varepsilon_j = 1$, $\varepsilon_k = \varepsilon_l = 0$. We will denote first derivatives with respect to some node $p \in \{i, j, k, l\}$ by ∇_p and second derivatives by $H_{qp} = \nabla_q \nabla_p$, where $q \in \{i, j, k, l\}$. Wherever a distinction is necessary, quantities with a tilde refer to variables living in the *deformed* domain $\tilde{\mathbf{S}}$, *e.g.* $\tilde{\theta}_E = \theta_{\Phi(E)}$. Likewise we write $\tilde{p}$ if we refer to some node living in the deformed doamin. According to results from above we have for $p \in \{i, j, k, l\}$:

$$\nabla_{\tilde{p}} \mathcal{H}_E = -2(\theta_E - \tilde{\theta}_E) \frac{|E|^2}{A} \nabla_{\tilde{p}} \theta_E = -2 \frac{\Delta\theta \, |E|^2}{A} \nabla_{\tilde{p}} \theta_E$$

and

$$\nabla_p \mathcal{H}_E = 2\Delta\theta \frac{|E|^2}{A} \nabla_p \theta_E - \frac{(\Delta\theta)^2}{A^2} |E|^2 \left(\nabla_p A_l + \nabla_p A_k\right) + \varepsilon_p 2 \frac{(\Delta\theta)^2}{A} E \, .$$

Writing $a \otimes b = ab^T$ for some vectors $a, b \in \mathbb{R}^3$, we obtain for $q \in \{i, j, k, l\}$:

$$\nabla_{\tilde{q}} \nabla_{\tilde{p}} \mathcal{H}_E = 2 \frac{|E|^2}{A} \left(\nabla_{\tilde{p}} \theta_E \otimes \nabla_{\tilde{q}} \theta_E - \Delta\theta \, \tilde{H}_{pq} \theta_E \right)$$

and

$$\begin{aligned}
\nabla_q \nabla_p \mathcal{H}_E = {} & 2 \, \nabla_p \theta_E \otimes \left[\frac{|E|^2}{A} \nabla_q \theta_E - \frac{|E|^2 \Delta\theta}{A^2} \left(\nabla_q A_l + \nabla_q A_k\right) + \varepsilon_q 2 \frac{\Delta\theta}{A} E \right] + 2 \frac{|E|^2 \Delta\theta}{A} H_{pq} \theta_E \\
& - \left(\nabla_p A_l + \nabla_p A_k\right) \otimes \left[2 \frac{|E|^2 \Delta\theta}{A^2} \nabla_q \theta_E - 2 \frac{|E|^2 (\Delta\theta)^2}{A^3} \left(\nabla_q A_l + \nabla_q A_k\right) + \varepsilon_q 2 \frac{(\Delta\theta)^2}{A^2} E \right] \\
& - \frac{|E|^2 (\Delta\theta)^2}{A^2} \left(H_{pq} A_l + H_{pq} A_k \right) \\
& + 2 \, \varepsilon_p E \otimes \left[2 \frac{\Delta\theta}{A} \nabla_q \theta_E - \frac{(\Delta\theta)^2}{A^2} \left(\nabla_q A_l + \nabla_q A_k\right) \right] + 2 \, \varepsilon_p \frac{(\Delta\theta)^2}{A} D_q E
\end{aligned}$$

as well as

$$\nabla_q \nabla_{\tilde{p}} \mathcal{H}_E = -\frac{2}{A} \nabla_{\tilde{p}} \theta_E \otimes \left[|E|^2 \nabla_q \theta_E - \frac{\Delta\theta}{A_k + A_l} \left(\nabla_q A_k + \nabla_q A_l\right) + 2 \, \Delta\theta \, \varepsilon_q E \right] ,$$

and

$$\nabla_{\tilde{q}} \nabla_p \mathcal{H}_E = -\frac{2}{A} \left[|E|^2 \nabla_p \theta_E - \frac{\Delta\theta}{A_k + A_l} \left(\nabla_p A_k + \nabla_p A_l\right) + 2 \, \Delta\theta \, \varepsilon_p E \right] \otimes \nabla_{\tilde{q}} \theta_E \, .$$

Remarks: We have to be careful when commuting the operators ∇_p and $\nabla_{\tilde{q}}$ as the $\otimes$-operator is not symmetric. An easy example is given by $f : \mathbb{R}^n \times \mathbb{R}^n \to \mathbb{R}$, $f : (x, y) \mapsto \frac{1}{4} |x|^2 \cdot |y|^2$. Then $\nabla_x \nabla_y f(x, y) = y \otimes x \neq x \otimes y = \nabla_y \nabla_x f(x, y)$. But obviously

$$\nabla_q \nabla_{\tilde{p}} \mathcal{H}_E = (\nabla_{\tilde{p}} \nabla_q \mathcal{H}_E)^T, \quad \nabla_{\tilde{q}} \nabla_{\tilde{p}} \mathcal{H}_E = (\nabla_{\tilde{p}} \nabla_{\tilde{q}} \mathcal{H}_E)^T \quad \nabla_q \nabla_p \mathcal{H}_E = (\nabla_p \nabla_q \mathcal{H}_E)^T \, .$$

Let $f : \mathbb{R}^3 \to \mathbb{R}$ be a scalar valued function and $n = (n_1, n_2, n_3)^T : \mathbb{R}^3 \to \mathbb{R}^3$ be a vector field. Then:

$$D(f(x) \cdot n(x)) = n(x) \otimes \nabla f(x) + f(x) \cdot Dn(x) \ \in \mathbb{R}^{3,3} \, .$$

Here and in what follows we will write D for the Jacobian and ∇ for the gradient, *i.e.* $\nabla f = (Df)^T$.

Geometric derivatives

Here we compute $H_{pq}\theta_e, H_{pq}A_r, D_q E \in \mathbb{R}^{3,3}$ for $r \in \{k,l\}$ and $p,q \in \{i,j,k,l\}$. We define

$$N := N_T := \frac{E_k \times E_i}{|E_k \times E_i|} = \frac{E_i \times E_j}{|E_i \times E_j|} = \frac{E_j \times E_k}{|E_j \times E_k|},$$

where $E_p = X_{p+1} - X_{p-1}$ is the edge opposite node X_p in T and

$$A := |T| = \frac{|E_k \times E_i|}{2} = \frac{|E_i \times E_j|}{2} = \frac{|E_j \times E_k|}{2}.$$

For some $f : \mathbb{R}^n \to \mathbb{R}^n$ and $g := |.| : \mathbb{R}^n \to \mathbb{R}$ we have $\nabla|f(x)| \in \mathbb{R}^n$, *i.e.* the chain rule implies

$$\nabla|f(x)| = \Big(D(g \circ f)(x)\Big)^T = \Big(Dg\big(f(x)\big)Df(x)\Big)^T = \Big((\nabla g)^T \big(f(x)\big)Df(x)\Big)^T = \Big(\frac{f(x)^T}{|f(x)|}Df(x)\Big)^T.$$

Hence we obtain for $\nabla_p A = \frac{1}{2}\nabla_p|E_k \times E_i|$:

$$\nabla_p A = \frac{1}{2}\Big(\frac{(E_k \times E_i)^T}{|E_k \times E_i|}\underbrace{\big((\nabla_p E_k) \times E_i + E_k \times (\nabla_p E_i)\big)}_{=E_p\times}\Big)^T$$

$$= \frac{1}{2}(-E_p) \times N = \frac{1}{2}N \times E_p.$$

For $a, b \in \mathbb{R}^3$ we define $a\times : b \mapsto a \times b$, *i.e.* $a\times$ is a skew-symmetric 3×3-matrix, $P_a : b \mapsto (\mathrm{id} - a \otimes a)b$ is a projection map and $R_a : b \mapsto (\mathrm{id} - 2a \otimes a)b$ is a reflection map. Then

$$D_p N = D_p\Big(|E_k \times E_i|^{-1}(E_k \times E_i)\Big) = -|E_k \times E_i|^{-2}(E_k \times E_i) \otimes (N \times E_p) + |E_k \times E_i|^{-1}E_p\times$$

$$= |E_k \times E_i|^{-1}\Big(-(N \otimes N)E_p \times + E_p \times\Big) = \frac{1}{2A}(\mathrm{id} - N \otimes N)E_p\times =: (2A)^{-1}P_N\, E_p\times,$$

where we have used that $a \otimes (a \times b) = -a(b \times a)^T = aa^T b\times = (a \otimes a)b\times$. We can deduce

$$D_p(A^{-1}N) = -A^{-2}N \otimes \nabla_p A + A^{-1}D_p N$$

$$= \frac{-A^{-2}}{2}\underbrace{N \otimes (N \times E_p)}_{N\otimes N\, E_p\times} + A^{-1}\big((2A)^{-1}\underbrace{P_N}_{\mathrm{id} - N\otimes N}\, E_p \times\big)$$

$$= \frac{1}{2A^2}(\mathrm{id} - 2N \otimes N)E_p\times =: \frac{1}{2A^2}R_N\, E_p \times.$$

Next we compute second derivatives H_{pq} of dihedral angles θ_e w.r.t. nodes $p,q \in \{i,j,k,l\}$. Recall:

$$\nabla_k \theta_E = -\frac{|E|}{2A_k}N_k, \quad \nabla_l \theta_E = -\frac{|E|}{2A_l}N_l.$$

With the calculations for $\nabla_p(A^{-1}N) = (D_p(A^{-1}N))^T$ above we get

$$H_{kk}\theta_E = -\frac{|E|}{2}\nabla_k(A_k^{-1}N_k) = -\frac{|E|}{(2A_k)^2}\big(R_{N_k}(E\times)\big)^T,$$

$$H_{ll}\theta_E = -\frac{|E|}{2}\nabla_l(A_l^{-1}N_l) = -\frac{|E|}{(2A_l)^2}\big(R_{N_l}(-E\times)\big)^T,$$

and obviously $H_{kl} = H_{lk} = 0$. In the implementation we used $-\big(R_{N_k}(E\times)\big)^T = (E\times) + 4\,\nabla_k A \otimes N_k$.

Recall further

$$\nabla_i \theta_E = \frac{\cot \alpha}{|E|} N_k + \frac{\cot \beta}{|E|} N_l \;=\; \frac{|d| \cos \alpha}{2A_k} N_k + \frac{|c| \cos \beta}{2A_l} N_l \;=\; \frac{-E * d}{|E|^2} \big(-\nabla_k \theta_E \big) + \frac{E * c}{|E|^2} \big(-\nabla_l \theta_E \big)$$

$$= \frac{-E * d}{|E|^2} \Big(\frac{|E|}{2A_k} N_k \Big) + \frac{E * c}{|E|^2} \Big(\frac{|E|}{2A_l} N_l \Big) = \frac{-E * d}{2|E|} \Big(A_k^{-1} N_k \Big) + \frac{E * c}{2|E|} \Big(A_l^{-1} N_l \Big)$$

and

$$\nabla_j \theta_E = \frac{\cot \delta}{|E|} N_k + \frac{\cot \gamma}{|E|} N_l \;=\; \frac{|a| \cos \delta}{2A_k} N_k + \frac{|b| \cos \gamma}{2A_l} N_l \;=\; \frac{-E * a}{|E|^2} \big(-\nabla_k \theta_E \big) + \frac{E * b}{|E|^2} \big(-\nabla_l \theta_E \big)$$

$$= \frac{-E * a}{|E|^2} \Big(\frac{|E|}{2A_k} N_k \Big) + \frac{E * b}{|E|^2} \Big(\frac{|E|}{2A_l} N_l \Big) = \frac{-E * a}{2|E|} \Big(A_k^{-1} N_k \Big) + \frac{E * b}{2|E|} \Big(A_l^{-1} N_l \Big).$$

Hence

$$H_{ik} \theta_E = \frac{1}{2} (A_k^{-1} N_k) \otimes \frac{-E}{|E|} - \frac{|E|}{2} D_i (A_k^{-1} N_k) = \frac{-1}{2A_k |E|} (N_k \otimes E) + \frac{E * d}{|E|^2} H_{kk} \theta_E,$$

$$H_{jk} \theta_E = \frac{1}{2} (A_k^{-1} N_k) \otimes \frac{E}{|E|} - \frac{|E|}{2} D_j (A_k^{-1} N_k) = \frac{1}{2A_k |E|} (N_k \otimes E) + \frac{E * a}{|E|^2} H_{kk} \theta_E,$$

$$H_{il} \theta_E = \frac{1}{2} (A_l^{-1} N_l) \otimes \frac{-E}{|E|} - \frac{|E|}{2} D_i (A_l^{-1} N_l) = \frac{-1}{2A_l |E|} (N_l \otimes E) - \frac{E * c}{|E|^2} H_{ll} \theta_E,$$

$$H_{jl} \theta_E = \frac{1}{2} (A_l^{-1} N_l) \otimes \frac{E}{|E|} - \frac{|E|}{2} D_j (A_l^{-1} N_l) = \frac{1}{2A_l |E|} (N_l \otimes E) - \frac{E * b}{|E|^2} H_{ll} \theta_E,$$

and

$$H_{ii} \theta_E = \nabla_i \Big(|E|^{-2} \big((E * d) \nabla_k \theta_E - (E * c) \nabla_l \theta_E \big) \Big)$$

$$= -\frac{2}{|E|^3} \big((E * d) \nabla_k \theta_E - (E * c) \nabla_l \theta_E \big) \otimes \frac{-E}{|E|}$$

$$+ |E|^{-2} \Big[\nabla_k \theta_E \otimes \underbrace{\nabla_i (E * d)}_{= -d} + (E * d) H_{ik} \theta_E - \nabla_l \theta_E \otimes \underbrace{\nabla_i (E * c)}_{= -c} - (E * c) H_{il} \theta_E \Big]$$

$$= |E|^{-2} \Big[2 \nabla_i \theta_E \otimes E - \nabla_k \theta_E \otimes d + \nabla_l \theta_E \otimes c + (E * d) H_{ik} \theta_E - (E * c) H_{il} \theta_E \Big],$$

and

$$H_{jj} \theta_E = \nabla_j \Big(|E|^{-2} \big((E * a) \nabla_k \theta_E - (E * b) \nabla_l \theta_E \big) \Big)$$

$$= -\frac{2}{|E|^3} \big((E * a) \nabla_k \theta_E - (E * b) \nabla_l \theta_E \big) \otimes \frac{E}{|E|}$$

$$+ |E|^{-2} \Big[\nabla_k \theta_E \otimes \underbrace{\nabla_j (E * a)}_{= a} + (E * a) H_{jk} \theta_E - \nabla_l \theta_E \otimes \underbrace{\nabla_j (E * b)}_{= b} - (E * b) H_{jl} \theta_E \Big]$$

$$= |E|^{-2} \Big[-2 \nabla_j \theta_E \otimes E + \nabla_k \theta_E \otimes a - \nabla_l \theta_E \otimes b + (E * a) H_{jk} \theta_E - (E * b) H_{jl} \theta_E \Big],$$

and

$$H_{ji} \theta_E = \nabla_j \Big(|E|^{-2} \big((E * d) \nabla_k \theta_E - (E * c) \nabla_l \theta_E \big) \Big)$$

$$= -\frac{2}{|E|^3} \big((E * d) \nabla_k \theta_E - (E * c) \nabla_l \theta_E \big) \otimes \frac{E}{|E|}$$

$$+ |E|^{-2} \Big[\nabla_k \theta_E \otimes \underbrace{\nabla_j (E * d)}_{= d - E} + (E * d) H_{jk} \theta_E - \nabla_l \theta_E \otimes \underbrace{\nabla_j (E * c)}_{= c + E} - (E * c) H_{jl} \theta_E \Big]$$

$$= |E|^{-2} \Big[-2 \nabla_i \theta_E \otimes E + \nabla_k \theta_E \otimes (d - E) - \nabla_l \theta_E \otimes (c + E) + (E * d) H_{jk} \theta_E - (E * c) H_{jl} \theta_E \Big].$$

We further have $H_{ki} = H_{ik}$, $H_{kj} = H_{jk}$, $H_{li} = H_{il}$, $H_{lj} = H_{jl}$ and $H_{ij} = H_{ji}$.

Remark on the calculation of dihedral angles: For every edge E we have to calculate the dihedral angle, *i.e.* the angle from N_k to N_l. We use the formula $a \times b = |a|\,|b|\,\sin(\sphericalangle(a,b))\frac{a \times b}{|a \times b|}$, thus we obtain

$$\theta_E = \sin^{-1}\left((N_k \times N_l) \cdot \frac{E}{|E|}\right).$$

Derivatives for the membrane energy

Let $\mathcal{S} \subset \mathbb{R}^3$ be an embedded surface, parametrized by the mapping $x : \omega \subset \mathbb{R}^2 \to \mathbb{R}^3$. In the discrete setting, $\mathcal{S}$ is replaced by a triangle mesh $\mathbf{S}$ and ω is replaced by a topological reference mesh $\Omega \subset \mathbb{R}^2$. On the one hand, Ω inherits the connectivity from the mesh $\mathbf{S}$ appoximating the hypersurface $\mathcal{S}$. On the other hand, Ω consists of unit triangles only, as it solely prescribes the topology. A local parametrization of a triangle $T_i \subset \mathbf{S}$ over the unit triangle is given by X_{T_i}, a global paramtrization is a collection of local parametrizations, *i.e.* $X = (X_i)_i : \Omega \to \mathbf{S}$.
When we assume that the integrand f is constant on elements, *i.e.* $f = (f_T)_{T \in \mathcal{T}}$, we have

$$\int_{\mathbf{S}} f\,\mathrm{d}a = \int_{\Omega} f(X(\xi))\sqrt{\det G(\xi)}\,\mathrm{d}\xi = \frac{1}{2}\sum_{T \in \mathcal{T}} f_T \sqrt{\det G_T}\,,$$

where the discrete first fundamental form is also constant on faces, *i.e.* $G_T = DX_T^T DX_T$. The factor $\frac{1}{2}$ represents the area of a single unit triangle. For a (discrete) variation Ψ of the (discrete) parametrization X we write $\Psi = (\Psi_1, \Psi_2, \Psi_3) : \Omega \to \mathbb{R}^3$, *i.e.* $\nabla\Psi_i \in \mathbb{R}^2$ and $D\Psi \in \mathbb{R}^{3,2}$. According to the interface functions provided in the QuocMesh library, we long for a representation

$$\partial_X\left(\int_{\mathbf{S}} f\,\mathrm{d}a\right)(\Psi) = \frac{1}{2}\sum_{T \in \mathcal{T}} \partial_X\left(f_T\sqrt{\det g|_T}\right)(\Psi) = \frac{1}{2}\sum_{T} A\big|_T : D\Psi \tag{A.5.1}$$

for the first variation and

$$\partial_X^2\left(\int_{\mathbf{S}} f\,\mathrm{d}a\right)(\Psi, \Phi) = \frac{1}{2}\sum_{T \in \mathcal{T}} \partial_X^2\left(f_T\sqrt{\det g|_T}\right)(\Psi, \Phi)$$

$$= \frac{1}{2}\sum_{T \in \mathcal{T}}\left(\mathrm{tr}\,(A_1 D\Phi A_2 D\Psi) + \mathrm{tr}\,(A_3 D\Phi^T A_4 D\Psi) + \mathrm{tr}\,(A_5 D\Phi)\mathrm{tr}\,(A_6 D\Psi)\right)$$

for the second variation, with some matrices $A, A_3 \in \mathbb{R}^{3,2}$ and $A_i \in \mathbb{R}^{2,3}$ for $i \neq 3$, that have to be computed in derived classes.

However, whren computing variations it is more convenient to start in the continuous setup. We consider two surfaces $\mathcal{S}_1, \mathcal{S}_2$ being parametrized via $x_{1,2} : \omega \to \mathbb{R}^3$, the membrane energy is defined by

$$\mathcal{W}_{\mathrm{mem}}[\mathcal{S}_1, \mathcal{S}_2] := \int_{\mathcal{S}_1} W_{\mathrm{mem}}(g_1^{-1} g_2)\,\mathrm{d}x$$

with

$$W_{\mathrm{mem}}(A) := \frac{\mu}{2}\mathrm{tr}\,A + \frac{\lambda}{4}\det A - \left(\frac{\mu}{2} + \frac{\lambda}{4}\right)\log\det A - \mu - \frac{\lambda}{4}\,.$$

We define $\mathcal{G} := g_1^{-1} g_2$, with $g_{1,2}$ denoting first fundamental forms, and $\alpha := \frac{\lambda}{2}\det\mathcal{G} - \mu - \frac{\lambda}{2}$. For a continuous variation $\psi : \omega \to \mathbb{R}^3$ of x_2 resp. x_1 we obtain

$$\partial_{x_2}\mathcal{W}_{\mathrm{mem}}[\mathcal{S}_1, \mathcal{S}_2](\psi) = \int_{\omega} \underbrace{Dx_2\left(\mu g_1^{-1} + \alpha g_2^{-1}\right)\sqrt{\det g_1}}_{=A \in \mathbb{R}^{3,2}} : D\psi\,\mathrm{d}\xi \tag{A.5.2}$$

and

$$\partial_{x_1}\mathcal{W}_{\mathrm{mem}}[\mathcal{S}_1, \mathcal{S}_2](\psi) = \int_\omega \underbrace{-Dx_1\left(\mu g_1^{-1}g_2g_1^{-1} + \left(\alpha - W(\mathcal{G})\right)g_1^{-1}\right)\sqrt{\det g_1}}_{=A\in\mathbb{R}^{3,2}} : D\psi \, d\xi \,. \qquad (A.5.3)$$

Note that in the discrete setup, the matrix-valued function A is constant on triangles, *i.e.* we obtain $A = (A_T)_T$, which can be plugged into (A.5.1).

For the second variations we consider another continuous variation $\phi : \omega \to \mathbb{R}^3$. We make use of the notation $\partial_{x_i}g_i(\phi) = D\phi^T Dx_i + Dx_i^T D\phi$, as well as

$$d_1W = \mu\mathcal{G} + \left(\alpha - W(\mathcal{G})\right)\mathbb{1}\,, \qquad d_2W = \mu g_1^{-1} + \alpha g_2^{-1}\,.$$

First, we compute $\partial_{x_2}\partial_{x_2}\mathcal{W}_{\mathrm{mem}}[\mathcal{S}_1, \mathcal{S}_2](\phi, \psi)$. Differentiating the integrand of (A.5.2) yields:

$$\partial_{x_2}\Big[Dx_2d_2W : D\psi\Big](\phi) = D\phi d_2W : D\psi + Dx_2\left[\left(\frac{\lambda}{2}\det\mathcal{G}\, g_1g_2^{-1} : g_1^{-1}\big(\partial_2 g_2(\phi)\big)\right)g_2^{-1} - \alpha g_2^{-1}\big(\partial_2 g_2(\phi)\big)g_2^{-1}\right] : D\psi$$

$$= \mathrm{tr}\left(D\psi^T\mathbb{1}D\phi d_2W\right) + \frac{\lambda}{2}\det\mathcal{G}\left(g_2^{-1} : \big(D\phi^T Dx_2 + Dx_2^T D\phi\big)\right)Dx_2\, g_2^{-1} : D\psi$$
$$- \alpha\left[Dx_2 g_2^{-1}\big(D\phi^T Dx_2 + Dx_2^T D\phi\big)g_2^{-1}\right] : D\psi$$

$$= \mathrm{tr}\left(d_2WD\phi^T\mathbb{1}D\psi\right) + \lambda\det\mathcal{G}\,\mathrm{tr}\left(g_2^{-1}Dx_2^T D\phi\right)\cdot\mathrm{tr}\left(g_2^{-1}Dx_2^T D\psi\right)$$
$$- \alpha\mathrm{tr}\left(D\psi^T Dx_2 g_2^{-1}D\phi^T Dx_2 g_2^{-1}\right) - \alpha\mathrm{tr}\left(D\psi^T Dx_2 g_2^{-1}Dx_2^T D\phi g_2^{-1}\right)$$

$$= \mathrm{tr}\left(d_2WD\phi^T\mathbb{1}D\psi\right) + \lambda\det\mathcal{G}\,\mathrm{tr}\left(AD\phi\right)\cdot\mathrm{tr}\left(AD\psi\right)$$
$$- \alpha\mathrm{tr}\left(AD\phi AD\psi\right) - \alpha\mathrm{tr}\left(g_2^{-1}D\phi^T BD\psi\right)$$

where $A := g_2^{-1}Dx_2^T \in \mathbb{R}^{2,3}$ and $B := Dx_2 g_2^{-1}Dx_2^T \in \mathbb{R}^{3,3}$.

Next, we compute $\partial_{x_1}\partial_{x_1}\mathcal{W}_{\mathrm{mem}}[\mathcal{S}_1, \mathcal{S}_2](\phi, \psi)$, *i.e.* we differentiate the integrand of (A.5.3). Using

$$I_1 := -\sqrt{\det g_1}\left(Dx_1 d_1W g_1^{-1}\right)$$

we obtain:

$$\partial_{x_1}\Big[I_1 : D\psi\Big](\phi) = -\frac{1}{2}\sqrt{\det g_1}\left(g_1^{-1} : \partial_{x_1}g_1(\phi)\right)\left(Dx_1 d_1W g_1^{-1} : D\psi\right) - \sqrt{\det g_1}D\phi d_1W g_1^{-1} : D\psi$$
$$- \sqrt{\det g_1}\,Dx_1\left(\partial_{x_1}d_1W\right)(\phi)\,g_1^{-1} : D\psi + \sqrt{\det g_1}\,Dx_1\, d_1W\, g_1^{-1}\partial_{x_1}g_1(\phi)\,g_1^{-1} : D\psi\,.$$

We define $A := g_1^{-1}$ and $B = d_1W\, g_1^{-1}$. Furthermore, we introduce the notation $M_r := MDx_1^T$, $M_l := Dx_1 M$ and $M_{lr} := Dx_1 M Dx_1^T$ for matrices $M \in \mathbb{R}^{2,2}$. We get

$$(\det g_1)^{-\frac{1}{2}}\partial_{x_1}\Big[I_1 : D\psi\Big](\phi) = -\mathrm{tr}\left(A_r D\phi\right)\mathrm{tr}\left(B_r D\psi\right) - \mathrm{tr}\left(g_1^{-1}(d_1W)^T D\phi^T\mathbb{1}D\psi\right) - Dx_1\left(\partial_{x_1}d_1W\right)(\phi)\,g_1^{-1} : D\psi$$
$$+ \mathrm{tr}\left(D\psi^T Dx_1\, d_1W\, g_1^{-1}D\phi^T Dx_1\, g_1^{-1}\right) + \mathrm{tr}\left(D\psi^T Dx_1\, d_1W\, g_1^{-1}Dx_1^T D\phi\, g_1^{-1}\right)$$

$$= \mathrm{tr}\left(A_r D\phi\right)\mathrm{tr}\left(B_r D\psi\right) + \mathrm{tr}\left(B^T D\phi^T\mathbb{1}D\psi\right) + Dx_1\left(\partial_{x_1}d_1W\right)(\phi)\,g_1^{-1} : D\psi$$
$$- \mathrm{tr}\left(A_r D\phi B_l^T D\psi\right) - \mathrm{tr}\left(AD\phi^T B_{lr}^T D\psi\right)\,,$$

where

$$\partial_{x_1} d_1 W(\phi) = - \mu g_1^{-1} \partial_{x_1} g_1(\phi) \, g_1^{-1} g_2 - \left(\frac{\lambda \det \mathcal{G}}{2} g_1 g_2^{-1} : g_1^{-1} \partial_{x_1} g_1(\phi) \, g_1^{-1} g_2 \right) \mathbb{1}$$

$$- \left(-\frac{\mu}{2} \mathbb{1} : g_1^{-1} \partial_{x_1} g_1(\phi) \, g_1^{-1} g_2 - \left(\frac{\lambda}{4} \det \mathcal{G} - \frac{\mu}{2} - \frac{\lambda}{4} \right) g_1 g_2^{-1} : g_1^{-1} \partial_{x_1} g_1(\phi) \, g_1^{-1} g_2 \right) \mathbb{1}$$

$$= - \mu g_1^{-1} D\phi^T Dx_1 \, \mathcal{G} - \mu g_1^{-1} Dx_1^T D\phi \, \mathcal{G} - \lambda \det \mathcal{G} \mathrm{tr} \left(D\phi^T Dx_1 g_1^{-1} \right) \mathbb{1}$$

$$+ \frac{\mu}{2} \left[\mathrm{tr} \left(g_1^{-1} D\phi^T Dx_1 g_1^{-1} g_2 \right) + \mathrm{tr} \left(g_1^{-1} Dx_1^T D\phi g_1^{-1} g_2 \right) \right] \mathbb{1}$$

$$+ \left(\frac{\lambda}{2} \det \mathcal{G} - \mu - \frac{\lambda}{2} \right) \mathrm{tr} \left(Dx_1^T D\phi g_1^{-1} \right) \mathbb{1}$$

$$= - \mu g_1^{-1} D\phi^T Dx_1 \, \mathcal{G} - \mu g_1^{-1} Dx_1^T D\phi \, \mathcal{G}$$

$$+ \mu \mathrm{tr} \left(g_1^{-1} g_2 g_1^{-1} Dx_1^T D\phi \right) \mathbb{1} - \beta \mathrm{tr} \left(A_r D\phi \right) \mathbb{1} \, .$$

where $\beta = \frac{\lambda}{2} \det \mathcal{G} + \mu + \frac{\lambda}{2}$. Hence, with $C = g_1^{-1} g_2 g_1^{-1}$ we get

$$Dx_1 \left(\partial_{x_1} d_1 W \right)(\phi) \, g_1^{-1} : D\psi = - \mu \mathrm{tr} \left(D\psi^T Dx_1 g_1^{-1} D\phi^T Dx_1 \, g_1^{-1} g_2 g_1^{-1} \right)$$

$$- \mu \mathrm{tr} \left(D\psi^T Dx_1 g_1^{-1} Dx_1^T D\phi \, g_1^{-1} g_2 g_1^{-1} \right)$$

$$+ \mu \mathrm{tr} \left(C_r D\phi \right) \mathrm{tr} \left(A_r D\psi \right) - \beta \mathrm{tr} \left(A_r D\phi \right) \mathrm{tr} \left(A_r D\psi \right)$$

$$= - \mu \mathrm{tr} \left(C_r D\phi A_r D\psi \right) - \mu \mathrm{tr} \left(C D\phi^T A_{lr} D\psi \right)$$

$$+ \mu \mathrm{tr} \left(C_r D\phi \right) \mathrm{tr} \left(A_r D\psi \right) - \beta \mathrm{tr} \left(A_r D\phi \right) \mathrm{tr} \left(A_r D\psi \right)$$

and

$$(\det g_1)^{-\frac{1}{2}} \partial_{x_1} \left[I_1 : D\psi \right](\phi) = - \mathrm{tr} \left(A_r D\phi \right) \mathrm{tr} \left(B_r D\psi \right) - \mathrm{tr} \left(B^T D\phi^T \mathbb{1} D\psi \right) + \mu \mathrm{tr} \left(C_r D\phi A_r D\psi \right)$$

$$+ \mu \mathrm{tr} \left(C D\phi^T A_{lr} D\psi \right) - \mu \mathrm{tr} \left(C_r D\phi \right) \mathrm{tr} \left(A_r D\psi \right) + \beta \mathrm{tr} \left(A_r D\phi \right) \mathrm{tr} \left(A_r D\psi \right)$$

$$+ \mathrm{tr} \left(A_r D\phi B_l^T D\psi \right) + \mathrm{tr} \left(A D\phi^T B_{lr}^T D\psi \right) \, .$$

Finally, we compute the mixed derivative $\partial_{x_2} \partial_{x_1} \mathcal{W}_{\mathrm{mem}} [\mathcal{S}_1, \mathcal{S}_2](\phi, \psi)$ and obtain:

$$Dx_1 \, \partial_{x_2} (d_1 W)(\phi) \, g_1^{-1} : D\psi = \mu \, \mathrm{tr} \left(Dx_1 g_1^{-1} (D\phi^T Dx_2 + Dx_2^T D\phi) g_1^{-1} D\psi^T \right)$$

$$+ \partial_{x_2} \left(\frac{\lambda}{2} \det \mathcal{G} - W(\mathcal{G}) \right)(\phi) \cdot \mathrm{tr} \left(Dx_1 g_1^{-1} D\psi^T \right)$$

$$= \mu \, \mathrm{tr} \left(\underbrace{g_1^{-1} Dx_2^T}_{=:A_2} D\phi \underbrace{g_1^{-1} Dx_1^T}_{=:A_1} D\psi \right) + \mu \, \mathrm{tr} \left(\underbrace{g_1^{-1}}_{=:A} D\phi^T \underbrace{Dx_2 g_1^{-1} Dx_1^T}_{B} D\psi \right)$$

$$- \partial_{x_2} \left(W(\mathcal{G}) - \frac{\lambda}{2} \det \mathcal{G} \right)(\phi) \cdot \mathrm{tr} \left(\underbrace{g_1^{-1} Dx_1^T}_{=:A_1} D\psi \right) \, ,$$

where

$$\partial_{x_2} \left(W(\mathcal{G}) - \frac{\lambda}{2} \det \mathcal{G} \right)(\phi) = Dx_2 (\mu g_1^{-1} + \alpha g_2^{-1}) : D\phi - \frac{\lambda}{2} \det \mathcal{G} \cdot g_1 g_2^{-1} : g_1^{-1} (D\phi^T Dx_2 + Dx_2^T D\phi)$$

$$= \mathrm{tr} \left(\left(\mu g_1^{-1} + \left(\frac{\lambda}{2} \det \mathcal{G} - \mu - \frac{\lambda}{2} \right) g_2^{-1} \right) Dx_2^T D\phi \right) - \lambda \det \mathcal{G} \mathrm{tr} \left(g_2^{-1} Dx_2^T D\phi \right)$$

$$= \mathrm{tr} \left(\left(\mu g_1^{-1} - \underbrace{\left(\frac{\lambda}{2} \det \mathcal{G} + \mu + \frac{\lambda}{2} \right)}_{=\beta} g_2^{-1} \right) Dx_2^T D\phi \right) \, .$$

Hence with $A = g_1^{-1}$, $A_j = ADx_j^T$, $B = Dx_2 g_1^{-1} Dx_1^T$ and $C = (\mu g_1^{-1} - \beta g_2^{-1}) Dx_2^T$:

$$-Dx_1 \, \partial_{x_2} d_1 W(\phi) \, g_1^{-1} : D\psi = -\mu \mathrm{tr}\left(A_2 D\phi A_1 D\psi\right) - \mu \mathrm{tr}\left(AD\phi^T BD\psi\right) + \mathrm{tr}\left(CD\phi\right) \cdot \mathrm{tr}\left(A_1 D\psi\right).$$

To use the interfaces in the QuocMesh library we need some matrix expressions (with $m = 2$ and $n = 3$). Assume $\phi, \psi : \mathbb{R}^m \to \mathbb{R}^n$ are differentiable functions with $\phi = (\phi^1, \ldots, \phi^n)$ and $D\phi^T = [\nabla\phi^1|\ldots|\nabla\phi^n] \in \mathbb{R}^{m,n}$, where $\nabla\phi^i = (D\phi_{ij})_j \in \mathbb{R}^m$. Let $A, B \in \mathbb{R}^{m,n}$ with $A = (A_{ij})_{ij} = [a_1|\ldots|a_n]$ and $B = (B_{ij})_{ij} = [b_1|\ldots|b_n]$. Then we have:

$$
\begin{aligned}
\mathrm{tr}\left(AD\phi BD\psi\right) &= \sum_i (AD\phi BD\psi)_{ii} = \sum_{i,j,k,l} A_{ij} D\phi_{jk} B_{kl} D\psi_{li} = \sum_{i,j,k,l} D\psi_{li} A_{ij} \cdot D\phi_{jk} B_{kl} \\
&= \sum_{j,l} (\nabla\psi^l)^T a_j \cdot (\nabla\phi^j)^T b_l = \sum_{j,l} (\nabla\psi^l)^T a_j b_l^T \nabla\phi^j = \sum_{k,l} (\nabla\psi^l)^T a_k b_l^T \nabla\phi^k \\
&= \sum_{k,l=1}^n \underbrace{a_k b_l^T}_{\in \mathbb{R}^{m,m}} \nabla\phi^k \cdot \nabla\psi^l,
\end{aligned}
$$

$$
\begin{aligned}
\mathrm{tr}\left(AD\phi\right)\mathrm{tr}\left(BD\psi\right) &= \sum_{i,j} A_{ij} D\phi_{ji} \cdot \sum_{k,l} B_{kl} D\psi_{lk} = \sum_{i,j,k,l} A_{ij} D\phi_{ji} B_{kl} D\psi_{lk} = \sum_{i,j,k,l} D\psi_{lk} B_{kl} \cdot D\phi_{ji} A_{ij} \\
&= \sum_{j,l} (\nabla\psi^l)^T b_l \cdot (\nabla\phi^j)^T a_j = \sum_{j,l} (\nabla\psi^l)^T b_l a_j^T \nabla\phi^j = \sum_{k,l} (\nabla\psi^l)^T b_l a_k^T \nabla\phi^k \\
&= \sum_{k,l=1}^n \underbrace{b_l a_k^T}_{\in \mathbb{R}^{m,m}} \nabla\phi^k \cdot \nabla\psi^l.
\end{aligned}
$$

Let $A \in \mathbb{R}^{m,m}$ and $B \in \mathbb{R}^{n,n}$ with $A = (A_{ij})_{ij} = [a_1|\ldots|a_m]$ and $B = (B_{ij})_{ij}$. Then we have:

$$
\begin{aligned}
\mathrm{tr}\left(AD\phi^T BD\psi\right) &= \sum_i (AD\phi^T BD\psi)_{ii} = \sum_{i,j,k,l} A_{ij} D\phi_{kj} B_{kl} D\psi_{li} = \sum_{i,j,k,l} D\psi_{li} A_{ij} \cdot D\phi_{kj} B_{kl} \\
&= \sum_{j,k,l} (\nabla\psi^l)^T a_j \cdot D\phi_{kj} B_{kl} = \sum_{k,l} (\nabla\psi^l)^T B_{kl} \sum_j D\phi_{kj} a_j = \sum_{k,l} (\nabla\psi^l)^T B_{kl} A \nabla\phi^k \\
&= \sum_{k,l=1}^n \underbrace{B_{kl} A}_{\in \mathbb{R}^{m,m}} \nabla\phi^k \cdot \nabla\psi^l.
\end{aligned}
$$

Acknowledegements

Martin Rumpf for being an excellent advisor, providing all sorts of ressources, sharing his mathematical knowledge, supporting and enabling (mathematical) education beyond the scope of this thesis, putting trust in my mathematical and personal abilities, being in particular understanding in terms of family related issues and giving sincere advice for my future plans.

Benedikt Wirth (University of Münster) for his everlasting mathematical supervision, numerous intense discussions, various fruitful collaborations and his unlimited helpfulness.

Patrick Dondl (University of Freiburg) for sharing his knowledge on subdivision surfaces and material sciences, providing his code and participating in a long-term collaboration on branching patterns. I am in particular thankful to him for having me as guest at Durham University and being an excellent host.

Peter Schröder (Caltech) for having me as a guest at Caltech and taking a plenty of time for intense discussions—in terms of mathematical and personal education it was a pleasure and a wonderful time. In this context I am also thankful to Mathieu Desbrun, Fernando de Goes, Patrick Sanan and Keenan Crane for the pleasant atmosphere and the scientific input.

Max Wardetzky (University of Göttingen) for multiple intense collaborations and crucial mathematical input in particular in terms of (discrete) differential geometry; Benjamin Berkels (RWTH Aachen University) for an effective joint work on a generalized regression model and helpful assistance in coding issues; William Smith (York University) for sharing lots of data and excellent ideas as well as Chao Zhang (York University) for an interesting and on-going collaboration on shell PCA; Sergio Conti, Barbara Zwicknagl and Johannes Diermeier (University of Bonn) for several discussions on a reduced branching model.

Ricardo Perl for being a perfect officemate, for intense discussions about mathematical and non-mathematical matters as well as for lots of relaxing and inspiring coffee breaks. Benedict Geihe for long-term assistance in various mathematical and technical problems and an exciting conference trip as well as Alexander Effland, Martina Franken, Pascal Huber, Martin Lenz, Stefan Simon, Gabi Sodoge-Stork, Sascha Tölkes and Orestis Vantzos for being cooperative colleagues, providing a pleasant working atmosphere and helping me with all sorts of mathematical, technical and personal issues.

Dennis Tiege for spending much of his precious time on rendering our results on splines and creating beautiful video sequences.

Gesine Heeren for her everlasting support, honest sympathy and pivotal encouragement. ♡

Data The finger skeleton in Fig. 6.1, the elephants, *e.g.* in Fig. 6.11, the cats in Fig. 6.3 and the Armadillo in Fig. 7.5 were taken from [KMP07]; the cactus rest pose, *e.g.* in Fig. 7.3, was taken from [BS08]; the hand poses, *e.g.* in Fig. 6.7, were taken from [YLSL11] (courtesy of the AIM@SHAPE project); the face expressions, *e.g.* in Fig. 6.10 and Fig. 6.14, were originally from [FGR$^+$10] and pre-processed by William Smith; the body data in Fig. 7.2 was taken from [BRLB14]; the horse poses in Fig. 7.6 were taken from [SP04]. The corpus callosum shape data was derived from MRI and provided by the OASIS brain database; the 3D volumetric data of sugar beets acquired by MRI are courtesy of Ralph Metzner (Forschungszentrum Jülich). I am in particular thankful to Mario Botsch as well as to Kai Hormann and Tim Winkler, for providing their results for comparison (*cf*. Fig. 6.9 and Fig. 6.11).

Source code All implementations are done within the QuocMesh library (see `http://numod.ins.uni-bonn.de/software/quocmesh/`), the triangle mesh data structure is based on the Open-Mesh library (see `https://www.openmesh.org/` and [BSBK02]).